

Dissertation
submitted to the
Combined Faculties of the Natural Sciences and Mathematics
of the Ruperto-Carola-University of Heidelberg, Germany
for the degree of
Doctor of Natural Sciences

Put forward by
Daniel Rahner
born in Trier, Germany
Oral examination: June 18, 2019

Stellar Feedback and the Self-Regulation of Star Formation in Giant Molecular Clouds

A new semi-analytic approach

Referees:

Prof. Dr. Simon Glover

Priv.-Doz. Dr. Geneviève Parmentier

Abstract

Stars and the gas between them – the interstellar medium – are intrinsically coupled. Massive stars form in clouds of molecular gas and illuminate them with their radiation, thus creating regions of ionized hydrogen (HII regions) and photodissociation regions. Eventually these stars destroy their parent clouds via powerful feedback mechanisms: stellar winds, ionizing radiation, and supernova explosions. These feedback processes are a crucial self-regulation mechanism of star formation, since, as soon as the first massive stars have formed, further star formation is suppressed.

Stellar winds, radiation, and supernova feedback interact with each other in a highly non-linear manner. This complexity poses a problem not only for purely analytic approaches but also for three-dimensional hydrodynamical simulations due to the high computational cost. Here, I present a novel, semi-analytic, one-dimensional model, called `WARPFIELD`, which allows the cost-efficient simulation of the effects of stellar feedback from a massive star cluster on its natal giant molecular cloud (GMC). With `WARPFIELD` we can show that the strength of each feedback process depends strongly on time and environment. For a large range of GMC and star cluster properties we can also demonstrate that stellar feedback can naturally explain the observed inefficiency of star formation.

Zusammenfassung

Sterne und das Gas zwischen ihnen – das interstellare Medium – sind miteinander gekoppelt. Masse-reiche Sterne entstehen in Wolken aus molekularem Gas und erleuchten diese mit ihrer Strahlung. Dabei entstehen Gebiete aus ionisiertem Wasserstoff (HII-Regionen) und Photodissoziationsregionen. Schließlich zerstören massereiche Sterne die Wolken, in denen sie geboren wurden, durch verschiedene Rückkopplungsprozesse: stellare Winde, ionisierende Strahlung und Supernova-Explosionen. Diese Rückkopplungsprozesse stellen einen wichtigen Selbstregulierungsmechanismus der Sternentstehung dar, denn sobald sich die ersten massereichen Sterne gebildet haben, wird weitere Sternentstehung unterdrückt. Stellare Winde, Strahlung und Supernova-Explosionen wechselwirken auf hochgradig nicht-lineare Art miteinander. Diese Komplexität stellt ein Problem sowohl für rein analytische Ansätze dar als auch – aufgrund des hohen Rechenaufwands – für dreidimensionale hydrodynamische Simulationen. In dieser Arbeit stelle ich ein neues, semi-analytisches, eindimensionales Modell namens `WARPFIELD` vor, das es erlaubt, die Effekte stellarer Rückkopplungsprozesse eines massereichen Sternhaufens auf die mütterliche Riesenmolekülwolke mit niedrigem Rechenaufwand zu simulieren. Mit `WARPFIELD` lässt sich zeigen, dass die Stärke eines jeden Rückkopplungsprozesses stark zeit- und umgebungsabhängig ist. Außerdem können wir demonstrieren, dass stellare Rückkopplungsprozesse auf natürliche Art und Weise die beobachtete Ineffizienz von Sternentstehung erklären können.

Table of Contents

List of Figures	ix
List of Tables	xi
List of Publications	xiii
1 Introduction	1
1.1 Star Formation in Giant Molecular Clouds	2
1.1.1 Properties of Giant Molecular Clouds	3
1.1.2 From Prestellar Cores to the Initial Mass Function	7
1.1.3 High-Mass Star Formation	10
1.1.4 Star Formation Efficiencies of Giant Molecular Clouds	11
1.2 Stellar Feedback	14
1.2.1 Stellar Winds	14
1.2.2 Stellar Radiation	24
1.2.3 Supernovae	29
1.2.4 Effects of Stellar Feedback	33
1.3 Open Questions, Obstacles, and How to Address Them	36
2 Publications	41
2.1 Winds and Radiation in Unison	41
2.2 Forming Clusters within Clusters	62
2.3 WARPFIELD 2.0	68
3 Conclusion and Outlook	83
3.1 Conclusion	83
3.2 Outlook	87
Acknowledgements	91
Appendix A Abbreviations, Nomenclature, and Glossary	93
References	97

List of Figures

1.1	A cartoon representation of the life and death of a giant molecular cloud	3
1.2	Evolutionary sequence of molecular clouds	5
1.3	The Kroupa-Initial Mass Function	9
1.4	The massive star-forming region 30 Doradus in the Large Magellanic Cloud	12
1.5	Doppler shift in line-driven stellar winds	16
1.6	Structure of a wind/supernova-blown bubble in the energy-driven limit	19
1.7	Evolution of the wind terminal velocity, the mass loss rate, and the mechanical wind luminosity of a massive star cluster	23
1.8	Spectrum of a massive star cluster at an age of 0, 5, and 10 Myr	24
1.9	Evolution of the ionizing and non-ionizing luminosity of a massive star cluster	25
1.10	Structure of an expanding HII region during the second expansion phase	27
1.11	Collapse and neutrino-heating in a core-collapse supernova	30
2.1	The massive young cluster R136 at the centre of NGC 2070	62
3.1	Comparison of the distribution of WARPFIELD-EMP models of star-forming regions and observed HII regions in NGC 628 in a BPT-diagram	88
3.2	Synthetic H α observation of a Milky Way type galaxy	89

List of Tables

1.1	Physical properties of giant molecular clouds, clumps, and cores.	5
1.2	Overview of self-similarity solutions (for an environment with constant density ρ_0 and no gravity) of the form $R_2 \propto \rho_0^\alpha t^\beta$	34

List of Publications

Publications marked with an asterisk (*) are presented in this thesis. Abbreviations used here, e.g. for journal names, and throughout the thesis are explained in Appendix A.

1. Reissl S., Klessen R. S., Pellegrini E. W., **Rahner D.**, Pakmor R., Grand R., Gómez F., Marinacci F., and Springel V. Faithful reproduction of the Milky Way’s Faraday rotation measure map in galaxy simulations, *submitted to Nature*
2. Rousseau-Nepton, L., et al. (inc. **Rahner D.**). SIGNALS: I. Project Description, Science Goals, and Galaxy Sample, *submitted to MNRAS*
3. * **Rahner D.**, Pellegrini E. W., Glover S. C. O., Klessen R. S., (2019). WARPFIELD 2.0: Feedback-regulated minimum star formation efficiencies of giant molecular clouds, *MNRAS*, 483, 2547-2560
4. Rugel M. R., **Rahner D.**, Beuther H., Pellegrini E. W., Wang Y., Soler J. D., Ott J., Brunthaler A., Anderson L. D., Mottram J. C., Henning T., Goldsmith P. F., Heyer M., Klessen R. S., Bühr S., Menten K. M., Smith R. J., Urquhart J. S., Ragan S. E., Glover S. C. O., McClure-Griffiths N. M., Bigiel F., and Roy N., (2019). Feedback in W49A diagnosed with Radio Recombination Lines and Models, *A&A*, 622, 48
5. Ardizzone L., Kruse J., Wirkert S., **Rahner D.**, Pellegrini E. W., Klessen R. S., Maier-Hein L., Rother C., Köthe U., (2019). Analyzing Inverse Problems with Invertible Neural Networks, *ICLR conference paper*, New Orleans, USA
6. * **Rahner D.**, Pellegrini E. W., Glover S. C. O., Klessen R. S., (2018). Forming clusters within clusters: how 30 Doradus recollapsd and gave birth again, *MNRAS*, 473, L11–L15
7. * **Rahner D.**, Pellegrini E. W., Glover S. C. O., Klessen R. S., (2017). Winds and radiation in unison: a new semi-analytic feedback model for cloud dissolution, *MNRAS*, 470, 4453–4472

Chapter 1

Introduction

For life on Earth our star, the Sun, is indispensable. And yet, in the vastness of the Milky Way galaxy it is just one among hundreds of billions of stars – a rather small and unimposing one, for that matter, given there are stars that have masses more than a hundred times that of the Sun.¹ Clusters of stars form in dense regions inside huge associations of gas (mostly molecular hydrogen) which undergo gravitational collapse. In turn, the largest of such gas associations, giant molecular clouds, form in galactic spiral arms at large-scale shock fronts (see McKee and Ostriker 2007).

Fundamentally, star formation seems to be an inevitable consequence of gravity. However, there is a problem with this simple picture. The total mass of H_2 in the Milky Way is $\sim 6.5 \times 10^8 M_\odot$, most of which resides in molecular clouds (Roman-Duval et al. 2016; see also Stahler and Palla 2004). Typically, molecular clouds are gravitationally bound, so one would expect them to collapse and convert their gas into stars on a timescale comparable to the free-fall time (see Section 1.1.1). Consequently, with a typical H_2 density in giant molecular clouds of $n_{\text{H}_2} \sim 100 \text{ cm}^{-3}$ the star formation rate in the Milky Way should be $\sim 200 M_\odot \text{ yr}^{-1}$. The observed star formation rate in the Milky Way, however, is only $\sim 2 M_\odot \text{ yr}^{-1}$ (Licquia and Newman 2015). This disagreement of two orders of magnitude between theory and observation has puzzled scientists for many years and various hypotheses for why star formation is so slow and inefficient have been suggested (see e.g. Mac Low and Klessen 2004; Shu et al. 1987; Zuckerman and Palmer 1974). Today we know that one of the primary reasons is stellar feedback from massive stars (Krumholz et al. 2014).

Feedback comes in two forms. In general terms, positive feedback is the enhancement of a process by its own influence. Conversely, negative feedback is the suppression of a process by its own influence (Oxford Dictionary 2019). The process at hand – star formation – affects itself via various mechanisms, collectively referred to as stellar feedback. These are, among others, stellar winds, i.e. supersonic

¹The mass of the Sun is $M_\odot = 1.99 \times 10^{33} \text{ g}$ (Carroll and Ostlie 2007). In the following I will follow the nomenclature used in Zinnecker and Yorke (2007) and call a star a massive star or a high-mass star whenever its mass is sufficient to produce a core-collapse supernova at the end end of its lifetime (see Section 1.2.3). This is the case when the stellar mass M_* exceeds $\sim 8 M_\odot$ (corresponding to spectral types O and early B). Furthermore, I will refer to a star as very massive when $M_* \gtrsim 40 M_\odot$ (corresponding to early O stars and Wolf-Rayet stars). See Appendix A for a glossary of common astrophysical terms such as “Wolf-Rayet star”.

Introduction

ejections of material from the stellar surface, radiation, which both heats the ambient gas and transfers momentum to it, and supernovae, which are energetic explosions at the end of a massive star's life (i.e. $\sim 3 - 30$ Myr after the star is born). While stellar feedback can be positive, that is, the formation of a massive star triggers the formation of further stars, it is mostly negative. When sufficiently many massive stars have formed, stellar winds, radiation and supernova explosions inject enough energy and momentum into the surrounding gas to accelerate it to high velocities and to destroy the natal cloud in the process. Hence, stellar feedback is an important self-regulation mechanism of star formation.

Yet, how in detail this is achieved is still an open question. Large parameter studies, hampered by the high computational cost of three-dimensional hydrodynamic simulations and too high a degree of complexity for analytic approaches, are still missing. This is where I hope to contribute with this dissertation. In it I present a new approach to understand the self-regulation of star formation with a semi-analytic feedback model.

The thesis consists of three chapters. This first chapter serves as an introduction to the topic of star formation and stellar feedback. Its structure follows the evolutionary steps in the life of a giant molecular cloud (see Figure 1.1). Section 1.1 deals with the early days: The properties of giant molecular clouds, mostly before star formation, including how they can be observed, are presented in Section 1.1.1 followed by a discussion of star formation in general in Section 1.1.2 and the formation of massive stars in particular in Section 1.1.3. Section 1.1.4 represents the transition to adulthood, where I discuss the efficiency with which gas is converted into stars. Particular focus lies on the mismatch between (low) observed star formation efficiencies and (high) predicted star formation efficiencies.

The giant molecular cloud begins its final days as stellar feedback enters the stage in Section 1.2. Each feedback process is thoroughly discussed (stellar winds in Section 1.2.1, radiation in Section 1.2.2, and supernovae in Section 1.2.3) with a focus on how the process works and what its impact on the ambient cloud material is. Finally, the effects of stellar feedback, from the disruption of the natal cloud and triggered star formation to the eventual dissolution of the star cluster itself are explained in Section 1.2.4. Section 1.3 outlines where recent progress in the field of star formation and stellar feedback has been made, where obstacles exist, and where this thesis fits in.

Chapter 2 contains the publications which constitute the core of this thesis. A more detailed outline of the motivation for these studies can be found in Section 1.3 and in the introductory sections of the respective papers. Finally, Chapter 3 contains a conclusion and an outlook.

1.1 Star Formation in Giant Molecular Clouds

The idea that the Sun and the Solar System formed from a rotating cloud of nebular matter is old. This “nebular hypothesis” dates back to 18th century work by the philosophers and scientists Emanuel Swedenborg, Immanuel Kant, and Pierre-Simon Laplace (see Carroll and Ostlie 2007; Goodwin 2013). While parts of the nebular hypothesis have been proven wrong, its basis still stands: Molecular clouds are the nurseries of stars.

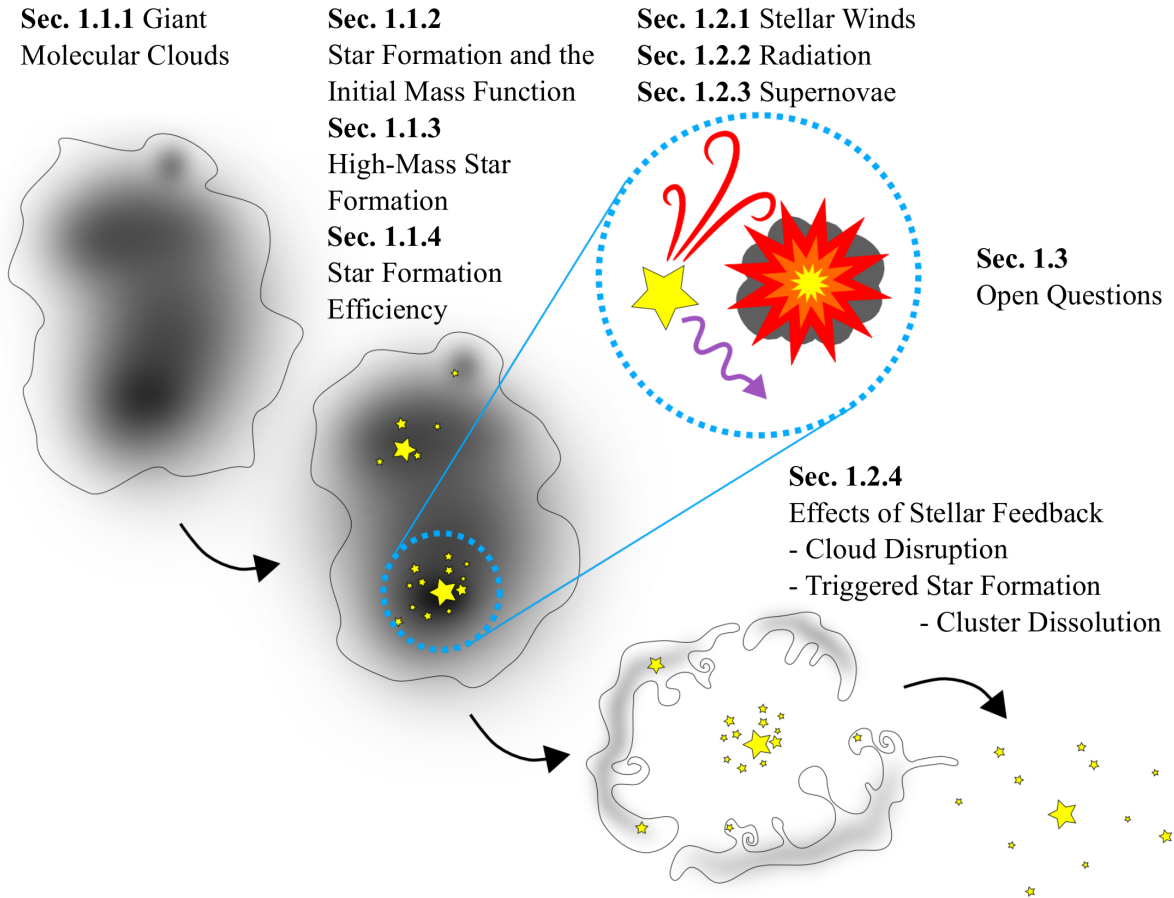


Fig. 1.1 A cartoon representation of the life and death of a giant molecular cloud. The various evolutionary stages are discussed in the corresponding sections.

1.1.1 Properties of Giant Molecular Clouds

Observations of Molecular Clouds

While H_2 is by far the most abundant molecule present in molecular clouds (at least a factor 10^4 more abundant in number density than the second most abundant molecule, CO), it is also the hardest to detect (Stahler and Palla 2004). Since H_2 lacks a dipole moment, its excited states decay primarily via quadrupole transitions. The temperature corresponding to the lowest transition is 510 K (equivalent to a wavelength of $28.2\mu\text{m}$), much hotter than typical molecular cloud temperatures of ~ 10 K. Still, detections of infrared-emission from shock-heated H_2 are possible via space-based telescopes (e.g. Rho et al. 2017).

Having a dipole moment and emitting strongly at radio frequencies, the primary tracer of molecular gas in molecular clouds is carbon monoxide (Klessen and Glover 2016). The temperature corresponding to the $J = 1 \rightarrow 0$ transition of $^{12}\text{C}^{16}\text{O}$ is 5.5 K (Stahler and Palla 2004). Hence, in molecular clouds with $T \sim 10$ K, the levels with rotational quantum number $J = 1$ and even with $J = 2$ are densely

Introduction

populated. From the CO ($J = 1 \rightarrow 0$) intensity distribution the size of the cloud can be derived while the line profile traces the velocity distribution of the molecular gas (Fukui and Kawamura 2010).

In order to estimate the amount of H₂, a conversion factor between observed ¹²CO integrated intensity and H₂ column density has to be assumed. In the Milky Way disk, this so-called X-factor is typically estimated to be $2 \times 10^{20} \text{ cm}^{-2} \text{ K}^{-1} \text{ km}^{-1} \text{ s}$ (Bolatto et al. 2013 and references therein). However, as Shetty et al. (2011), Glover and Mac Low (2011), and others show in hydrodynamical simulations which include a chemical network, the conversion factor can vary strongly depending on the environment. While the H₂ abundance is mainly set by the gas density and metallicity, the CO abundance is strongly influenced by the flux of dissociating photons. Consequently, the CO abundance falls rapidly below a mean extinction $\langle A_V \rangle \lesssim 3$ where CO-photodissociations become significant whereas the H₂ abundance is only affected at much lower extinction values (Glover and Mac Low 2011).

Clouds, Clumps, and Cores

These complications aside, surveys employing CO and other tracers of dense gas have been very successful at characterizing molecular clouds. First studies of molecular clouds took place in the 1970s via large-scale CO ($J = 1 \rightarrow 0$) surveys of the Galactic plane (Combes 1991; Fukui and Kawamura 2010, and references therein). The most massive molecular clouds, so-called giant molecular clouds (GMCs) have masses between 10^4 and $10^7 M_\odot$ (Blitz 1993) and their sizes range from tens to hundreds of pc. The characteristic density of a GMC is $n_{\text{H}_2} \sim 100 \text{ cm}^{-3}$ but GMCs exist in a large range of average densities, $30 \lesssim n_{\text{H}_2} \lesssim 1000 \text{ cm}^{-3}$ (e.g. Colombo et al. 2014; Hughes et al. 2010; Miville-Deschênes et al. 2017). In the Milky Way $\sim 80\%$ of H₂ is located in GMCs (Stahler and Palla 2004).

High-density ($n_{\text{H}_2} \gtrsim 1000 \text{ cm}^{-3}$) regions within molecular clouds are called clumps. They have sizes of ~ 1 pc, masses of $\sim 100 - 1000 M_\odot$ and are the sites of star cluster formation (Goodwin 2013; Rathborne et al. 2006). Even denser regions within a cloud are referred to as cores. Cores, with sizes below 0.1 pc, masses of $1 - 100 M_\odot$ and densities of $n_{\text{H}_2} \gtrsim 10^5 \text{ cm}^{-3}$, are the sites where individual stars or multiple systems form (Rathborne et al. 2006). A summary of the properties of GMCs, clumps, and cores is presented in Table 1.1. These definitions are not strict but somewhat fuzzy, just as there is probably a continuous transition between the different types of objects (compare also with definitions presented in Goodwin 2013; Klessen and Glover 2016, and references therein).

Lifetimes of Giant Molecular Clouds

Observationally, GMCs can be separated into three distinct evolutionary categories (Fukui et al. 1999, see Fig. 1.2):

- **type I:** no O stars observed in the GMC
- **type II:** GMC only contains regions of ionized hydrogen (so-called HII regions) with low H α luminosity ($L_{\text{H}\alpha} < 10^{37} \text{ erg s}^{-1}$)

1.1 Star Formation in Giant Molecular Clouds

Table 1.1 Physical properties of giant molecular clouds*, clumps†, and cores‡.

Object	n_{H_2} (cm^{-3})	R (pc)	T (K)	M (M_{\odot})
GMC	~ 100	10 – 100	10 – 20	$10^4 - 10^7$
Clump	$10^3 - 10^7$	~ 1	50 – 200	$10^2 - 10^3$
Core	$> 10^5$	< 0.2	10 – 250‡	1 – 100

*Blitz (1993); Goodwin (2013); Stahler and Palla (2004)

†Rathborne et al. (2006)

‡Cores with temperatures above 50 K are so-called “hot cores” which are internally heated and associated with high-mass star formation.

- **type III:** GMC contains both luminous HII regions and star clusters

How these categories describe an evolutionary sequence of star formation in GMCs will become clear in Section 1.2. From CO observations of 191 GMCs in the Large Magellanic Cloud (LMC) Kawamura et al. (2009) estimate that half of all GMCs are type II clouds, while roughly a quarter are classified as type I and III (24 % and 26 % respectively). About 66 % of star clusters younger than 10 Myr are still associated with their parent GMC; therefore – assuming a constant cluster formation rate over the last 10 Myr – the lifetime of type III clouds is estimated to be ~ 7 Myr (Kawamura et al. 2009). From this follows a timescale of ~ 6 and ~ 13 Myr for type I and II clouds respectively, with a total GMC lifetime of $t_{\text{GMC}} \sim 26$ Myr.

More recently, Kruijssen and Longmore (2014) presented another method to estimate timescales for cloud lifetimes and star formation which does not require individual clouds to be resolved. Their

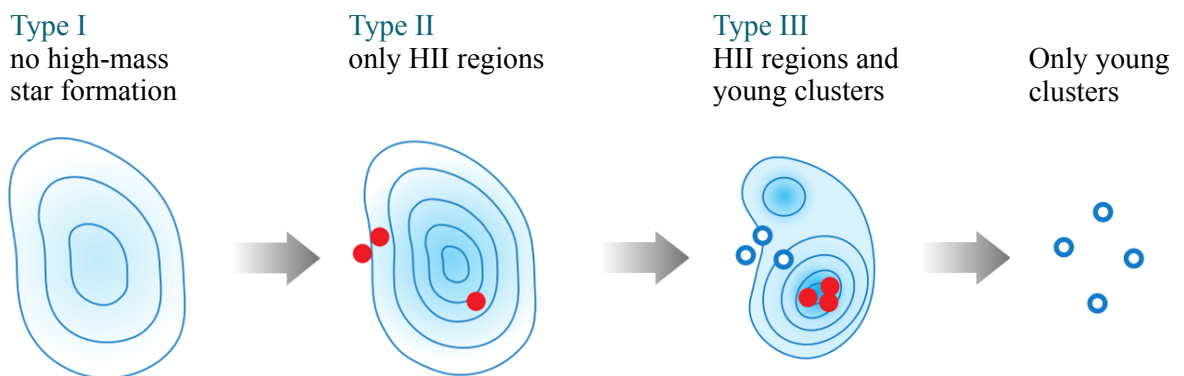


Fig. 1.2 Evolutionary sequence of molecular clouds. Filled red circles represent HII regions and blue circles represent star clusters. Contours and blue shading denote the gas surface density. Adapted from Fukui and Kawamura (2010) with permission from Annual Reviews.

Introduction

method builds on the observation that the Schmidt-Kennicutt law of star formation² (Kennicutt 1998; Schmidt 1959) breaks down on small spatial scales. Focusing moderately small apertures ($\lesssim 300$ pc) on either CO peaks or H α peaks (the latter are associated with ongoing star formation) results in very different gas depletion times (Schruba et al. 2010). This scale-dependent difference in depletion times can be used to obtain a statistical average of how long dense gas is detectable before the onset of star formation and how long star formation in a GMC lasts (Kruijssen and Longmore 2014; Kruijssen et al. 2018).

Turbulence

Without any support against gravitational collapse, a cloud would collapse in a free-fall time t_{ff} , which for a spherical object with density ρ is defined as

$$t_{\text{ff}} = \sqrt{\frac{3\pi}{32G\rho}} \quad (1.1)$$

where G is the gravitational constant. For a GMC with a typical density $n_{\text{H}_2} = 100 \text{ cm}^{-3}$ the free-fall time is only 4 Myr, so the question arises how GMCs can live for more than 10 Myr. Part of the answer is turbulence, i.e. disorderly and randomly fluctuating gas flows inside the cloud (Elmegreen and Scalo 2004; Klessen and Glover 2016; Mac Low and Klessen 2004). Velocity dispersions in GMCs are related to their effective radius R_e via

$$\sigma_{\text{1D}} = 0.7 \left(\frac{R_e}{\text{pc}} \right)^{0.5} \text{ km s}^{-1} \quad (1.2)$$

(Solomon et al. 1987), a relation originally found by Larson (1981) but with a slightly different exponent. Obviously, for typical GMC sizes ($R_e \geq 10$ pc) the turbulent motions of the gas are highly supersonic with respect to the sound speed of molecular gas, $c_s \sim 0.2 \text{ km s}^{-1}$. In addition, the interstellar medium (ISM) in molecular clouds is also super-Alfénic (e.g. Heyer and Brunt 2012) which means that the turbulent energy density dominates over both the thermal and the magnetic energy density (Klessen and Glover 2016).

As first shown in simulations by Heitsch et al. (2001); Klessen et al. (2000) the role of turbulence is twofold: On the one hand, it stabilizes the cloud against global collapse; without a high degree of turbulence, a GMC would indeed collapse under the influence of self-gravity with nearly the free-fall speed and star formation would occur very fast. On the other hand, supersonic turbulence can compress the ISM to high densities. If a thus compressed region becomes sufficiently dense, gravity takes over and collapse ensues. On local scales, turbulence can thus drive star formation.

Energy from large scales is gradually transferred to smaller scales in what is known as the turbulent cascade. At very small scales, close to the particle mean free path, molecular viscosity causes the

²The Schmidt-Kennicutt law relates gas surface densities with star formation rate surface densities, i.e. $\Sigma_{\text{SFR}} \propto \Sigma_{\text{gas}}^n$ with $n \sim 1.4$.

turbulence to dissipate by converting kinetic energy to thermal energy which is then radiated away (see e.g. reviews by Hennebelle and Falgarone 2012; Mac Low and Klessen 2004). The timescale for dissipation of the turbulent energy t_d is comparable to the turbulent crossing time,

$$t_d \sim \frac{L}{\sigma_{\text{ID}}} \quad (1.3)$$

where L is the scale at which turbulence is injected into the system (Mac Low 1999). Thus, the turbulence in a GMC with a radius of 10 pc should decay significantly on a timescale comparable to a free-fall time, regardless of the magnetic field strengths present (Mac Low and Klessen 2004). But even at late times a cloud is not in free-fall collapse. Energy to keep up turbulence is being continuously injected into the cloud – in part from external sources such as gas inflow from the large-scale filaments (Klessen and Hennebelle 2010), in part internally via stellar feedback processes (see Section 1.2).

1.1.2 From Prestellar Cores to the Initial Mass Function

Core Collapse

Gravitationally bound cores form in shocks at stagnation points of convergent flows in GMCs caused by turbulent motions (see Section 1.1.1). When a region's mass exceeds the local Jeans mass (Jeans 1902)

$$\begin{aligned} M_J &= \frac{\pi}{6} \frac{c_s^3}{G^{3/2} \rho^{1/2}} \\ &\approx 2M_\odot \left(\frac{c_s}{0.2 \text{ km s}^{-1}} \right)^3 \left(\frac{n}{10^3 \text{ cm}^{-3}} \right)^{-1/2} \end{aligned} \quad (1.4)$$

where n is the number density and c_s is the sound speed of the gas, it collapses on a free-fall timescale (Shu et al. 1987).

Gravitational collapse of the core starts isothermally as dust grains in the ISM are able to radiate away heat created by the contracting core (Larson 1969, see also Goodwin 2013). However, at a critical density of $\rho_{\text{crit}} \sim 10^{-13} \text{ g cm}^{-3}$ the ISM becomes opaque to infrared emission from dust (Larson 1973, and references therein). Thus, heat cannot be radiated away efficiently any more and the collapse becomes adiabatic. A protostar with a size of $\sim 1 \text{ AU}$ forms and, as it continues to accrete material, its temperatures rises, slowing down the gravitational collapse (Larson 1969). At $T \gtrsim 2000 \text{ K}$, thermal dissociation of H_2 becomes efficient (Lockwood et al. 1964). The dissociation of molecular hydrogen acts as a heat sink allowing the gas to collapse rapidly to stellar densities, $\rho \sim 1 \text{ g cm}^{-3}$. After all H_2 has been dissociated, the pre-main sequence star contracts slowly, its temperature rises with the onset of hydrogen fusion and it enters the main sequence.

From Eq. (1.4) follows that a prestellar core forms, for example, when turbulence compresses ~ 1 or $2M_\odot$ of gas to densities higher than 10^3 cm^{-3} . For less massive cores a higher density and thus stronger turbulent compression is necessary. On the other hand, a more massive core becomes

Introduction

Jeans-unstable at a lower density but is expected to fragment into multiple smaller cores (Goodwin 2013). Hence, the core mass function (CMF), i.e. the probability distribution of masses for a population of prestellar cores, peaks at $\sim 1 - 2 M_{\odot}$ and falls off towards higher and lower masses (e.g. Cheng et al. 2018; Liu et al. 2018).

The Origin of the Initial Mass Function

Observationally, the CMF and the mass distribution of stars that have just entered the main sequence (the initial mass function, IMF) have been found to be remarkably similar (Alves et al. 2007; André et al. 2010; Motte et al. 1998; Nutter and Ward-Thompson 2007). One explanation is that the CMF, whose shape is set by the properties of turbulence, assembles first and afterwards core collapse ensues with a one-to-one mapping from the CMF to the IMF (e.g. Hennebelle and Chabrier 2008). However there are problems with this simple scenario, such as an inherent dependence of the IMF on the turbulent Mach number (Hennebelle and Chabrier 2008; Padoan and Nordlund 2002), which is not observed (Bastian et al. 2010), and a timescale problem³ (Clark et al. 2007).

In the opposing model of competitive accretion, the CMF is inconsequential for the IMF. Instead, cores and later protostars continuously accrete material from the cloud’s gas reservoir (Bonnell et al. 2001a,b; see also Bonnell et al. 2007). In this scenario star formation and the gathering of mass occur simultaneously. Since some cores by chance sit in regions of higher densities they accrete more material than cores sitting in low-density regions of the cloud. These “lucky” cores grow faster and increase their gravitational attraction. They are thus able to accrete even more gas, depleting the reservoir for the remaining cores (see also Girichidis et al. 2012; Peters et al. 2010). A massive star could thus have started as a low mass core that happened to accrete more ambient gas than its “unlucky” neighbour.

Bonnell et al. (2007) and Goodwin (2013) argue that in reality both processes, direct formation of stars from cores which formed via turbulent fragmentation and competitive accretion of gas onto these cores, are probably important. While turbulent fragmentation may set the peaked shape of the IMF, competitive accretion certainly plays a role for the formation of massive stars in very dense environments where accretion during the star formation process is unavoidable (Goodwin 2013). In addition, the high-mass end of the IMF is probably affected by (proto-)stellar feedback, which typically lowers the number of massive stars (Dale et al. 2012a) and possibly sets an upper mass limit (see Section 1.1.3). For a more comprehensive description of the possible origin of the IMF, see Offner et al. (2014) and Klessen and Glover (2016).

Parametrizing the Initial Mass Function

The shape of the IMF is crucial for the fate of the natal molecular cloud and the star cluster itself as the amount of stellar wind and supernova feedback is sensitive to the number of massive stars present

³For a core with mass M_c to be star-forming it must hold that $M_c \geq M_J$. If at the onset of collapse all star-forming cores have similar multiples of the Jeans mass, more massive star-forming cores must have lower densities (see Eq. 1.4) and it follows that $t_{\text{ff}} \propto M_c$. Since the CMF is time-independent, one would therefore expect the IMF to be steeper than the CMF (because low-mass stars form faster and hence in greater number).

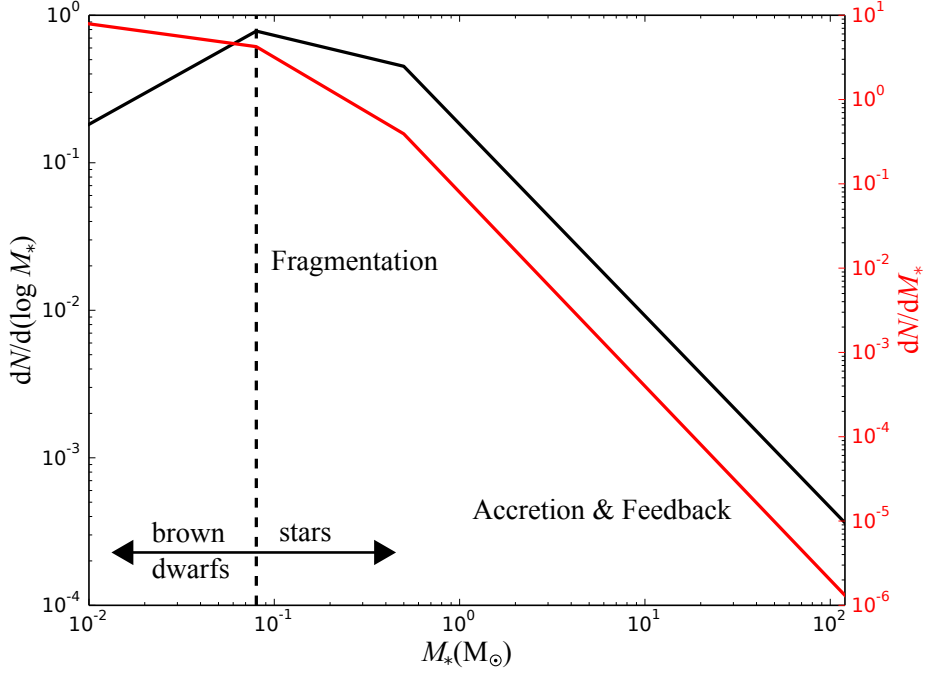


Fig. 1.3 The Kroupa-IMF in logarithmic (black) and linear mass units (red), normalized to $N = 1$ (assuming $M_{*,\max} = 120 M_{\odot}$). The dashed line marks the border between sub-stellar objects and stars. The peak of the IMF is likely set by gravitational fragmentation of a collapsing region while the the high-mass end is influenced by ongoing accretion onto protostars and feedback (see main text and Bonnell et al. 2007).

(see Section 1.2). Fortunately, the IMF appears to be remarkably universal (Bastian et al. 2010) and all parametrizations of the IMF agree on the high-mass end (e.g. Chabrier 2003; Kroupa 2001; Salpeter 1955; see Figure 1 in Offner et al. 2014). One popular parametrization of the IMF which will be the focus here has been introduced by Kroupa (2001, 2002). The number of stars N with mass M_* is given by

$$\frac{dN}{d\log(M_*)} \propto \begin{cases} M_*^{0.7}, & 0.01 M_{\odot} < M_* \leq 0.08 M_{\odot} \\ M_*^{-0.3}, & 0.08 M_{\odot} < M_* \leq 0.5 M_{\odot} \\ M_*^{-1.3}, & 0.5 M_{\odot} < M_* \leq M_{*,\max} \end{cases} \quad (1.5)$$

(see Figure 1.3) where the first of the three power-law parts corresponds to sub-stellar objects. The upper mass limit $M_{*,\max}$ of the IMF is debated (see Section 1.1.3).

There are two features of the IMF that are worth pointing out here: firstly, the peak at $\sim 0.1 - 0.5 M_{\odot}$ and secondly, the rarity of massive stars. A star cluster with a stellar mass of $10^4 M_{\odot}$ has only a handful of stars more massive than $100 M_{\odot}$ (the exact number depends on the exact shape of the IMF at the low-mass end and on the upper mass limit for stars) with the average mass of a newborn star

Introduction

being $\sim 0.5 M_{\odot}$ (hence the vast majority of stars are M dwarfs). In less massive star clusters the IMF appears to be stochastically sampled (Lamb et al. 2010, but see also Section 1.1.3). For example, of two young star clusters with a total stellar mass of $1000 M_{\odot}$ one might host a very massive star while the other might not. This has important consequences for star formation and the evolution of the parental cloud since stellar wind feedback is dominated by very massive stars (see Section 1.2).

Furthermore, as stars undergo stellar evolution, the mass distribution changes as stellar winds of very massive stars blow away their outer atmospheres causing them to lose a large fraction of their mass⁴ (Limongi 2017). In addition, very massive stars live only for a short amount of time (3 – 4 Myr for a $120 M_{\odot}$ star, Ekström et al. 2012) and dynamical evolution of star clusters preferably ejects low-mass stars. The present day mass function of stars inside a star cluster can thus strongly deviate from the original IMF.

1.1.3 High-Mass Star Formation

Since the most massive stars only live for several Myr and are also the easiest ones to detect, they serve as an important indicator of the “current” star formation rate of a system (Osterbrock and Ferland 2006). The birth process of massive stars can be summarized by compression, collapse, accretion, and disruption (Zinnecker and Yorke 2007). First, gravo-turbulent compression and fragmentation of the cloud produces prestellar cores (Mac Low and Klessen 2004, see also Section 1.1.2). Second, parts of these cores collapse into pressure-supported protostellar embryos with initial masses of the order $10^{-3} M_{\odot}$ (Larson 1969). Third, accretion onto these massive star precursors commences while they evolve toward the main sequence. As soon as a young massive star starts to emit radiation and to launch outflows and winds, accretion of material onto the star is hindered. Finally, the parental cloud is destroyed by stellar feedback, further star formation is shut off, and a cluster of OB stars or an OB association emerges from the gas (compare with GMC types presented in Section 1.1.1).

Stellar feedback constitutes a problem for the formation of very massive stars. If radiation pressure from the star counteracts accretion, how can stars grow to masses of $100 M_{\odot}$? Close to the star, at temperatures above ~ 1500 K, dust grains get evaporated making the infalling ISM nearly transparent to the stellar radiation (Stahler and Palla 2004). Farther out, though, at the dust sublimation radius and beyond, where dust grains are still intact, photons can deposit their momentum. Assuming spherical symmetry, at the sublimation radius the ratio of radiation pressure to ram-pressure from gas free-falling towards the star Γ is given by

$$\Gamma \approx 2 \times 10^{-5} \frac{(L/L_{\odot})^{6/5}}{(M_*/M_{\odot})^{3/5}} \quad (1.6)$$

(Larson and Starfield 1971) where L is the stellar bolometric luminosity. This ratio approaches unity at $M_* \sim 25 M_{\odot}$ and in more massive stars outward directed radiation pressure would prevent any

⁴The mass loss due to stellar winds depends not only on the initial mass of the star but also its metallicity and rotational speed. A non-rotating star at with an initial mass of $40 M_{\odot}$ ($120 M_{\odot}$) at solar metallicity loses $\sim 10\%$ (60%) of its mass over its lifetime. The mass loss rates tend to increase for higher rotational speeds and to decrease for lower metallicities (Limongi 2017, see also Section 1.2.1).

accretion.⁵ This result has been qualitatively reproduced by Kahn (1974) and Kuiper et al. (2010), among others, who find an upper limit of $40 M_{\odot}$. Exacerbating the problem is the brief lifespan of these stars of only several Myr (Ekström et al. 2012). Thus, the time available for accretion is short and high accretion rates are hence indispensable for the formation of very massive stars. If collapse and accretion were spherically symmetric, this would indeed prevent the formation of stars more massive than $\sim 40 M_{\odot}$ (Zinnecker and Yorke 2007).

However, it has been shown in two- and three-dimensional simulations that accretion can continue through a centrifugally supported, optically thick circumstellar disk: While radiation pressure halts and even reverses the infall of matter in the polar regions, forming low-density cavities there, the star can still accrete in its equator region, an effect known as the “flashlight effect” (Yorke and Sonnhalter 2002). These disks live sufficiently long to allow for the formation of stars exceeding $100 M_{\odot}$ (Kuiper et al. 2010). Taking into account protostellar outflows and photoionization as well, simulations by Kuiper and Hosokawa (2018) demonstrated that at least the formation of stars with $M_* \sim 95 M_{\odot}$ is still possible.

Observationally, the high-mass limit of the IMF is also still debated. Observations have previously suggested a value of $M_{*,\max} \sim 150 M_{\odot}$ (for present-day, roughly solar metallicity stars; Figer 2005; Koen 2006). There is evidence, however, that the IMF extends to even higher masses. 30 Doradus (also known as the Tarantula Nebula, shown in Figure 1.4) is a massive star-forming region in the LMC (see also Section 2.2). Four stars within its central starburst cluster R136 may exceed the canonical upper mass limit, having masses in the range $165 \leq M_* \leq 320 M_{\odot}$ (Crowther et al. 2010). Banerjee et al. (2012a,b) argue that these stars may have formed via dynamically induced binary mergers.

There is also an ongoing debate on whether the IMF is populated in a stochastic or in an ordered, bottom-up fashion (e.g. Gouliermis et al. 2018; Lamb et al. 2010; Weidner and Kroupa 2006). In the latter scenario, where massive stars only ever form when a sufficient number of low-mass stars are present, a strict relation between the mass of a star cluster and the mass of its most massive member is to be expected.⁶ If, on the other hand, the IMF is stochastically sampled, that is, the mass of each star is drawn randomly, massive stars could in principle also form in isolation, although with a low probability. In that case any star cluster could host a star with a mass of $M_{*,\max}$. While there are indications that isolated young massive stars may not exist, neither scenario is yet conclusively ruled out (Gouliermis et al. 2018; Stephens et al. 2017).

1.1.4 Star Formation Efficiencies of Giant Molecular Clouds

Consider a GMC which, while initially being supported by turbulence, has now lost most of its turbulent support through dissipation of energy. Without any injection of new energy into the system, collapse ensues. In that case, it only takes a few free-fall times for nearly all the available gas to collapse into dense cores in which then protostars form (Klessen and Burkert 2001). This is not what is observed.

⁵This is similar to the Eddington limit (Eddington 1926).

⁶For example, O stars should only form as members of star clusters with masses above $250 M_{\odot}$ (Weidner and Kroupa 2006).

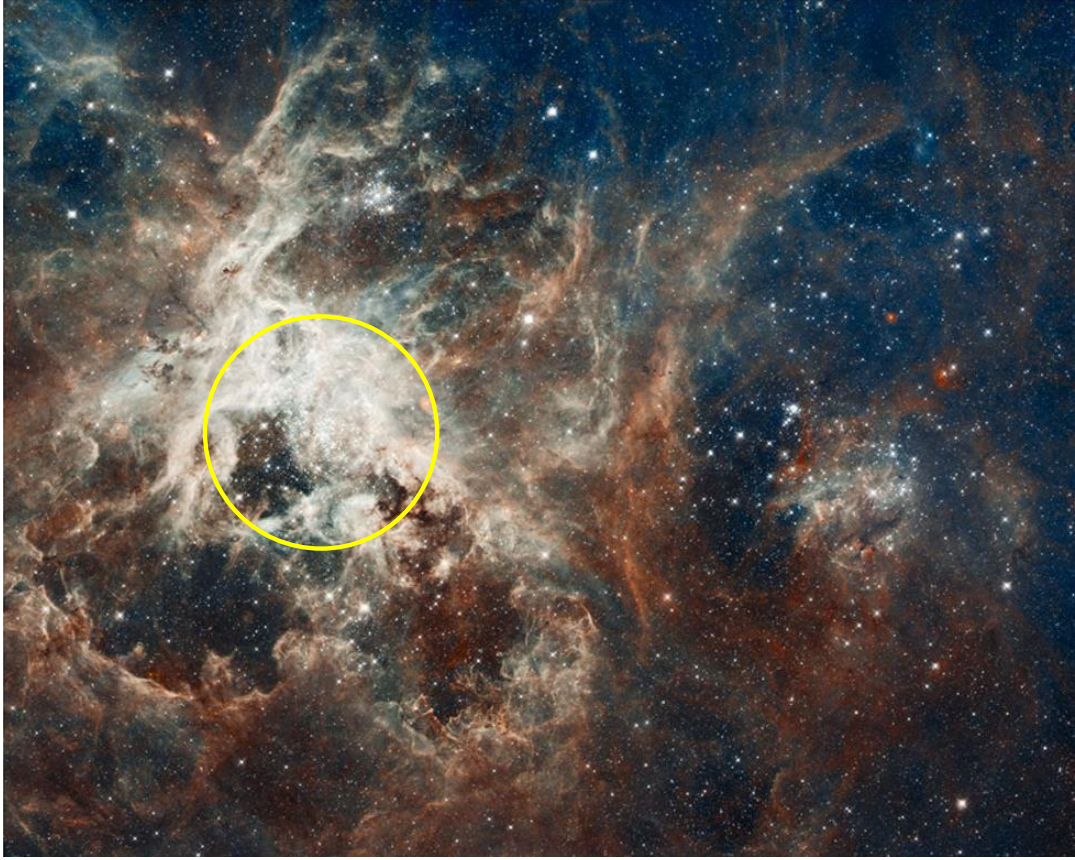


Fig. 1.4 Colour composite image of the massive star-forming region 30 Doradus in the LMC (details in Cignoni et al. 2015). The massive star cluster NGC 2070 which contains R136 at its centre (see also Figure 2.1) is marked with a circle. The occurrence of various shells and X-ray emitting bubbles in 30 Dor is also an indicator that the birth of massive stars has profound impact not only on the shape of the IMF but on the natal cloud as well. Credit: ESA/Hubble & NASA.

In order to describe what *is* observed, it is convenient to define the star formation efficiency (SFE) ϵ_{SF} of a system. The SFE is the fraction of initial gas mass $M_{\text{gas},0}$ (before the onset of star formation) that is converted into stellar mass M_* . As the initial gas mass is in general not accessible to the observer when measuring the star formation efficiency, the initial gas mass has to be reconstructed from the gas mass still present after star formation $M_{\text{gas},1}$. Thus,

$$\epsilon_{\text{SF}} \equiv \frac{M_*}{M_{\text{gas},0}} = \frac{M_*}{M_* + M_{\text{gas},1}}. \quad (1.7)$$

The star formation efficiency per free-fall time

$$\epsilon_{\text{ff}} \equiv \frac{\langle \dot{M}_* \rangle}{M_{\text{gas},0}} t_{\text{ff}} \quad (1.8)$$

1.1 Star Formation in Giant Molecular Clouds

is a measure of the specific star formation rate $\langle \dot{M}_* \rangle / M_{\text{gas},0}$ in time units of the free-fall time t_{ff} (Krumholz and McKee 2005). Unimpeded collapse of the cloud would suggest a high value for the SFE per free-fall time ($\epsilon_{\text{ff}} \gtrsim 0.3$ in the case of Klessen and Burkert 2001) and a final SFE of 1.

In a study of local molecular clouds with $M_{\text{gas},1} < 10^5 M_{\odot}$, Lada et al. (2010) found $\epsilon_{\text{SF}} \sim 0.01$, albeit with large scatter, $0.002 < \epsilon_{\text{SF}} < 0.1$. SFEs in GMCs with $M_{\text{gas},1} > 10^5 M_{\odot}$ have a similar range with a luminosity-weighted average of $\langle \epsilon_{\text{SF}} \rangle = 0.08$ (Murray 2011). Obviously, this is far from a full conversion of gas into stars. Observed star formation efficiencies per free-fall time are of the order ~ 0.01 , although with some notable exceptions (see Figure 5 in Krumholz and Tan 2007 and references therein).

This mismatch between theoretical predictions and observations has required a refinement of theoretical models and several solutions have been put forward (see Krumholz et al. 2018). Magnetic fields stabilize molecular clouds against gravitational collapse making them an obstacle to rapid star formation (Shu et al. 1987). However, at typical densities of GMCs and above, i.e. $n_{\text{H}_2} \gtrsim 150 \text{ cm}^{-3}$, gravity dominates over magnetic pressure (see review by Crutcher 2012). Another possible reason could lie in the boundness (or rather lack thereof) of molecular clouds. An unbound cloud would dissipate on a dynamical timescale with little star formation taking place. However, observational evidence suggests that the dense gas, for which ϵ_{SF} and ϵ_{ff} is typically measured, is indeed gravitationally bound and star formation is initiated quickly (Urquhart et al. 2018).

This leaves two mechanisms which are typically invoked to explain the inefficiency of star formation: turbulence and stellar feedback. In part, these two processes are two sides of the same coin. For turbulence to suppress star formation in the long term, it has to be maintained by energy that is injected into the cloud; otherwise turbulence dissipates roughly within a cloud crossing time (Mac Low 1999). While some part of this energy is provided by external sources such as accretion from the large-scale reservoir onto the molecular cloud (Elmegreen and Burkert 2010; Goldbaum et al. 2011; Klessen and Hennebelle 2010), another part is injected internally by stellar feedback (Goldbaum et al. 2011; Offner and Liu 2018; see also the review by Hennebelle and Falgarone 2012 on turbulence).⁷

⁷Goldbaum et al. (2011) find that similar amounts of energy are injected by accretion and photoionization feedback respectively.

1.2 Stellar Feedback

Stellar feedback influences the star formation process both directly and indirectly. It drives turbulence, making star formation slow, and, if strong enough, destroys the natal cloud by accelerating the ISM to the escape velocity, thereby shutting off star formation all together. How star formation regulates itself via various stellar feedback processes is the focus of this section. Some forms of early (protostellar) feedback have already been mentioned in Section 1.1.3; e.g. how accretion of matter onto a protostar proceeds is regulated by its radiation pressure as well as protostellar outflows. While outflows and jets⁸ are important on small scales by breaking up dense gas regions and driving turbulence in low-mass, low-density clouds, on large scales and in massive clouds their influence wanes; when massive stars are present, other feedback processes dominate (Bally 2011, 2016; Krumholz et al. 2018; Matzner 2007).

Let us now focus on forms of stellar feedback that occur after the star has entered the main sequence.⁹ These are

- stellar winds (see Section 1.2.1)
- stellar radiation (photoionization and radiation pressure, see Section 1.2.2)
- supernova explosions (see Section 1.2.3)

The effects of stellar feedback from a massive star cluster on the fate of the parent molecular cloud as a whole (including dispersal of the cloud and triggered star formation within the cloud) and on the star cluster itself are discussed in Section 1.2.4.

1.2.1 Stellar Winds

A stellar wind is the supersonic, more or less continuous ejection of matter from the stellar surface which is characterized by the rate at which mass is removed \dot{M} (the mass loss rate) and the wind's terminal velocity v_∞ , i.e. the ejecta's velocity at large distances from the star (Lamers and Cassinelli 1999). Not only the Sun but nearly all stars drive stellar winds which can be categorized into three classes (Owocki 2013):

1. Coronal winds which are driven by high thermal pressure in the corona of a star. The solar wind and winds of other cool main sequence stars are coronal winds. Since the mass loss rate is very small ($\dot{M} \sim 10^{-14} M_\odot$ in the case of the Sun, i. e. $\sim 0.01\%$ of its total mass over its lifetime; Aschwanden et al. 2001, and references therein), the effect on the star's evolution is negligible.
2. Winds from cool giants and supergiants. Due to their size, such stars have a lower surface gravity which facilitates stronger but slower winds. In the case of a Red Giant, $v_\infty \sim 10 - 50 \text{ km s}^{-1}$ and

⁸Protostellar jets are highly collimated with velocities $v \sim 100 - 1000 \text{ km s}^{-1}$, probably driven by magnetohydrodynamics processes in the interaction between the star and the rotating disk, while (molecular) outflows are less collimated with $v \lesssim 30 \text{ km s}^{-1}$ (Frank et al. 2014).

⁹Note that there could well be some time-overlap with the afore-mentioned processes.

$\dot{M} \sim 10^{-8} M_{\odot} \text{ yr}^{-1}$. In later evolutionary stages, stellar pulsations can launch even stronger winds with significant mass loss.

3. Winds from hot, massive, luminous stars which are driven by radiation pressure on electrons and ions. In OB stars the radiation couples to the gas via line scattering (mainly on metals¹⁰ such as C, N, O, ...). Such winds reach terminal velocities of $\sim 1000 - 3000 \text{ km s}^{-1}$ and cause a mass loss of $\sim 10^{-10} - 10^{-5} M_{\odot} \text{ yr}^{-1}$. In Wolf-Rayet stars the mass loss rate is so high that the stellar photosphere lies within the wind itself. Evolved Wolf-Rayet stars are strongly depleted in hydrogen because their hydrogen envelope has been blown away. Mass loss rates are even higher if a star is undergoing the luminous blue variable phase during which “superwinds” are launched (lasting years or decades) with $\dot{M} \sim 0.1 - 1 M_{\odot} \text{ yr}^{-1}$. Line-driven winds from massive stars are the focus of this section and they will be discussed in more detail below.

Line-Driven Winds from Massive Stars

Each photon emitted by a star carries the momentum $h\nu/c$ where h is the Planck constant, ν is the frequency, and c is the speed of light. Continuum processes (scattering on electrons, scattering or absorption on dust, and bound-free transitions) are characterized by their opacity κ (Owocki 2013). The total absorption of radiation is given by the optical depth

$$\tau = \int_{R_*}^{\infty} \kappa \rho(r) dr \quad (1.9)$$

where the integral extends from the stellar surface (R_* is the stellar radius) to the observer at infinity. Let us consider a wind that is steadily free-streaming at a constant velocity into a surrounding vacuum. The density profile at $r > R_*$ is then given by

$$\rho(r) = \frac{\dot{M}}{4\pi r^2 v_{\infty}} \quad (1.10)$$

and thus

$$\tau = \frac{\kappa \dot{M}}{4\pi R_* v_{\infty}}. \quad (1.11)$$

Using appropriate values for the solar wind and the opacity of electron scattering, one finds $\tau \sim 10^{-8}$ (Owocki 2013). Clearly, electron scattering is not important here.¹¹ In Wolf-Rayet stars on the other hand with much higher \dot{M} the winds can become optically thick even to electron scattering.

Scattering on free electrons is not confined to narrow wavelength ranges, unlike bound-bound transitions (line-scattering). Nevertheless, it is line-scattering that plays the dominant role in driving winds in massive stars (Puls et al. 2008). When atomic lines resonate with continuum photons they

¹⁰Astronomers are used to referring to anything heavier than He as a metal.

¹¹As a side note, the re-emitted photon does not contribute to the net momentum as it emitted isotropically so that the momentum integral over all directions vanishes and only the radial contribution from the first scattering remains.

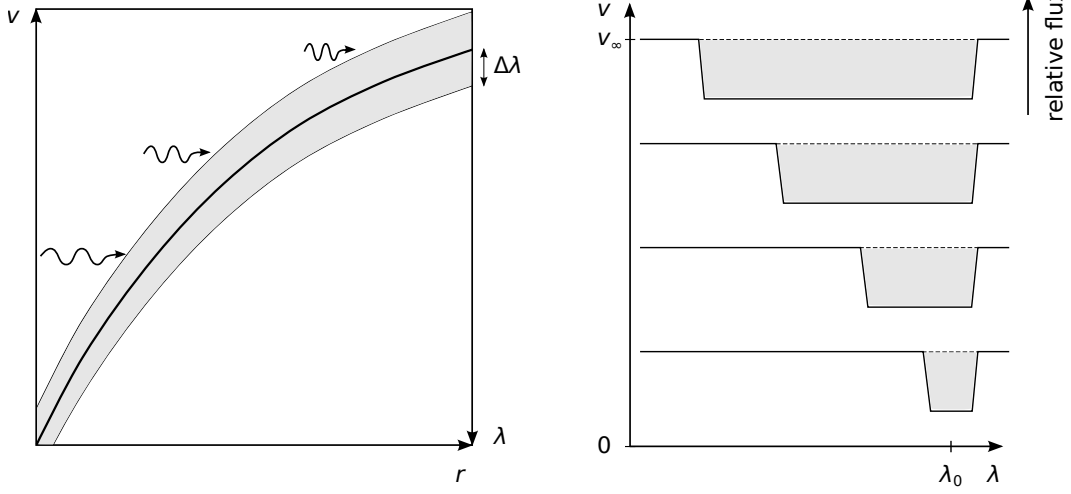


Fig. 1.5 *Left*: The wind velocity v as a function of distance from the star r and the corresponding resonant wavelength in the rest frame of the star λ'_0 (thick solid line). The grey area shows the wavelength range of photons that can be absorbed by the wind material, i.e. $\lambda'_0 - \Delta\lambda \leq \lambda \leq \lambda'_0 + \Delta\lambda$. At larger distances from the star where the wind is faster, photons with smaller λ are absorbed. *Right*: With increasing wind velocity a Doppler-broadened line-absorption trough towards wavelengths smaller than λ_0 is carved out. Adapted from Owocki (2013) with permission from Springer Nature and Springer eBook.

respond dramatically, yielding an enormous scattering cross section, albeit only in the narrow frequency range of the transition (Gayley 1995). However, the frequency range for line-scattering is strongly increased by the Doppler effect.

As the wind is launched from the star, its velocity is low at first. Let us denote the resonant wavelength of a line transition in the rest frame of the ion with λ_0 . Due to thermal broadening the resonance has a line width $\Delta\lambda = \lambda_0 v_{\text{th}}/c$ with $v_{\text{th}} \sim 10 \text{ km s}^{-1}$ for C, N, and O in winds with temperatures of a few times 10^4 K . At $r > R_*$, the resonant wavelength in the rest frame of the star is given by

$$\lambda'_0(r) = \lambda_0 \left(1 - \frac{v(r)}{c} \right) \quad (1.12)$$

so that a photon with $\lambda < \lambda_0 - \Delta\lambda$ deposits its momentum at the radius r where it is in resonance with the Doppler shifted line. This accelerates the wind and the resonance is shifted to even smaller wavelengths (see Figure 1.5). With increasing radius and wind velocity, photons with decreasing wavelength can be absorbed, so that a Doppler-broadened line-absorption trough blueward from the line centre is carved out. At wind velocities $v \sim 1000 \text{ km s}^{-1}$ the Doppler broadening due to the wind speed clearly dominates over the thermal broadening. When the optical depth of a line has been calculated (considering the Doppler effect), all that is left to do is to add up all contributing metal lines to estimate the terminal velocity of the wind and the star's mass loss rate.¹²

¹²This is conveniently done in the CAK approximation (Castor et al. 1975b).

The wind mass loss rate is strongly affected by the stellar effective temperature T_{eff} and luminosity L . For O stars,

$$\dot{M} \propto L^\chi \quad (1.13)$$

with $\chi \approx 2$ (cf. Vink et al. 2000, Eq. 12 therein; see *ibidem* for the dependence of \dot{M} on T_{eff}). Because radiation is less coupled to a star with fewer metals in its atmosphere, the star's metallicity Z is another fundamental quantity in setting the wind mass loss rate – low-metallicity stars drive weaker winds than high-metallicity stars (cf. Puls et al. 2000, 2008). For example, a massive star with an effective temperature $T_{\text{eff}} = 4 \times 10^4$ K at $Z = 0.1 Z_\odot$ has roughly a tenth of the mass loss rate of a star with the same effective temperature but at solar metallicity; for a wider range of metallicities the scaling is sublinear, with

$$\dot{M} \propto Z^{0.7} \quad (1.14)$$

for O stars (Vink et al. 2001). The terminal velocity v_∞ on the other hand is primarily affected by the escape velocity of the star, and thus its size and rotational speed.

Wind-Blown Bubbles

When winds are launched from a massive star they initially expand into the surrounding ISM nearly unimpeded at almost their terminal velocity as the mass of the ejecta dominates over the swept-up mass. This so-called free-expansion phase of the wind ends when the mass of the swept-up ISM becomes comparable to the mass ejected by the star. Assuming a homogeneous ISM of mass density ρ_0 (and corresponding number density n_0) this is the case after

$$t_1 = \sqrt{\frac{3}{4\pi} \frac{\dot{M}}{\rho_0 v_\infty^3}} \quad (1.15)$$

(Lamers and Cassinelli 1999). For very massive stars this initial phase is very short – even in a low-density cloud with $n_0 = 10 \text{ cm}^{-3}$, t_1 is less than 100 yr.

More and more of the (more or less) static cloud material is swept-up by the winds and accumulates in a dense shell. Due to conservation of momentum the shell gradually slows down. Soon, besides the outward facing expanding shock, an inward facing shock forms as highly supersonic winds pile up downstream from the outer shock. The structure of the wind-blown bubble at this point, first described by Castor et al. (1975a) and Weaver et al. (1977) and shown in Figure 1.6, is as follows (from inside to outside):

- (i) A cavity where the wind ejecta flow outward at their terminal velocity. The density in this free-streaming zone is proportional to r^{-2} where r is the distance from the star. At a distance R_1 the wind material encounters the inner (adiabatic) shock.
- (ii) A region where shocked wind material accumulates. As wind material passes through the adiabatic shock at R_1 it is compressed and slowed down by a factor 4. The temperature of the

Introduction

gas at the shock T_{shock} is given by

$$T_{\text{shock}} = (1.4 \times 10^5 \text{ K}) \left(\frac{\Delta v}{100 \text{ km s}^{-1}} \right)^2 \quad (1.16)$$

where Δv is the velocity change across the shock front (Lamers and Cassinelli 1999). With $1000 \text{ km s}^{-1} \lesssim \Delta v \lesssim 3000 \text{ km s}^{-1}$ as appropriate for very massive stars, the shock temperature lies in the range $10^7 \text{ K} \lesssim T_{\text{shock}} \lesssim 10^8 \text{ K}$.

- (iii) A thin shell of swept-up ISM. Initially, the shell material is also shock-heated to high temperatures but it cools down on a relatively short characteristic cooling timescale¹³

$$t_2 = (2.3 \times 10^4 \text{ yr}) \left(\frac{n_0}{\text{cm}^{-3}} \right)^{-0.71} \left(\frac{Z}{Z_{\odot}} \right)^{-0.42} \left(\frac{L_w}{10^{38} \text{ erg s}^{-1}} \right)^{0.29} \quad (1.17)$$

(Mac Low and McCray 1988; Martínez-González et al. 2014). The mechanical wind luminosity L_w is the kinetic energy injected into the system per unit time by the stellar wind (which is then converted into thermal energy),

$$L_w = \frac{1}{2} \dot{M} v_{\infty}^2. \quad (1.18)$$

For $n_0 = 10 \text{ cm}^{-3}$, $Z = Z_{\odot}$, and $L_w = 10^{38} \text{ erg s}^{-1}$ the shell cools in $\sim 4000 \text{ yr}$ to temperatures of $\sim 10^2 - 10^4 \text{ K}$, depending on whether the swept-up ISM is photoionized or not.

- (iv) The ambient cloud material which has not yet been affected by the wind.

Both the free-expansion phase and the adiabatic expansion phase with a hot shell are short (see Eqs. 1.15 and 1.17) and therefore they are typically not observed (Lamers and Cassinelli 1999). However, the cooling of the shocked wind region (ii) takes significantly longer and the high thermal pressure leads to a fast expansion of the bubble. Until the bubble material has cooled to the temperature of the ambient gas, the system is said to be in the adiabatic or energy-driven expansion phase. The dynamics of the bubble in this phase were first described by Avedisova (1972), Castor et al. (1975a) and, more rigorously, Weaver et al. (1977). The most important results will be presented in the following.

The goal is to derive an equation for the radius of the thin shell $R_2(t)$ as it expands into the ambient medium and sweeps up the mass $M_{\text{sh}}(t)$. The evolution of the shell and the bubble it envelopes is given

¹³Here, the cooling time t_2 is defined as the time when the total energy removed by radiative cooling equals the shell's thermal energy at that time, i.e. $t_2 \propto nkT/(du/dt)$. The cooling rate per unit volume is defined as $du/dt \equiv n_e n \Lambda$ where Λ is the cooling function which is approximated as $\Lambda \propto Z T^{-0.7}$ in Mac Low and McCray (1988). The temperature at the forward shock is proportional to \dot{R}_2^2 (see Eq. 1.16) where \dot{R}_2 is the velocity of the outward facing expanding shock. Thus, $t_2 \propto \dot{R}_2^{3.4}/(n_e Z)$. Assuming an expansion velocity of the shell at $t = t_2$ of $\dot{R}_2 \propto L_w^{1/5} n_0^{-1/5} t_2^{-2/5}$ (Weaver et al. 1977) and $n_0 \propto n_e$ the cooling time as given in Eq. (1.17) follows.

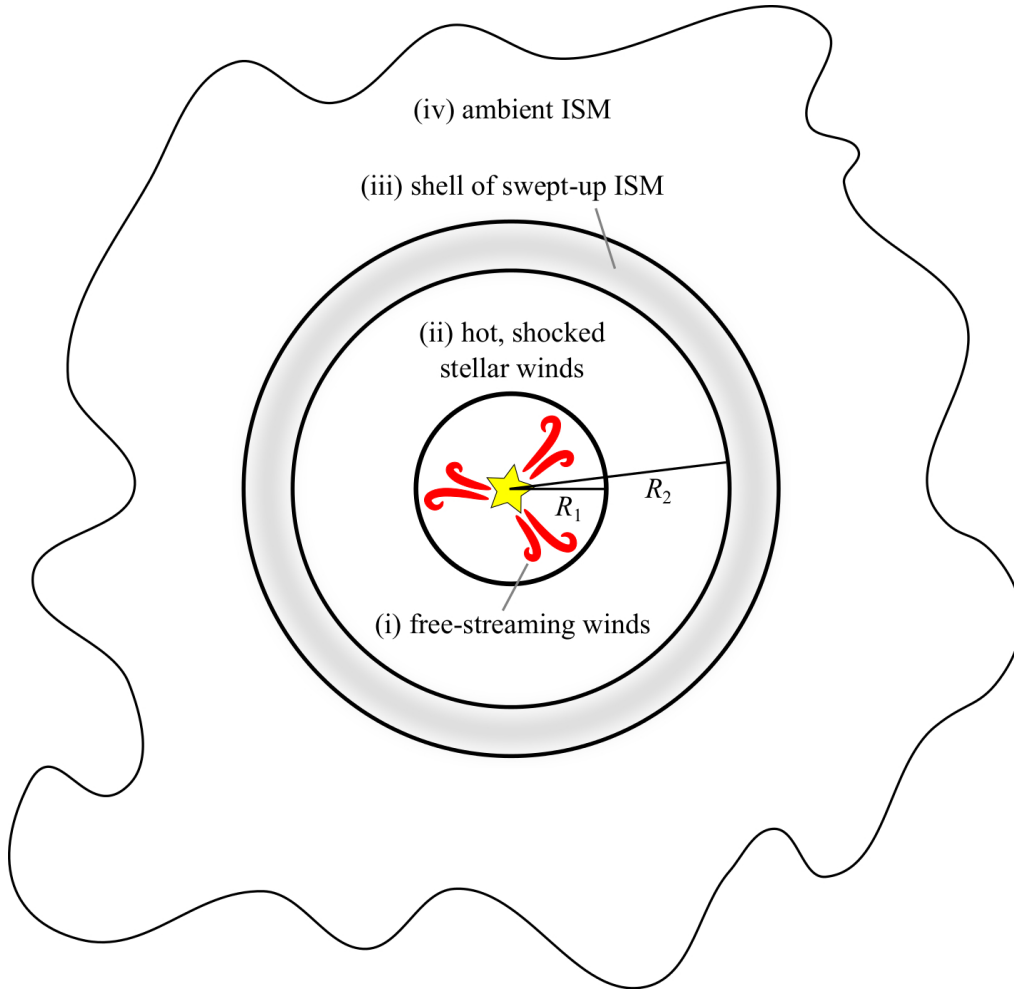


Fig. 1.6 Structure of a wind-blown bubble in the energy-driven (adiabatic) phase (cf. Lamers and Cassinelli 1999; Weaver et al. 1977). Replace the word “winds” by “supernova ejecta” to get the structure of a supernova remnant (cf. Reynolds 2017). For details, see main text, Section 1.2.1 and 1.2.3.

by the momentum equation and the energy equation,

$$\frac{d}{dt} (M_{\text{sh}} \dot{R}_2) = 4\pi R_2^2 P_b \quad (1.19)$$

$$\frac{dE_b}{dt} = L_w - P_b \frac{dV_b}{dt} - L_{\text{cool}}, \quad (1.20)$$

where the subscript “b” stands for “bubble” and L_{cool} denotes the energy loss rate due to radiative cooling. In spherical symmetry the time derivative of the bubble volume is given by

$$\frac{dV_b}{dt} = 4\pi R_2^2 \dot{R}_2. \quad (1.21)$$

The pressure P_b and the energy E_b of the bubble are related via

Introduction

$$P_b = \frac{(\gamma - 1)E_b}{\frac{4\pi}{3}(R_2^3 - R_1^3)} \quad (1.22)$$

where γ is the adiabatic index. The free-streaming winds exert a ram-pressure force of

$$F_{\text{ram}} = \dot{M}v_\infty \quad (1.23)$$

at the inner shock at R_1 where pressure equilibrium between the free-streaming wind zone and the shocked region demands

$$\frac{F_{\text{ram}}}{4\pi R_1^2} = P_b. \quad (1.24)$$

From this follows an implicit equation for the radius of the free-streaming zone,

$$R_1 = \left[\frac{F_{\text{ram}}}{2E_b} (R_2^3 - R_1^3) \right]^{1/2}. \quad (1.25)$$

In order to solve the system of ordinary differential equations (ODEs, Eqs. 1.19 and 1.20) two limiting cases are typically considered. In the energy-driven limit, radiative cooling in the bubble is negligible, i.e. $L_{\text{cool}} \ll L_w$ (this is why this phase is also called energy-conserving, e.g. Lamers and Cassinelli 1999). This is usually the case at early times, after the free expansion phase ends. Due to the high thermal pressure of the bubble, it holds that $R_1 \ll R_2$ (see Eq. 1.24) and Eq. (1.22) simplifies to

$$P_b \approx \frac{3(\gamma - 1)E_b}{4\pi R_2^3}. \quad (1.26)$$

One can then combine Eqs. (1.20) and (1.19) to find the following single ordinary differential equation (ODE) which governs the expansion of the bubble and the shell,

$$\ddot{R}_2 = \frac{3(\gamma - 1)L_w}{M_{\text{sh}}R_2} - \frac{\dot{M}_{\text{sh}}\dot{R}_2^2}{M_{\text{sh}}R_2}(3\gamma - 2) - \frac{\dot{R}_2\ddot{R}_2}{R_2}(3\gamma - 2) - \frac{\ddot{M}_{\text{sh}}\dot{R}_2}{M_{\text{sh}}} - \frac{2\dot{M}_{\text{sh}}\ddot{R}_2}{M_{\text{sh}}}. \quad (1.27)$$

Assuming a uniform ambient medium of density ρ_0 , the swept-up mass of the shell is given by

$$M_{\text{sh}} = \frac{4\pi}{3}R_2^3\rho_0. \quad (1.28)$$

Eq. (1.27) then becomes

$$\ddot{R}_2 = \frac{9(\gamma - 1)L_w}{4\pi\rho_0}R_2^{-4} - 9\gamma R_2^{-2}\dot{R}_2^3 - (7 + 3\gamma)R_2^{-1}\dot{R}_2\ddot{R}_2 \quad (1.29)$$

(see also Bisnovaty-Kogan and Silich 1995) which can be solved analytically. With $\gamma = 5/3$, as appropriate for an ideal gas, and initial conditions $\lim_{t \rightarrow 0} R_2 = 0$, $\lim_{t \rightarrow 0} \dot{R}_2 = 0$, $\lim_{t \rightarrow 0} \ddot{R}_2 = \infty$ (i.e.

neglecting the initial free-expansion phase) the solution for $t > t_1$ is

$$R_2 = \left(\frac{250}{308\pi} \frac{L_w}{\rho_0} \right)^{1/5} t^{3/5} \quad (1.30)$$

$$\dot{R}_2 = \frac{3}{5} \left(\frac{250}{308\pi} \frac{L_w}{\rho_0} \right)^{1/5} t^{-2/5} \quad (1.31)$$

$$E_b = \frac{5}{11} L_w t \quad (1.32)$$

$$P_b = \frac{7}{(3850\pi)^{2/5}} L_w^{2/5} \rho_0^{3/5} t^{-4/5} \quad (1.33)$$

(Bisnovatyi-Kogan and Silich 1995; Weaver et al. 1977).

As the material in the bubble cools adiabatically to temperatures below 10^6 K, radiative cooling becomes important (the cooling function Λ peaks at $T \sim 10^5$ K, e.g. Gnat and Ferland 2012). A timescale for the duration of the energy-driven phase is given by the cooling time of the bubble¹⁴

$$t_3 = (1.6 \times 10^7 \text{ yr}) \left(\frac{n_0}{\text{cm}^{-3}} \right)^{-8/11} \left(\frac{Z}{Z_\odot} \right)^{-35/22} \left(\frac{L_w}{10^{38} \text{ erg s}^{-1}} \right)^{3/11} \quad (1.34)$$

(Mac Low and McCray 1988). At this time the shell has expanded to a radius which I will denote R_c in the following, $R_c \equiv R_2(t_3)$. One can now consider cooling to be maximally efficient, that is, all energy of the bubble is immediately radiated away. This is the beginning of the momentum-driven phase as the expansion of the shell is now driven purely by the wind momentum.¹⁵ Alternatively, the expansion can become momentum-driven even earlier if the hot bubble material can escape through holes in the shell.

As the thermal pressure of the bubble drops, the inner shock is pushed outward. Eventually, there is no intervening layer of shocked wind any more, i.e. $R_1 = R_2$, and it is the wind ram pressure rather than the thermal pressure of shocked wind material that is pushing the shell outward (Weaver et al. 1977 remark that this situation might not occur if only cooling is considered as an energy loss term). The pressure of the bubble is now given by

$$P_b = \frac{F_{\text{ram}}}{4\pi R_2^2}. \quad (1.35)$$

For a uniform ambient ISM, the momentum equation (Eq. 1.19) turns into

$$\frac{d}{dt} \left(\frac{4\pi}{3} \rho_0 R_2^3 \dot{R}_2 \right) = F_{\text{ram}} \quad (1.36)$$

¹⁴The cooling time of the bubble t_3 is defined as the time when the energy injected into the bubble via stellar winds equals the energy lost via radiative cooling, i.e. $\int_0^{t_3} dt \int_{V_b} dV (du/dt) = E_b(t_3) = (5/11)L_w t_3$ (see Eq. 1.32). To estimate the amount of cooling, one needs to consider the density and temperature distribution in the bubble. Mac Low and McCray (1988) used the self-similarity profiles derived in Weaver et al. (1977), Eq. (37) therein. However, this should be treated with caution as these profiles are derived under the assumption that cooling is negligible (for more details, see Section 2.3).

¹⁵In reality the transition between energy-driven phase and momentum-driven phase is of course gradual (see Section 2.3).

Introduction

which – with the state of the system at $t = t_3$ as initial conditions – is solved by

$$R_2 = R_c \left[\frac{3F_{\text{ram}}(t^2 + t_3^2)}{2\pi\rho_0 R_c^4} + \left(\frac{12}{5} - \frac{3F_{\text{ram}}t_3^2}{\pi\rho_0 R_c^4} \right) \frac{t}{t_3} - \frac{7}{5} \right]^{1/4} \quad (1.37)$$

$$\dot{R}_2 = \left(\frac{3F_{\text{ram}}}{4\pi\rho_0 R_2^3} \right) t + \frac{1}{R_2^3} \left(\frac{3}{5} \frac{R_c^4}{t_3} - \frac{3F_{\text{ram}}t_3}{4\pi\rho_0} \right) \quad (1.38)$$

(Silich and Tenorio-Tagle 2013). For $t \gg t_3$ the shell radius converges to

$$R_2 = \left(\frac{3}{2\pi} \frac{F_{\text{ram}}}{\rho_0} \right)^{1/4} t^{1/2} \quad (1.39)$$

(Koo and McKee 1992a). Koo and McKee (1992b) also present analytic solutions for shells expanding in the momentum limit into environments where the density falls radially off as a power-law.

Wind Feedback from a Massive Star Cluster

So far, the evolution of wind-blown bubbles has been discussed for a single star. For a massive star cluster each massive star will create its own bubble. However, for typical cloud and cluster conditions these bubbles quickly merge and a single large bubble soon envelopes the whole cluster (Silich and Tenorio-Tagle 2017). Another complication we have ignored so far is the time-dependence of stellar feedback. For the derivation of Eqs. (1.30)–(1.33) and (1.37)–(1.39), the stellar winds have been assumed to be constant in time. In reality, this is not the case.

The time evolution of the total mass loss rate \dot{M} and the average terminal velocity $\langle v_\infty \rangle$ of winds from a young massive star cluster are shown in Figure 1.7. When stars more massive than $\sim 20 M_\odot$ leave the main sequence they undergo a so-called Wolf-Rayet phase which is characterized by a strong increase in mass loss rates but a decrease in terminal wind velocities (Massey 2003). The onset of the Wolf-Rayet phase of the most massive stars ($M_* \geq 100 M_\odot$) at $t \sim 3 \text{ Myr}$ causes the mechanical wind luminosity of a massive star cluster to almost double.

With the death of the most massive stars after $\sim 4 \text{ Myr}$ the mass loss rate and the wind luminosity of the whole cluster drop dramatically. After $\sim 6 \text{ Myr}$, which corresponds to the lifetime of stars with an initial mass of $\sim 40 M_\odot$ (Ekström et al. 2012), L_w has dropped to roughly a quarter of the peak value. In a massive star cluster, stars with initial masses $M_* \geq 40$ (corresponding to stars of spectral type O5.5 and earlier, Weidner and Vink 2010), which make up less than 0.1 % of stars in a cluster, are thus vastly dominant in terms of stellar wind feedback (cf. Eq. 1.13).¹⁶ While the mechanical luminosity of the winds drops, the total mechanical luminosity $L_{\text{tot}} = L_w + L_{\text{SN}}$ remains roughly constant due to ongoing supernova explosions with high mechanical supernova luminosities L_{SN} (see Section 1.2.3).¹⁷

¹⁶Less massive stars live for a longer time, so they eject (weaker) winds for a longer time span. However, the natal cloud is less affected by winds at late times as the shock-heated gas is not efficiently confined any more.

¹⁷The star cluster is massive enough that supernova explosions are frequent. Therefore, they can be treated as a continuum process with mechanical luminosity L_{SN} instead of distinct explosions.

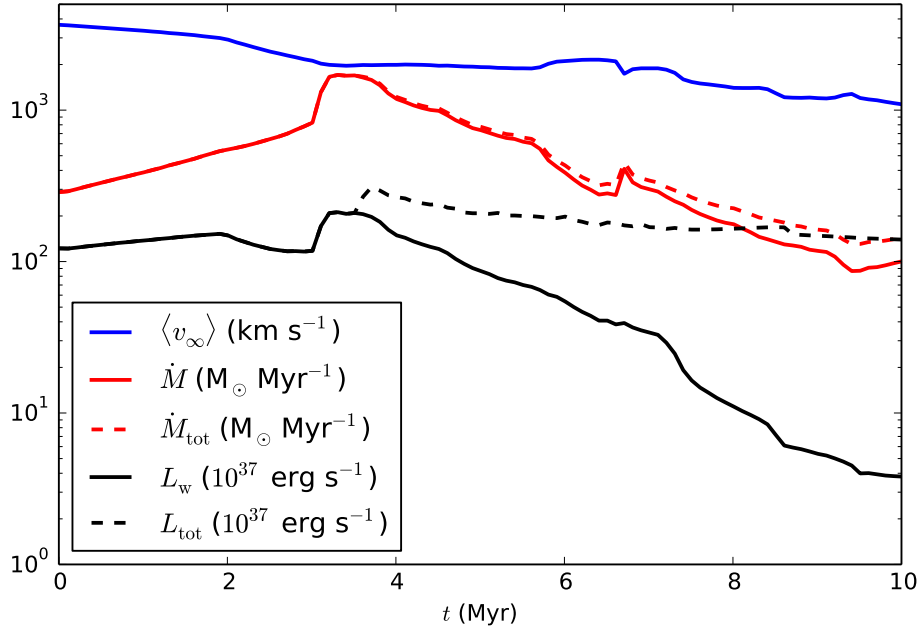


Fig. 1.7 Evolution of the wind terminal velocity averaged by the mass of the ejecta $\langle v_\infty \rangle$, the mass loss rate due to stellar winds \dot{M} , and the mechanical luminosity of winds L_w of a massive star cluster ($M_* = 10^5 M_\odot$) where the (Kroupa-)IMF is fully sampled. The total mass loss rate \dot{M}_{tot} and the total mechanical luminosity L_{tot} , where in addition to winds the ejection of mass via supernova explosions has been taken into account as well (assuming these ejecta have terminal velocities of 10^4 km s^{-1}), are shown as dashed lines. The data have been produced with the STARBURST99 population synthesis code (Leitherer et al. 2014) using Geneva evolutionary tracks for rotating stars (Ekström et al. 2012) at solar metallicity and Pauldrach/Hillier atmospheres, i.e. WM-BASIC models (Pauldrach et al. 2001) when the star cluster is younger than 3 Myr and CMFGEN models (Hillier and Miller 1998) thereafter.

Even if L_{tot} only varies by a factor ~ 2 until the cluster is 30 Myr old (when all stars with $M_* > 8 M_\odot$ have exploded as a supernova), there are other complications to the simple picture of a wind-blown bubble presented above. First, a bubble is rarely fully energy-driven or fully momentum-driven but there is gradual transition between the two limits. Second, no analytic solutions exist if gravity is included as an additional force term. Third, while L_{tot} does not vary strongly as a function of time, the ram-pressure force F_{ram} does (due to the strong decrease in \dot{M}), which is important for the bubble expansion in the momentum-driven limit. These complications and the presence of other feedback sources, some of which are strongly time-dependent, make a numerical treatment of the problem necessary. Nevertheless, I will still discuss the effect of other feedback terms in isolation first before then considering them together in Section 2.

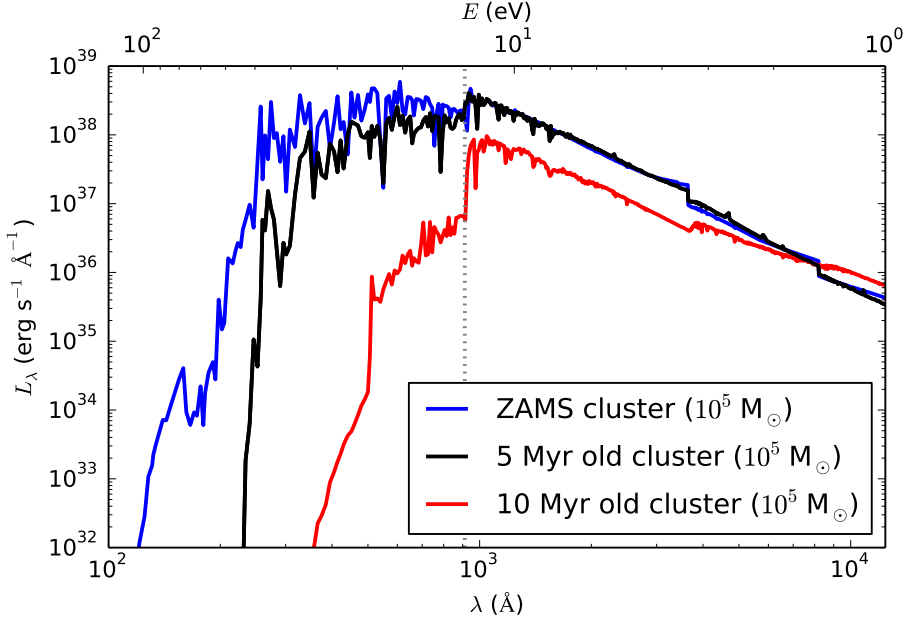


Fig. 1.8 Spectrum of a massive star cluster ($M_* = 10^5 M_\odot$) where the (Kroupa-)IMF is fully sampled. The spectrum is shown at three different ages of the cluster (all stars are assumed coeval): 0 Myr (zero-age main sequence, ZAMS), 5 Myr, and 10 Myr. The monochromatic luminosity L_λ is related to the bolometric luminosity via $L = \int_{-\infty}^{\infty} L_\lambda d\lambda$. Photons with wavelengths $\lambda < 912 \text{ \AA}$ ($E > 13.6 \text{ eV}$), i.e. left from the vertical dotted line, are able to ionize atomic hydrogen. The spectra have been produced with the STARBURST99 population synthesis code (Leitherer et al. 2014) using Geneva evolutionary tracks for rotating stars (Ekström et al. 2012) at solar metallicity and Pauldrach/Hillier atmospheres, i.e. WM-BASIC models (Pauldrach et al. 2001) when the star cluster is younger than 3 Myr and CMFGEN models (Hillier and Miller 1998) thereafter.

1.2.2 Stellar Radiation

Stars can be roughly approximated as black body radiators (Carroll and Ostlie 2007). As such, stars with higher effective temperatures emit more radiation than cooler stars. A star's bolometric luminosity relates to its mass via

$$L \propto M_*^\eta \quad (1.40)$$

with $2 \leq \eta \leq 4.5$ for $M_* < 20 M_\odot$ and $\eta \approx 1$ for $M_* \geq 20 M_\odot$ (Salaris and Cassisi 2005). In particular, more massive stars emit more radiation in the high-energy part of the spectrum than less massive stars. As an example the spectrum of a massive cluster for three different ages is shown in Figure 1.8. While the cluster is young a large fraction of the bolometric luminosity L is in photons with $E > 13.6 \text{ eV}$ (see also Figure 1.9). As the cluster ages and the most massive stars die (at $t \sim 4 \text{ Myr}$) the luminosity, in particular in the the high-energy end of the spectrum, drops.

While H_2 is abundant in a GMC before the onset of star formation, the presence of massive stars causes molecular hydrogen to dissociate. In gas shock-heated by winds from massive stars, H_2 is

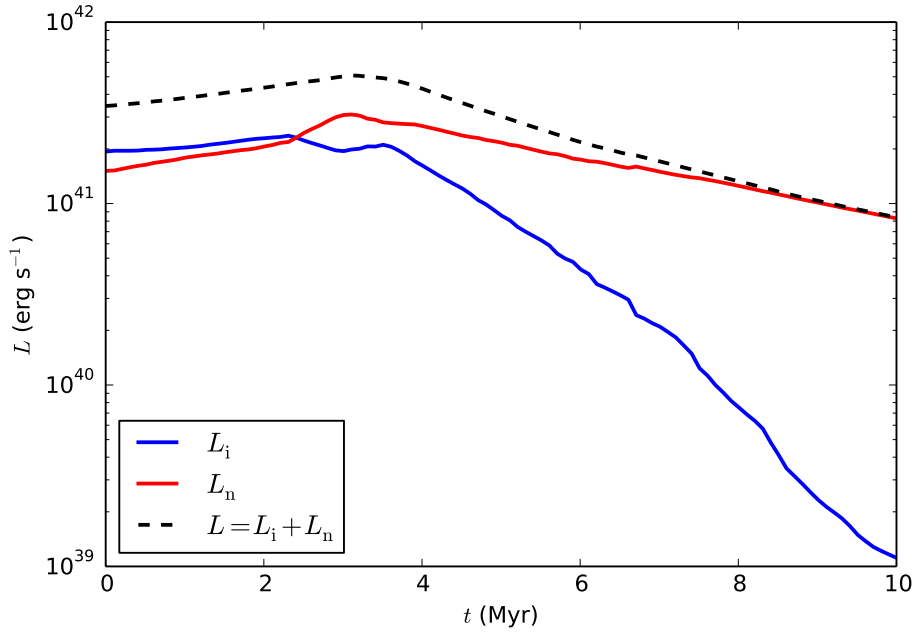


Fig. 1.9 Luminosity of a massive star cluster ($M_* = 10^5 M_\odot$) where the (Kroupa-)IMF is fully sampled. The bolometric luminosity L (black dashed line) is the sum of the luminosity in hydrogen-ionizing radiation L_i ($E \geq 13.6$ eV, blue line) and non-ionizing radiation L_n ($E < 13.6$ eV, red line). The data have been produced with the STARBURST99 population synthesis code (Leitherer et al. 2014) using Geneva evolutionary tracks for rotating stars (Ekström et al. 2012) at solar metallicity and Pauldrach/Hillier atmospheres, i.e. WM-BASIC models (Pauldrach et al. 2001) when the star cluster is younger than 3 Myr and CMFGEN models (Hillier and Miller 1998) thereafter.

readily dissociated via collisions but in absence of temperatures above ~ 2000 K H_2 -dissociation occurs mainly via photodissociation. For radiation with $E > 15.4$ eV this is for example achieved by photoionization of H_2 followed by dissociative recombination (Glover and Brand 2001, and references therein). But even less energetic radiation with $E > 11.2$ eV can cause photoexcitation into an excited electronic state (corresponding to an absorption in the Lyman Werner bands) from which a fraction of $\sim 15\%$ of the decays occur into an unbound level (Draine and Bertoldi 1996). This latter two-step photodissociation process is known as the Solomon process (Osterbrock and Ferland 2006).

Lyman-Werner radiation heats the ambient gas, thus causing it to expand. However, photodissociation regions have only moderate temperatures, $T \lesssim 400$ K (Osterbrock and Ferland 2006). Radiation with $E > 13.6$ eV on the other hand can ionize atomic hydrogen. This ionizing radiation from massive stars creates regions of H^+ (called HII regions following the spectroscopic notation) with $T \sim 10^4$ K which are strongly overpressured with respect to their surroundings.

Introduction

Expanding HII regions

Let us consider a new-born massive star that starts to emit ionizing photons with a rate Q_i into the ambient neutral medium with a hydrogen density n_0 and temperature $T_1 = 100$ K. Although the following outline of events ignores stellar winds, it is still convenient in order to demonstrate the effect of ionizing radiation.

An HII region, bound by an ionization front (I-front) with radius R_i , inside which hydrogen is fully ionized, expands from the star outwards. Hydrogen ions and electrons recombine inside the HII region with a rate $\alpha_B n_0 n_e$ but are immediately ionized again. Here α_B is the case B recombination coefficient¹⁸ and n_e is the electron number density. Assuming that $n_e \approx n_0$, the change rate of the total number of electrons in the HII region $N_e = (4\pi/3)n_0 R_i^3$ is given by

$$\frac{dN_e}{dt} = Q_i - \alpha_B n_0^2 \frac{4\pi}{3} R_i^3. \quad (1.41)$$

Further assuming that the ISM does not immediately react dynamically to the change in thermal pressure and the density remains constant (which at early times is justified), the evolution of the I-front follows from Eq. (1.41),

$$R_i = \min \left[ct, R_S \left(1 - \exp \left(-\frac{t}{t_R} \right) \right)^{1/3} \right] \quad (1.42)$$

(Spitzer 2004), where the solution has been modified to not exceed expansion with the speed of light at very early times (see Shu 1992; Yorke 1986). Here, $t_R \equiv 1/(n_0 \alpha_B)$ is the recombination time and R_S is the the Strömgren radius (Strömgren 1939), that is, the steady-state solution of Eq. (1.41),

$$R_S = \left(\frac{3Q_i}{4\pi\alpha_B n_0^2} \right)^{1/3}. \quad (1.43)$$

While the I-front initially expands supersonically (a weak R-type front in the notation of Spitzer) with respect to the sound speed of the ionized gas $c_{II} \sim 10 \text{ km s}^{-1}$ without significantly changing the gas density distribution, it gradually slows down according to Eq. (1.42). The HII region with a temperature $T_{II} \sim 10^4$ K is highly overpressured with respect to the ambient neutral gas and when $\dot{R}_i \sim 2c_{II}$ the pressure wave can catch up with the I-front. At the time t_0 when this happens¹⁹ an isothermal shock forms in front of the I-front (which now becomes D-type, see Spitzer 2004). This configuration is shown in Figure 1.10.

In the second expansion phase ($t > t_0$), both I-front and shock (which is only detached from the I-front by a thin shell of neutral hydrogen, HI) expand according to

¹⁸Recombination directly to the ground state produces a photon which, if absorbed, can ionize another nearby hydrogen atom. Usage of the case B recombination coefficient (instead of the case A recombination coefficient) takes into account that in optically thick environments such transitions do not count toward the net recombination (Osterbrock and Ferland 2006).

¹⁹Typically, $t_0 \sim 5 \times 10^3$ yr for an O5 star in a cloud with $n_0 = 10 \text{ cm}^{-3}$, (Shu et al. 1987). The I-front has expanded to a radius of $R_i(t_0) \approx R_S$ at this point.

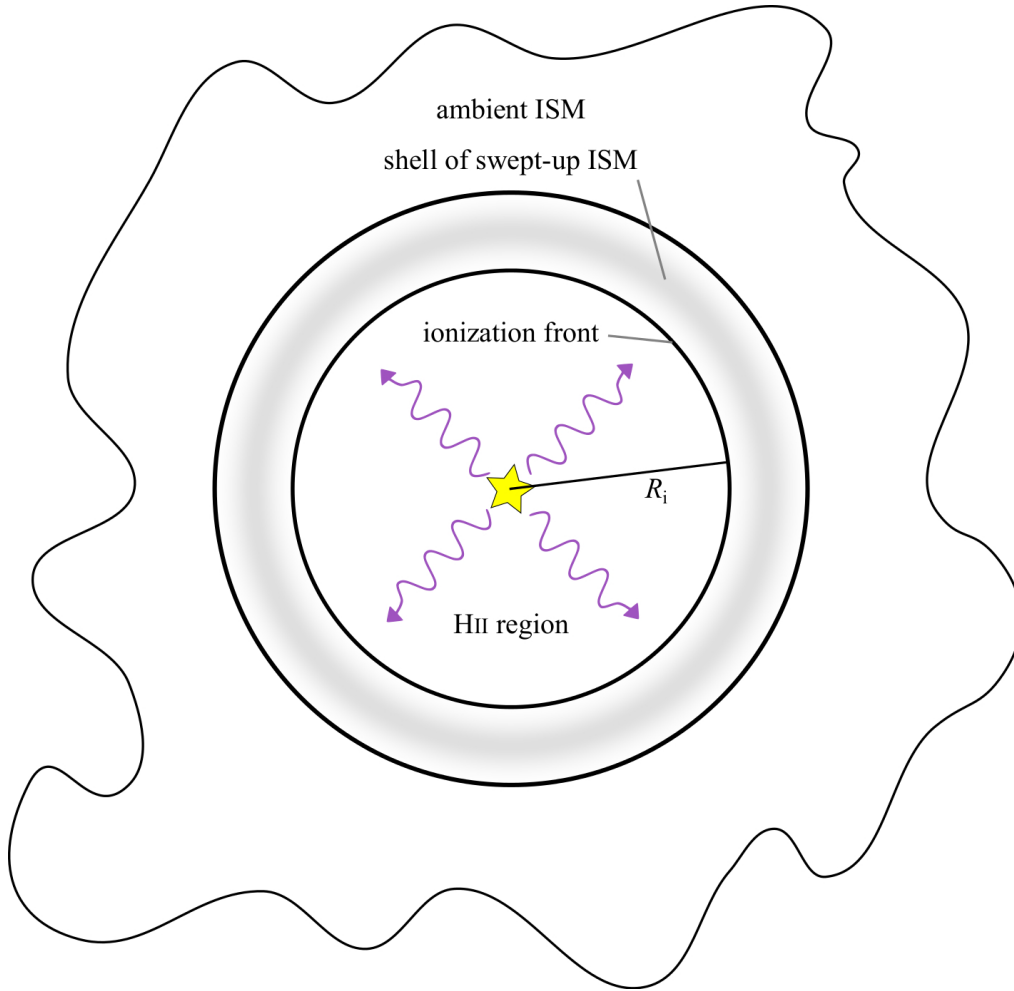


Fig. 1.10 Structure of an expanding HII region during the second expansion phase. The compressed material in the shell is neutral and bound by the I-front on the inside and the shock front on the outside (cf. Shu 1992).

$$R_i = R_S \left(1 + \frac{7}{4} \frac{c_{\text{II}} t}{R_S} \right)^{4/7} \quad (1.44)$$

$$\dot{R}_i = c_{\text{II}} \frac{R_S}{R_i} \quad (1.45)$$

(Spitzer 2004). Keeping the emission rate of ionizing photons constant, the expansion would continue until the HII region is in pressure equilibrium with the ambient ISM at a radius

$$R_{\text{final}} = \left(\frac{3Q_i}{4\pi\alpha_B n_{\text{final}}^2} \right)^{1/3} \quad (1.46)$$

Introduction

where $n_0 k T_I = 2n_{\text{final}} k T_{\text{II}}$. However, the life-span of a massive star is typically shorter than it takes for the I-front to reach R_{final} , so that either the ionized hydrogen recombines as the emission rate of ionizing photons decreases or the HII region gets disrupted in a supernova explosion (Shu 1992; Yorke 1986, see also Section 1.2.3 for a discussion of supernovae).

Radiation Pressure

As mentioned in Section 1.2.1, photons can also transfer their momentum to the ISM and thus exert radiation pressure. Radiation pressure alone can push the ISM away from sites of star formation. In contrast to stellar winds, however, where it is justified to treat the ejecta as fully interacting with the ambient ISM, radiation is not necessarily fully coupled to the ISM (e.g. only few photons with $E < 13.6$ eV are absorbed by atomic hydrogen). Let us here for simplicity assume that the radiation emitted by a newborn star cluster is absorbed only by dust with a cross section σ_d and that the dust and the gas (which, as before, is homogeneously distributed with density ρ_0) are fully coupled. The momentum equation of the shell (Eq. 1.19 in the case of stellar winds) now reads

$$\frac{d}{dt} (M_{\text{sh}} \dot{R}_2) \approx \frac{\tau_d L}{c} \quad (1.47)$$

where L is the cluster's bolometric luminosity.²⁰ For a fixed dust number density n_d the optical depth is given by $\tau_d = n_d \sigma_d R_2$. This leads to a self-similarity solution for the time evolution of the shell radius,

$$R_2 = \left(\frac{27}{44\pi} \frac{L n_d \sigma_d}{\rho_0 c} \right)^{1/3} t^{2/3} \quad (1.48)$$

(O'Dell et al. 1967). In the case of a constant gas-to-dust ratio, i.e. $n_d/\rho_0 = \text{const.}$, the solution becomes independent of the ambient density (Elmegreen and Chiang 1982). Under these simplifying assumptions the expansion velocity of a radiation pressure-driven shell does therefore not decrease in denser environments, in contrast to HII regions (Eq. 1.44), wind-blown bubbles (Eqs. 1.30 and 1.39) and supernova remnants (Eq. 1.54).

As mentioned before, in reality radiation is not only coupled to dust. Photons with energies $E > 13.6$ eV are absorbed by neutral hydrogen while photons below this energy but above 11.2 eV can result in dissociation of H_2 via the Solomon process (see above). Since in contrast to the above mentioned continuum processes (absorption on dust and on neutral hydrogen with $E > 13.6$ eV) Lyman-Werner photons are strongly affected by self-shielding of H_2 (Klessen and Glover 2016) their transferred momentum is only significant in comparison with momentum transfer onto dust grains when the radiation field is weak (Krumholz et al. 2008). In addition, radiation absorbed by dust is re-emitted at infrared wavelengths. If the dust column density is sufficiently high (and it needs to be high because dust absorption coefficients are low in the infrared, Osterbrock and Ferland 2006; Weingartner and Draine 2001), the infrared photons are re-absorbed and can again transfer momentum

²⁰Eq. (1.47) is valid for $\tau_d \ll 1$. For large τ_d the exact form of the right-hand side, $[1 - \exp(-\tau_d)]L/c$, has to be used.

to the ISM. This is known as indirect radiation pressure, whereas the first absorption is referred to as direct radiation pressure.

1.2.3 Supernovae

The guest star has vanished [...]. Earlier, during the first year of the Zhihe reign period, fifth lunar month, it appeared in daybreak at the eastern direction [...]. It was seen at daytime, like Venus. It had pointed rays in all directions and its color was pale red. In total it was seen for 23 days.

(Chinese Astron. Bureau, August 27, 1054; quoted in Blandford and Bühler 2017)

This “guest star”, which was observed nearly 1000 years ago, was a supernova (SN) explosion inside the Milky Way galaxy, bright enough to be visible with the naked eye for 23 days during the day and for more than one year during the night (Green 2017). In fact, the well-known Crab Nebula at a distance of 2 kpc is the remnant of that explosion (Duyvendak 1942). Obviously, SN explosions are very energetic. Due to the large amount of energy released in a short period of time, supernovae can be an important source of feedback in star-forming regions.

As first noted by Minkowski (1941), there are two types of SNe which can be distinguished by their spectra – those that show signatures of hydrogen (type I) and those that do not (type II). Later, more subclasses were catalogued such as type Ia, Ib, and Ic (none of these shows any hydrogen signatures). SNe Ia are the most commonly observed SNe (Arcavi 2017). Due to their very high luminosity, however, they are over-represented in flux-limited surveys. Intrinsically, type II SNe are the most common (57 % of all SNe), followed by type Ia SNe (24 %) and type Ib/c SNe (19 %).

Today we know the progenitor star of type Ia SNe is a white dwarf, i.e. the remnant of a star less massive than $\sim 8 M_{\odot}$, whose mass has been pushed over the Chandrasekhar limit (see below) by accretion from a nearby binary or through merging with another white dwarf (Alsabti and Murdin 2017; Gal-Yam 2017; Koester 2002). Because all the progenitor’s hydrogen has been converted to heavier elements or has been blown away by stellar winds, a type Ia supernova spectrum does not show any hydrogen features. Since white dwarfs only form after $\gtrsim 30 - 40$ Myr of stellar evolution (corresponding to the lifetimes of the most massive progenitors of white dwarfs; Ekström et al. 2012), they are typically not associated with star-forming regions. They are therefore not the focus of this thesis.

The progenitor of type Ib/c and type II SNe is a massive star ($M_* > 8 M_{\odot}$) where hydrogen is still present in the outer layer (type II) or from which the hydrogen envelope has been stripped, e.g. due to strong stellar winds or mass transfer in a binary system (type Ib/c²¹, Alsabti and Murdin 2017; Gal-Yam 2017). All but the most massive ($M_* \gtrsim 140 M_{\odot}$) of such stars undergo a so-called core-collapse SN.²²

²¹The distinction between type Ib and Ic is made according to the presence of He features in the spectrum with type Ic showing no strong He features.

²²Stars with masses higher than $\sim 140 M_{\odot}$ explode before they have built up an iron core because a runaway production of electrons and positrons in the oxygen core decreases the radiation pressure from gamma rays. Such a SN is called a pair-instability SN. Usually, pair-instability SNe are only thought to occur at low metallicity because of the high mass loss rates (due to stellar winds) at solar metallicity and above, which drastically reduce the progenitor’s mass (Heger et al. 2003,

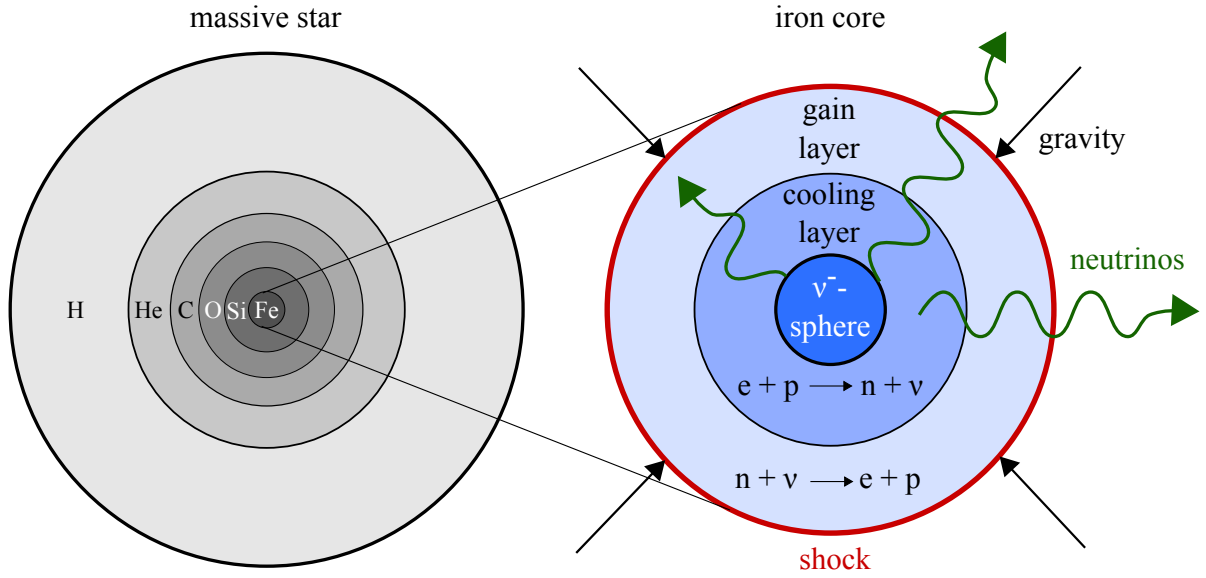


Fig. 1.11 *Left*: Onion structure of a massive star as collapse of the iron core commences. Heavy elements accumulate in the star’s centre. *Right*: Zoom-in on the iron core ~ 0.5 s after the onset of collapse. Some of the neutrinos produced in the neutrino-sphere and the cooling layer around it are absorbed in the gain layer but most escape unimpeded. The various regions are not to scale. Adapted from Foglizzo (2017) with permission from Springer Nature and Springer eBooks.

Since massive stars live only for several Myr, core-collapse SN explosions take place in star-forming regions. Hence, the mechanism is discussed in more detail below.

Explosion Physics of Core-Collapse Supernovae

A core-collapse SN marks the end of a massive star’s life. After several Myr of nuclear fusion a massive star has developed an onion-shell structure with successively heavier elements towards the centre (cf. Figure 1.11). Since no thermonuclear energy can be gained from the fusion of iron to yet heavier elements, the iron core is supported against self-gravity induced collapse only by the pressure from degenerate electrons. When the mass of the iron core exceeds a critical limit, the pressure from degenerate electrons is insufficient to support it and collapse ensues.²³ This limit was first derived by Chandrasekhar (1931) and is now estimated to be

$$M_{\text{ch}} \approx 1.4 M_{\odot} \left(\frac{Y_e}{0.5} \right)^2 \quad (1.49)$$

(Foglizzo 2017). Here, Y_e is the electron fraction in the core. As the mass of the core approaches the Chandrasekhar limit, its density increases. This leads to a decrease in Y_e due to an increase in electron

and references therein). However, there are indications that pair-instability SNe can also occur at solar metallicity if the star has a moderate surface magnetic field which reduces the mass loss rates (Georgy et al. 2017).

²³In stars with masses between 9 and 10 M_{\odot} , the core reaches this limit before iron burning is initiated when the core consists of O, Ne, and Mg and the star explodes as a so-called electron-capture SN.

capture on heavy nuclei and on free protons,

$$e^- + (A, Z) \rightarrow \nu_e + (A, Z - 1) \quad (1.50)$$

$$e^- + p \rightarrow \nu_e + n, \quad (1.51)$$

and due to photodissociation of heavy nuclei (Janka 2017). Here, e^- , p , n , and ν_e stand for electrons, protons, neutrons, and electron neutrinos respectively, while A and Z denote an atom's mass number and atomic number. Since the removal of free electrons leads to a drop in the internal pressure, the core's density increases further, lowering the number of free electrons even more. As a result the Chandrasekhar mass decreases according to Eq. (1.49) in a runaway process (Foglizzo 2017).

As the collapse is initiated, neutrons (and neutrinos) form via inverse β -decay, giving rise to a proto-neutron star with a typical size of 30 km and a density of the order $10^{15} \text{ g cm}^{-3}$ (compared to the iron core where $\rho \sim 10^9 \text{ g cm}^{-3}$). The collapse is reversed as the infalling material bounces on the proto-neutron star's hard surface (Alsabti and Murdin 2017). However, the escape from the steep potential well close to the proto-neutron star proves difficult, even more so as the outward moving material is slowed down by the remaining parts of the iron core which are still in the process of collapse. Thus, while the initial phase of the collapse and bounce takes less than one second, the shock only breaks out of the star's surface after several hours via a mechanism known as neutrino-driven explosion (Bethe and Wilson 1985), explained below.

The kinetic energy of the collapsing iron core is $\sim 10^{53}$ erg. However, both the energy necessary to unbind the stellar matter from the core and the kinetic energy of the SN ejecta are only of the order 10^{51} erg (see Foglizzo 2017 and references therein). A large part of the remaining energy is stored in neutrinos which are created as iron is transformed into neutrons. As shown in Figure 1.11, the proto-neutron star is surrounded by a neutrino-sphere which can be regarded as a black-body emitter of neutrinos. It is surrounded by a cooling layer where more neutrinos are created via electron capture on free protons (Eq. 1.51). In the surrounding gain layer, however, neutrinos are absorbed via

$$n + \nu_e \rightarrow p + e^- \quad (1.52)$$

$$p + \bar{\nu}_e \rightarrow n + e^+. \quad (1.53)$$

This is the main source of heating close to the shock and the absorption of neutrinos in the gain layer is crucial to accelerate the shock outwards. Hydrodynamic instabilities which develop hundreds of ms after the bounce can push the shock further out increasing the size of the gain layer which leads to a larger fraction of the neutrinos being absorbed.

Still, most neutrinos escape from the stellar matter unimpeded. These emerging neutrinos, together with gravitational waves in cases of asymmetrical collapse, can provide important observational clues about the first seconds of a SN explosion. One-dimensional simulations of SN explosions by stars with $9 \leq M_* \leq 120 M_\odot$ showed that heating by absorbed neutrinos is sufficient to drive explosions in most stars with $M_* \lesssim 22 M_\odot$ (Sukhbold et al. 2016). However, neutrino heating failed to produce SN

Introduction

explosions for a large fraction of more massive stars; instead several “islands of explodability” exist in the mass range. For very massive stars transverse motions from hydrodynamic instabilities are thought to be important for neutrino-driven explosions to work but open questions still remain (Foglizzo 2017).

Expansion of Supernova Remnants

The shell of debris expanding from the explosion site and sweeping up ambient gas is called a supernova remnant (SNR, Seeds and Backman 2013). In the case of a type Ia SN, the region surrounding the explosion is typically already devoid of ISM. In the case of a core-collapse SN however, which occurs only several Myr after the birth of a massive star, dense gas is often still present. The evolution of an SNR is similar to a shell blown by winds from massive star discussed in Section 1.2.1 but with the difference that stellar winds are continuously launched from the star for several Myr whereas a SN explosion constitutes a very short burst of energy and momentum.²⁴ Due to these similarities, the following description of the evolution of SNRs will be brief.

Nevertheless, there are complications not present (to this degree) in wind-blown bubbles that are worth mentioning. Rotation of the progenitor star and instabilities inside the iron core during the launch of the SN shock wave can cause deviations from spherical symmetry of the explosion (Reynolds 2017). Furthermore, the density profile of the ejecta is structured with a steep power law, $\rho \propto r^{-s}$ with $s \sim 10 - 12$ in the outer regions, and a roughly constant density in the central regions. In between, there is a density jump by a factor 3 – 10 which corresponds to the location of the interface of the hydrogen envelope and the stellar interior in the progenitor star (Matzner and Mckee 1999). Ignoring asymmetries, the shock radius can be described by a single value, which I will call R_2 to reflect the similarity to wind-blown bubbles. The explosion is characterized by the mass of the ejecta M_{ej} and their terminal velocity v_{∞} . The stellar ejecta reach terminal velocities of up to $3 \times 10^4 \text{ km s}^{-1}$, with typical average velocities in the range 5×10^3 to $1 \times 10^4 \text{ km s}^{-1}$ (Alsabti and Murdin 2017; Colgate 1973; Reynolds 2017).

Initially, the expansion is said to be ejecta-driven (also called the free expansion phase) where the ejecta expand more or less unimpeded into the surrounding ISM (Reynolds 2017). As the ejecta are slowed down by the ambient ISM, they shock-heat the gas to X-ray emitting temperatures and a reverse shock develops (this is similar to wind-blown bubbles, cf. Figure 1.6). At early times, the reverse shock moves outwards as denser and denser material with higher ram pressure from the progenitor star’s envelope arrives.

With the arrival of the central ejecta with roughly uniform density, the pressure of the shocked material between forward and reverse shock pushes the reverse shock back towards the explosion centre. This marks the transition to the Sedov phase (Sedov 1961). At this point all SN ejecta have been shocked. The expansion of the forward shock with radius R_2 follows the energy and momentum equation, Eqs. 1.19 and 1.22, with $R_1 = 0$ and $E_b = E_{\text{SN}} = \text{const.}$, where E_{SN} is the kinetic energy of

²⁴It is obvious that a SN explosion and the explosion of a military bomb share certain similarities. For this reason, blast waves stemming from point explosions have first been investigated in a military context. Only later have these works been applied to astrophysical problems (Sedov 1961).

the supernova ejecta ($E_{\text{SN}} \sim 10^{51}$ erg). In the case of constant density ambient ISM and $\gamma = 5/3$, the self-similarity solution reads

$$R_2 = \left(\frac{25 E_{\text{SN}}}{4\pi \rho_0} \right)^{1/5} t^{2/5}. \quad (1.54)$$

Self-similar solutions for the case of an ambient ISM with an arbitrary power law exist (Sedov 1961) but in most cases a constant density profile is the best approximation (Reynolds 2017).

Eventually, as the temperature inside the hot region between the forward and reverse shocks drops due to adiabatic expansion, radiative cooling becomes important (when $T \sim 10^5$ K) and the energy is radiated away. This marks the onset of the radiative phase at a time t_r . As for stellar winds, in reality the transition is gradual and could occur earlier if the shock-heated gas is not efficiently confined. If the hot gas in the SNR interior is confined, the remnant enters a “pressure-driven snowplough phase” with $R_2 \propto t^\delta$, $\delta \sim 0.3$ (Chevalier 1974; McKee and Ostriker 1977). Otherwise, the remnant coasts with only its momentum being conserved. In that case

$$R_2 = \left(\frac{25 E_{\text{SN}}}{4\pi \rho_0} \right)^{1/5} t_r^{3/20} t^{1/4} \quad (1.55)$$

for $t > t_r$ (cf. Reynolds 2017). The transition time t_r is also some (unknown) function of ρ_0 but since no simple analytic expressions exist when hydrodynamic instabilities and density inhomogeneities are considered (cf. Section 2.3) I ignore this complication here. At this late stage, irregularities and hydrodynamic instabilities cause the shell to break up. Eventually, when the velocity has dropped to values comparable to the local sound speed the shell dissipates into the ISM.

In the Milky Way ~ 300 SNRs are identified (Green 2014). These remnants are in different evolutionary stages, with ages of the order 1000 to 10 000 years. Older remnants become very faint and difficult to observe (Green 2017).

1.2.4 Effects of Stellar Feedback

Cloud Disruption and Regulation of Star Formation

As presented in the previous sections, newborn massive stars have drastic effects on their birth environment. Fundamentally, all previously discussed feedback processes have in common that they push the ambient gas away from sites of massive-star formation, either by heating it to high temperatures or by directly transferring momentum to it. How the gas reacts to various feedback processes, as expressed in simple self-similarity solutions for the radius of the feedback-driven shell, is summarized in Table 1.2. Note however, that none of these results takes gravity into account which would slow down the expansion of the gas.

Let us now return to the molecular cloud mentioned at the beginning of Section 1.1.4 which had lost its turbulent support and started to form stars. By transferring momentum to the gas, stellar feedback (which was not included in the simulations by Klessen and Burkert 2001) will eventually

Introduction

Table 1.2 Overview of self-similarity solutions (for an environment with constant density ρ_0 and no gravity) of the form $R_2 \propto \rho_0^\alpha t^\beta$.

limit/phase	stellar winds		radiative feedback		supernovae	
	energy*	momentum	HII region	radiation pressure	energy*	momentum
α	$-1/5$	$-1/4$	$-2/7^\dagger$	0	$-1/5$	$-1/5$
β	$3/5$	$1/2$	$4/7$	$2/3$	$2/5$	$1/4$
equation	(1.30)	(1.39)	(1.44)	(1.48)	(1.54)	(1.55)
reference	W77 ¹	K92 ²	S04 ³	O67 ⁴	S61 ⁵	R17 ⁶

* also known as adiabatic phase

[†] for $R_2 \gg R_S$

¹ Weaver et al. (1977), ² Koo and McKee (1992a), ³ Spitzer (2004), ⁴ O’Dell et al. (1967), ⁵ Sedov (1961), ⁶ Reynolds (2017)

unbind it and destroy the cloud in the process. Hence, stellar feedback is an obvious suspect for causing the observed low star formation efficiencies.

Indeed, also in observations, the profound effects of stellar feedback are ubiquitous. The presence of feedback-driven shells and highly overpressured X-ray emitting bubbles demonstrates the destructive consequences of feedback (e.g. Townsley et al. 2011, and references therein). Consequently, several analytic studies (Fall et al. 2010; Kim et al. 2016; Matzner 2002; Matzner and Jumper 2015) and hydrodynamic simulations (Geen et al. 2017; Haid et al. 2019; Howard et al. 2017; Walch et al. 2012) have demonstrated that stellar feedback suppresses further star formation. This suppression of star formation by star formation constitutes a fundamental self-regulation mechanism.

However, open questions remain, e.g. how the different feedback processes are coupled and how many stars can form before the natal cloud is disrupted. This is discussed in more detail in Section 1.3. Furthermore, while the net effect of massive-star formation is to disrupt the natal GMC and impede the formation of additional stars, feedback can also trigger the formation of new stars (see below).

Triggered Star Formation

It has been suggested by Elmegreen and Lada (1977) that stellar feedback can also be positive: Gas accumulating downstream from supersonic shock fronts driven by OB stars becomes gravitationally unstable, collapses, and new stars form. For example, the Solar System might have formed in this fashion (Dwarkadas et al. 2017). Dale et al. (2007) introduced the term “strong triggering” for feedback inducing star formation that would otherwise not happen, i.e. by leading to the collapse of structures that would – in the absence of feedback – be stable (in contrast to “weak triggering” which would only accelerate star formation).²⁵

However, it is not trivial for stellar feedback to induce collapse of an otherwise stable structure. Starting from a stable clump, Boss et al. (2010) have shown that an incoming shock which is too fast

²⁵As a side note, star formation can of course not only be triggered by stellar feedback but by many other processes as well, e.g. cloud-cloud collisions or galaxy mergers. In this section, however, I solely refer to triggering by stellar feedback.

($v > 70 \text{ km s}^{-1}$ in their particular set-up) does not induce collapse but instead destroys the clump. Therefore, SN ejecta and winds from massive stars would first need to decelerate from a velocity $v > 1000 \text{ km s}^{-1}$ down to $v < 70 \text{ km s}^{-1}$ by ploughing into dense ambient ISM for several pc (and several 10^5 yr) before star formation could be triggered. Thus, on small spatial scales feedback remains negative. This is not necessarily the case for other sources of feedback where typical velocities are of the order 10 km s^{-1} , such as winds from asymptotic giant branch stars and photoionization feedback. In simulations Dale et al. (2007) showed that photoionization feedback can cause both weak and strong triggering. However, any increase in the SFE is modest. As demonstrated by Walch et al. (2012), in the long run the net effect of photoionization feedback on the SFE is still negative.

Observationally, it is even harder to quantify the contribution of triggered star formation to the total amount of star formation. Typically, young stars in the vicinity of bubbles, I-fronts, cometary features or other structures reminiscent of feedback are associated with triggered star formation (e.g. Deb et al. 2018; Duronea et al. 2017, see also Dale et al. 2015 for a list of observational papers on feedback-triggered star formation, mostly from the years 2000-2014) but in the absence of theoretical modelling of the star-forming region in different feedback scenarios (such as in Rugel et al. 2019), reaching a definitive conclusion is impossible. As Krumholz et al. (2014) point out, while on large scales feedback may indeed be positive, it is inherently difficult to distinguish feedback-triggered star formation from star formation merely induced by large-scale turbulence - which would have occurred anyway (see also Dale et al. 2015).

Dissolution of Star Clusters

Virtually all stars are born in clusters (Lada and Lada 2003). However, at an age of $\lesssim 10 \text{ Myr}$ the fraction of total stellar mass in bound clusters is only $\sim 10 - 30\%$ (Chandar et al. 2017) and varies widely with environment (Krumholz et al. 2018, Figure 8, and references therein) implying that most star clusters dissolve soon after they are born.

Most dense clumps in the Milky Way are bound (with virial parameters²⁶ $\alpha_{\text{vir}} < 2$, Urquhart et al. 2018), from which follows that newborn clusters should also be bound. The reason why clusters still dissolve at an early age lies in the removal of gas. Following Hills (1980), let us consider a star cluster with effective radius $R_{e,0}$ that is initially (when gas is still present) in virial equilibrium, $2E_{\text{kin}} = -E_{\text{grav}}$, i.e.

$$M_0 \sigma_v^2 = \frac{GM_0^2}{2R_{e,0}} \quad (1.57)$$

²⁶The virial parameter α_{vir} is a measure of the ratio of internal kinetic (thermal and turbulent) energy E_{kin} to gravitational energy E_{grav} . For a spherical gas clump with mass M_{clump} , effective radius R_e , and velocity dispersion σ_v the virial parameter is defined as

$$\alpha_{\text{vir}} \equiv \frac{5\sigma_v^2 R_e}{GM_{\text{clump}}} = \frac{2E_{\text{kin}}}{|E_{\text{grav}}|} \quad (1.56)$$

(Bertoldi and Mckee 1992). With this definition, $\alpha_{\text{vir}} < 2$ implies that the clump is bound, otherwise it is unbound and will disperse in the absence of pressure confinement from the ambient medium (Urquhart et al. 2018).

Introduction

where $M_0 = M_* + M_{\text{gas},1}$ is the total mass of stars and gas and σ_v is the velocity dispersion. If the gas is removed on a timescale which is short compared to the dynamical time $t_D = (G\rho)^{-1/2}$, the stars find themselves in a supervirial state. In order to virialize again the cluster has to expand to a new effective radius R_e . This dynamical response of the star cluster is called violent relaxation. The new virial equilibrium is reached when

$$\frac{R_e}{R_{e,0}} = \frac{M_*}{M_* - M_{\text{gas},1}}. \quad (1.58)$$

As Hills (1980) pointed out, the new radius diverges if $M_{\text{gas},1} = M_*$ and switches sign for even higher gas masses. In terms of the star formation efficiency ϵ_{SF} , Eq. (1.58) becomes

$$\frac{R_e}{R_{e,0}} = \frac{\epsilon_{\text{SF}}}{2\epsilon_{\text{SF}} - 1} \quad (1.59)$$

and hence the cluster is expected to dissolve when $\epsilon_{\text{SF}} \leq 0.5$ (see also Tutukov 1978). Qualitatively, this has been reproduced in N -body simulations by Boily and Kroupa (2003); Fellhauer and Kroupa (2005); Geyer and Burkert (2001); Lada et al. (1984) who find the SFE threshold to form a bound cluster to be $\sim 0.3 - 0.4$ (for a comparison see also Figure 1 in Parmentier and Gilmore 2007 or Figure 3 in Baumgardt and Kroupa 2007). If gas removal on the other hand is slow, i.e. on a timescale which is long compared to t_D , the cluster is kept in virial equilibrium as it expands, and the cluster does not dissolve (Hills 1980).²⁷

In reality, the gas removal is neither instantaneous nor infinitely slow but somewhere in between. Removing the gas exponentially on a characteristic timescale of $10 \times t_D$, Baumgardt and Kroupa (2007); Geyer and Burkert (2001) derived an SFE threshold of $\sim 0.1 - 0.2$ above which clusters remain bound. Furthermore, Shukirgaliyev et al. (2017) have shown that even if gas removal is instantaneous, the threshold can decrease when the gas density profile is less steep than the density distribution of the stars²⁸ (a cluster with $\epsilon_{\text{SF}} \gtrsim 0.15$ remains bound in their particular setup). The survivability of a star cluster is also enhanced if it forms in a subvirial state or it is substructured (Goodwin 2009; Lee and Goodwin 2016).

1.3 Open Questions, Obstacles, and How to Address Them

Stellar feedback is an inevitable consequence of star formation. In the previous sections I have discussed how stellar winds, radiation, and supernova feedback affect the gas around the sites of massive star formation. So far, each of these processes has been considered in isolation. However, in a massive star cluster, winds, radiation and – after a delay of a few Myr – supernovae all occur simultaneously,

²⁷At least not immediately. In the long run ($t \gg 30$ Myr), many clusters dissolve e.g. due to the tidal field of their host galaxy (Shukirgaliyev et al. 2018). Additionally, after ~ 100 Myr two-body relaxations between stars within the cluster lead to a Maxwellian velocity distribution, so that the velocities of some stars at the distribution's high-velocity end exceed the escape velocity and leave the cluster (Krumholz et al. 2018) – just as the Earth's atmosphere constantly loses particles to space.

²⁸Such a density profile is expected when star formation occurs at a constant SFE per free-fall time in a clump with a centrally peaked density profile (Parmentier and Pfalzner 2013).

1.3 Open Questions, Obstacles, and How to Address Them

complicating the situation enormously. Naturally, the question arises whether one of these processes dominates over all others, in which case ignoring them would be safe. Similarly, while it has been demonstrated that various feedback processes on their own limit the star formation efficiency achieved in molecular clouds, it is not clear yet to what degree star formation is suppressed if – as in reality – all feedback processes act in unison.

The results for the expansion of feedback-driven shells (presented in Sections 1.2.1 - 1.2.3 and summarized in Table 1.2), as well as analytic work and simulations, e.g. by Krumholz et al. (2006); Matzner (2002); Walch et al. (2012); Whitworth (1979), indicate that thermal pressure from HII regions should be one of the dominant feedback sources and that already a low star formation efficiency may be sufficient to lead to the destruction of the natal cloud. However, as pointed out by Dale et al. (2012b), ionizing radiation alone cannot unbind gas from GMCs where the escape velocity is larger than the sound speed of the ionized gas, $c_{\text{II}} \sim 10 \text{ km s}^{-1}$ (note that the Spitzer solution for the expansion velocity of HII regions, Eq. 1.45, does not include gravity). Consequently, while HII regions can disrupt clouds with masses $M_{\text{cl},0} \lesssim 10^4 M_{\odot}$ as demonstrated in simulations by Walch et al. (2012), GMCs with $M_{\text{cl},0} \gtrsim 10^5 M_{\odot}$ are not strongly affected by HII regions (Dale et al. 2012b; Howard et al. 2016).

Stellar winds are very effective in accelerating the ambient gas as long as the wind bubble is in the energy-driven limit (see Table 1.2). How long the energy-driven phase lasts depends on the radiative cooling of the bubble and the confinement of the shock-heated gas. Both cooling and confinement in turn depend on the interaction between the various types of feedback (see Section 2.3). The efficiency of stellar winds is thus still debated. Similarly, while SNe inject an enormous amount of energy into the ISM, they occur only at rather late times when the star-forming region has already been exposed to stellar winds and radiative feedback for at least 3 Myr.

Typically, studies of stellar feedback focus on one or two feedback processes, e.g. just supernovae (Gatto et al. 2015; Walch and Naab 2015), supernovae and stellar winds (Gatto et al. 2017; Rogers and Pittard 2013), photoionization and supernovae (Geen et al. 2016), just photoionization (Dale and Bonnell 2011; Haid et al. 2019), photoionization and radiation pressure (Ali et al. 2018; Howard et al. 2016; Kim et al. 2016, 2018), photoionization and winds (Dale et al. 2014), and winds and radiation pressure (Silich and Tenorio-Tagle 2013).²⁹

The reason why there are very few three-dimensional hydrodynamic simulation that include more than one or two feedback processes is, in a nutshell, the high computational cost. Since, for example, the efficiency of radiation as a feedback source is set by its coupling with the ISM, high resolution is absolutely mandatory for realistic simulations (e.g. Krumholz 2018). High resolution is also necessary in order to correctly model hydrodynamic instabilities (important for wind confinement) which are dampened if the resolution is too low (e.g. Lamberts et al. 2011).

However, high-resolution hydrodynamic simulations of stellar winds are computationally expensive. In part, this is because explicit integration schemes are only numerically stable if the Courant-

²⁹This list is by no means exhaustive. For example, Geen et al. (2015) investigate stellar winds, photoionization and supernova feedback albeit only for a single $15 M_{\odot}$ star. Other recent studies are discussed in the respective papers (Sections 2.1 - 2.3) and in the Conclusion (Section 3.1).

Introduction

Friedrichs-Lewy condition is fulfilled (Courant et al. 1928). In the one-dimensional case this condition reads

$$\frac{v\Delta t}{\Delta x} \stackrel{!}{<} 1, \quad (1.60)$$

where v is the velocity, Δt is the time step, and Δx is the length interval (i.e. the cell size in mesh codes). In the case of fast winds ($v > 1000 \text{ km s}^{-1}$ as appropriate for massive stars), small cell sizes are only achievable when a very small time step is used, slowing down the computation drastically. Thus, high-resolution studies ($\Delta x < 0.1 \text{ pc}$) of a large parameter space of various GMC initial conditions (density, mass, boundness, star formation efficiency, metallicity, ...) are currently not feasible, even when limiting oneself to just one or two feedback processes.

On the other hand, analytic studies are often limited to one or two feedback processes because the coupling between the individual processes is highly non-linear. Those that treat several processes do so in a very approximate fashion by focusing on one feedback source and then introducing a factor which accounts for the amplification by other processes which they can only very crudely estimate (f_{trap} in Krumholz and Matzner 2009). Furthermore, realistic synthetic observations³⁰, which are key to comparing models with real observational data, are typically too complicated for purely analytical models.

Therefore, there is currently a high demand for a method which (i) is computationally inexpensive so that a large parameter space of cloud and cluster properties can be investigated, (ii) contains a sufficiently sophisticated model of subgrid physics so that the interaction between various feedback processes can be modelled without relying on poorly constrained secondary coupling parameters, and (iii) has high enough spatial resolution to correctly model radiative feedback and allow for realistic synthetic observations.

In summary, the fact that stellar feedback suppresses and regulates star formation in GMCs has been demonstrated in several analytic studies (e.g. Fall et al. 2010; Kim et al. 2016; Matzner 2002; Matzner and Jumper 2015) and hydrodynamic simulations (e.g. Green 2017; Haid et al. 2019; Howard et al. 2017; Walch et al. 2012). How in detail this is achieved, i.e. what type of feedback dominates as a function of time and environment, how many massive stars exactly need to form before a cloud is destroyed, how in detail star formation proceeds if feedback is yet insufficient to disrupt its natal GMC, and whether stellar feedback can be invoked to explain peculiar age spreads in young clusters, is still an open question. The purpose of this thesis is to shed light on this question.

Each of the three publications presented in Section 2 focuses on a different aspect of this question. In the first paper (Section 2.1), we present a new semi-analytic feedback model which includes stellar winds, radiation pressure, and supernova feedback and fulfils the three demands outlined above. The strengths of these feedback processes are compared with one another, the coupling of radiation to the ISM is investigated, and the minimum star formation efficiencies above which clouds are disrupted by stellar feedback are derived for two cloud densities, two different metallicities, and a range of cloud masses. In the second paper (Section 2.2), the model is applied to the massive star-forming region

³⁰Synthetic observations are predictions of how an object that has been built from a theoretical model will appear to an observer (see review by Haworth et al. 2018).

1.3 Open Questions, Obstacles, and How to Address Them

30 Doradus (see Figure 1.4) to investigate the peculiar distribution of stellar ages in the central star cluster and its possible connection to stellar feedback. In the third paper (Section 2.3), we focus on the cooling and confinement of stellar winds (while still modelling the other feedback processes) and derive minimum star formation efficiencies for a much larger grid of initial conditions. Finally, in Section 3 the implications of the three papers as a whole are discussed.

Chapter 2

Publications

In the following, three publications which appeared in Monthly Notices of the Royal Astronomical Society (MNRAS) are presented. The publications are ordered by their date of appearance. Note that page and section numbers follow the original MNRAS-internal numbering.

2.1 Winds and Radiation in Unison: A New Semi-Analytic Feedback Model for Cloud Dissolution

Distribution of work: Simon Glover and Ralf Klessen had the idea to investigate stellar feedback in star-forming regions via numerical methods in general. I developed the idea for this particular publication, wrote the code `WARPFIELD`, ran and analysed the models (in close collaboration with Eric Pellegrini), created all figures, and wrote most of the text (except for the introduction). Eric Pellegrini, Simon Glover and Ralf Klessen contributed ideas during the preparation of the manuscript and provided pieces of text and proofreading.

Winds and radiation in unison: a new semi-analytic feedback model for cloud dissolution

Daniel Rahner,¹★ Eric W. Pellegrini,¹★ Simon C. O. Glover¹ and Ralf S. Klessen^{1,2}

¹Zentrum für Astronomie, Institut für Theoretische Astrophysik, Universität Heidelberg, Albert-Ueberle-Straße 2, D-69120 Heidelberg, Germany

²Interdisziplinäres Zentrum für Wissenschaftliches Rechnen, Universität Heidelberg, Im Neuenheimer Feld 205, D-69120 Heidelberg, Germany

Accepted 2017 June 15. Received 2017 June 8; in original form 2017 April 13

ABSTRACT

Star clusters interact with the interstellar medium (ISM) in various ways, most importantly in the destruction of molecular star-forming clouds, resulting in inefficient star formation on galactic scales. On cloud scales, ionizing radiation creates H II regions, while stellar winds and supernovae (SNe) drive the ISM into thin shells. These shells are accelerated by the combined effect of winds, radiation pressure, and SN explosions, and slowed down by gravity. Since radiative and mechanical feedback is highly interconnected, they must be taken into account in a self-consistent and combined manner, including the coupling of radiation and matter. We present a new semi-analytic 1D feedback model for isolated massive clouds ($\geq 10^5 M_{\odot}$) to calculate shell dynamics and shell structure simultaneously. It allows us to scan a large range of physical parameters (gas density, star formation efficiency, and metallicity) and to estimate escape fractions of ionizing radiation $f_{\text{esc, i}}$, the minimum star formation efficiency ϵ_{min} required to drive an outflow, and recollapse time-scales for clouds that are not destroyed by feedback. Our results show that there is no simple answer to the question of what dominates cloud dynamics, and that each feedback process significantly influences the efficiency of the others. We find that variations in natal cloud density can very easily explain differences between dense-bound and diffuse-open star clusters. We also predict, as a consequence of feedback, a 4–6 Myr age difference for massive clusters with multiple generations.

Key words: radiation: dynamics – ISM: bubbles – ISM: clouds – H II regions – ISM: kinematics and dynamics – galaxies: star formation.

1 INTRODUCTION

The formation of stars from the cold, dense interstellar medium (ISM) marks the onset of the conversion of nuclear binding energy into radiative and mechanical energy. Injected back into the immediate surroundings of the stars, this energy drives a rapid chemical and dynamic evolution of the very molecular cloud from which the stars formed. This chain of events, where the creation of stars leads to energy injection by stars which disrupt the clouds, is known as stellar feedback. In the case of massive stellar clusters ($M_{*} > 10^3 M_{\odot}$), the energetic processes are dominated by three main forms of feedback: ultraviolet (UV) radiation, colliding stellar winds, and supernovae (SNe). Each of these processes provides a source of energy and momentum that acts in opposition to gravity (for a review about stellar feedback, see Krumholz et al. 2014).

Around young massive clusters, confined interacting winds produce hot ($T \sim 10^6$ – 10^8 K) bubbles (Weaver et al. 1977, hereafter

W77; Dunne et al. 2003). These adiabatically expand, compressing the gas ahead of them into a thin dense shell. The bubbles are characterized by a rarefied, collisionally ionized gas. While this gas remains hot, its high thermal pressure drives the expansion of the surrounding shell (W77). Once the gas cools, however, the winds from the central cluster push the remainder of the gas from the bubble into the shell. Thereafter, the wind momentum is deposited directly into the shell in the form of ram pressure. SNe exploding within the bubble add their energy to the existing thermal and mechanical energy of the gas in the bubble.

The optical depth of the gas inside a wind bubble is very low, and so radiation from the central stellar cluster easily reaches the dense shell surrounding the bubble (Townsend et al. 2003; Gupta et al. 2016). UV photons with energies $E > 13.6$ eV photoionize hydrogen in this shell, resulting in one of two outcomes: either the entire shell becomes ionized, or only the inner layers become so, with the outer layers of the shell remaining neutral (e.g. Martínez-González, Silich & Tenorio-Tagle 2014).

Photons that are absorbed in the shell not only heat it and potentially change its chemical state, but also deposit momentum (Lebedew 1901). Essentially, the radiation exerts a pressure force

* E-mail: daniel.rahner@uni-heidelberg.de (DR); eric.pellegrini@uni-heidelberg.de (EWP)

on the gas and dust that acts radially outwards from the central stellar cluster. If this radiation pressure is sufficiently large, then it can become dynamically significant and can play a major role in driving the evolution of the shell (Mathews 1967; Draine 2011; Kim, Kim & Ostriker 2016). One of the key factors that determine whether or not radiation pressure becomes significant is the efficiency with which radiation couples with the shell (Krumholz & Matzner 2009). For ionizing radiation, this is determined by the amount of neutral and molecular material as well as dust absorbing the radiation. When the column density of the gas is high enough to absorb all the ionizing photons (i.e. when the layer is optically thick to ionizing radiation), the system is ‘radiation bounded’, coupling is efficient and momentum is transferred effectively. However, the shells surrounding many observed star-forming regions are optically thin to ionizing radiation, suggesting that coupling is not always effective (Pellegrini et al. 2012; Seon 2009). For non-ionizing radiation ($E < 13.6$ eV), the optical depth is again the main factor determining whether or not coupling is efficient, but in this case the dominant source of opacity is provided by dust unless the radiation field is weak (Krumholz, McKee & Tumlinson 2008).

Previous simplified models of the growth of shells and bubbles around young massive clusters have typically assumed that the dynamics of the shell are dominated by the effect of winds (e.g. W77; Chevalier & Clegg 1985; Mac Low & McCray 1988; Koo & McKee 1992; Canto, Raga & Rodríguez 2000; Silich & Tenorio-Tagle 2013, hereafter ST13) or radiation pressure (e.g. Krumholz & Matzner 2009; Murray, Quataert & Thompson 2010; Kim, Kim & Ostriker 2016). However, as we will see later, in the general case both must be included in order for the model to be self-consistent and hence both processes are important. In addition, in the treatments that do account for radiation pressure, the shell is often assumed to be completely opaque to radiation (Krumholz & Matzner 2009; Murray et al. 2010), whereas in reality the escape fraction can often be significant (see Section 6).

In this paper, we present a new model for the growth of shells around clusters that properly accounts for both winds and radiation, and that carefully treats the structure of the shell and its influence on the fraction of the radiation that is absorbed. In Section 2, we present our model for the structure and dynamics of the shell, and in Section 3, we discuss the evolution of an exemplary cloud and compare to analytic solutions. In Section 4, we examine how well coupled radiation is to the shell and use those results in Section 5 to explore the conditions in which each of the different feedback processes (winds, SNe, and radiation) dominates, examining this both as a function of time during the expansion, and in an integrated form over the entire lifetime of the cloud. Our model also allows us to make predictions for the evolution of the escape fraction of ionizing radiation during the growth of the shell, which we present in Section 6. In Section 7, we discuss what we can learn from our model about the star formation efficiency ϵ of the cloud, and how this varies as a function of the mass, mean density, and metallicity of the cloud. We conclude in Section 8 with a summary of the key results of our study.

2 MODEL

For our model, we consider a spherical cloud with a constant density ρ_{cl} . We assume the ISM of the cloud has a standard chemical composition of 1 He atom per 10 H atoms; thus the mean mass per nucleus $\mu_n = (14/11)m_{\text{H}}$ and the mean mass per particle $\mu_p = (14/23)m_{\text{H}}$, where m_{H} is the proton mass. The cloud’s radius is

given by

$$R_{\text{cl}} = 19.7 \text{ pc} \times \left(\frac{M_{\text{cl}}/10^5 M_{\odot}}{n_{\text{cl}}/100 \text{ cm}^{-3}} \right)^{1/3}, \quad (1)$$

where M_{cl} is the cloud mass, and $n_{\text{cl}} = \rho_{\text{cl}}/\mu_n$ is the number density of atoms/ions in the cloud. At $t = 0$, a star cluster of mass M_* forms at the cloud’s centre. It injects feedback into the surrounding ISM in the form of stellar winds, radiation, and eventually SN explosions. As outlined in the Introduction, the combined effects of radiation and winds from a massive cluster will create an expanding bubble of tenuous and hot ionized gas which is surrounded by a much denser and colder shell of swept-up cloud material. In order to calculate the resulting expansion speed, or – if gravity starts to dominate at some stage – to compute the corresponding contraction velocity, we need to have a detailed understanding of the strength of the different forces acting on the shell. For this, we need to take into account the aging population of the star cluster, the morphological and kinematical structure of the bubble and the shell, and their chemical composition. In this section, we first outline our physical model for the shell dynamics, then discuss the structure of the dense shell, and finally introduce our scheme to couple both together.

2.1 Shell dynamics

We model three phases of expansion of the natal cloud around the cluster. Early expansion is adiabatic and dominated by wind energy which sweeps the cloud interior into a thin shell (Phase I). This phase lasts so long as the energy is confined and radiative losses are small. After that, shell acceleration is determined by momentum input by winds, radiation, and eventually by SN explosions opposing gravity (Phases II and III). In Phase II, the expanding shell continues to sweep-up material. Once the whole cloud has been swept up, the shell can freely expand into the ambient ISM (Phase III). These phases are outlined in Fig. 1, and are now discussed in more detail. Since we only model isolated clouds, we do not take into account any effects of an external galactic potential like shearing, which would introduce differential rotation and tidal torques, or the coupling to the larger scale turbulent flows in the ISM.

2.1.1 Phase I: energy-dominated winds

Initially, radiation with $E > 13.6$ eV creates a large ionized region around the cluster (the so-called Strömgren sphere). At the same time, winds from the star cluster expand freely into the ISM. Due to its very short duration, however, this initial phase can be neglected (Lamers & Cassinelli 1999). Soon, several distinct zones form around the cluster (W77): an inner free wind zone is surrounded by a hot shocked wind region. Together they make up the wind bubble (red region in Fig. 1) which works against a dense shell consisting of swept-up material. Since the density in the shell is higher than in the cloud, the recombination rate increases and the ionization front travels inwards until it lies inside the shell. The shocked wind material reaches temperatures of 10^6 – 10^8 K causing a fast, adiabatic expansion. During this phase, we can ignore the effect of gravity and radiation pressure as they are second-order effects. If the shell runs into ISM of a constant density, the equation of motion in the thin shell limit according to Bisnovatyi-Kogan & Silich (1995) is

$$\frac{d^2}{dt^2} (R^3 \dot{R}) + (3\gamma - 2) \frac{\dot{R}}{R} \frac{d}{dt} (R^3 \dot{R}) = \frac{9(\gamma - 1)L_w}{4\pi\rho_{\text{cl}}} \frac{1}{R}. \quad (2)$$

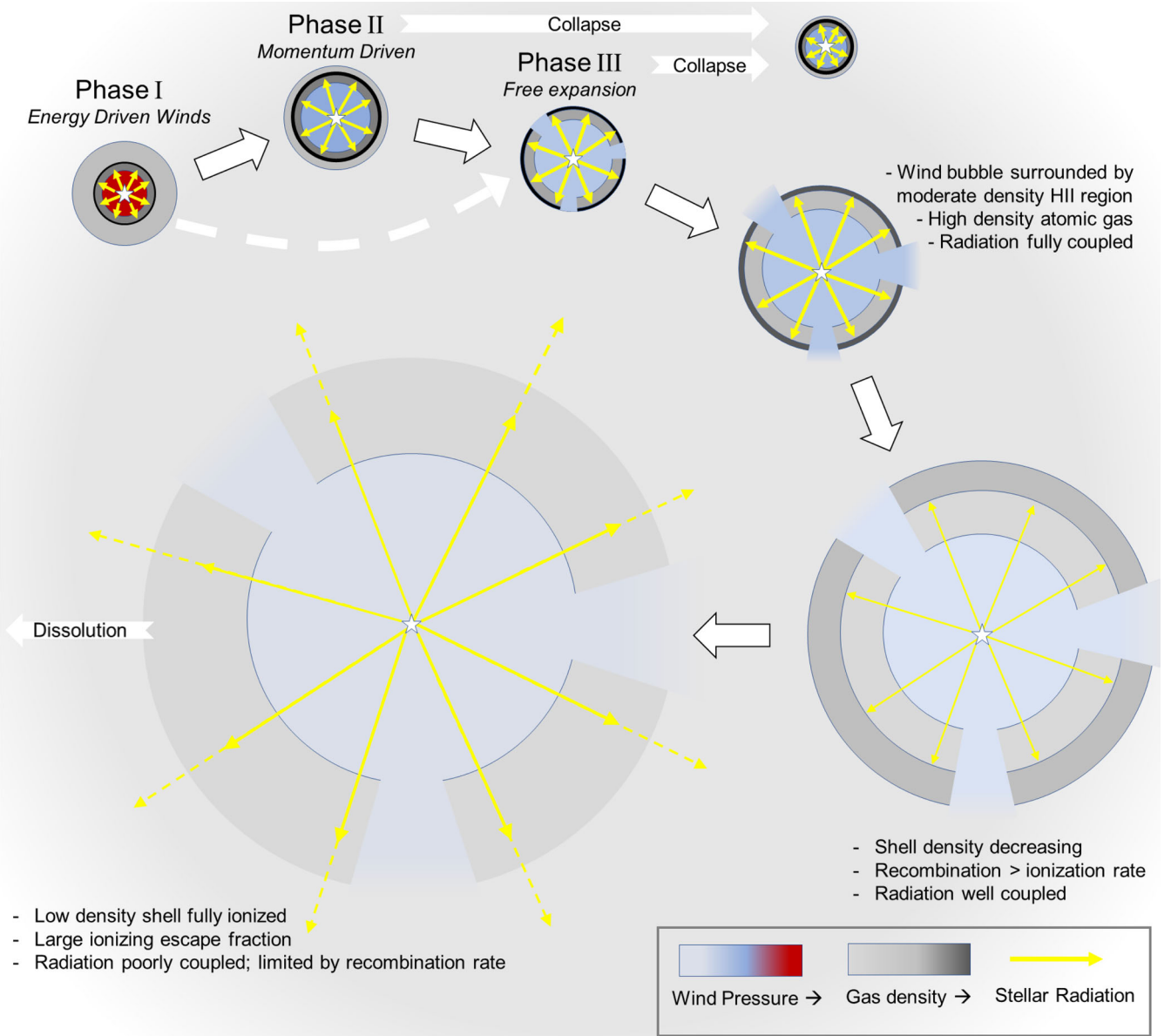


Figure 1. Overview of the shell evolution from the initial adiabatic phase to recollapse or dissolution.

Here, R is the (inner) radius of the shell and γ is the adiabatic index, with $\gamma = 5/3$ for an ideal gas. If the mechanical luminosity of the winds L_w is a constant, equation (2) can be solved analytically, yielding $R \propto t^{3/5}$ (Avedisova 1972; Castor, McCray & Weaver 1975, hereafter C75, and W77). However, stellar evolution models (e.g. Leitherer et al. 2014) show that L_w is time-dependent, especially in the Wolf-Rayet and pre-SN phases and we will thus use equation (2) instead of the analytic solution for constant L_w . From Bisnovatyi-Kogan & Silich (1995), during the adiabatic phase of the shell expansion, the pressure of the hot bubble is

$$P_b = 7\rho_{\text{cl}}^{1/3} \left[\frac{3(\gamma - 1)L_w}{28(9\gamma - 4)\pi R^2} \right]^{2/3}. \quad (3)$$

Evaporative flows from the shell gradually increase the density in the shocked wind region, leading to strong radiative cooling. When radiative losses become comparable to the wind energy input, the bubble loses the driving pressure of the hot gas and the adiabatic phase ends. The cooling time t_{cool} of a hot wind bubble is given by

Mac Low & McCray (1988) as

$$t_{\text{cool}} = 16 \text{ Myr} \times (Z/Z_{\odot})^{-35/22} n_{\text{cl}}^{-8/11} L_{38}^{3/11}, \quad (4)$$

where Z is the metallicity, n_{cl} is given in cm^{-3} and $L_{38} = L_w / (10^{38} \text{ erg s}^{-1})$.

Alternatively, as the shell expands, inhomogeneities or asymmetries in the cloud may provide low-density pathways along which the hot gas can escape (Rogers & Pittard 2013). If this occurs, instead of expanding and doing work, the hot gas will escape into the low-density/pressure ambient ISM. However, here we argue that in a rather high-density environment as investigated in this paper, and given the resulting rapid expansion in the adiabatic phase, it is reasonable to assume the bubble does not ‘burst’ until the expansion is of the order of the initial cloud radius. At this time, t_{sweep} , the entire cloud has been swept up in the shell. Further expansion begins to stretch the shell without significantly adding to its mass. The shell’s average density begins to decrease, possibly becoming unstable and leading to the formation of channels. Modelling the formation of

low-density channels goes beyond the scope of a 1D model. For simplicity, we assume that before t_{sweep} , the formation of any leaks gets hampered. After t_{sweep} , we assume the remaining shell structure is coherent, but does not effectively confine the winds. The time, when Phase I transitions to the next phase is thus given by $t_{\text{tran}} = \min(t_{\text{cool}}, t_{\text{sweep}})$.

2.1.2 Phase II: momentum-dominated sweeping

Once the hot X-ray emitting gas in the bubble cools, causing its thermal pressure to drop dramatically, the reverse shock quickly moves towards the shell as the shocked wind region is pushed into the shell (ST13). This evacuates almost all of the remaining gas from the bubble (now represented by the blue region in Fig. 1), and therefore during Phases II and III, it is a good approximation to treat the bubble as if it were completely empty. This allows us to assume that the wind thereafter imparts its momentum directly on the shell and that no absorption of radiation occurs before the radiation reaches the shell. In reality, the transition between energy driving in Phase I and momentum driving in Phase II will be gradual and even at $t > t_{\text{tran}}$ some thermal pressure from the shocked wind material will be present. However, the remaining hot gas is dynamically weak (Gupta et al. 2016; Rahner et al., in preparation) and we will ignore it here.

Following the evacuation of the bubble, the further expansion of the shell is driven by a combination of radiation pressure and ram pressure from winds and – at later times – SNe, all of which act to oppose gravity. If the hot gas cooled before the cloud was swept up, the shell continues to expand into high-density ISM, so that the mass of the shell grows as $M_{\text{sh}} = (4\pi/3)R^3\rho_{\text{cl}}$ (as in Phase I). During this phase, the shell's equation of motion is

$$\frac{d}{dt}(M_{\text{sh}}\dot{R}) = F_{\text{ram}} + F_{\text{rad}} - F_{\text{grav}}, \quad (5)$$

where F_{ram} , F_{rad} , and F_{grav} are the forces corresponding to ram pressure from stellar winds and type II SNe, radiation pressure, and gravity, respectively. Since we assume that the bubble is efficiently evacuated by feedback from the cluster, its density is too low to exert any significant amount of thermal pressure on the shell. Also, Dale, Ercolano & Bonnell (2012) have shown that massive clouds are largely unaffected by thermal pressure from ionizing radiation. In our model, we hence assume that thermal pressure from the bubble is negligible for the dynamics of the shell (thermal pressure does however influence the shell structure, as described in Section 2.2). We note that this argument does not apply for low-mass systems, where thermal pressure from H II regions plays a significant role in driving outflows (e.g. Walch et al. 2012; Dale et al. 2012).

The star clusters investigated in this work are large enough that as soon as the first SNe occur, treating them as a continuum process rather than distinct explosions is a good approximation. The ram pressure force term is then

$$\begin{aligned} F_{\text{ram}} &= F_{\text{wind}} + F_{\text{SN}} \\ &= \dot{M}_{\text{w}}v_{\text{w}} + \dot{M}_{\text{SN}}v_{\text{SN}}. \end{aligned} \quad (6)$$

Here, \dot{M}_{w} and \dot{M}_{SN} are the mass-loss rates due to stellar winds and SNe, and v_{w} and v_{SN} are the terminal velocities of the winds and SN ejecta. The ram pressure at the edge of the bubble is then

$$P_{\text{b}} = \frac{F_{\text{ram}}}{4\pi R^2}. \quad (7)$$

The full amount of the ram pressure is always transmitted to the shell. However, the shell does not absorb all photons emitted by the

cluster. Consequently, it will feel only a fraction f_{abs} of the maximum radiation pressure that the photons from the stellar cluster can potentially exert (cf. Section 2.2). Additionally, radiation absorbed by dust grains is re-emitted isotropically in the infrared (IR) which leads to an enhancement of radiation pressure. The total force due to radiation pressure is thus given by a direct and an indirect term,

$$\begin{aligned} F_{\text{rad}} &= F_{\text{direct}} + F_{\text{indirect}} \\ &\approx f_{\text{abs}} \frac{L_{\text{bol}}}{c} (1 + \tau_{\text{IR}}), \end{aligned} \quad (8)$$

where L_{bol} is the bolometric luminosity of the star cluster and c is the speed of light. The quantity $f_{\text{abs}}(1 + \tau_{\text{IR}})$ is sometimes referred to as the trapping factor (e.g. Krumholz & Matzner 2009). The optical depth of the shell in the IR is given by

$$\tau_{\text{IR}} = \kappa_{\text{IR}} \int_R^{R_{\text{out}}} \mu_{\text{n}} n_{\text{sh}} dr, \quad (9)$$

where κ_{IR} is the Rosseland mean dust opacity, n_{sh} is the number density of atoms/ions in the shell, and R_{out} is the shell's outer radius. For simplicity, we do not relate κ_{IR} to the dust temperature but use a constant $\kappa_{\text{IR}} = 4 \text{ cm}^2 \text{ g}^{-1}$ as would be appropriate for M17. For more details about the M17 model, see Pellegrini et al. (2007, hereafter P07).

In our treatment of gravity, we consider both gravity between the cluster and the shell, and the self-gravity of the shell. Thus,

$$F_{\text{grav}} = \frac{GM_{\text{sh}}}{R^2} \left(M_* + \frac{M_{\text{sh}}}{2} \right), \quad (10)$$

where G is the gravitational constant. We do not, however, consider any gravitational collapse by the parts of the cloud that have not yet been incorporated into the shell as we assume the cloud is in virial equilibrium.

2.1.3 Phase III: free expansion into low-density ISM or recollapse

If feedback is strong enough, the shell eventually overtakes the initial cloud radius R_{cl} . The shell then expands into the low-density ambient ISM. It is assumed to become leaky at t_{sweep} so that any shocked, hot wind material cools after t_{sweep} at the latest. Thus, if $t_{\text{sweep}} < t_{\text{cool}}$, Phase III follows directly after Phase I (indicated by the dashed white arrow in Fig. 1).

Here, we take the ambient ISM to have a mass density $\rho_{\text{ISM}} = 1.67 \times 10^{-25} \text{ g cm}^{-3}$, corresponding to a number density of $\sim 0.1 \text{ cm}^{-3}$. The equation of motion is still given by equation (5), but the mass of the shell is now

$$M_{\text{sh}} = M_{\text{cl}} + \frac{4\pi}{3} (R^3 - R_{\text{cl}}^3) \rho_{\text{ISM}}. \quad (11)$$

We also ran tests with $\rho_{\text{ISM}} = 1.67 \times 10^{-24} \text{ g cm}^{-3}$ and found that this leads to somewhat slower expansions but overall the effect is small.

There are two options now. If feedback is strong enough the shell will expand to very large radii. As the shell expands, it thins out, its density drops and it eventually becomes indistinguishable from the diffuse ambient ISM. Even before this, we can no longer represent the shell using the thin shell limit, and so equation (5) does not adequately describe its dynamics any longer. To account for this, we stop the integration if the density of the densest part of the shell drops below 1 cm^{-3} for an extended period of time (more than 1 Myr) as we consider the shell dissolved. If we would immediately

stop, we might miss the reformation of a shell, e.g. during the Wolf–Rayet phase which drastically increases the wind ram pressure. We call the time when the shell dissolves the dissolution time t_{dis} .

If, on the other hand, gravity overcomes stellar feedback, the shell collapses back on itself. The equation of motion during the collapse is the same as before except that the mass of the shell is kept constant. Collapse can happen either during Phase II or III (but not during Phase I as no gravity is included there) and we follow the collapse until the inner radius of the shell has shrunk to 1 pc. We define the time when this happens as the collapse time t_{collapse} . We stop the integration at this point, but already note that a collapse leads to more star formation (see Section 7) and thus possibly renewed expansion.

2.2 Shell structure

In order to determine how well-coupled radiation is to the shell and its momentum deposition rate, we need to determine the fraction of absorbed radiation f_{abs} . Numerical codes like CLOUDY (Ferland et al. 2013) provide powerful tools for calculating the chemistry, density, and temperature structure of shells. However, here we choose a simpler set of equations which sacrifice a detailed treatment of the chemical and thermal structure of the shell in exchange for a great increase in the speed with which one can calculate the volume of ionized gas. Our simple approach here also makes it easier to assess the relative importance of the different forms of feedback responsible for driving the dynamical evolution of the shell.

During Phase I, dust inside the hot bubble is destroyed by sputtering and hydrogen is collisionally ionized, allowing radiation to pass through unattenuated. During Phases II and III, the density inside the bubble quickly drops below 1 cm^{-3} (see Section 2.1), so that only little attenuation of radiation occurs. Thus, ionizing photons from the cluster can reach and ionize at least the inner edge of the shell (and potentially the whole of the shell, as we explain below).

Beyond the wind bubble, the momentum carried by radiation has a pronounced effect on the density structure of the ISM. Our model assumes the ionized and neutral/molecular phases of the shell are in the quasi-hydrostatic equilibrium described by the equation of state outlined in P07 (hereafter the P07-EOS). The work by P07 was the first to validate a hydrostatic equation of state by reproducing an observed $\text{H}^+/\text{H}/\text{H}_2$ star-forming ISM interface. The final pressure law defining a hydrostatic shell subject to external radiation states that the total pressure P_{tot} at a radius $r > R$, measured from the star cluster to a point in the shell, equals the sum of the pressure P_0 at the inner boundary of the shell and a term arising from radiative acceleration a_{rad} from photons deposited in the shell:

$$P_0(R) + \int_R^r a_{\text{rad}} \rho_{\text{sh}} \, dr' = P_{\text{tot}}(r) \\ = P_{\text{therm}} + P_{\text{turb}} + P_{\text{mag}}. \quad (12)$$

Here, ρ_{sh} is the density of the shell and P_{therm} , P_{turb} , and P_{mag} are the thermal pressure, the turbulent pressure,¹ and the magnetic pressure in the shell, respectively.

It is important to understand that a hydrostatic shell is not at constant pressure when exposed to a radiation field. By definition, the condition of hydrostatic equilibrium implies that there is no differential acceleration within the shell. In a hydrostatic shell, at

any interior point, the net external force (excluding gravity) acting on a layer with thickness dr is proportional to the amount of stellar radiation absorbed. Since absorption by each previous layer reduces the transmitted flux of ionizing and non-ionizing UV flux, if we want the amount of radiation per unit mass absorbed in each layer (and hence the amount of momentum deposited per unit mass) to remain constant, then the optical depth τ of each layer must progressively increase. In ionized gas, this means increasing the gas density of the layer. However, if we increase the density of the layer, we also increase its mass, and hence require an even higher momentum deposition rate in order to keep it accelerating at the same rate as the previous layer. This implies that the density of the layer must increase even more, in order to provide the necessary increase in τ . In shells with an outward density gradient due to radiation pressure, a monotonically increasing total pressure is required to produce uniform acceleration.

The terms in the P07-EOS have been validated against the density, chemical, and velocity structures of observed multiphase shells. A very strong magnetic field could provide additional pressure support even in the ionized gas, lowering the gas densities and recombination rate. Following P07, we can estimate the potential importance of the magnetic field by examining the peak magnetic field

$$B = \sqrt{8\pi P_0 + \frac{2Q_i h\bar{\nu}}{R_i^2 c}}, \quad (13)$$

where Q_i is the rate at which ionizing photons are emitted by the central source, $h\bar{\nu}$ is the average energy of a stellar photon, and R_i is the radius of the ionization front.

We have computed the peak magnetic pressure predicted by this equation for the clusters and gas densities modelled here and find that magnetic pressure is only marginally significant in the ionized gas while $R_i \leq R_{\text{cl}}$. At larger radii and/or late times when the winds are momentum-driven, magnetic pressure is much smaller than the radiation pressure, and decreases in significance as the shell evolves. The magnetic field may still provide a dominant source of pressure in the atomic gas, but the momentum deposited there is proportional to the dust column only (cf. equation 20), and is therefore not affected by the structure of the atomic gas layer. Thus, in our calculations, we ignore the effect of magnetic fields.

We also neglect the effects of turbulence, which is unlikely to be important in the ionized gas, unless the turbulence velocity dispersion is large ($\sigma_{\text{rms}} \gg 10 \text{ km s}^{-1}$ in the ionized shell). However, in star-forming regions like Orion, the turbulent velocities in the H II region are clearly subsonic (Arthur, Medina & Henney 2016) and turbulence is thus of limited importance for determining the structure of the ionized shell. In the atomic gas, turbulence may play an important role in structuring the material but since, as mentioned above, there the absorbed fraction of radiation depends only on the column density, turbulence does not play a significant role in the overall dynamics of the shell.

Detailed studies of observations find that the inner edge of the shell and the wind bubble are in pressure equilibrium (see e.g. P07). In this case, $P_0(R) = P_b$. Neglecting magnetic and turbulent pressure, the number density of the atomic nuclei n_{sh} at the inner radius of the shell R must then satisfy

$$n_{\text{sh}}(R) = \frac{\mu_p}{\mu_n k T_i} P_b, \quad (14)$$

where k is the Boltzmann constant and T_i is the temperature of the inner (ionized) region of the shell. The pressure of the bubble P_b is given by equation (3) during Phase I and by equation (7) during

¹ Note that this assumes that the turbulence is dominated by motions on scales that are small compared to the shell thickness.

Phases II and III. Note that pressure equilibrium implies that the shell is expanding at the same rate as the bubble.

For simplicity, we also assume that the ionized gas is at a constant temperature of $T_i = 10^4$ K. Under these assumptions, the condition of hydrostatic equilibrium, equation (12), dictates that the gradient in the total pressure be offset by the external forces, in this case the force from radiation pressure, leading to

$$a_{\text{rad}}\rho_{\text{sh}} = \frac{d}{dr} \left(\frac{\mu_n}{\mu_p} n_{\text{sh}} k T_i \right). \quad (15)$$

The radiative transfer of equation (15), can be reduced to two energy bands: ionizing radiation (photons with energies above 13.6 eV) which is absorbed by hydrogen and dust, and non-ionizing radiation which is absorbed by dust only.² Recombination is assumed to occur only via case B recombination with a recombination coefficient $\alpha_B = 2.59 \times 10^{-13} \text{ cm}^3 \text{ s}^{-1}$ (Osterbrock & Ferland 2006). These simplifying assumptions, and a conversion from acceleration times density to force per volume, give rise to the following set of coupled differential equations for the number density of the shell $n_{\text{sh}}(r)$, the attenuation function for ionizing radiation $\phi(r)$, and the optical depth $\tau_d(r)$ of dust in the shell, which have been applied to dusty H II regions by Draine (2011) and to shells by Martínez-González et al. (2014):

$$\frac{d}{dr} \left(\frac{\mu_n}{\mu_p} n_{\text{sh}} k T_i \right) = \frac{1}{4\pi r^2 c} \frac{d}{dr} (L_n e^{-\tau_d} + L_i \phi), \quad (16)$$

$$\frac{d\phi}{dr} = -\frac{4\pi r^2}{Q_i} \alpha_B n_{\text{sh}}^2 - n_{\text{sh}} \sigma_d \phi, \quad (17)$$

$$\frac{d\tau_d}{dr} = n_{\text{sh}} \sigma_d. \quad (18)$$

Here, L_n and L_i are the luminosities of non-ionizing and ionizing radiations. We assume the dust cross-section σ_d scales linearly with metallicity, $\sigma_d = \sigma_0 Z/Z_\odot$ where $\sigma_0 = 1.5 \times 10^{-21} \text{ cm}^2$ (Draine 2011) and neglect any formation or destruction of dust in the shell. During Phase I, with temperatures of the shocked wind material in excess of 10^6 K, neglecting dust sublimation is certainly not correct. However, we treat this early phase as being dominated by ram pressure anyway and ignore radiation pressure on dust altogether. At later times, gas temperatures in the shell reach at most 10^4 K, at which point the dust-to-gas ratio is not so different from the general ISM (Osterbrock & Ferland 2006). Destruction of dust is only important close to the illuminated face of the shell and even if dust destruction is taken into account, the majority of ionizing photons will continue to be absorbed by dust (Arthur et al. 2004). The formation of dust is never significant at the densities considered in this paper.

Equations (16)–(18) hold at all radii $r < R_i$ within the shell. The radius of the ionization front corresponds to the transition between the ionized and non-ionized parts of the shell and hence marks the point at which the ionizing photon flux drops to zero, i.e. $\phi(R_i) = 0$. Beyond the ionization front, we assume the gas is purely atomic with a temperature of $T_a = 100$ K. At radii $r > R_i$, we then have

$$\frac{d}{dr} (n_{\text{sh}} k T_a) = \frac{1}{4\pi r^2 c} \frac{d}{dr} (L_n e^{-\tau_d}), \quad (19)$$

$$\frac{d\tau_d}{dr} = n_{\text{sh}} \sigma_d. \quad (20)$$

² Photons in the energy range 11.2–13.6 eV can also be absorbed in the Lyman–Werner bands of H_2 , but this is significant in comparison to dust absorption only when the radiation field is relatively soft (Krumholz et al. 2008).

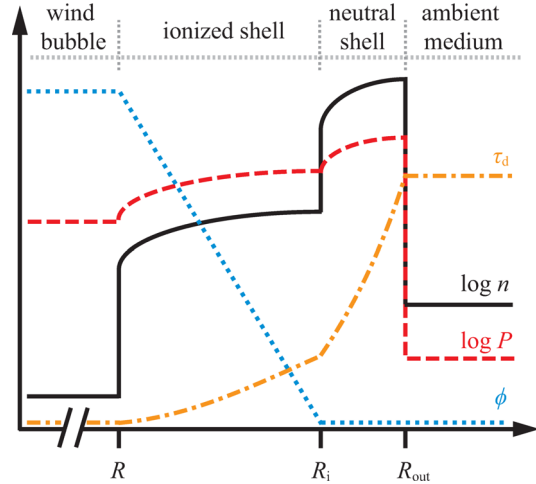


Figure 2. Sketch of number density n , dust optical depth τ_d , and attenuation of ionizing radiation ϕ as a function of radius. The red dashed line shows the pressures of the wind bubble P_b , the thermal gas pressure P_{therm} of the shell, and lastly of the ambient medium. At very early and late times when the column density of the shell and/or the pressure from winds is low, the shell may be fully ionized (not shown). See also Martínez-González et al. (2014).

Note that the condition of pressure equilibrium between the ionized and the non-ionized gas leads to a discontinuous increase in n_{sh} by a factor $\mu_n T_i / (\mu_p T_a)$ at R_i .

Since the density inside the bubble is assumed to be very low, any absorption inside the bubble is negligible and the boundary conditions used for solving equations (16)–(18) are given by equation (14), $\phi(R) = 1$, and $\tau_d(R) = 0$. We stop the integration at a radius R_{out} , once we have accounted for all of the shell’s mass, i.e.

$$4\pi\mu_n \int_R^{R_{\text{out}}} n_{\text{sh}}(r) r^2 dr = M_{\text{sh}}. \quad (21)$$

Fig. 2 shows a sketch of the density, pressure, and attenuation of radiation across the shell as obtained from equations (16) to (20).

We can now calculate the fraction of absorbed ionizing and non-ionizing radiations:

$$f_{\text{abs},i} = 1 - \phi(R_{\text{out}}), \quad (22)$$

$$f_{\text{abs},n} = 1 - \exp[-\tau_d(R_{\text{out}})]. \quad (23)$$

Finally, the total absorption fraction f_{abs} is defined as a luminosity weighted average of $f_{\text{abs},i}$ and $f_{\text{abs},n}$,

$$f_{\text{abs}} = \frac{f_{\text{abs},i} L_i + f_{\text{abs},n} L_n}{L_{\text{bol}}}, \quad (24)$$

where $L_{\text{bol}} = L_i + L_n$.

By ignoring absorption of Lyman–Werner radiation on H_2 , we underestimate f_{abs} . We recalculated some of our shell structure models with CLOUDY to explore the effect chemistry has on opacity and find that a significant amount of H_2 only forms when the shell is dense and quite optically thick, i. e. if $f_{\text{abs}} \sim 1$. In lower density, expanded shells, the interstellar radiation field suppresses the formation of H_2 , and a more detailed chemical model does not lead to substantially different escape fractions.

A larger caveat is that we fix the dust cross-section σ_0 (for a fixed metallicity). In reality, σ_0 is a function of the effective stellar temperature and decreases as the massive stars die (Draine 2011).

Table 1. Summary of 1D shell dynamical models. Included and neglected physical processes are marked with \checkmark and $-$, respectively.

Model	Mass reservoir	Gravity	Wind (\dot{E})	Wind (\dot{p})	Radiation (\dot{E})	Radiation (\dot{p})	Shell structure	Stellar evolution	SNe	Turbulence
This work	Finite	\checkmark	\checkmark	\checkmark	\checkmark	\checkmark	\checkmark	\checkmark	\checkmark	-
K16 ^a	Finite	\checkmark	-	-	\checkmark	\checkmark	-	-	-	-
ST13 ^b	Infinite	-	\checkmark	\checkmark	-	-	-	-	-	-
M10 ^c	Finite	\checkmark	(\checkmark)	-	\checkmark	\checkmark	-	-	-	\checkmark
W77 ^d	Infinite	-	\checkmark	-	-	-	-	-	-	-

Notes. ^aKim et al. (2016); ^bSilich & Tenorio-Tagle (2013); ^cMurray et al. (2010); ^dWeaver et al. (1977). \dot{E} and \dot{p} stand for energy- and momentum-driven, respectively.

Again using CLOUDY, we find that at later times ($t \gtrsim 3$ Myr) in our simplified treatment, we are overestimating f_{abs} by ~ 25 per cent. But since, as we will show, at late times radiation pressure is rarely the dominating source of feedback, this does not strongly affect the dynamics of shells. In a future iteration of our method, we plan to self-consistently calculate σ_0 from the time-variable stellar spectrum.

2.3 Coupling structure and dynamics

There have been many attempts to model the dynamic evolution of feedback-driven shells (see Table 1). In the wind energy-driven model by C75 and W77 mentioned above,

$$R \propto t^{3/5} \quad (25)$$

if cooling is neglected and the ISM is assumed to be infinite and homogeneous. ST13, expanded that model and included momentum feedback from winds after the wind energy has been radiated away. Still for an infinite, homogeneous ISM, they show that

$$R \propto (At^2 + Bt + C)^{1/4} \quad \text{if } t > t_{\text{cool}}, \quad (26)$$

where A , B , and C depend on wind parameters, the cloud density, and the cooling time. Both these models neglect the influence of gravity, radiation pressure, and SNe on the dynamics. Kim et al. (2016) study the combined effect of radiation pressure and gravity but neglect winds, similar to Murray et al. (2010) who include energy from hot winds in one of their models but always neglect wind momentum. We also note Krumholz & Matzner (2009), who calculated the dynamics under the influence of radiative momentum deposition, albeit under the assumption of full absorption and while neglecting gravity.

At one point or another, all of these models fall short of a full, self-consistent treatment of feedback. The expansion rate of the shell depends on how well coupled it is to radiation, which in turn depends on the shell structure. However, as we have seen, the shell structure itself depends on the expansion rate of the shell. To complicate things even further winds, radiation and SNe output depend on cluster mass and age. It is therefore necessary to simultaneously solve for the expansion rate and structure of the shell, while accounting for an evolving stellar population.

Expanding shells in the ISM are not truly hydrostatic – in the sense that parts of the shell do not move radially with respect to each other – as they tend to become thicker over time. If the ‘thickening velocity’ $v_t \equiv d(R_{\text{out}} - R)/dt$ is lower than the shell’s sound speed c_s , the pressure distribution within the shell can readjust itself on a time-scale short compared to that on which the shell thickness changes, and the shell therefore rapidly settles into a quasi-hydrostatic equilibrium. In such a case, the assumption of local hydrostatic equilibrium is a good approximation.

We find that in our models v_t is subsonic except for short times when we switch from the adiabatic phase to Phase II or III and around the occurrence of the first SNe. Over the whole simulated time span, the short periods when the quasi-hydrostatic assumption breaks down are expected to be negligible for the dynamics. Additionally, observations suggest that hydrostatic models as adopted here provide reasonable approximations for expanding gas shells (e.g. Pellegrini et al. 2007).

In order to self-consistently model, the dynamics of feedback-driven shells we thus take the following approach:

(1) A star cluster with mass M_* , following a Kroupa initial mass function (IMF, Kroupa 2001), forms at $t = 0$ in the centre of a gas cloud. All stars in the cluster are assumed to be coeval. We do not consider any ongoing star formation. The cloud has mass M_{cl} and constant density n_{cl} .

(2) We take the relevant parameters for stellar feedback L_w , L_i , L_n , Q_1 , \dot{M}_w , \dot{M}_{SN} , and v_w from the population synthesis code STARBURST99 (Leitherer et al. 1999, 2014), v7.0.1, using the Geneva evolution tracks (Ekström et al. 2012; Georgy et al. 2012, 2013) for non-rotating stars (fiducial model) and rotating stars (see Appendix A1). The terminal velocity of the SN ejecta v_{SN} is set to a constant 10^4 km s^{-1} . These feedback parameters as well τ_{IR} and f_{abs} (which are 0 at $t = 0$ as no shell yet exists) are used to calculate the shell dynamics via the expansion equations (2) and (5).

(3) After a certain time-step Δt , the feedback parameters are updated and the shell structure is modelled via equations (16)–(20). From the shell structure, we get τ_{IR} and f_{abs} . The time-step is adaptive: it is small (~ 0.02 Myr) during the early phase and around the time of the first SNe (at $t \sim 3$ Myr), when f_{abs} is strongly time-dependent.

Steps 2 and 3 are repeated until the end of the simulation is reached at a time t_{end} . The code WARPFIELD (Winds And Radiation Pressure: Feedback Induced Expansion, colLapse and Dissolution) developed for this work is publicly available for download under <https://bitbucket.org/drahner/warpfield>.

2.4 Investigated parameter space

We explore the evolution of shells in clouds with masses in the range $10^5 M_{\odot} \leq M_{\text{cl}} \leq 10^8 M_{\odot}$, i.e. giant molecular clouds (GMCs) and giant molecular associations. For simplicity, we will refer to them as clouds, independent of their mass. The masses are equally spaced in log space with $\Delta \log(M_{\text{cl}}) = 0.25$. We investigate star formation efficiencies

$$\epsilon \equiv \frac{M_*}{M_{\text{cl}} + M_*} \quad (27)$$

varying from 0.01 to 0.25 with $\Delta \epsilon = 0.01$. The investigated parameter space thus includes a small region where the star clusters

Table 2. Investigated parameter space.

Cloud number density	n_{cl}	100, 1000	cm^{-3}
Metallicity	Z	0.15, 1	Z_{\odot}
Cloud mass	M_{cl}	10^5 – 10^8	M_{\odot}
Star formation efficiency	ϵ	0.01 – 0.25	–

are not massive enough to fully sample the IMF ($M_{\star} \lesssim 10^4 M_{\odot}$), namely clouds with $M_{\text{cl}} < 10^6 M_{\odot}$ and with very low star formation efficiencies. In the stochastic regime, the assumption of continuous SN explosions after $t \sim 3$ Myr and the values for L_i and L_w obtained from scaling down a fully sampled star cluster are not valid anymore and hence we do not include this regime in our analysis. Also, shells around low-mass GMCs ($M_{\text{cl}} \sim 10^5 M_{\odot}$) with very high star formation efficiencies ($\epsilon \gtrsim 0.2$) are not in quasi-hydrostatic equilibrium as $v_i > c_s$ after the stellar winds of the most massive stars disappear and the pressure at shell's inner edge drops significantly, thus leading to a rapid increase in the shell's thickness. However, these are shells which are close to dissolution and for which radiation pressure is already negligible. Hence, the absolute error we make when calculating the amount of momentum deposited by radiation into such shells is small.

We examine two different natal cloud densities, $n_{\text{cl}} = 100$ and 1000 cm^{-3} , corresponding to diffuse and translucent molecular clouds, respectively (Snow & McCall 2006). In later sections, we will refer to these as low- and high-density runs. Some GMCs contain clumps and cores in excess of $n = 10^4 \text{ cm}^{-3}$ but on average their density is ~ 100 – 1000 cm^{-3} . We do not yet include a density profile for our clouds but plan to do so in the future. We also model two different metallicities, $Z = Z_{\odot}$ and $0.15 Z_{\odot}$. Note that Z refers to both the metallicity of the cloud, affecting the amount of dust and the time-scale for radiative cooling, and to the metallicity of the cluster, affecting the energy and momentum output by stellar winds and to a lesser extent by radiation. We call these the solar Z and low Z runs, respectively.

Table 2 lists the parameter space described above. The expansion of the shell is modelled until either it dissolves into the ambient ISM, or it recollapses, or 7 free-fall times τ_{ff} have passed; thus, $t_{\text{end}} = \min(t_{\text{dis}}, t_{\text{collapse}}, 7\tau_{\text{ff}})$. The free-fall time is defined as

$$\tau_{\text{ff}} \equiv \sqrt{\frac{3\pi}{32G\rho_{\text{cl}}}}, \quad (28)$$

and so $7\tau_{\text{ff}}$ corresponds to $t \sim 10$ and 32 Myr for the high- and low-density runs, respectively. Note that in the low-density case, this time is close to the time at which the last of the SNe associated with the cluster would have exploded, which marks the point at which the effects of stellar feedback drop to a very low value.

3 A FEEDBACK-DRIVEN DYNAMIC TIMELINE

We will now attempt to summarize the contribution of each feedback mechanism and its variation with time. Our aim is to highlight the different physical regimes where simple scaling relations fall short. There is no simple answer to the question of which feedback mechanism is dominant. Instead this complex problem must be addressed by quantifying how their relative contributions vary with time in an effort to combat gravity.

We start by showing the expansion of a shell that is driven by feedback from a cluster in a dense molecular cloud with cloud mass $M_{\text{cl}} = 10^5 M_{\odot}$ and star formation efficiency $\epsilon = 0.1$ (see Fig. 3). An overview of the shell dynamics for a large number of

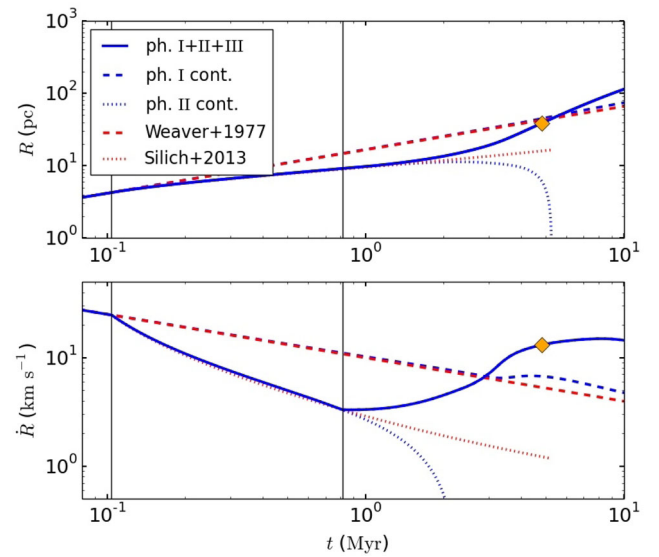


Figure 3. *Top:* evolution of the inner radius of the shell as a function of time for a model with $M_{\text{cl}} = 10^5 M_{\odot}$, $\epsilon = 0.1$, $Z = Z_{\odot}$, and $n_{\text{cl}} = 1000 \text{ cm}^{-3}$. *Bottom:* expansion velocity of the shell. The vertical black lines mark the transition between the expansion phases (marked by the Roman numerals I, II, and III) at t_{cool} and t_{sweep} . The yellow diamond indicates where the shell becomes fully ionized and ionizing radiation starts to leak out. The blue dashed and dotted lines show a continuation of Phase I (assuming no cooling and an infinite mass reservoir) and Phase II (assuming an infinite mass reservoir only), respectively. The actual evolution of the shell is shown by the solid blue line. The red dashed and dotted lines show analytic solutions for comparison, equation (21) in W77 and equation (13) in ST13.

other models can be found in Appendix A2. In this example, both the cloud and the cluster have solar metallicity. Rapid expansion in the adiabatic phase (Phase I) is followed by strong deceleration after $t_{\text{cool}} \sim 0.1$ Myr as the thermal pressure from the shocked wind bubble vanishes and the shell accumulates more and more mass (Phase II). At $t_{\text{sweep}} \sim 0.8$ Myr, the whole cloud has been swept up by the shell. Expanding into low-density ISM (Phase III), the shell now accelerates again.

We have also simulated how the cloud would evolve if Phase I (Phase II) would continue indefinitely as one would expect for an infinite ISM reservoir without cooling (after cooling). This allows us to compare our results with analytic solutions for the equation of motion, i.e. equation (21) in W77 and equation (13) in ST13. For the particular cloud shown here, W77 and ST13 provide good approximations for the shell expansion in Phases I and II (some small deviations towards faster expansion in our model in Phase II are due to radiation pressure). However, for a model with the same cluster mass but a larger cloud size, ST13 would seriously overestimate the shell's velocity and radius at late times (due to their neglect of gravity). Even though we follow W77 in neglecting gravity in Phase I, we do always take into account stellar evolution. This is why at late times, our continued Phase I model differs from equation (25).

An important consequence of including gravity is that for all models investigated here, shells expanding into an infinite ISM reservoir will always recollapse. Sweeping up more and more mass, the shell eventually becomes too massive for gravity to be balanced by the outward forces. If the shell approaches this point asymptotically, it can keep roughly that size until the massive stars have died and feedback decreases. Usually, however, the shell passes the point of force balance with a positive velocity. As soon as this happens, the

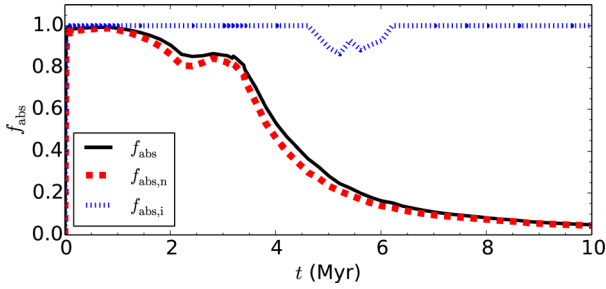


Figure 4. Absorbed fraction of non-ionizing radiation $f_{\text{abs},n}$, ionizing radiation $f_{\text{abs},i}$, and the luminosity weighted mean f_{abs} . The model is the same as in Fig. 3.

shell starts to lose momentum and eventually recollapses. This is shown by the blue dotted line in Fig. 3. If gravity is included and the mass reservoir is infinite, the shell reaches a turning point at $t \sim 2$ Myr as the expansion velocity becomes negative and the radius of the shell starts to significantly deviate from the ST13 model.

In some models, ionizing radiation can completely overpower the shell. This is the moment when ionizing radiation starts to leak out (see yellow diamond in Fig. 3). Coupling of radiation and the escape fraction of ionizing radiation will be discussed in the following sections.

4 RADIATION COUPLING

For young star clusters, momentum carried by radiation exceeds momentum carried by winds by a factor of a few for solar metallicity and by a few decades at $0.15 Z_{\odot}$ (Leitherer et al. 2014). However, this does not mean that radiation always dominates over winds as a source of feedback. Rather, it is the coupling between radiation and the ISM, quantified by f_{abs} in our model, that ultimately determines which of these feedback sources dominates. Any attempt to determine how radiation pressure and ram pressure compare to each other must therefore begin by quantifying f_{abs} .

Ionizing and non-ionizing radiation behave differently. While $f_{\text{abs},n}$ is only influenced by the column density of the shell, $f_{\text{abs},i}$ depends also on the volume density (since the recombination rate is proportional to n_{sh}^2) and on the rate of ionizing photons Q_i emitted by the cluster, cf. equations (17) and (18). Thus, $f_{\text{abs},n}$ is solely set by how far out the shell has expanded and how much mass it has swept up in the process, whereas $f_{\text{abs},i}$ is also dependent on the cluster’s current output in terms of ram pressure from winds and radiation pressure, which set $n_{\text{sh}}(r)$ via equations (14) and (16), and its current emission rate of ionizing photons. Since the shell expansion is a result of the history of feedback, we might say that $f_{\text{abs},n}$ only cares about the past while $f_{\text{abs},i}$ is determined by both the past and the present.

After a dense shell has formed, radiation is initially well coupled (see Fig. 4). However, after the shell enters the free expansion phase (Phase III), the expansion velocity increases, while at the same time, the mass growth nearly stalls. The gas in the shell thus stretches over an ever-increasing surface area, reducing the shell’s surface density and leading to a decrease of f_{abs} . At the same time, ram pressure drops as R^{-2} , the volume density decreases and the shell becomes thicker. As a result, f_{abs} decreases even further. In the particular example shown in Fig. 4, f_{abs} starts to differ significantly from unity at $t \sim 1$ Myr, just after the cloud has been swept up. The bump at $t \sim 3$ Myr is caused by the increase in ram pressure during the Wolf–Rayet and pre-SN phases. At $t \sim 5$ Myr, ionizing

Table 3. Fit parameters for f_{abs} for the investigated parameter space (see equation 30). The reduced chi-squared statistic χ_{ν}^2 has been calculated assuming a variance of 0.01. For further details, see Section 6.

n (cm^{-3})	Z (Z_{\odot})	a	b	c	d	e	χ_{ν}^2
1000	1	-0.323	0.129	-1.119	-0.143	1.975	1.07
1000	0.15	-0.118	0.085	-0.695	0.102	0.140	2.01
100	1	-0.109	0.063	-0.579	0.084	0.363	1.18
100	0.15	-0.020	0.037	-0.312	0.097	-0.034	3.18

radiation decouples from the shell. At that point, the whole shell is ionized. However, the time period during which ionizing radiation can pass through the shell is short: at late times, the output of ionizing radiation is greatly reduced due to the death of the very massive stars. Ionizing radiation is then again fully absorbed by the ISM. At $t \sim 8$ Myr, f_{abs} drops below 0.1. At this point, less than 10 per cent of the radiation, which has already been diminished due to the aging of the cluster, is transmitted to the shell, greatly reducing the efficiency of radiation pressure as a source of feedback.

As explained above, the gas density of the shell which determines radiation momentum coupling depends on many quantities in a non-linear way. To reduce the result into a digestible statement, it is useful to examine a fit to the absorption fraction as a function of the most important model parameters. Between 1 and 10 Myr and for fully sampled IMFs ($M_* \gtrsim 10^4 M_{\odot}$), f_{abs} is well fitted by

$$f_{\text{abs}} = \begin{cases} 0 & \text{if } \tilde{f} \leq 0, \\ \tilde{f} & \text{if } 0 < \tilde{f} < 1, \\ 1 & \text{if } \tilde{f} \geq 1, \end{cases} \quad (29)$$

with

$$\tilde{f} = \left(a \log \epsilon + b \log \left(\frac{M_{\text{cl}}}{M_{\odot}} \right) + c \right) \frac{t}{\text{Myr}} + d \log \left(\frac{M_{\text{cl}}}{M_{\odot}} \right) + e. \quad (30)$$

The fit parameters a , b , c , d , and e are provided in Table 3 for the combinations of density and metallicity examined in this study. We also list the reduced chi-squared statistic in each case, to indicate the goodness of fit.

From the signs of the fit parameters a (negative) and b (positive), we can already draw two conclusions:

- Keeping the cloud mass constant, an increase in star formation efficiency leads to a faster decoupling with time.
- Keeping the star formation efficiency constant, an increase in cloud mass leads to a slower decoupling with time.

To understand these trends, imagine a cloud with a given mass and density. If the cloud has a high star formation efficiency, two effects play a role: first, as a more massive cluster outputs more energy and momentum in winds and SNe, the ram pressure at the inner edge of the shell rises. The shell thus becomes denser and ionizing radiation is more coupled. However, there is a second, competing effect. Stronger feedback (both ram and radiation pressure) leads to a faster expansion of the shell. The column density thus drops faster (as soon as the cloud has been swept up), leading to weaker coupling of radiation. The negative sign of a shows that on average the second effect dominates.

Now consider a fixed cluster mass, but a variable cloud mass. The higher the cloud mass, the higher the column density radiation has to pass through. Also, gravity becomes more important as the cloud mass is scaled up, slowing the expansion of the shell down

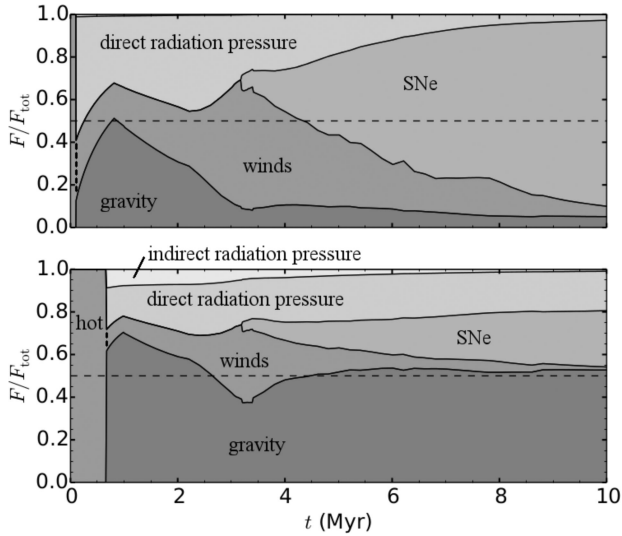


Figure 5. Comparison of relative forces from direct and indirect radiation pressure, winds, SNe, and gravity. If the contribution from gravity is above the 50 per cent margin (dashed horizontal line), the shell loses momentum. *Top:* $M_{\text{cl}} = 10^5 M_{\odot}$, $\epsilon = 0.1$, $Z = Z_{\odot}$, and $n_{\text{cl}} = 1000 \text{ cm}^{-3}$ (same parameters as in Fig. 3). The contribution from indirect radiation pressure fraction is so small, it is barely visible (< 1 per cent). *Bottom:* same n_{cl} and Z as in the top panel, but with a higher cloud mass and star formation efficiency ($M_{\text{cl}} = 3 \times 10^7 M_{\odot}$ and $\epsilon = 0.25$). For more information see Section 5.

and increasing the coupling of radiation. If instead of a fixed cluster mass, ϵ is kept constant, the same arguments applies, albeit in a somewhat weakened form as the cluster mass and its feedback also increase as we increase the cloud mass. In summary, radiation coupling is stronger in massive clouds, explaining the positive sign of b .

5 WHICH TYPE OF FEEDBACK DOMINATES?

Now that we have quantified radiation coupling, we can start answering the question ‘Which type of feedback dominates?’ When asking this, it is crucial to distinguish between the instantaneous and the cumulative effect of feedback. The current density/chemical structure of the ISM is a bellwether of instantaneous feedback, while cumulative feedback is traced by shell dynamics.

Instantaneous feedback, as measured by its exerted force, is highly time-dependent. It is therefore necessary to specify what evolutionary stage one is interested in. To demonstrate this, we show in Fig. 5 for two examples the relative contributions from the various forces influencing the shell. These are the forces associated to winds and SNe, F_{wind} and F_{SN} , direct and indirect radiation pressure, F_{direct} and F_{indirect} , as well as gravity F_{grav} (cf. Section 2.1.2). To allow easy comparison between the various terms, the forces are normalized to their sum, $F_{\text{tot}} = F_{\text{wind}} + F_{\text{SN}} + F_{\text{direct}} + F_{\text{indirect}} + F_{\text{grav}}$. The feedback term that dominates at a given time t can be read off from the vertical width in Fig. 5. Note that here for the sake of comparison, gravity receives a positive sign. Therefore, if $F_{\text{grav}}/F_{\text{tot}} < 0.5$, the shell gains momentum, otherwise it loses momentum. During the adiabatic phase, the force associated to thermal pressure from shocked winds F_{hot} is the only force we consider in our model.

Before we discuss the importance of the different feedback terms, it is also instructive to consider the integrated forces. The momentum p injected by the various feedback terms (or removed in case

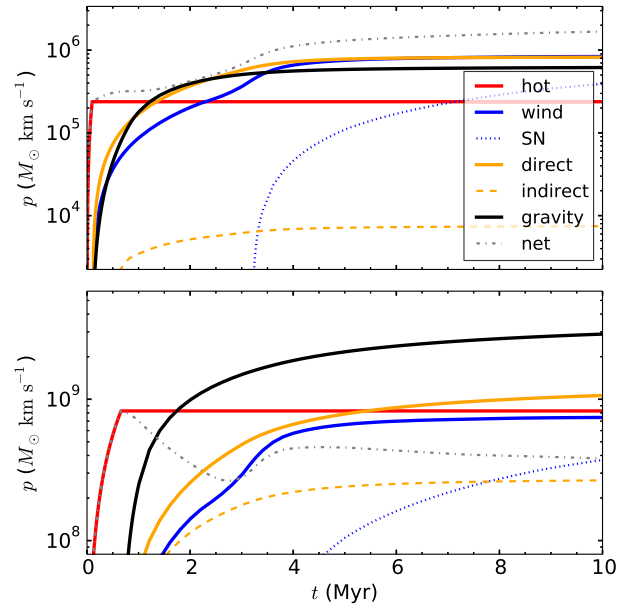


Figure 6. Comparison of momentum p deposited by the various feedback terms. The red line labelled ‘hot’ corresponds to feedback from hot shocked wind material during the adiabatic phase, the other terms are as in equation (5), i.e. ram pressure in blue, radiation pressure in yellow, and gravity, which has a negative contribution, in black. The parameters of the clouds examined in the two panels are the same as in Fig. 5.

of gravity) up to a time t can be calculated via

$$p_i(t) = \int_0^t F_i dt', \quad (31)$$

where the index i stands for the particular feedback term (wind, SN, etc.). The net momentum of the shell is $p_{\text{net}} = p_{\text{hot}} + p_{\text{wind}} + p_{\text{SN}} + p_{\text{direct}} + p_{\text{indirect}} - p_{\text{grav}}$. The evolution of p is shown in Fig. 6 for the same models as in Fig. 5.

During Phase I, gas pressure from hot winds is the only source driving the shell (cf. Fig. 5), but as soon as the shell enters Phase II, this force is shut off so that p_{hot} remains constant. After the adiabatic phase, direct radiation pressure becomes the main driving force until at $t \sim 2\text{--}3$ Myr first momentum from winds and then from SNe starts to dominate the feedback budget. At the end of the simulation, the cumulative contribution from direct radiation pressure equals that from wind ram pressure in the case of the low-mass cloud (Fig. 6, top panel) and exceeds the contribution from wind ram pressure by a factor of 1.5 in the case of the high-mass cloud with higher star formation efficiency (Fig. 6, bottom panel). In the low-mass cloud case shown, the absorption fraction drops rapidly after 3 Myr (cf. Fig. 3) making radiation pressure a very ineffective feedback process at late times. This coincides with the death of massive stars marking a reduction in wind feedback and an increase in ram pressure from SNe. This additional pressure is not sufficient to raise the shell density, leading to a weak coupling between radiation and the swept-up ISM.

Although SNe become the main driving force at late times, the momentum injected by them over the whole simulation time is lower than that injected by winds or direct radiation pressure, albeit still of the same order of magnitude. In massive clouds, the relative importance of SNe is lower than in less massive clouds, as the exerted force associated with direct radiation pressure remained comparable with the force from SN feedback for a long time span.

Whereas feedback parameters like luminosity scale linearly with a cluster’s mass for a fully sampled IMF, the gravitational force increases quadratically. With increasing cloud mass, F_{grav} thus undergoes a superlinear increase, in contrast to the radiation pressure and ram pressure output of a cluster. This is the reason why in the massive cloud case shown, gravity dominates for most of the time after the end of Phase I and the cloud loses momentum. However, the shell still expands with a positive velocity caused by the initial velocity kick from the adiabatic phase (and a smaller kick during the Wolf–Rayet phase). Due to the slow expansion, radiation remains well coupled. Thus, feedback from radiation pressure continues to exceed wind ram pressure feedback.

In all but the most massive clouds ($M_{\text{cl}} \gtrsim 10^7 M_{\odot}$), which produce very massive and dense shells, the contribution from indirect radiation pressure is small. During the expansion phase, even for a shell that forms in a $10^8 M_{\odot}$ cloud, τ_{IR} never exceeds 0.8, supporting findings by Skinner & Ostriker (2015), Martínez-González et al. (2014), and Reißl et al. (in preparation). Only at late times during recollapse can τ_{IR} exceed unity, but indirect radiation is still not strong enough to stall the collapse. However, for certain cloud–cluster combinations, it can provide just enough momentum to keep the expansion of the shell going until the entire cloud has been swept up and the shell accelerates again. In such a case, indirect radiation pressure can make the difference between continued expansion and recollapse.

In order to determine whether the expansion of a shell up to a time t was driven mainly by winds and SNe or by radiation pressure, it is instructive to compare p_{ram} and p_{rad} where, as before, $p_{\text{rad}} = p_{\text{direct}} + p_{\text{indirect}}$ and $p_{\text{ram}} = p_{\text{wind}} + p_{\text{SN}}$. We therefore introduce the relative radiation pressure strength parameter

$$\Omega_{\text{rad}}(t) \equiv \frac{p_{\text{rad}}(t)}{p_{\text{rad}}(t) + p_{\text{ram}}(t)}. \quad (32)$$

If $\Omega_{\text{rad}}(t) > 0.5$, radiation pressure dominates over ram pressure from winds and SNe, in the sense that up to time t more momentum has been injected by radiation pressure than by ram pressure. To include the contribution from winds during the adiabatic phase, we also introduce the associated relative radiation pressure strength parameter

$$\Omega'_{\text{rad}}(t) \equiv \frac{p_{\text{rad}}(t)}{p_{\text{rad}}(t) + p_{\text{ram}}(t) + p_{\text{hot}}(t)}. \quad (33)$$

Following this definition, if $\Omega'_{\text{rad}}(t) > 0.5$, radiation pressure has injected more momentum than ram pressure and hot gas pressure taken together. In Fig. 7, we show the regimes $\Omega'_{\text{rad}}(t_{\text{end}}) > 0.5$ (white area) which corresponds to the regime in which radiation pressure dominates over winds and SNe, $\Omega_{\text{rad}}(t_{\text{end}}) > 0.5$ (light grey area) which corresponds to the regime where radiation pressure only dominates if momentum injected during the adiabatic phase is not taken into account, and $\Omega_{\text{rad}}(t_{\text{end}}) < 0.5$ (dark grey area) which corresponds to the regime where winds and SNe dominate.

Fig. 7 shows that the dynamics of shells forming in high-mass natal clouds are dominated by radiation pressure, while the dynamics of shells in low-mass clouds are dominated by winds (and to a lesser extent SNe). Also, ram pressure tends to dominate for high star formation efficiencies, as was expected from equation (29).

Interestingly, even in the low-metallicity case, where momentum output from winds is roughly one order of magnitude lower than for solar metallicity, there is still a large regime where they dominate over radiation pressure (Fig. 7, bottom panel). This has two reasons: first, the low amount of dust in metal-poor cloud leads to radiation being less coupled to the ISM. Second, the low ram pressure on

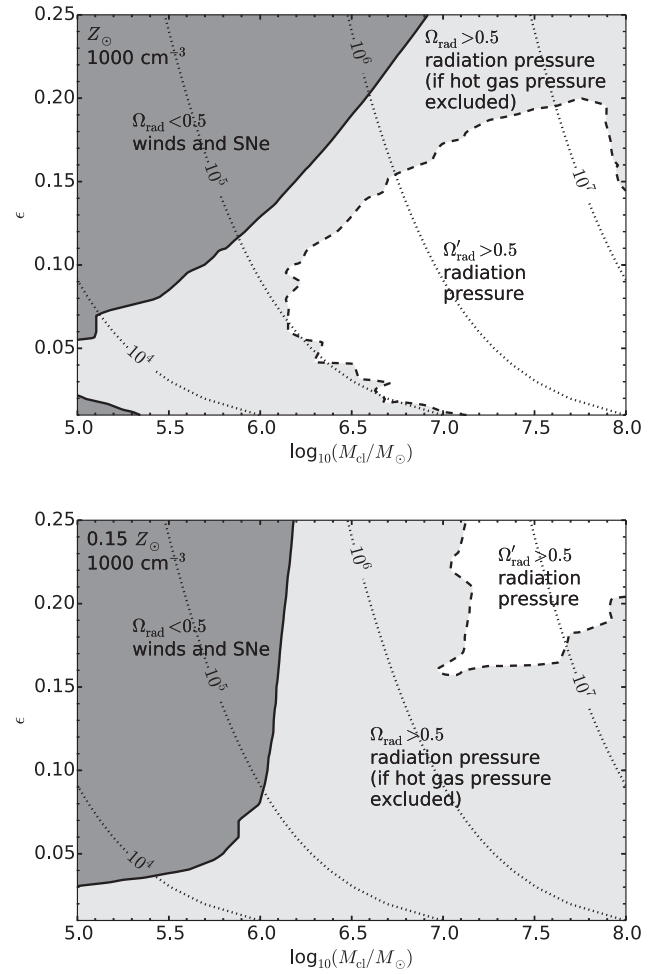


Figure 7. Regimes in which momentum, integrated over the whole simulation time t_{end} , has mainly been injected by radiation or winds/SNe for the high-density runs with solar metallicity (top) and low metallicity (bottom). In white areas, the total momentum injected by radiation pressure exceeds the total momentum injected by ram pressure from winds/SNe and hot, shocked wind material ($\Omega'_{\text{rad}} > 0.5$). In light grey areas, momentum from radiation pressure exceeds momentum from ram pressure, but not momentum from ram pressure and hot gas combined ($\Omega_{\text{rad}} > 0.5$). In dark grey areas, ram pressure dominates over radiation pressure ($\Omega_{\text{rad}} < 0.5$). Black dotted curves indicate lines of constant cluster mass from 10^4 to $10^7 M_{\odot}$.

the inner side of the shell causes the shell to be extended and low density; in such shells the recombination rate is small and ionizing radiation can easily escape without depositing its momentum. Thus, even though metallicity of a cluster does not strongly affect its radiative output, the entwinement between winds and radiation pressure still leads to a weakening of the efficiency with which radiation is deposited in the surrounding gas. A change in ram pressure output is always accompanied by a change in radiation coupling.

Our results show that for dense clouds, there is a large parameter range in which radiation pressure dominates. This shed doubts on findings by Martínez-González et al. (2014) who reported that radiation pressure is not the dominant feedback force for dense clouds. Their models, however, were not able to include radiation pressure in their shell expansion model. Instead they relied on an indirect diagnostic.

For our low-density models, ram pressure dominates the whole parameter space. The main reason for this is not that these models

were simulated up to later times when SN feedback increases but rather that the shells driven in low-density environments have a lower density themselves and are thus less coupled to radiation. However, ram pressure only dominates by a factor of 1–4 over radiation pressure, meaning that radiation is still not a negligible driving force.

6 ESCAPE FRACTION OF IONIZING RADIATION

While f_{abs} determines how well coupled the total radiation is to the shell, the escape fraction of ionizing radiation $f_{\text{esc},i}$ from the whole cloud is of particular interest for larger scale simulations. For its calculation, we have to take into account not only absorptions of ionizing photons by the shell but also – at early times – by the natal cloud. We can estimate the coupling of ionizing radiation at $t = 0$ using a Strömgren approximation (Strömgren 1939). For a classic Strömgren sphere, the mass ionized in a constant density cloud $M_{\text{Strom}} = (4\pi/3)R_{\text{Strom}}^3\rho_{\text{cl}}$, where R_{Strom} is the Strömgren radius, can be formulated as

$$M_{\text{Strom}} = \frac{Q_i \mu_n}{\alpha_B n_{\text{cl}}}. \quad (34)$$

We can calculate the star formation efficiency needed to ionize such a cloud ($M_{\text{cl}} = M_{\text{Strom}}$), above which ionizing radiation is no longer fully coupled. Assuming an ionizing photon output that scales linearly with cluster mass ($Q_i = 4 \times 10^{51} \text{ s}^{-1} \times M_* / 10^5 M_\odot$), the star formation efficiency needed to fully ionize a constant density cloud and decouple radiation dynamically at early times is

$$\epsilon_{\text{ionize}} = \left(\frac{\mu_n}{n_{\text{cl}} \alpha_B} \frac{Q_i}{M_*} + 1 \right)^{-1}. \quad (35)$$

This corresponds to star formation efficiencies of 0.86 and 0.38, respectively, for the 1000 and 100 cm^{-3} models examined here.

Initial expansion of the wind bubble increases the density of the shell and hence the global cloud recombination rate, which will not decrease until the expansion radius exceeds the initial cloud radius. Therefore, ionizing radiation cannot escape in any of our models as long as the shell is still confined by the cloud. Thus,

$$f_{\text{esc},i} = \begin{cases} 0 & \text{if } t < t_{\text{sweep}}, \\ 1 - f_{\text{abs},i} & \text{otherwise.} \end{cases} \quad (36)$$

In Figs 8 and 9, we show how the escape fraction varies as a function of time for 10^5 and $10^6 M_\odot$ clouds with a range of densities and metallicities. For clouds more massive than $10^7 M_\odot$, $f_{\text{esc},i}$ remains 0 at all times. Note, however, that we do not take into account fragmentation of the shell. Hence, the escape fractions provided here purely consider radiation escaping through the isotropic shell ignoring any holes and clumps. Consequently, in most cases, the escape fractions derived here will be lower limits on the true values.

For solar metallicity (Fig. 8), $f_{\text{esc},i}$ reaches its highest values around 5 Myr. We have tested how the escape fraction would evolve if we would continue the expansion of the ‘shell’ even after it has dissolved and found that $f_{\text{esc},i}$ always drops after $t \sim 5$ Myr. At late times, the strong reduction in L_i due to the death of the massive stars causes a decrease in $f_{\text{esc},i}$, even though the shell has a low column and volume density by then. Both the time span during which ionizing radiation can escape and the amount of escaping ionizing radiation depend on the cloud mass (more escape for low M_{cl}) and cloud density (more escape for low n_{cl}). Additionally, the fact that the shell dissolves before 10 Myr for some models does

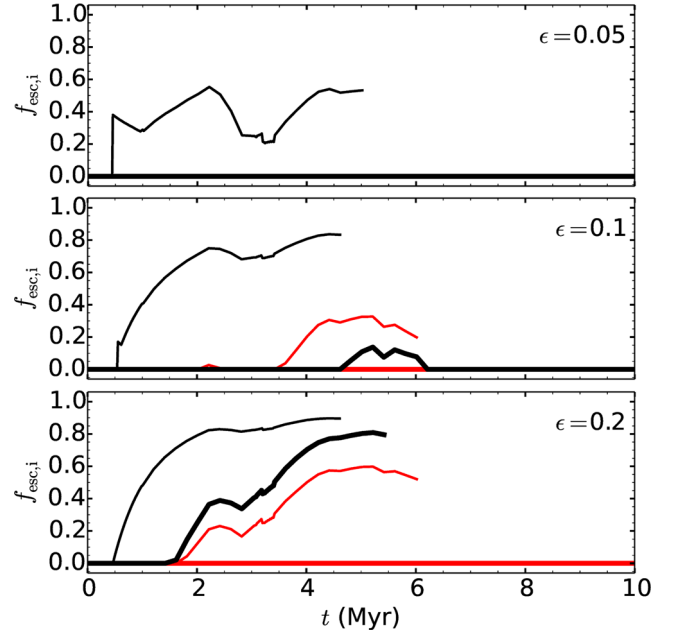


Figure 8. Escape fractions for ionizing radiation $f_{\text{esc},i}$ for $\epsilon = 0.05, 0.1$, and 0.2 (top, middle, and bottom panels, respectively) for $Z = Z_\odot$. The black lines are for a $10^5 M_\odot$ cloud, and the red lines for a $10^6 M_\odot$ cloud. Thick and thin lines correspond to cloud densities of $n_{\text{cl}} = 1000$ and 100 cm^{-3} , respectively. Lines that stop before 10 Myr belong to shells that have dissolved into the ambient ISM before this time.

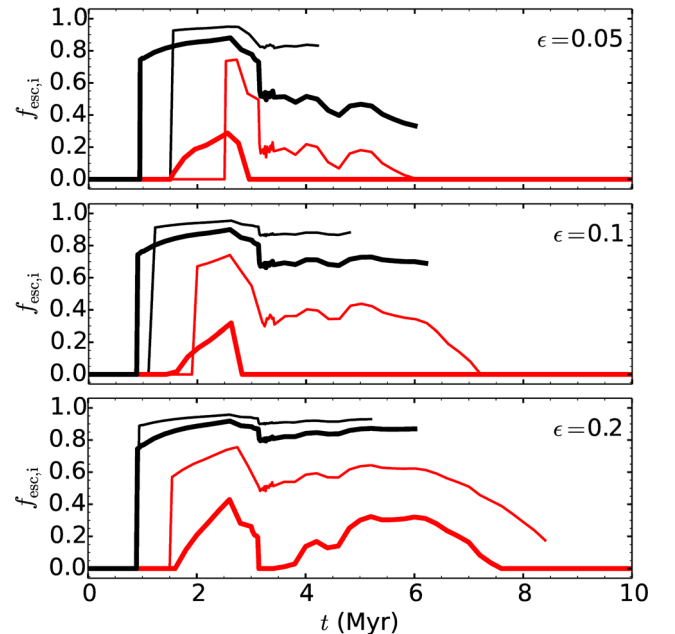


Figure 9. Escape fractions for ionizing radiation $f_{\text{esc},i}$ for $\epsilon = 0.05, 0.1$, and 0.2 (top, middle, and bottom panels, respectively) for $Z = 0.15 Z_\odot$. The black lines are for a $10^5 M_\odot$ cloud, and the red lines for a $10^6 M_\odot$ cloud. Thick and thin lines correspond to cloud densities of $n_{\text{cl}} = 1000$ and 100 cm^{-3} , respectively. Lines that stop before 10 Myr belong to shells that have dissolved into the ambient ISM before this time.

not mean that all ionizing radiation can escape. With a decrease in L_i at late times, even a diffuse medium of $\lesssim 1 \text{ cm}^{-3}$ can be enough to absorb a large part of the ionizing radiation.

Low-metallicity models (Fig. 9) have higher integrated ionizing escape fractions than solar metallicity models and $f_{\text{esc}, i}$ peaks earlier, at ~ 2.5 Myr, as less radiation is absorbed by dust. Also, even at low ϵ , dense clouds become optically thin to ionizing radiation before the first SNe. Thus, the Wolf–Rayet phase and the first SNe lead to a significant reduction in $f_{\text{esc}, i}$ between ~ 3 – 4 Myr. Even though we neglect turbulence, which can open and close low-density channels in the ISM through which radiation can escape, we show that some strong variability in $f_{\text{esc}, i}$ is expected purely due to stellar evolution.

Our results are in good agreement with 3D MHD simulations by Howard, Pudritz & Klessen (2017) for a cloud with $M_{\text{cl}} = 10^6 M_{\odot}$, $\epsilon = 0.1$, and $n_{\text{cl}} = 100 \text{ cm}^{-3}$ and solar metallicity even though they include turbulence but neglect stellar winds. Furthermore, our results are consistent with ionization parameter mappings of the Magellanic Clouds³ carried out by Pellegrini et al. (2012), who find average ionizing escape fractions of 0.4. These escape fractions are dominated by H II regions with two types of geometries: blister-type H II and classical density-bounded nebulae. Our model is most applicable to the density-bounded regions, which are consistent with fully ionized shells.

7 WHEN FEEDBACK FAILS – RECOLLAPSE AND SEQUENTIAL STAR FORMATION

It is not a given that stellar feedback is always able to overpower gravity and drive an outflow. If ϵ is lower than some minimum star formation efficiency ϵ_{min} , the shell eventually collapses back on itself, initiating more star formation. One possible example for this could be the core of 30 Doradus where two distinct stellar clusters of different age coexist (e.g. Sabbi et al. 2012). The collapse time thus sets what we coin the cadence of star formation. Only when $\epsilon > \epsilon_{\text{min}}$ can further star formation be shut off (neglecting triggered star formation in the shell). Since we cannot follow the expansion of each shell ad infinitum, we regard shells as non-collapsing if they have either dissolved or have not collapsed by $t = t_{\text{end}}$. We hence might miss a small number of shells that take longer than $7\tau_{\text{ff}}$ to collapse.

Fig. 10 shows the collapse time t_{collapse} for high-density runs. It is remarkable that a vast majority of models that collapse share a similar collapse time: $t_{\text{collapse}} = 2$ – $4\tau_{\text{ff}}$ (~ 3 – 6 Myr) for solar metallicity and $t_{\text{collapse}} = 4$ – $5\tau_{\text{ff}}$ (~ 6 – 7 Myr) in our low-metallicity run. No shell in the investigated range collapsed in less than $2\tau_{\text{ff}}$. Even though in our model all stars formed in an instantaneous starburst, we can define a time-averaged star formation rate $\langle \dot{M}_* \rangle \equiv M_*/t_{\text{collapse}}$. Following Krumholz & McKee (2005), we then define the dimensionless star formation rate per free-fall time

$$\epsilon_{\text{ff}} \equiv \frac{\langle \dot{M}_* \rangle}{M_* + M_{\text{cl}}} \tau_{\text{ff}}, \quad (37)$$

which can be rewritten as $\epsilon_{\text{ff}} = \epsilon \tau_{\text{ff}}/t_{\text{collapse}}$. Our recollapsing models have ϵ_{ff} of the order 0.01 and never exceed 0.07, in very good agreement with observations (e.g. Krumholz & Tan 2007).

³Typical sampled cloud masses associated with massive clusters in the Large Magellanic Cloud and Small Magellanic Cloud are $> 10^4 M_{\odot}$ (the same as those shown in Figs 8 and 9; see e.g. Wong et al. 2011), but the characteristic metallicity of the gas in these two galaxies is $0.5 Z_{\odot}$ (in between the metallicities, we investigated) and $0.2 Z_{\odot}$ (slightly above our low-Z model), respectively.

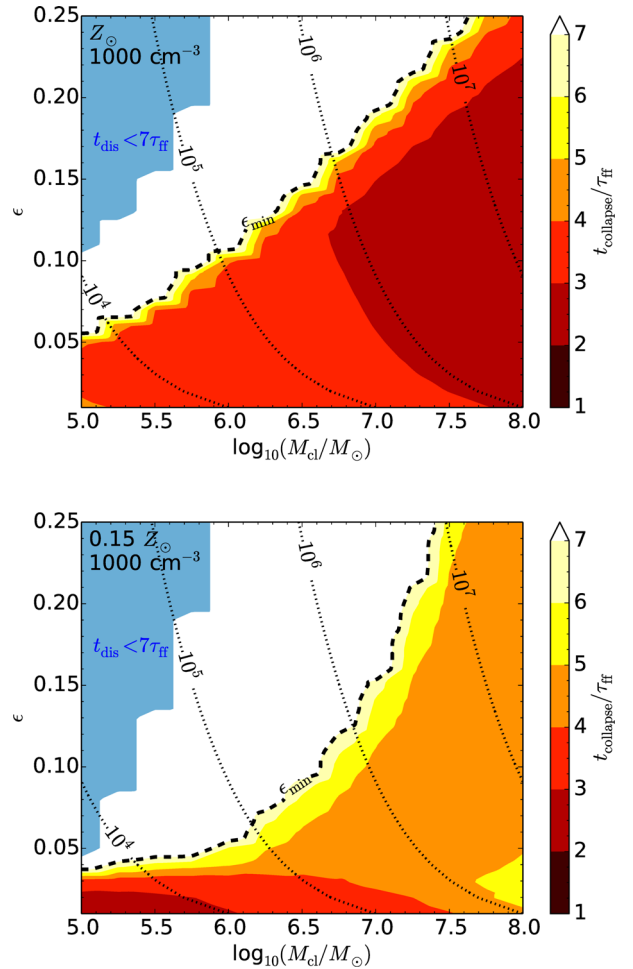


Figure 10. Collapse time t_{collapse} in multiples of τ_{ff} (1.4 Myr) as a function of cloud mass and star formation efficiency for high-density runs with solar metallicity (top) and low metallicity (bottom). The black dashed line shows the minimum star formation efficiency ϵ_{min} (see the main text). Shells in the light blue regime have dissolved before $t = 7\tau_{\text{ff}}$ and are assumed to never recollapse. Black dotted curves indicate lines of constant cluster mass from 10^4 to $10^7 M_{\odot}$.

The dashed contour line between recollapsing and non-collapsing models shows the minimum star formation efficiency ϵ_{min} . It increases with increasing cloud mass as gravity prevents outflows in massive clouds. We find that for solar metallicity, ϵ_{min} scales linearly with $\log M_{\text{cl}}$, while for the low Z , high-density model $\log \epsilon_{\text{min}}$ scales linearly with $\log M_{\text{cl}}$. For all but the most massive clouds, ϵ_{min} is lower for low metallicity.

The blue area in Fig. 10 shows models in which the shells dissolve before $7\tau_{\text{ff}}$ (~ 10 Myr). The earliest dissolutions take place after 4 Myr. Using numerical simulations, this is also what Inutsuka et al. (2015) find for the destruction time of $\sim 10^5 M_{\odot}$ clouds, albeit for lower star formation efficiencies. 4 Myr is clearly shorter than what observational studies usually estimate for the lifetimes of molecular clouds after the onset of star formation, i.e. ~ 20 Myr (see Dobbs et al. 2014 for an overview). We note this calls into question the existence of clouds with low masses and high star formation efficiencies.

In Fig. 11, we show t_{collapse} for our low-density models. Recollapse is limited to the most massive clouds or small star formation efficiencies in the case of solar metallicity. At low metallicity, only

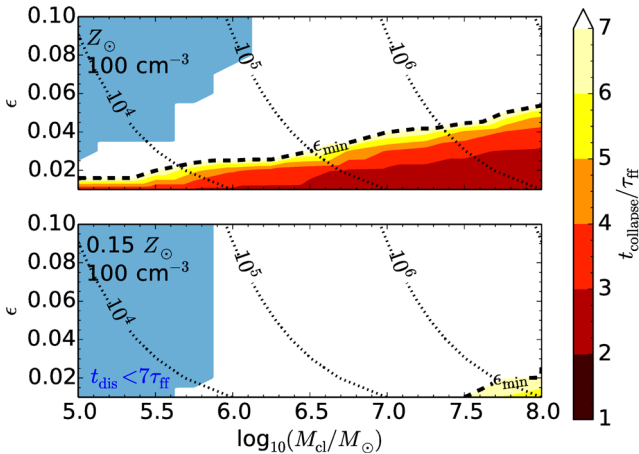


Figure 11. Collapse time t_{collapse} in multiples of τ_{ff} (4.6 Myr) as a function of cloud mass and star formation efficiency for low-density runs with solar metallicity (*top*) and low metallicity (*bottom*). The black dashed line shows the minimum star formation efficiency ϵ_{min} (see the main text). Shells in the light blue regime have dissolved before $t = 7\tau_{\text{ff}}$ and are assumed to never recollapse. Black dotted curves indicate lines of constant cluster mass from 10^4 to $10^7 M_{\odot}$. Only star formation efficiencies up to $\epsilon = 0.1$ are shown.

shells that form in clouds with masses close to $10^8 M_{\odot}$ and $\epsilon \leq 0.02$ collapse. Recollapsing low-density models have lower ϵ_{ff} values than high-density models, but are still consistent with observations (e.g. Murray 2011).

The trend of increasing ϵ_{min} for increasing cloud mass hints at star formation being more efficient for massive clouds. Observationally, this is hard to test. Some studies that found the opposite trend, i.e. lower ϵ with increasing cloud mass, were probably limited by sampling and selection effects (Murray 2011).

Kim et al. (2016) present ϵ_{min} for various cloud densities. As an example, for a $2 \times 10^6 M_{\odot}$ cloud with $n_{\text{cl}} = 1000 \text{ cm}^{-3}$, they find ϵ_{min} anywhere between 0.2 and 0.7 depending on which of their definitions for ϵ_{min} they use. Our results suggest a lower value of $\epsilon_{\text{min}} = 0.12$ for such a cloud. This difference, however, is not surprising, since Kim et al. (2016) ignore wind and SN feedback in their model.

Studies of the effect of gas expulsion on star cluster evolution show that a majority of stars remain bound only if $\epsilon \gtrsim 0.1 - 0.2$ (Geyer & Burkert 2001; Baumgardt & Kroupa 2007; Shukirgaliyev et al. 2017). Since clouds with a low gas density or a low mass have a lower minimum star formation efficiency than this value, our model predicts that such clouds will form gravitationally unbound OB associations rather than gravitationally bound star clusters. Similarly, the lower values of ϵ_{min} that we find in our lower metallicity models suggest that the formation of unbound associations rather than bound clusters may be more common in these systems.

8 CONCLUSIONS AND SUMMARY

We have developed a new model that simultaneously and self-consistently calculates the structure and the expansion of shells driven by feedback from stellar winds, SNe, and radiation pressure. The model has been put to use to investigate the conditions in which the various different sources of feedback dominate, the amount of radiation that can escape through the shell, and to derive minimum star formation efficiencies for a large parameter space of clouds and clusters. Our main results are summarized below.

8.1 What is the dominant source of feedback?

(i) Radiation pressure and ram pressure are interconnected. Any attempt to estimate the momentum that radiation injects into the ISM without accounting for ram pressure by winds and SNe will yield incorrect results. Changing the momentum imparted by winds always leads to a change in the efficiency of radiation pressure.

(ii) The evolution of a star-forming molecular cloud is strongly influenced by the effects of stellar evolution. The Wolf-Rayet phase and SN explosions do not only increase the effect of ram pressure but also indirectly increase the effect of radiation pressure (see above). It is thus imperative to include proper stellar evolution when investigating feedback.

(iii) After the shocked wind material has cooled, radiation dominates the driving of the shell as long as the shell remains optically thick. This is usually the case when the star cluster is still young ($t \lesssim 2-3$ Myr). In massive clouds, which tend to expand more slowly due to the quadratic dependence of the gravitational force on mass, radiation pressure remains dominant for an even longer time span. Thus, in more massive clouds, the time-integrated effect of radiation pressure compared to ram pressure increases. Indirect radiation pressure is negligible for low-mass clouds and is only of some importance during the early phases of massive cloud evolution or during recollapse.

(iv) Stellar winds are more important than radiation pressure in dense clouds only if the cloud mass is towards the lower end of the range studied here ($M \sim 10^5-10^6 M_{\odot}$). They always dominate over radiation pressure if the cloud density is low. At low metallicity, the momentum output by winds is decreased but radiation also couples more weakly with the shell, and so winds can still dominate over radiation.

(v) SNe dominate at late times. However, in most cases, over the whole cloud lifetime SN feedback does not exceed either feedback from winds or from radiation pressure. Also, feedback from SNe is not always sufficient to destroy a molecular cloud.

8.2 How well coupled is radiation to the shell?

As we have demonstrated, classical Strömgren calculations show a full ionization of a massive molecular cloud by a star cluster is practically impossible. Despite this, we find the escape of ionizing radiation from a spherically symmetric expanding cloud is significant, and a direct result of the shell structure responding to stellar feedback. This is an unavoidable consequence of the dynamic evolution caused by feedback driving an expansion and stretching the gas over a larger volume, decreasing its density.

(i) Radiation decouples more rapidly from the ISM for higher star formation efficiency, lower metallicity, lower cloud density or lower cloud mass. This is true for both ionizing and non-ionizing radiation.

(ii) For our calculations of ionizing escape fractions $f_{\text{esc, i}}$, we consider the radiation escaping through a shell but neglect any fragmentation of shell. Our escape fractions are thus independent of the solid angle on the sky and, in most cases, are lower limits to real total escape fractions.

8.3 What is the minimum star formation efficiency required to prevent recollapse?

(i) We find minimum star formation efficiencies ϵ_{min} of a few per cent for low-mass clouds, increasing to ~ 25 per cent or more for very massive clouds. Clouds with star formation efficiencies above

these values are disrupted by the effects of stellar feedback and do not recollapse.

(ii) The values we recover for ϵ_{\min} are considerably smaller than those found by Kim et al. (2016), likely because those authors do not account for the effects of stellar winds or SNe.

(iii) The cadence of star formation (i.e. the delay between episodes of star formation in clouds that recollapse) is 3–6 Myr ($2-4 \tau_{\text{ff}}$) for dense clouds with solar metallicity and is somewhat higher for lower metallicity clouds. Low-density clouds are much easier to disrupt by feedback (especially if they are metal poor), thus suggesting that they earlier shut off further star formation and hence tend to have a lower star formation efficiency.

(iv) Our results suggest that dense, massive and/or metal-rich clouds are more likely to form gravitationally bound star clusters, while less dense, less massive and/or more metal-poor clouds are more likely to form unbound OB associations.

ACKNOWLEDGEMENTS

We thank Sam Geen, Mordecai-Mark Mac Low, Avery Meiksin, Stefan Reißl, Stefanie Walch, and Robin Williams for helpful discussions. We acknowledge support from the Deutsche Forschungsgemeinschaft in the Collaborative Research Centre (SFB 881) ‘The Milky Way System’ (subprojects B1, B2, and B8) and in the Priority Program SPP 1573 ‘Physics of the Interstellar Medium’ (grant numbers KL 1358/18.1, KL 1358/19.2, and GL 668/2-1). RSK furthermore thanks the European Research Council for funding in the ERC Advanced Grant STARLIGHT (project number 339177).

REFERENCES

- Arthur S. J., Kurtz S. E., Franco J., Albarran M. Y., 2004, *ApJ*, 608, 282
- Arthur S. J., Medina S.-N. X., Henney W. J., 2016, *MNRAS*, 463, 2864
- Avedisova V. S., 1972, *SvA*, 15, 708
- Baumgardt H., Kroupa P., 2007, *MNRAS*, 380, 1589
- Bisnovatyi-Kogan G. S., Silich S. A., 1995, *Rev. Mod. Phys.*, 67, 661
- Canto J., Raga a. C., Rodriguez L. F., 2000, *ApJ*, 536, 896
- Castor J., McCray R., Weaver R., 1975, *ApJ*, 200, L107
- Chevalier R. A., Clegg A. W., 1985, *Nature*, 317, 44
- Dale J. E., Ercolano B., Bonnell I. A., 2012, *MNRAS*, 424, 377
- Dobbs C. L. et al., 2014, in Beuther H., Klessen R. S., Dullemond C. P., Henning Th. eds, *Protostars and Planets VI*, Vol. 944, University of Arizona Press, Tucson, AZ, p. 3
- Draine B. T., 2011, *ApJ*, 732, 100
- Dunne B. C., Chu Y.-H., Chen C.-H. R., Lowry J. D., Townsley L., Gruendl R. A., Guerrero M. A., Rosado M., 2003, *ApJ*, 590, 306
- Ekström S., Georgy C., Meynet G., Massey P., Levesque E. M., Hirschi R., Eggenberger P., Maeder A., 2012, *A&A*, 542, A29
- Ferland G. J. et al., 2013, *Rev. Mex. Astron. Astrofis.*, 49, 137
- Georgy C., Ekström S., Meynet G., Massey P., Levesque E. M., Hirschi R., Eggenberger P., Maeder A., 2012, *A&A*, 542, A29
- Georgy C. et al., 2013, *A&A*, 558, A103
- Geyer M. P., Burkert A., 2001, *MNRAS*, 323, 988
- Gupta S., Nath B. B., Sharma P., Shekulinov Y., 2016, *MNRAS*, 462, 4532
- Howard C., Pudritz R., Klessen R., 2017, *ApJ*, 834, 40
- Inutsuka S.-i., Inoue T., Iwasaki K., Hosokawa T., 2015, *A&A*, 580, A49
- Kim J.-G., Kim W.-T., Ostriker E. C., 2016, *ApJ*, 819, 137
- Koo B.-C., McKee C., 1992, *ApJ*, 388, 93
- Kroupa P., 2001, *MNRAS*, 322, 231
- Krumholz M. R., Matzner C. D., 2009, *ApJ*, 703, 1352
- Krumholz M. R., McKee C. F., 2005, *ApJ*, 630, 250
- Krumholz M. R., Tan J. C., 2007, *ApJ*, 654, 304
- Krumholz M. R., McKee C. F., Tumlinson J., 2008, *ApJ*, 689, 865
- Krumholz M. R., Bate M. R., Arce H. G., Dale J. E., Gutermuth R., Klein R. I., Li Z.-Y., Nakamura F., Zhang Q., 2014, in Beuther H., Klessen R. S., Dullemond C. P., Henning Th. eds, *Protostars and Planets VI*, Vol. 944, University of Arizona Press, Tucson, AZ, p. 243
- Lamers H. J. G. L. M., Cassinelli J. P., 1999, *Introduction to Stellar Winds*. Cambridge Univ. Press, Cambridge
- Lebedev P., 1901, *Ann. Phys.*, 311, 433
- Leitherer C. et al., 1999, *ApJS*, 123, 3
- Leitherer C., Ekström S., Meynet G., Schaerer D., Agienko K. B., Levesque E. M., 2014, *ApJS*, 212, 14
- Levesque E., Leitherer C., Ekstrom S., Meynet G., Schaerer D., 2012, *ApJ*, 751, 67
- Mac Low M.-M., McCray R., 1988, *ApJ*, 324, 776
- Martínez-González S., Silich S., Tenorio-Tagle G., 2014, *ApJ*, 785, 164
- Martins F., Palacios A., 2013, *A&A*, 560, A16
- Mathews W. G., 1967, *ApJ*, 147, 965
- Murray N., 2011, *ApJ*, 729, 133
- Murray N., Quataert E., Thompson T. A., 2010, *ApJ*, 709, 191
- Osterbrock D. E., Ferland G. J., 2006, *Astrophysics of Gaseous Nebulae and Active Galactic Nuclei*, 2nd edn. University Science Books, Sausalito, CA
- Pellegrini E. W. et al., 2007, *ApJ*, 658, 1119
- Pellegrini E. W., Oey M. S., Winkler P. F., Points S. D., Smith R. C., Jaskot A. E., Zastrow J., 2012, *ApJ*, 755, 138
- Rogers H., Pittard J. M., 2013, *MNRAS*, 431, 1337
- Sabbi E. et al., 2012, *ApJ*, 754, L37
- Seon K.-I., 2009, *ApJ*, 703, 1159
- Shukirgaliyev B., Parmentier G., Just A., Berczik P., 2017, *A&A*, preprint ([arXiv:1706.03228v2](https://arxiv.org/abs/1706.03228v2))
- Silich S., Tenorio-Tagle G., 2013, *ApJ*, 765, 43
- Skinner M. A., Ostriker E. C., 2015, *ApJ*, 809, 187
- Snow T. P., McCall B. J., 2006, *ARA&A*, 44, 367
- Strömgren B., 1939, *ApJ*, 89, 526
- Townsley L. K., Feigelson E. D., Montmerle T., Broos P. S., Chu Y.-H., Garmire G. P., 2003, *ApJ*, 593, 874
- Walch S. K., Whitworth A. P., Bisbas T., Wunsch R., Hubber D., 2012, *MNRAS*, 427, 625
- Weaver R., McCray R., Castor J., Shapiro P., Moore R., 1977, *ApJ*, 218, 377
- Wong T. et al., 2011, *ApJS*, 197, 16

APPENDIX A:

A1 The effect of stellar rotation

Models that include stellar rotation can better reproduce the observed main-sequence width and stellar surface abundances and velocities than models of non-rotating stars and are therefore thought to provide a more realistic view (Ekström et al. 2012). Given that rotating stars produce more ionizing radiation at later times (Levesque et al. 2012), it is interesting to see how stellar rotation effects the escape fractions of ionizing radiation in our models.

We reran all models including stellar rotation and found that the effects on the dynamics of the shell are small. However, since most ionizing radiation gets emitted at late times when the density of the shell has already dropped, $f_{\text{esc},i}$ is larger at late times for rotating stars than for non-rotating stars (see Fig. A1). On the other hand, at early times stellar rotation does not considerably decrease $f_{\text{esc},i}$. Taken together, the time-integrated escape fractions of ionizing radiation are higher if stellar rotation is included.

For our simulations, we have used the rotating models by Ekström et al. (2012), which assume a stellar rotation velocity of 40 per cent of the break-up velocity on the zero-age main sequence. However,

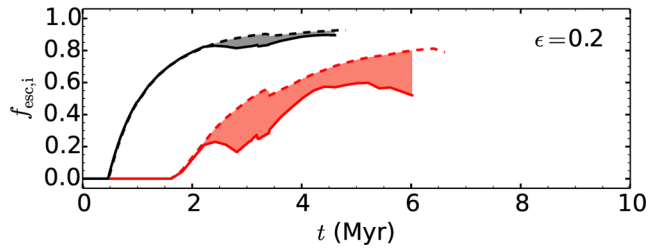


Figure A1. Example of the dependence of $f_{\text{esc},i}$ on stellar rotation for $n_{\text{cl}} = 100 \text{ cm}^{-3}$ and solar metallicity. The dashed lines correspond to the model which includes stellar rotation. The solid lines correspond to the non-rotating model. We show results for clouds with masses $M_{\text{cl}} = 10^5 M_{\odot}$ (black) and $M_{\text{cl}} = 10^6 M_{\odot}$ (red), as in Fig. 8. Since the assumed stellar rotation might be too high (see the main text), realistic escape fractions are expected to lie in the grey- and red-shaded areas, respectively.

as Martins & Palacios (2013) point out, this value might be too extreme. The results obtained from including such a high rotation velocity should thus be regarded as an upper limit for $f_{\text{esc},i}$ while non-rotating models provide a lower limit.

A2 Overview of models

On the following pages, we provide figures showing the shell radius and velocity, the absorption fraction of ionizing and non-ionizing radiations as well as momentum and force comparisons for models with a cloud mass of $10^5 M_{\odot}$ and star formation efficiencies of 0.1, 0.15, 0.2, and 0.25 (Fig. A2) and models with cloud masses $M_{\text{cl}} = 10^6, 10^7,$ and $10^8 M_{\odot}$ and star formation efficiencies $\epsilon = 0.02, 0.05, 0.1,$ and 0.25 (Figs A3–A5). Densities of $n_{\text{cl}} = 100, 100 \text{ cm}^{-3}$ are shown; the metallicity is solar. Dashed lines in the expansion velocity and momentum plots show negative values.

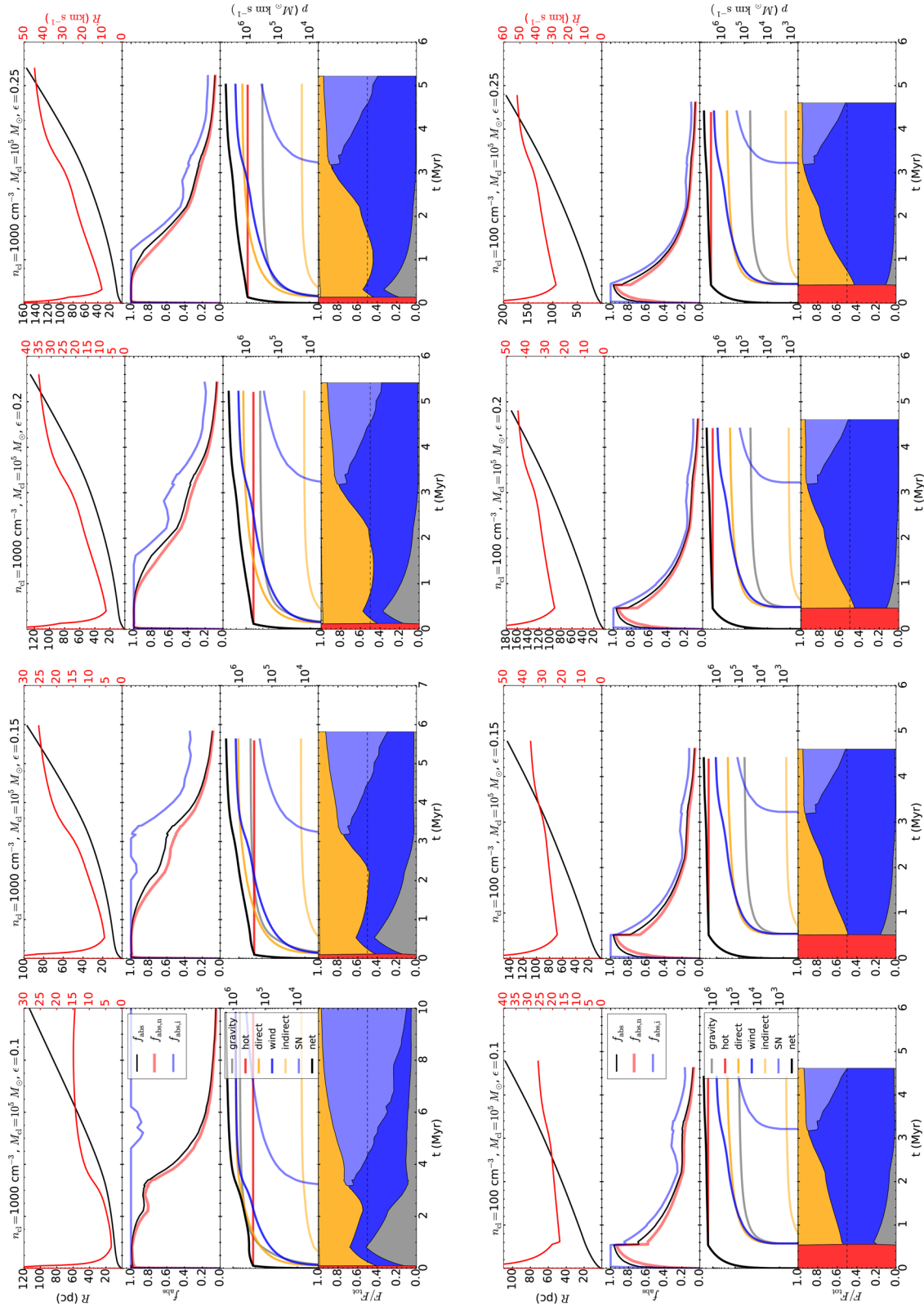


Figure A2. Models for clouds with $M_{cl} = 10^5 M_{\odot}$ and $\epsilon = 0.1, 0.15, 0.2,$ and 0.25 .

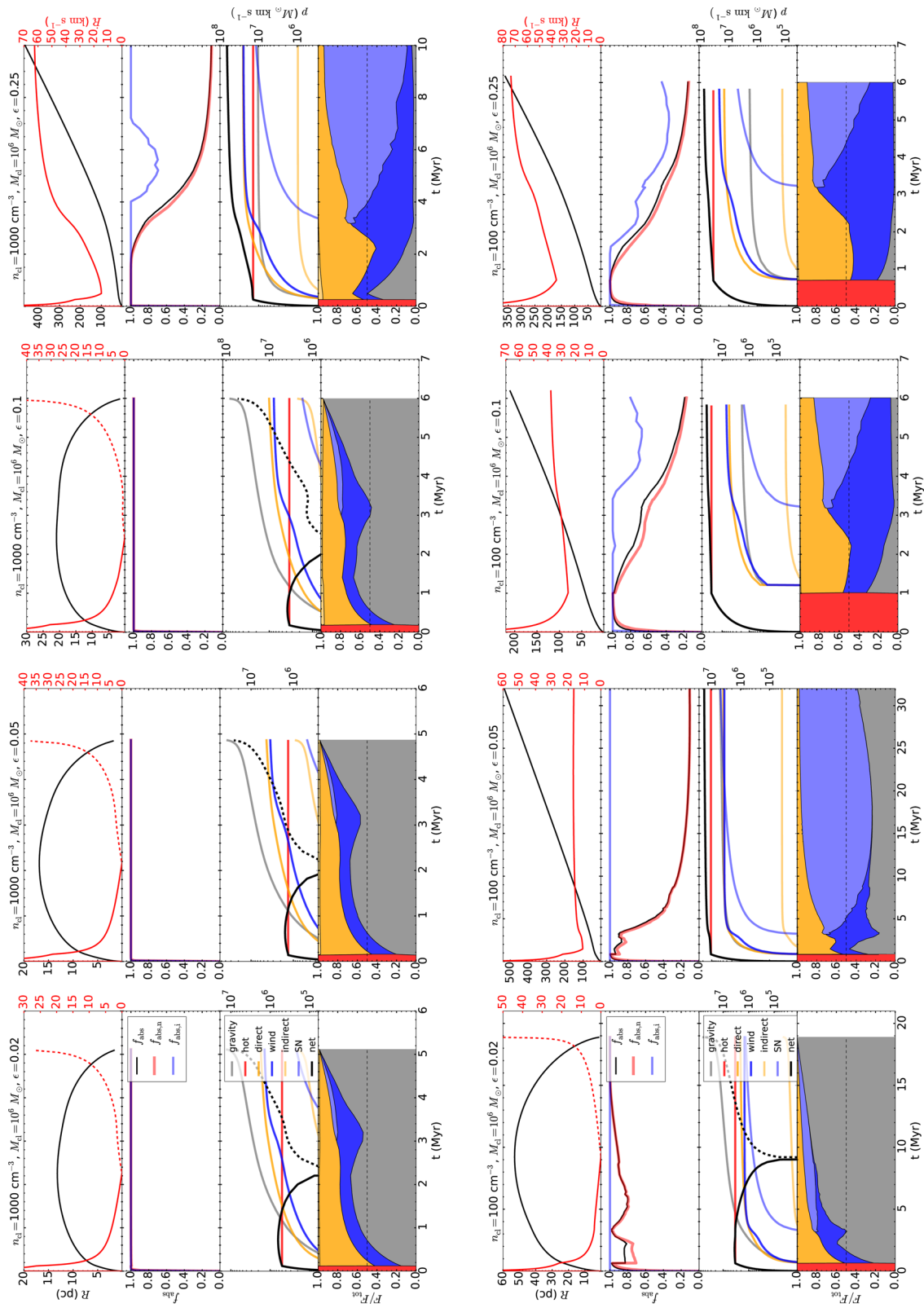


Figure A3. Models for clouds with $M_{cl} = 10^6 M_{\odot}$ and $\epsilon = 0.02, 0.05, 0.1,$ and 0.25 .

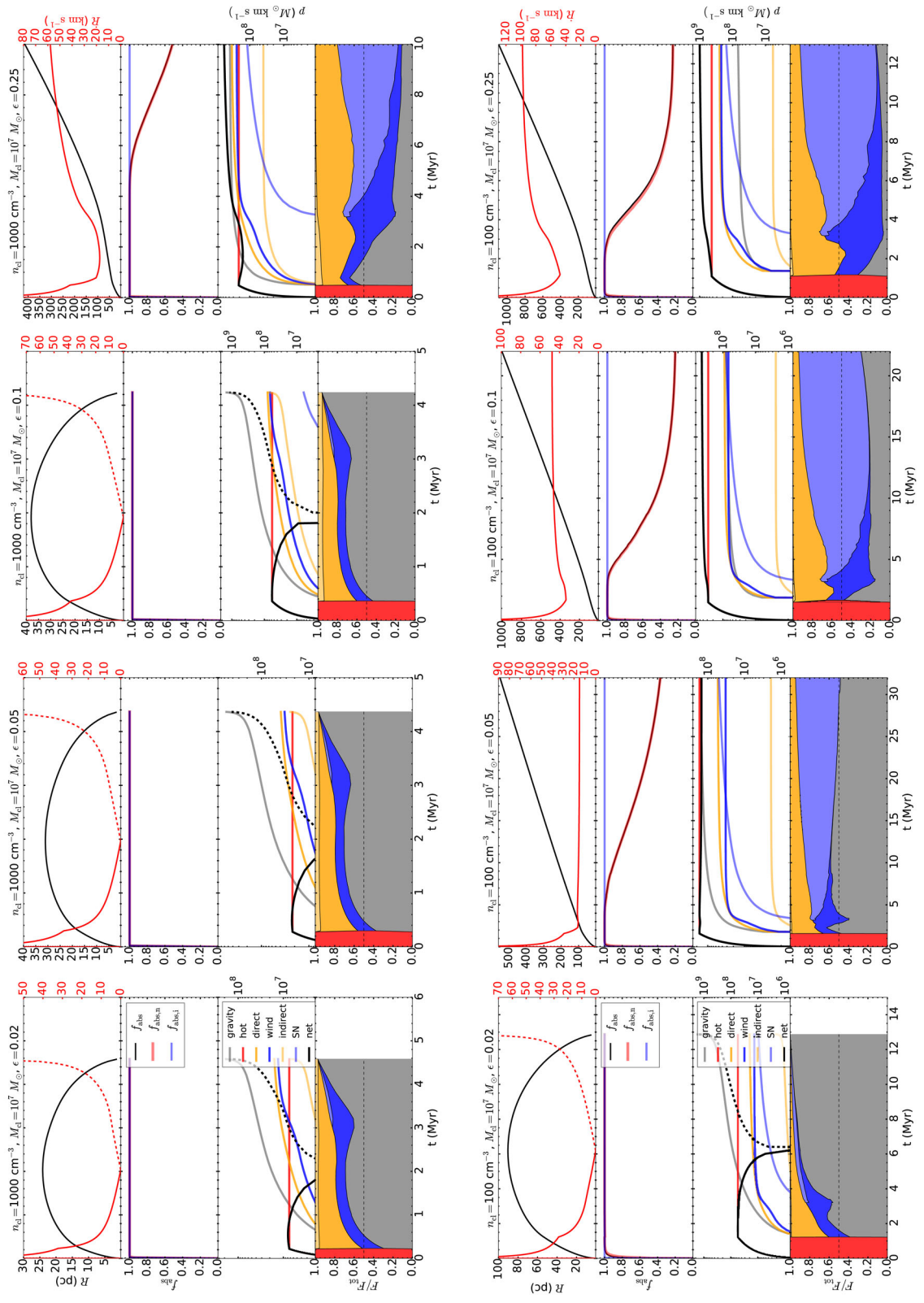


Figure A4. Models for clouds with $M_{cl} = 10^7 M_{\odot}$ and $\epsilon = 0.02, 0.05, 0.1,$ and 0.25 .

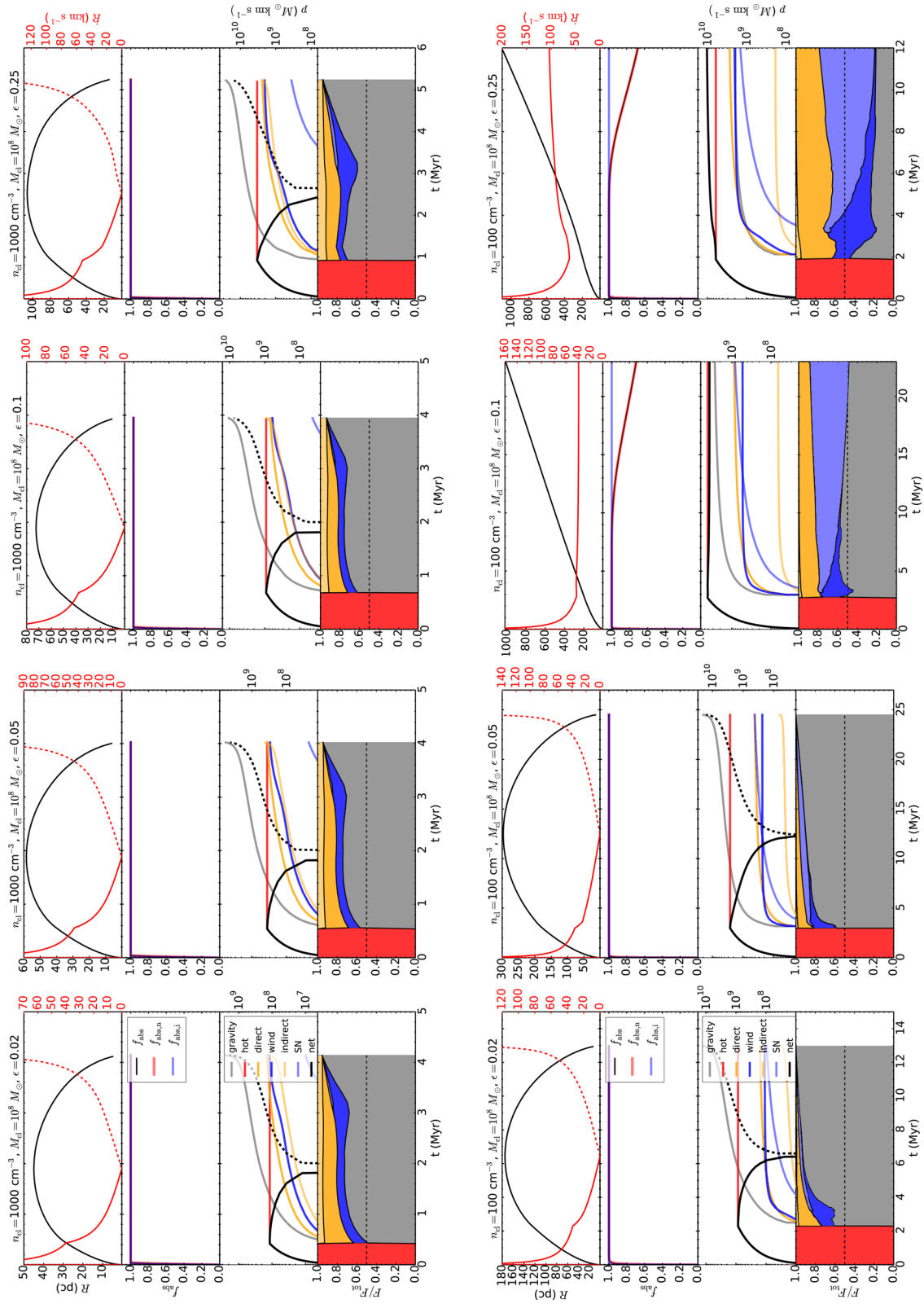


Figure A5. Models for clouds with $M_{cl} = 10^8 M_{\odot}$ and $\epsilon = 0.02, 0.05, 0.1, \text{ and } 0.25$.

This paper has been typeset from a \LaTeX file prepared by the author.

2.2 Forming Clusters within Clusters: How 30 Doradus Recollapsed and Gave Birth Again

Distribution of work: Eric Pellegrini developed the idea to model the inner cluster of NGC 2070 (R136, see Figure 2.1) inside the massive star-forming region 30 Doradus as the result of gas re-accretion. I expanded the code `WARPFIELD` to allow for multiple star formation events, I ran and analysed the models, created all figures, and wrote the text for the manuscript. Eric Pellegrini, Simon Glover and Ralf Klessen contributed ideas during the preparation of the manuscript and proofread and improved the text.



Fig. 2.1 The massive young cluster R136 at the centre of NGC 2070, the ionizing cluster of 30 Doradus. The region shown is $110''$ wide (corresponding to ~ 27.5 pc; Sabbi et al. 2012). Credit: ESA/Hubble. For a large-scale view of 30 Doradus, see Figure 1.4.

Forming clusters within clusters: how 30 Doradus recollapsed and gave birth again

Daniel Rahner,¹★ Eric W. Pellegrini,¹★ Simon C. O. Glover¹ and Ralf S. Klessen^{1,2}

¹Universität Heidelberg, Zentrum für Astronomie, Institut für Theoretische Astrophysik, Albert-Ueberle-Straße 2, D-69120 Heidelberg, Germany

²Universität Heidelberg, Interdisziplinäres Zentrum für Wissenschaftliches Rechnen, Im Neuenheimer Feld 205, D-69120 Heidelberg, Germany

Accepted 2017 September 20. Received 2017 September 19; in original form 2017 September 13

ABSTRACT

The 30 Doradus nebula in the Large Magellanic Cloud (LMC) contains the massive starburst cluster NGC 2070 with a massive and probably younger stellar sub clump at its centre: R136. It is not clear how such a massive inner cluster could form several million years after the older stars in NGC 2070, given that stellar feedback is usually thought to expel gas and inhibit further star formation. Using the recently developed 1D feedback scheme `WARPFIELD` to scan a large range of cloud and cluster properties, we show that an age offset of several million years between the stellar populations is in fact to be expected given the interplay between feedback and gravity in a giant molecular cloud with a density $\gtrsim 500 \text{ cm}^{-3}$ due to re-accretion of gas on to the older stellar population. Neither capture of field stars nor gas retention inside the cluster have to be invoked in order to explain the observed age offset in NGC 2070 as well as the structure of the interstellar medium around it.

Key words: ISM: individual objects: 30 Doradus – ISM: kinematics and dynamics – Magellanic Clouds – galaxies: star clusters: individual: R136 – galaxies: star formation.

1 INTRODUCTION

30 Doradus (a. k. a. the Tarantula Nebula) is a massive star-forming region in the Large Magellanic Cloud (LMC) with a complex geometry. In it resides the massive ionizing star cluster NGC 2070, which hosts the compact subcluster R136 (formally known as RMC 136) at its core. Numerous studies have concluded that R136 is a distinct stellar population considerably younger (~ 1 Myr) than the other stars in NGC 2070 (~ 5 Myr). This gives rise to the question of how two distinct stellar populations could form there.

Multiple generations of stars are usually discussed in the context of globular clusters, and various mechanisms for the formation of younger generations have been suggested, such as recollapse of the ejecta of first generation asymptotic giant branch stars (D’Ercole et al. 2008), fast-rotating massive stars (Decressin et al. 2007) or interacting massive binaries (De Mink et al. 2009). However, this debris accounts for only a small fraction of the mass of the first generation of stars. It is therefore difficult to form a massive second population in this fashion, particularly if the age separation between the populations is small, as in the case of NGC 2070. Furthermore, bimodal (or even multimodal) age distributions are not limited to globular clusters. They are observed in young star clusters, too, with age separations ranging from tens of Myr in Sandage-96 and possibly NGC 346 (Vinkó et al. 2009; De Marchi,

Panagia & Sabbi 2011) to 1 Myr or less in the Orion nebula Cluster (Beccari et al. 2017).

On one hand, stellar feedback is often assumed to disrupt molecular clouds and prevent or at least reduce further star formation (Murray 2011; Wang et al. 2010). On the other hand, feedback can also be positive, compressing the interstellar medium (ISM) into dense shells and triggering star formation *around* the first generation star cluster (Koenig et al. 2012). However, neither outcome is consistent with what is observed in the 30 Doradus region: The existence of a massive young cluster *within* another massive cluster produces serious challenges to normal models of star formation and feedback.

Thus, the old stellar population in NGC 2070 must not only have failed to destroy its natal cloud, but the cloud must also have retained or re-accreted enough dense gas to successfully form another massive cluster in a second burst of star formation. Silich & Tenorio-Tagle (2017) showed that in dense conditions (e.g. a clump with $n \gtrsim 10^5 \text{ cm}^{-3}$ in a $10^6 M_{\odot}$ cloud) stellar winds may not be strong enough to clear all of the gas out of a newly formed star cluster. Retained gas could then cool and form a second generation of stars inside the old star cluster, explaining how multiple stellar populations can form at the same location. However, the authors do not predict when the second generation of stars might form.

As we will show, even if no gas remains in the cluster, a second generation of stars might still form from gas that has been expelled but is later re-accreted. Pflamm-Altenburg & Kroupa (2009) presented a static model which explains accretion onto very

* E-mail: daniel.rahner@uni-heidelberg.de (DR); eric.pellegrini@uni-heidelberg.de (EWP)

massive star clusters ($>10^6 M_{\odot}$, i. e. more massive than NGC 2070) surrounded by warm ISM. They also point out that accretion onto less massive clusters is possible in the rather unlikely case of the surrounding material being (and remaining) cold.

In a recent paper (Rahner et al. 2017), we presented a 1D dynamical model, which accounts correctly for all major sources of feedback in isolated, massive star-forming regions. A major result of that work was the prediction of a relatively uniform recollapse time for molecular clouds where feedback is insufficient to disrupt the molecular cloud. In this Letter, we apply our model to the cloud responsible for forming NGC 2070 and R136, and show that it provides a viable explanation for the origin of the double cluster in 30 Doradus, as well as explaining the bulk of the observed nebular structure. The low-shear environment of the LMC (Thilliez et al. 2014) renders 30 Doradus a good test case for the model.

2 MODEL

The morphology of 30 Doradus is the superposition of numerous shell-like structures, seen in multiple phases of the ISM from ionized, neutral and molecular emission. The ionized gas forms bubbles containing hot, X-ray emitting gas (Townsend et al. 2006). Using [S II]/H α observations, Pellegrini, Baldwin & Ferland (2011) showed that the H II region around NGC 2070 has the shape of hemispherical bowl with a radius of 40–60 pc. R136 is offset approximately 12 pc from the centre of the bowl. The distance between R136 and the shell is thus ~ 30 –70 pc.

There is no consensus about the exact mass and age of the different populations in NGC 2070. Most observations agree, however, that there is an older and a younger population in NGC 2070.¹ The older stars have an age of ~ 3 –7 Myr (Brandl et al. 1996; Walborn & Blades 1997; Selman et al. 1999; Sabbi et al. 2012; Cignoni et al. 2015), while the younger population, which is mainly concentrated in R136, is ~ 0.5 –2 Myr old (Massey & Hunter 1998; Selman et al. 1999; Sabbi et al. 2012; Crowther et al. 2016). The mass of R136 is 2.2×10^4 – $1 \times 10^5 M_{\odot}$ (Hunter et al. 1995; Andersen et al. 2009; Cignoni et al. 2015) compared to NGC 2070’s mass as a whole of 6.8×10^4 – $5 \times 10^5 M_{\odot}$ (Selman et al. 1999; Bosch et al. 2001; Bosch, Terlevich & Terlevich 2009; Cignoni et al. 2015). At a projected distance of ~ 40 pc from R136 lies the much older star cluster Hodge 301. Due to its comparatively low stellar mass ($\sim 6000 M_{\odot}$; Grebel & Chu 2000) and its much weaker feedback, we will ignore it here. The gas in the 30 Doradus nebula has a mass of the order of $10^6 M_{\odot}$ (Dobashi et al. 2008; Faulkner 1967) to $10^7 M_{\odot}$ (as estimated by Sokal et al. 2015 from H I measurements in Kim et al. 2003).

Starting from these observations, we propose the following timeline to explain the structure of the inner 30 Doradus region (shown in Fig. 1):

(i) A massive cluster (the old population in NGC 2070) forms in a giant molecular cloud (GMC), the properties of which are rather unconstrained. Stellar feedback compresses the surrounding gas into a thin shell and accelerates it outwards.

(ii) Feedback is not strong enough to unbind a significant fraction of gas from the cloud. Instead, the swept-up material stalls, possibly

¹ Some, e.g. Selman et al. (1999), even report on three distinct starbursts. However, the age of the intermediate population might be the result of misclassification of main-sequence Wolf–Rayet stars, and we will focus on just two populations in this work.

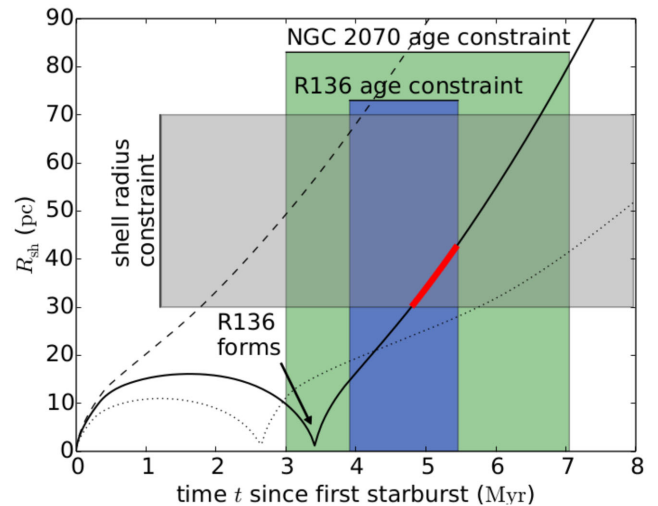


Figure 1. Time evolution of the shell radius (black solid line) for a model with $n = 2500 \text{ cm}^{-3}$, $M_{\text{cl},0} = 10^6 M_{\odot}$, $M_{*,1} = 3 \times 10^4 M_{\odot}$, $M_{*,2} = 10^5 M_{\odot}$. The various observational constraints are shown as grey, green and blue shaded areas, respectively. The thick red line shows where all three constraints are fulfilled. Also shown are examples of models that cannot fulfil all constraints: same parameters as before except for $M_{*,1} = 10^5 M_{\odot}$ (dashed line), $M_{*,1} = 2 \times 10^4 M_{\odot}$ (dotted line).

breaks up into fragments, and recollapses towards the cluster under the influence of gravity.

(iii) As the gas collapses back on to NGC 2070 and gets compressed to very high densities, a new, young, massive star cluster forms at the centre of NGC 2070: R136.

(iv) The combined feedback from R136 and the old population in NGC 2070 leads to a renewed expansion, giving rise to the shell around NGC 2070 as it is observed today.

We use the 1D feedback code `WARPFIELD` (Rahner et al. 2017) to model the expansion of the shell around NGC 2070 and to test the hypothesis described above. While we acknowledge that the latest 3D simulations of feedback in molecular clouds also include a wide range of relevant physics (e.g. Geen et al. 2016; Peters et al. 2017; Wareing, Pittard & Falle 2017), it is still prohibitively expensive to run a high number of simulations probing a large parameter space of initial conditions. Although some 3D results are not reproducible in 1D codes and could provide alternative explanations of the double cluster in 30 Doradus, the employed 1D model will help constrain the initial conditions that should be explored in computationally more demanding studies of 30 Doradus progenitors (Rahner et al., in preparation).

`WARPFIELD`, which is derived in part from observational studies of feedback in nearby star-forming regions, accounts for feedback from stellar winds, supernovae (SNe), direct and indirect radiation pressure, and gravity (self-gravity of the swept-up shell and gravity between the shell and the stars). We treat cooling of the hot, X-ray emitting wind bubble in an approximate fashion as in Mac Low & McCray (1988). The photoionized and neutral gas are set to constant temperatures of 10^4 and 10^2 K, respectively. We assume a metallicity of $Z = 0.43 Z_{\odot}$ for the gas and the stars in 30 Doradus (Choudhury, Annapurni & Cole 2016). Stellar evolution is modelled with `STARBURST99` (Leitherer et al. 1999, 2014) using Geneva evolution tracks for rotating stars up to $120 M_{\odot}$ by interpolating between models by Ekström et al. (2012) and Georgy et al. (2012). As there is evidence that the initial mass function (IMF) in 30 Doradus extends to $300 M_{\odot}$ (Crowther et al. 2010; Khorrami

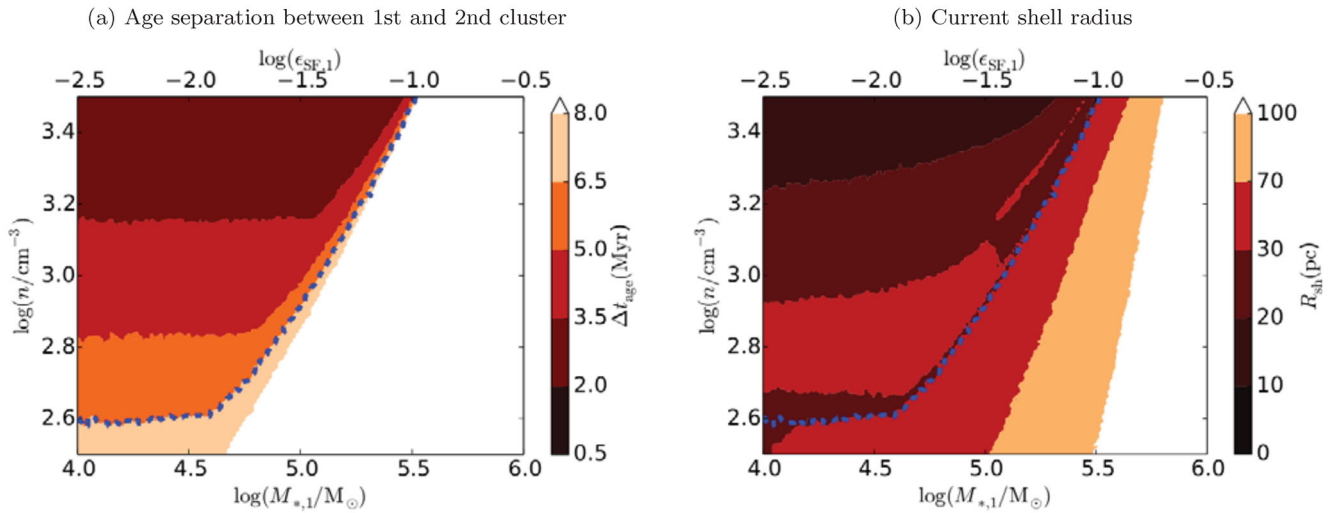


Figure 2. (a) Age separation between the two clusters and (b) current shell radius, both plotted as a function of the mass $M_{*,1}$ of the first cluster and the cloud density n . The cloud mass before star formation $M_{cl,0} = 10^{6.5} M_{\odot}$ and the mass of the second cluster $M_{*,2} = 10^5 M_{\odot}$ have been kept fixed. The blue dashed line divides regions with shells that recollapse on time-scales shorter than 6.5 Myr and are thus consistent with 30 Doradus (above the line), and shells that take longer to recollapse (or never do).

et al. 2017), for the first starburst we set the upper mass limit of the assumed Kroupa (2001) IMF to $300 M_{\odot}$. The most massive stars in R136 still exist and their masses have been determined (Crowther et al. 2010), so for the second starburst, we use a Kroupa IMF up to $120 M_{\odot}$ and add four additional stars of 165, 220, 240 and $300 M_{\odot}$ to the cluster. To estimate the mass-loss rate \dot{M}_w , bolometric luminosity L_{bol} and emission rate of ionizing photons Q_i for stars in the range $120\text{--}300 M_{\odot}$ on the main sequence, we interpolate between models presented in Crowther et al. (2010). The terminal wind velocity of these stars is set to 2500 km s^{-1} and the ionizing luminosity $L_i = 0.6L_{bol}$, as calculated with WMBASIC (Pauldrach, Hoffmann & Lennon 2001) for a 50 000 K star. We limit SN feedback to zero-age main-sequence masses between 8 and $40 M_{\odot}$ because more massive stars at subsolar metallicity are expected to end their lives in weak SN Ib/c explosions or as direct-collapse black holes (Heger et al. 2003). However, our results are not strongly affected by the choice of the upper mass cut-off.

Since the actual cloud and cluster parameters are somewhat uncertain, we consider the following proposed parameter range: cloud mass (before any stars have formed) $M_{cl,0} = 10^{5.5}\text{--}10^{7.5} M_{\odot}$, total stellar mass of the first generation of stars $M_{*,1} = 10^4\text{--}10^6 M_{\odot}$, total stellar mass of the second generation of stars (R136) $M_{*,2} = 2.2 \times 10^4\text{--}10^5 M_{\odot}$ and cloud density $n = 10^2\text{--}10^{3.5} \text{ cm}^{-3}$. For each combination ($M_{cl,0}, M_{*,1}, M_{*,2}, n$), we proceed as follows:

(i) At $t = 0$, we place a star cluster of mass $M_{*,1}$ in the centre of a cloud with constant density n and mass $M_{cl,1} = M_{cl,0} - M_{*,1}$. This star cluster represents the older population in NGC 2070.

(ii) We use WARPFIELD to model the evolution of the shell created by feedback from this star cluster in order to determine whether or not feedback successfully overcomes gravity.

(iii) If feedback is unable to overcome gravity, the cloud eventually recollapses. When the radius of the collapsing shell shrinks to 1 pc, we pause the simulation and define the time when this happens as the collapse time t_{coll} . We reset the velocity of the shell to 0.

(iv) We assume that due to the cloud recollapse a second star cluster instantaneously forms, leading to renewed expansion. The age separation between the two star clusters is then $\Delta t_{age} = t_{coll}$. The second star cluster has a stellar mass of $M_{*,2} = 2.2 \times 10^4 M_{\odot}$ or

$1 \times 10^5 M_{\odot}$ (representing the lower and upper mass estimates for R136). The expansion of the shell is now driven by a star cluster that consists of two distinct stellar populations. Before we continue the simulation, we redistribute the shell mass into a spherical cloud with the same density as before, but with a smaller mass $M_{cl,2} = M_{cl,1} - M_{*,2}$.

(v) At $t = 8$ Myr, we stop the simulation.

3 RESULTS

We will call a model (a given set of input parameters) consistent with the timeline described at the beginning of the previous section if at some time t it can fulfil all of the criteria below:

- (i) The older population in NGC 2070, which formed first, must have an age in the range $3 \leq t_{age,1} \leq 7$ Myr;
- (ii) R136 forms in a second starburst and must have an age in the range $0.5 \leq t_{age,2} \leq 2$ Myr; and
- (iii) The shell must have a radius in the range $30 \leq R_{sh} \leq 70$ pc.

A time at which all three criteria are met then marks the current, observed state of 30 Doradus. An example of a model that can reproduce all these constraints is shown in Fig. 1 (solid line), together with a model in which no second starburst occurs (and which is hence ruled out, dashed line) and a model in which feedback is too weak to push the shell to 30–70 pc in less than 2 Myr after R136 formed (dotted line).

A necessary (but insufficient) condition for meeting both constraints (i) and (ii) is $1 \leq \Delta t_{age} \leq 6.5$ Myr. In Fig. 2a, we show Δt_{age} for models with $M_{cl,0} = 10^{6.5} M_{\odot}$ and $M_{*,2} = 10^5 M_{\odot}$. We see that we can already exclude low cloud densities and high masses for NGC 2070, as these do not produce the correct age separation. When $n \lesssim 10^{2.6} \text{ cm}^{-3}$, it takes too long for the second cluster to form. Likewise, when $M_{*,1} \gtrsim 10^{5.5} M_{\odot}$, corresponding to a star formation efficiency of the first star formation event $\epsilon_{SF,1} \equiv M_{*,1}/M_{cl,0} \gtrsim 0.1$, the natal cloud is disrupted before a second starburst occurs ($\Delta t_{age} = \infty$).

In Fig. 2b, the current shell radius is shown, determined in the following way: First, for each model, we determine the time span

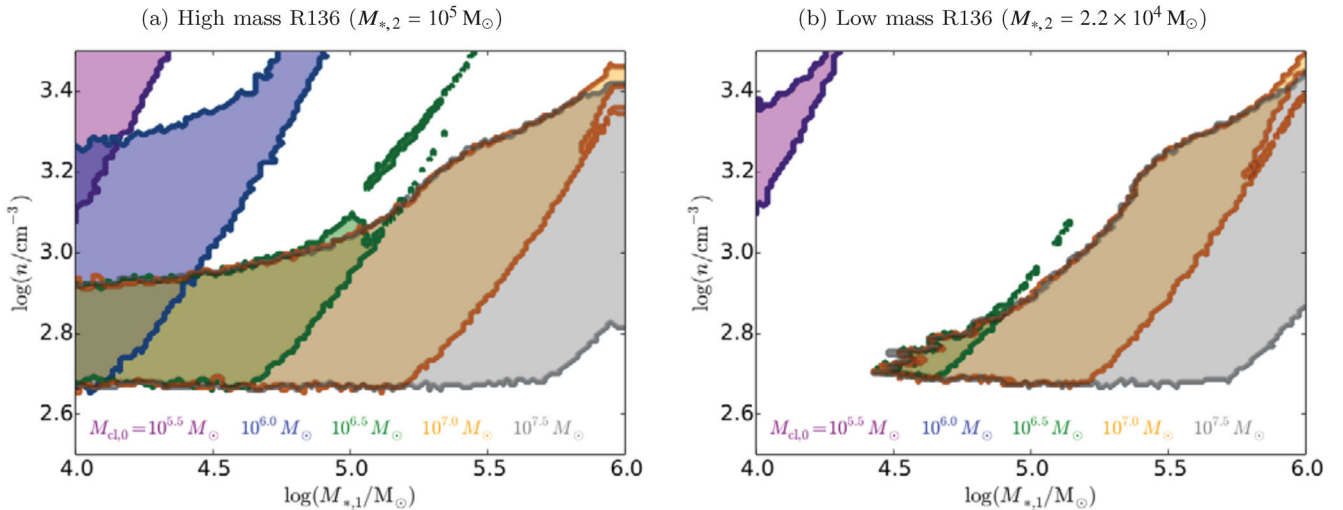


Figure 3. Regimes of mass of the first cluster $M_{*,1}$ and cloud density n for which models can reproduce both the observed current shell radius and the ages of the two clusters, shown for different initial cloud masses $M_{cl,0}$ (colours). For an initial cloud mass $M_{cl,0} = 10^6 M_{\odot}$ with $M_{*,2} = 2.2 \times 10^4 M_{\odot}$ (blue in right figure), no model in the investigated parameter space can reproduce the observations.

where condition (i) and, if possible, also (ii) are met.² We then select the radius (corresponding to a time in this time span) that is closest to the range 30–70 pc. In Fig. 2b, we show that high density clouds cannot reproduce the observed current shell radius, even though they can form two clusters with the correct Δt_{age} . Such models never simultaneously fulfill both (ii) and (iii). Low densities are also excluded because the second starburst occurs later, with insufficient time left to fulfil both (i) and (iii).

Models that yield the correct ages and shell radius are fully consistent with the described picture of gravity-induced cloud recollapse, a second star formation event and feedback-driven expansion of the shell to the current radius. In Fig. 3, we summarize the allowed regime for various cloud and cluster properties. Independent of R136’s mass, only clouds with average densities $n \gtrsim 10^{2.7} \text{ cm}^{-3}$ can fulfil (i), (ii) and (iii). This threshold is also independent of cloud mass.

In the model employed, clouds with a fixed density but different masses only differ in their size. We assume that parts of the cloud that have not been swept up by the cloud have enough turbulent support that they are stable against collapse. Hence, models with different cloud masses (but n , $M_{*,1}$, $M_{*,2}$ being equal) behave the same until the shell radius R_{sh} equals the initial cloud radius R_{cl} . So if a model is consistent with observations and $R_{cl} \geq 30$ pc, models with larger cloud masses are also consistent.

Interestingly, if the mass of R136 is low (Fig. 3b), an initial cloud mass of $10^6 M_{\odot}$ is excluded: On one hand, for a low-mass first generation (with weak stellar feedback), even the additional feedback of R136 is not enough to push the gas to 30 pc or more. On the other hand, if the older generation is massive (and feedback is stronger), the whole cloud can get swept up by the shell, delaying its recollapse, and the second star formation event takes place at a time when the majority of the most massive stars have already died. As stars more massive than $40 M_{\odot}$ do not contribute to SN feedback, again feedback is not strong enough to push gas far out.

² Models that cannot fulfil both (i) and (ii) are already excluded; however, if they can reproduce the observed shell radius via a single, unstalled expansion of the shell, they should be regarded as at least partly consistent.

For $M_{cl,0} > 10^6 M_{\odot}$, the cloud does not get swept up during the first expansion, the shell falls back earlier as it accumulates more mass, and some massive stars of the first generation can still contribute to the re-expansion. For $M_{cl,0} < 10^6 M_{\odot}$, the second starburst turns a significant fraction of the available gas into stars (corresponding to a high star formation efficiency), so that it is much easier to push the remainder of the gas to 30 pc or more.

4 DISCUSSION AND CONCLUSION

We have used the 1D stellar feedback scheme `WARPFIELD` (Rahner et al. 2017), which includes mechanical and radiative feedback as well as gravity, to test whether the properties of NGC 2070 and the ISM around it may be a result of initial gas expulsion from the cluster, followed by a gravity induced cloud recollapse, which leads to a second star formation event, creating the dense cluster R136, and finally renewed shell expansion. We show that there is a reasonable parameter regime in which both the observed ages of the young and old stellar population in NGC 2070 and the size of the current feedback-driven shell around NGC 2070 can be reproduced.

If the parental cloud does not turn more than ~ 10 per cent of the available gas into stars in a very short period of time and if the density of the cloud is quite high ($\gtrsim 500 \text{ cm}^{-3}$), due to shell recollapse a second star formation event *at the same location* several Myr later has to be expected, and no further mechanisms like capture of field stars or gas retention inside the cluster need be invoked. Typical star formation efficiencies of nearby molecular clouds are less than 10 per cent (Lada, Lombardi & Alves 2010), but only the densest GMCs in the LMC achieve densities of $\sim 500 \text{ cm}^{-3}$ (Hughes et al. 2010). If we settle for $n = 500 \text{ cm}^{-3}$ and an initial cloud mass of $M_{cl,0} = 3 \times 10^6 M_{\odot}$, we find a total stellar mass of NGC 2070 in the range $5 \times 10^4 \leq M_{*,1} + M_{*,2} \leq 1.5 \times 10^5 M_{\odot}$, which agrees well with mass estimates from observations.

Many more young star clusters could host multiple generations resulting from ISM recollapse, but we may not yet be able to identify them as the window of opportunity for unambiguously identifying such events is short. Within the Local Group, 30 Doradus is the only known system that is simultaneously: (1) massive enough for feedback to initially fail, (2) in close enough proximity and with

sufficiently low extinction for photometry and spectral observations to distinguish superimposed compact clusters, and (3) sufficiently young, making multiple generations of star formation with a few Myr offset distinct in observations. We speculate *James Webb Space Telescope* will reveal a population of post-recollapse, highly embedded clusters undergoing an unexpected and intense second event of star formation.

ACKNOWLEDGEMENTS

We acknowledge funding from the Deutsche Forschungsgemeinschaft in the Collaborative Research Centre (SFB 881) ‘The Milky Way System’ (subprojects B1, B2 and B8), the Priority Program SPP 1573 ‘Physics of the Interstellar Medium’ (grant numbers KL 1358/18.1, KL 1358/19.2 and GL 668/2-1) and the European Research Council in the ERC Advanced Grant STARLIGHT (project no. 339177).

REFERENCES

- Andersen M., Zinnecker H., Moneti A., McCaughrean M. J., Brandl B., Brandner W., Meylan G., Hunter D., 2009, *ApJ*, 707, 1347
- Beccari G. et al., 2017, *A&A*, 604, A22
- Bosch G., Selman F., Melnick J., Terlevich R., 2001, *A&A*, 380, 137
- Bosch G., Terlevich E., Terlevich R., 2009, *AJ*, 137, 3437
- Brandl B. et al., 1996, *ApJ*, 466, 254
- Choudhury S., Annapurni S., Cole A. A., 2016, *MNRAS*, 455, 1855
- Cignoni M. et al., 2015, *ApJ*, 811, 76
- Crowther P. A., Schnurr O., Hirschi R., Yusof N., Parker R. J., Goodwin S. P., Kassim H. A., 2010, *MNRAS*, 408, 731
- Crowther P. A. et al., 2016, *MNRAS*, 458, 624
- D’Ercole A., Vesperini E., D’Antona F., McMillan S. L. W., Recchi S., 2008, *MNRAS*, 391, 825
- De Marchi G., Panagia N., Sabbi E., 2011, *ApJ*, 740, 10
- De Mink S. E., Pols O. R., Langer N., Izzard R. G., 2009, *A&A*, 507, 1
- Decressin T., Meynet G., Charbonnel C., Prantzos N., Ekström S., 2007, *A&A*, 464, 1029
- Dobashi K., Bernard J.-P., Hughes A., Paradis D., Reach W. T., Kawamura A., 2008, *A&A*, 484, 205
- Ekström S., Georgy C., Meynet G., Massey P., Levesque E. M., Hirschi R., Eggenberger P., Maeder A., 2012, *A&A*, 542, A29
- Faulkner D. J., 1967, *MNRAS*, 135, 401
- Geen S., Hennebelle P., Tremblin P., Rosdahl J., 2016, *MNRAS*, 463, 3129
- Georgy C., Ekström S., Meynet G., Massey P., Levesque E. M., Hirschi R., Eggenberger P., Maeder A., 2012, *A&A*, 542, A29
- Grebel E. K., Chu Y.-H., 2000, *AJ*, 119, 787
- Heger A., Fryer C. L., Woosley S. E., Langer N., Hartmann D. H., 2003, *ApJ*, 591, 288
- Hughes A. et al., 2010, *MNRAS*, 406, 2065
- Hunter D., Shaya E., Holtzman J., Light R., O’Neil E., Jr, Lynds R., 1995, *ApJ*, 448, 179
- Khorrami Z. et al., 2017, *A&A*, 602, A56
- Kim S., Staveley-Smith L., Dopita M. A., Sault R. J., Freeman K. C., Lee Y., Chu Y.-H., 2003, *ApJS*, 148, 473
- Koenig X. P., Leisawitz D. T., Benford D. J., Rebull L. M., Padgett D. L., Assef R. J., 2012, *ApJ*, 744, 130
- Kroupa P., 2001, *MNRAS*, 322, 231
- Lada C. J., Lombardi M., Alves J. F., 2010, *ApJ*, 724, 687
- Leitherer C. et al., 1999, *ApJS*, 123, 3
- Leitherer C., Ekström S., Meynet G., Schaerer D., Agienko K. B., Levesque E. M., 2014, *ApJS*, 212, 14
- Mac Low M.-M., McCray R., 1988, *ApJ*, 324, 776
- Massey P., Hunter D., 1998, *ApJ*, 493, 180
- Murray N., 2011, *ApJ*, 729, 66
- Pauldrach A. W. A., Hoffmann T. L., Lennon M., 2001, *A&A*, 375, 161
- Pellegrini E. W., Baldwin J. A., Ferland G. J., 2011, *ApJ*, 738, 34
- Peters T. et al., 2017, *MNRAS*, 466, 3293
- Pflamm-Altenburg J., Kroupa P., 2009, *MNRAS*, 397, 488
- Rahner D., Pellegrini E. W., Glover S. C. O., Klessen R. S., 2017, *MNRAS*, 470, 4453
- Sabbi E. et al., 2012, *AJ*, 37, L6
- Selman F., Melnick J., Bosch G., Terlevich R., 1999, *A&A*, 549, 532
- Silich S., Tenorio-Tagle G., 2017, *MNRAS*, 465, 1375
- Sokal K. R., Johnson K. E., Indebetouw R., Reines A. E., 2015, *AJ*, 149, 115
- Thilliez E., Maddison S. T., Hughes A., Wong T., 2014, *Publ. Astron. Soc. Aust.*, 31, e003
- Townsley L. K., Broos P. S., Feigelson E. D., Garmire G. P., Getman K. V., 2006, *AJ*, 131, 2164
- Vinkó J. et al., 2009, *ApJ*, 695, 619
- Walborn N. R., Blades J. C., 1997, *ApJS*, 112, 457
- Wang P., Li Z.-Y., Abel T., Nakamura F., 2010, *ApJ*, 709, 27
- Wareing C. J., Pittard J. M., Falle S. A. E. G., 2017, *MNRAS*, 470, 2283

This paper has been typeset from a $\text{\TeX}/\text{\LaTeX}$ file prepared by the author.

2.3 WARPFIELD 2.0: Feedback-Regulated Minimum Star Formation Efficiencies of Giant Molecular Clouds

Distribution of work: I developed the idea for this publication. I expanded the code WARPFIELD to include cooling and shell fragmentation, ran and analysed the models, created all figures, and wrote the text for the manuscript. Eric Pellegrini, Simon Glover and Ralf Klessen contributed ideas during the preparation of the manuscript and proofread and improved the text.

WARPFIELD 2.0: feedback-regulated minimum star formation efficiencies of giant molecular clouds

Daniel Rahner,¹★ Eric W. Pellegrini,¹ Simon C. O. Glover¹ and Ralf S. Klessen^{1,2}

¹Zentrum für Astronomie, Institut für Theoretische Astrophysik, Universität Heidelberg, Albert-Ueberle-Straße 2, D-69120 Heidelberg, Germany

²Interdisziplinäres Zentrum für Wissenschaftliches Rechnen, Universität Heidelberg, Im Neuenheimer Feld 205, D-69120 Heidelberg, Germany

Accepted 2018 November 29. Received 2018 November 29; in original form 2018 October 24

ABSTRACT

Star formation is an inefficient process and in general only a small fraction of the gas in a giant molecular cloud (GMC) is turned into stars. This is partly due to the negative effect of stellar feedback from young massive star clusters. Recently, we introduced a novel 1D numerical treatment of the effects of stellar feedback from young massive clusters on their natal clouds, which we named WARPFIELD. Here, we present version 2 of the WARPFIELD code, containing improved treatments of the thermal evolution of the gas and the fragmentation of the feedback-driven shell. As part of this update, we have produced new cooling and heating tables that account for the combined effects of photoionization and collisional ionization on the cooling rate, which we now make publicly available. We employ our updated version of WARPFIELD to investigate the impact of stellar feedback on GMCs with a broad range of masses and surface densities and a variety of density profiles. We show that the minimum star formation efficiency (SFE) ϵ_{\min} , i.e. the SFE above which the cloud is destroyed by feedback, is mainly set by the average cloud surface density. An SFE of 1–6 per cent is generally sufficient to destroy a GMC. We also find an SFE per free-fall time $\epsilon_{\text{ff}} \sim 0.3$ per cent, in good agreement with recent observations. Our results imply that feedback alone is sufficient to explain the low observed SFE of GMCs. Finally, we show that very massive clouds with steep density profiles – possible proxies of the giant clumps observed in galaxies at $z \approx 2$ – are more resilient to feedback than typical GMCs, with ϵ_{\min} between 1 and 12 per cent.

Key words: stars: formation – stars: winds, outflows – ISM: bubbles – ISM: clouds – H II regions – ISM: kinematics and dynamics.

1 INTRODUCTION

One of the most important questions in the study of star formation in a galactic context is what determines the star formation activity of giant molecular clouds (GMCs). Both observations and theory agree that at least part of the answer is stellar feedback (see e.g. Mac Low & Klessen 2004; McKee & Ostriker 2007; Hennebelle & Falgarone 2012; Krumholz et al. 2014; Molinari et al. 2014; Klessen & Glover 2016). When massive stars form in GMCs, they disrupt their birth environment via powerful stellar winds and the emission of ionizing radiation. After several million years, the same massive stars end their lives in supernova (SN) explosions. Often the combination of these stellar feedback processes is sufficient to overcome the gravitational attraction of the gas, and consequently the parental cloud is destroyed and further star formation inhibited (Murray, Quataert & Thompson 2010; Wang et al.

2010; Silich & Tenorio-Tagle 2013; Rahner et al. 2017). If on the other hand stellar feedback is too weak, a new generation of stars can form from swept-up cloud material that has re-collapsed or from wind material that is trapped inside the cluster (e.g. Wunsch et al. 2017; Rahner et al. 2018; Rugel et al. 2018; Szécsi & Wunsch 2018).

A convenient way to quantify how effectively the GMCs in a given galaxy form stars is via the star formation efficiency (SFE), ϵ_{SF} . Although there are various different ways to define this quantity, the simplest, and the one which we use in this paper, is to define ϵ_{SF} simply as the fraction of the gas associated with a given GMC that is turned into stars during the lifetime of that GMC. Galactic observations yield values for ϵ_{SF} that are typically in the range of 1–10 per cent for GMCs in the mass range 10^5 – $10^7 M_{\odot}$ (see e.g. Murray 2011; Vutisalchavakul, Evans & Heyer 2016), while extragalactic observations yield values consistent with the lower end of this range if one assumes that a typical GMC survives for a few dynamical times (Leroy et al. 2017; Kreckel et al. 2018).

* E-mail: daniel.rahner@uni-heidelberg.de

An obvious question is how these observationally determined values for ε_{SF} compare with the minimal SFE necessary for feedback to disrupt the cloud, ε_{min} . Analytic models by Fall, Krumholz & Matzner (2010) and Kim, Kim & Ostriker (2016) hinted at somewhat higher values for ε_{min} than what is typically observed for ε_{SF} , a result which taken at face value would suggest that feedback is *not* the process primarily responsible for destroying the clouds. These models, however, either did not include mechanical feedback (i.e. winds and SNe) or accounted for it only in a very simplistic manner, as their primary focus was radiative feedback. As shown in Rahner et al. (2017), mechanical and radiative feedback are intrinsically linked and generally both need to be included to correctly model the dynamical evolution of massive clouds under the influence of stellar feedback.

When a stellar wind is launched from a massive star it creates a hot bubble of ionized gas. If there are several massive stars in a dense cluster, these bubbles quickly overlap to form one large bubble that envelopes the entire cluster (except in cases where star formation simultaneously takes place in a large volume of the cloud which is filled by very dense ($n \gtrsim 10^5 \text{ cm}^{-3}$) gas; see Silich & Tenorio-Tagle 2017). As discussed by Castor, McCray & Weaver (1975) and Weaver et al. (1977), the wind-blown bubble consists of several distinct parts (see Fig. 1). An inner low-density region, where the wind ejecta stream freely outwards, is surrounded by a region of shocked, hot gas ($10^5\text{--}10^8 \text{ K}$), which is bounded by an inner shock radius R_1 and an outer shock radius R_2 . The material in this shocked region is mainly gas that has evaporated from the comparatively cold ($10^2\text{--}10^4 \text{ K}$) surrounding shell of swept-up interstellar medium. Beyond the shell lies material of the natal cloud that is still unaffected by the stellar feedback. The standard picture assumes that the surrounding gas is in hydrostatic equilibrium and follows a roughly constant density profile. Leakage through holes and channels in the shell and radiative cooling of shocked material gradually leads to a transition from energy-driven expansion (where the thermal pressure of the bubble dominates) to momentum-driven expansion (where ram pressure and radiation pressure dominate). In either case, pressure from winds (and later, SNe), i.e. thermal pressure of shock-heated gas at early times and ram pressure at late times, is important for determining the coupling between the radiation and the gas and hence cannot be neglected. It governs the efficiency of radiation as a feedback source.

The optical depth of the gas inside the wind bubble is small and so the radiation from the central stellar cluster can easily reach the dense shell of swept-up material (Townsend et al. 2003; Gupta et al. 2016). Those photons with energies above 13.6 eV photoionize hydrogen in this shell. Depending on the density structure and chemical composition, either the entire shell becomes ionized or only the inner layers are affected (Martínez-González, Silich & Tenorio-Tagle 2014; Rahner et al. 2017). This has strong consequences for the optical depth and the resulting photon escape fraction at different frequencies. The absorbed photons exert a pressure force on gas and dust and push the shell outwards.

In Rahner et al. (2017), we introduced a new 1D stellar feedback model, called WARPFIELD, which was designed to model the evolution of such a bubble and its impact on the surrounding ISM in a self-consistent fashion. As explained in more detail in that paper, this involves solving simultaneously for the dynamics of the bubble and surrounding dense shell and for the structure of the shell. This is necessary, as the dynamical state of the shell – specifically, the pressure acting on its inner edge – influences its structure, while its structure determines how well radiation couples to the gas, and hence how effective radiation pressure is at driving the

expansion of the shell. This version of WARPFIELD has already been applied to model massive star-forming regions such as 30 Doradus (Rahner et al. 2018) and W49 (Rugel et al. 2018). However, it has the limitation that the transition from energy-driven expansion of the bubble to momentum-driven expansion is assumed to occur instantaneously, which is a significant simplification compared to the real physics of the problem. In this paper, we present version 2 of WARPFIELD, which removes this simplification. As an example of its use, we investigate how the value of ε_{min} predicted by the code varies as a function of cloud mass and surface density, and how these values compare with observationally determined values of ε_{SF} .

The paper is structured as follows. First, in Section 2, we describe the main improvements that we have made to the model of Rahner et al. (2017). One of the major improvements is the inclusion of a detailed model for the radiative cooling of the dense gas in the shell. This gas is strongly illuminated by the central stellar cluster, and its cooling therefore cannot be treated using standard ISM cooling curves, since these typically assume collisional ionization equilibrium (CIE). Instead, we have computed new cooling curves that account for the effects of both photoionization and collisional ionization that cover the parameter space relevant for cluster wind bubbles. These are presented in Section 3. Next, in Section 4, we present several applications of the updated model. In Sections 4.1 and 4.2, we use the model to follow the evolution of feedback-driven shells which expand into GMCs with varying density profiles and compare to results from the previous version of WARPFIELD. Finally, in Section 4.3 we present our results for the minimum star formation efficiencies of GMCs over a wide parameter range. The main results of this paper are summarized in Section 5.

2 MODELLING THE DYNAMICS OF A FEEDBACK-DRIVEN BUBBLE

Let us consider a GMC with a gas mass $M_{\text{cl},0}$ that is turning some fraction of its gas into a massive star cluster in its centre with a mass of

$$M_* = \varepsilon_{\text{SF}} M_{\text{cl},0}. \quad (1)$$

The remaining gas in the cloud, whose mass is now $M_{\text{cl}} = M_{\text{cl},0} - M_*$, is illuminated and accelerated by feedback from the central star cluster. Since we are only interested in massive clusters we use STARBURST99 to model a cluster where the initial mass function (IMF) is fully sampled. We adopt a Kroupa (2001) IMF with an upper stellar mass limit of $120 M_{\odot}$. The individual stars follow Geneva evolutionary tracks for rotating stars (Ekström et al. 2012; Georgy et al. 2012). The relevant feedback properties of the star cluster are its total bolometric luminosity $L_{\text{bol}}(t)$ and its mechanical luminosity

$$L_{\text{mech}}(t) = \frac{1}{2} \dot{M}_* v_{\infty}^2. \quad (2)$$

Here, \dot{M}_* is the mass-loss rate of the cluster due to material being ejected by stellar winds or supernovae and v_{∞} is the terminal velocity of the ejecta. The forces acting on the shell are due to the thermal pressure of the hot ionized inner bubble and the momentum input from radiation. At early times, ram pressure from stellar winds and supernovae

$$F_{\text{ram}}(t) = \dot{M}_* v_{\infty}. \quad (3)$$

hits the intervening layer of shock-heated gas and only at late times, when the bubble has lost the hot material due to radiative cooling and leakage, ram pressure is directly imparted on the shell. The

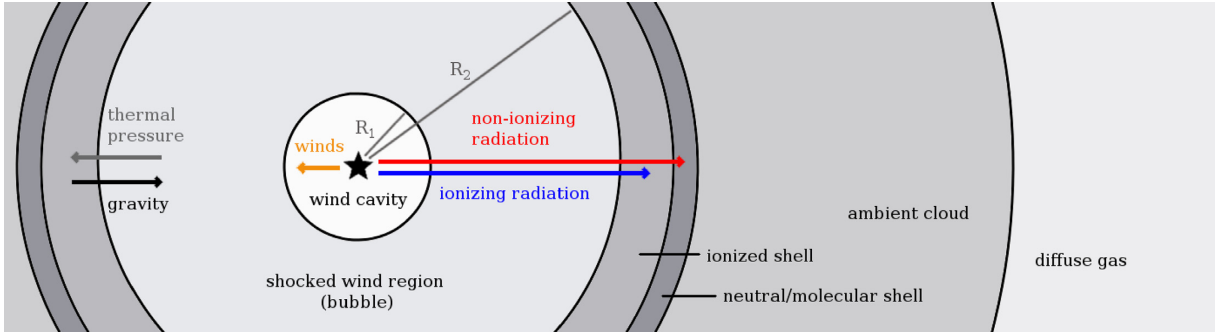


Figure 1. Schematic overview of the structure of a feedback-driven bubble expanding into a GMC during the early, energy-driven phase. The different shades of grey symbolize the density of the ISM with darker shades corresponding to denser gas. The cluster is marked by a star symbol.

opposing forces are gravity and ambient pressure which will slow down or even reverse the expansion of the shell. We consider GMCs in virial equilibrium and so we neglect ram pressure from inflow motions in the cloud for the time being.

2.1 Expansion

As feedback pushes the ISM away from the star cluster, a shell forms which consists of swept-up gas. The dynamics of the shell with radius R_2 and mass M_{sh} are given by the following set of ordinary differential equations (ODEs), the momentum and the energy equation,

$$\frac{d}{dt} (M_{\text{sh}} \dot{R}_2) = 4\pi R_2^2 (P_b - P_{\text{amb}}) - F_{\text{grav}} + F_{\text{rad}}, \quad (4)$$

$$\dot{E}_b = L_{\text{mech}} - L_{\text{cool}} - 4\pi R_2^2 \dot{R}_2 P_b, \quad (5)$$

which we explain further below. (Note that here and elsewhere, dots denote differentiation with respect to time.)

The pressure of the bubble P_b relates to its energy E_b via

$$P_b = (\gamma - 1) \frac{E_b}{\frac{4\pi}{3} (R_2^3 - R_1^3)}, \quad (6)$$

where γ is the adiabatic index. We will use $\gamma = 5/3$ as appropriate for an ideal monatomic gas. The inner shock radius R_1 is set by a pressure equilibrium between the free-streaming winds and the hot bubble, from which immediately follows the implicit equation

$$R_1 = \left[\frac{F_{\text{ram}}}{2E_b} (R_2^3 - R_1^3) \right]^{1/2}. \quad (7)$$

The ambient pressure P_{amb} outside of the shell is usually negligible in the regime we investigate here. However, if ionizing radiation from the star cluster escapes the confinement of the shell, it ionizes the ambient ISM, heating it to $T_i \sim 10^4$ K. At early times, when the immediate surrounding of the shell is very dense gas but ionizing radiation can still pass through the newly formed shell and ionize that gas, P_{amb} can be a large term. We thus use

$$P_{\text{amb}} = \begin{cases} P_0 + \frac{\mu_i}{\mu_p} n_{\text{cl}}(R_2) k T_i & \text{if } f_{\text{esc},i} > 0, \\ P_0 & \text{otherwise.} \end{cases} \quad (8)$$

Here, μ_i and μ_p are the mean molecular weights per ion and per particle, respectively ($\mu_i/\mu_p = 23/11$ for a composition with one helium atom per 10 hydrogen atoms), $n_{\text{cl}}(R_2)$ is the number density of the cloud directly outside of the shell, and $f_{\text{esc},i}$ is the escape fraction of ionizing radiation through the shell. The pressure P_0

of the ambient ISM in the absence of ionization depends on the galactic environment of the star-forming region.¹

The forces of gravity and radiation pressure are given by

$$F_{\text{grav}} = \frac{G M_{\text{sh}}}{R_2^2} \left(M_* + \frac{M_{\text{sh}}}{2} \right), \quad (9)$$

$$F_{\text{rad}} = f_{\text{abs}} \frac{L_{\text{bol}}}{c} (1 + \tau_{\text{IR}}), \quad (10)$$

where c is the speed of light. The fraction of radiation that is absorbed by the shell f_{abs} and its optical depth in the infrared τ_{IR} are determined using a hydrostatic approximation for the shell (see Rahner et al. 2017).

In the previous version of WARPFIELD, hereafter WARPFIELD1, we neglected the energy lost to cooling until the age of the system reached the cooling time t_{cool} and assumed that all the energy was lost thereafter. The cooling time is defined as

$$t_{\text{cool}} = 16 \text{ Myr} \times (Z/Z_{\odot})^{-35/22} n_{\text{cl}}^{-8/11} L_{38}^{3/11}, \quad (11)$$

with Z being the metallicity, n_{cl} the cloud density in cm^{-3} , and $L_{38} = L_{\text{mech}}/(10^{38} \text{ erg s}^{-1})$ (Mac Low & McCray 1988). However, equation (11) only holds for constant density profiles, and even then ignoring cooling when $t < t_{\text{cool}}$ and assuming immediate loss of all energy for $t \geq t_{\text{cool}}$ is a major simplification (Gupta et al. 2016). Here, instead, we couple the energy loss term due to cooling L_{cool} to the energy equation. The loss term is given by

$$L_{\text{cool}} = 4\pi \int_{R_1}^{R_2} \frac{dU}{dt} \Big|_{\text{rad}} r^2 dr, \quad (12)$$

where U is the internal energy density and where the integration runs from the inner shock at a radius R_1 to the outer radius of the bubble R_2 , which is also the radius of the thin shell. The rate of change of the radiative component of the internal energy density is given by

$$\begin{aligned} \frac{dU}{dt} \Big|_{\text{rad}} &= n n_e [\Gamma(T, \dots) - \Lambda(T, \dots)] \\ &= -n n_e \Lambda_{\text{net}}(T, \dots), \end{aligned} \quad (13)$$

where n and n_e are the ion and electron density, and Γ and Λ are the heating and cooling functions. We have used the dots to indicate

¹The value of P_0 should be adjusted to a value appropriate for the studied environment. For the purpose of the results presented in Section 4, we have taken P_0 to be negligible and set it to 0. However, this would not be an appropriate choice for studies of clusters in e.g. the Galactic Centre or a starburst galaxy.

that in general Γ and Λ are dependent on many parameters (and not just T) as we discuss in Section 3. Assuming that the pressure inside the bubble is independent of radius r and neglecting magnetic fields, we have

$$n(t, r) = \frac{\mu_p}{\mu_i} \frac{P_b(t)}{kT(t, r)}, \quad (14)$$

where again r runs from R_1 to R_2 .

Weaver et al. (1977) describes a procedure to calculate the temperature profile inside the bubble when thermal conduction between bubble and shell is taken into account. In short, T is a function (which is described in detail in Appendix A) of $t, r, R_2, \dot{R}_2, E_b, \dot{E}_b$, and \dot{T}_ξ , where T_ξ is the temperature measured at some fixed scaled radius inside the bubble, e.g. $\xi \equiv r/R_2 = 0.9$, i.e.

$$T_\xi = T(t, r = \xi R_2, R_2, \dot{R}_2, E_b, \dot{E}_b, \dot{T}_\xi). \quad (15)$$

It becomes clear that inserting T into equations (12) and (5) leads to \dot{E}_b being given only implicitly. Furthermore, \dot{T}_ξ is also only given implicitly by equation (15). In order to solve for the dynamical evolution of the shell it is thus necessary not only to augment the ODE system by equation (15), but in addition – due to the implicit nature of equations (5) and (15) – for each time-step a root finding algorithm must be used to find the values of \dot{E}_b and \dot{T}_ξ so that equations (5) and (15) are simultaneously satisfied. Such a scheme is implemented in the version of WARPFIELD presented here.

The system of ODEs which fully describes the dynamics of bubble and shell, equations (4), (5), and (15), is stiff. In order to solve it, WARPFIELD makes use of the SCIPY routine SOLVE_IVP which wraps around the FORTRAN solver LSODA (Hindmarsh 1983; Petzold 1983).

2.2 Stalling

2.2.1 Shell fragmentation

Cooling is not the only way for the bubble to lose energy. As soon as the shell surrounding the bubble fragments, the hot gas can leak out, introducing a second loss term. This phase of leakage is hard to describe analytically (cf. Harper-Clark & Murray 2009). The speed with which the energy leaks out is set by both the pressure inside the bubble and the size of the holes in the shell, which both vary as function of time. Furthermore, the assumption of pressure equilibrium used for the calculation of $T(r)$ becomes invalid and the previously outlined method to calculate L_{cool} breaks down.

Here, we employ a simplified treatment of leakage but note that this a weakness of the model which we plan to address in future work. In order to prevent leakage when the bubble is still deeply embedded in the cloud, we allow this process to occur only when the shell radius has reached 10 per cent of the cloud radius, i.e.

$$R_2 \geq 0.1 R_{\text{cl}}. \quad (16)$$

In our model, fragmentation occurs when the above, necessary condition as well as one of the following additional conditions is fulfilled:

(i) **Gravitational fragmentation** occurs when inside a region cut from the surface of the shell the combined kinetic divergent energy due to stretching as it expands and the thermal energy are outweighed by the gravitational binding energy of that region (Ostriker & Cowie 1981; McCray & Kafatos 1987). This is the case when

$$0.67 \frac{3GM_{\text{sh}}}{4\pi \dot{R}_2 R_2 c_{s,\text{sh}}} > 1. \quad (17)$$

Here, $c_{s,\text{sh}}$ is the lowest sound speed of the shell (typically 1 km s^{-1} , unless the shell is fully ionized).

(ii) **Rayleigh–Taylor (RT) instabilities** occur when a dense fluid is accelerated with respect to a fluid of lower density. As the shell decelerates while it sweeps up the cloud, radiation pressure counteracts the formation of RT instabilities. However, when the strength of feedback increases during the Wolf–Rayet phase and after the first SN explosions occur, the shell can accelerate again (if the density of the surrounding material is low enough). So, we take

$$\ddot{R}_2 > 0, \quad (18)$$

as the criterion for the occurrence of RT instabilities and shell fragmentation.

(iii) **Density inhomogeneities** are hard to model in a 1D code. As in Rahner et al. (2017) we assume that the lower density parts of the shell are opened up to feedback channels as soon as the parental cloud is swept up completely, i.e.

$$R_2 > R_{\text{cl}}. \quad (19)$$

However, we note that this will depend on the structural details of the cloud which is being modelled.

Thermal pressure-driven, decelerating shells expanding into ambient ISM are also thought to be prone to the Vishniac instability (Vishniac 1983). Ram pressure of the swept-up gas is always oriented antiparallel to the travel direction of the shell, i.e. radially inwards, while thermal pressure from the hot interior is always normal to the surface. When the shell is slightly perturbed, ram pressure and thermal pressure are not antiparallel any more introducing a net tangential force that causes shell material to accumulate in parts of the shell that lag behind. Here, we ignore the Vishniac instability for two reasons. First, as Michaut et al. (2012) point out, in hydrodynamical simulations fragmentation does not always occur as suggested by the theory of Vishniac (1983) and Ryu & Vishniac (1987) owing to several idealized assumptions about the shell. Secondly, the classic theory (as well as simulations by Michaut et al. 2012) ignores the effect of radiation pressure. When material accumulates in a part of the shell which lags behind, this denser part would be accelerated more than the rest of the shell as the number of absorbed ionizing photons per unit mass scales with density. Such an acceleration gradient would counteract the formation of Vishniac instabilities and we therefore ignore them here.

The fragmentation of the shell via gravitational instabilities, RT instabilities or density inhomogeneities at a time t_{frag} marks the end of the energy-driven expansion. Starting at $t = t_{\text{frag}}$, we remove the energy from the bubble over a sound crossing time

$$\dot{E}_b = - \frac{E_b(t_{\text{frag}})}{t_{s,\text{cr}}(t_{\text{frag}})} \quad (20)$$

with

$$t_{s,\text{cr}} = \frac{R_2}{c_{s,b}} \quad (21)$$

where $c_{s,b}$ is the sound speed corresponding to the volume-averaged temperature of the bubble. Usually, t_{frag} is of the order of $0.1 - 1 \text{ Myr}$ for GMCs investigated here (see Section 4.3).

During this phase of energy leakage, equation (20) replaces equation (5). It marks the transition between the energy-driven and momentum-driven phases and lasts until all energy has been removed from the bubble, i.e. $E_b = 0$, which is the case at $t = t_{\text{frag}} + t_{s,\text{cr}}(t_{\text{frag}})$. Afterwards, ram pressure from winds and SNe hits the shell without an intervening layer of shocked gas. From then

on, the dynamical evolution of the shell is controlled solely by the momentum equation with $4\pi R_2^2 P_b = F_{\text{ram}}$.

Fragmentation of the shell as discussed above can induce renewed star formation activity in the dense shell clumps (Elmegreen & Lada 1977; Tenorio-Tagle et al. 2003; Dale et al. 2009; Recchi et al. 2017). For the time being, we ignore star formation at this point and instead consider star formation when gas flows back towards the first generation of stars as we discuss below.

2.3 Collapse and sequential star formation

Should at any point in time the inward directed terms in equation (4) outweigh the outward directed terms, the shell loses momentum. In particular, this can happen as the bubble's energy is lost via cooling or leakage and its pressure drops dramatically. The pressure also drops soon after the death of the most massive stars when even the pressure from SN explosions of the slightly less massive stars is not sufficient to replace the missing stellar wind feedback. This is the case when the cluster is approximately 4–5 Myr old. If the shell starts to collapse back on to the central star cluster, we keep the shell mass constant and follow the evolution until the shell radius has shrunk to the 'collapse radius' $R_{\text{coll}} = 1$ pc. Collisions between fragmented clumps of the shell will induce the birth of new stars and so we take the time of re-collapse to mark the time t_{SF} of a new star formation event. Sequential star formation was already implemented in WARPFIELD1 and has been used to model multiple stellar populations in 30 Dor (Rahner et al. 2018). In the more general treatment present in WARPFIELD2, a new star cluster forms according to one of the following two prescriptions:

(i) The new star cluster forms with the same SFE ε_{SF} as the first cluster. Since the cloud is less massive than it was before the previous cluster formed the new cluster will be less massive as well:

$$M_{*,i} = M_{*,i-1}(1 - \varepsilon_{\text{SF}}), \quad (22)$$

where $M_{*,i}$ denotes the cluster mass of the i th generation.

(ii) We form the next star cluster with a fixed SFE per free-fall time ε_{ff} (see Krumholz & McKee 2005; Krumholz & Tan 2007), where we use the free-fall time t_{ff} which corresponds to the mean density of the cloud $\bar{\rho}$. The first cluster forms with $\varepsilon_{\text{SF},1} = \varepsilon_{\text{ff}}$. Each subsequent SFE is given by

$$\varepsilon_{\text{SF},i} = \frac{t_{\text{SF},i} - t_{\text{SF},i-1}}{t_{\text{ff}}} \varepsilon_{\text{ff}}. \quad (23)$$

This also allows the later clusters to form with higher masses than the previous cluster if the time difference between two star formation events is larger than the free-fall time of the cloud.

In either case, at the time a new star cluster forms, we reset the cloud structure and distribute the ISM according to the same density profile as before. The gas is now subject to feedback $\mathcal{F} \equiv \{L_{\text{bol}}, L_{\text{mech}}, F_{\text{ram}}\}$ originating from several generations of stars

$$\mathcal{F}(t) = \sum_{i=1}^{N_{\text{gen}}(t)} \mathcal{F}_i(M_{*,i}, t - t_{\text{SF},i}), \quad (24)$$

where $N_{\text{gen}}(t)$ is the number of cluster generations present at time t . Again, the expansion is initially driven mostly by energy and later, after the hot gas has cooled and leaked out of the bubble, by momentum. Should feedback again be insufficient to overcome gravity, another cluster forms and so on, until the shell dissolves. We regard the shell as dissolved when its maximum density has

dropped below 1 cm^{-3} for a duration of at least 1 Myr or when it has expanded to 1 kpc.² The age of the cloud when it dissolves marks its lifetime t_{life} . We also stop the simulation when 30 Myr have passed, which corresponds to lifetime estimates of GMCs in the Large Magellanic Cloud (LMC; Kawamura et al. 2009).

3 COOLING

The wind bubble is of double importance for the evolution of the shell. The overpressured bubble not only pushes the ISM outwards, but also sets the density at the inner shell boundary, thus determining the coupling between radiation and the shell (see equation 10 and Rahner et al. 2017 for more details). How the pressure of the bubble changes as a function of time depends on the amount of energy lost via radiative cooling. This in turn is dependent on the temperature profile of the bubble and on the net cooling function Λ_{net} (see equations 12 and 13). Therefore, an accurate treatment of cooling is of paramount importance to solving the evolution of the H II region.

Given a known set of elemental abundances in the gas – which in our case are fixed once we specify the metallicity – the value of Λ_{net} depends primarily on two things: the temperature of the gas and its overall ionization balance (i.e. for each element, what fraction is neutral, what fraction is singly ionized, etc.). In the simple case of CIE, the ionization balance itself depends solely on the temperature,³ and so Λ_{net} to a good approximation depends only on T . However, in our case, the bubble sits in close proximity to the star cluster, whose radiation is not shielded by the intervening ISM. Consequently, the influence of ionizing radiation from the star cluster is substantial and the gas is often not in CIE. In this case, the ionization balance, and hence the cooling rate, is determined by four parameters: the gas temperature T , the gas density n , the flux of ionizing photons Φ_i , and the age of the stellar cluster t_{age} . The temperature controls the collisional ionization and radiative recombination rate coefficients, as before, while the density and ionizing photon flux determine the relative importance of radiative recombination and photoionization. The age of the stellar cluster is important as it determines the spectral shape of the incident radiation, and this in turn plays a major role in controlling the impact that it has on the ionization balance of the gas. For example, if we are interested in the photoionization of hydrogen, which requires photons with energies ≥ 13.6 eV, or of metals with ionization potentials below that of hydrogen, then radiation from a large population of older B stars can be competitive with that from a small number of younger, brighter O stars. On the other hand, the production of O^{2+} , which has an ionization potential of 35 eV, requires photons from stars with effective temperatures above 36 000 K and hence is dominated by emission from O stars.

To deal with this complexity, we use CLOUDY (Ferland et al. 2017) to estimate Λ_{net} for a variety of different values of the main controlling parameters. In the simulations presented here, we consider two different metallicities, $Z = 0.014 = Z_{\odot}$ and $Z = 0.002 = 1/7 Z_{\odot}$, and a range of values for the gas temperature T , the number density n , the incident flux of ionizing photons Φ_i , and the age of the stellar cluster t_{age} . The range of values considered for each parameter is summarized in Table 1. Further details of the CLOUDY models are

²At this point, we assume galactic shear to have disrupted the cloud.

³There is no density dependence because both collisional ionization and radiative recombination have n^2 dependencies on density, and so changes in the density affect both equally, leaving the ionization balance unaffected.

Table 1. Overview of cooling grid. For each model the net cooling function Λ_{net} has been determined with CLOUDY. T : temperature, n : number density, $\Phi_{i,\text{cgs}}$: number flux of ionizing photons in $\text{cm}^{-2} \text{s}^{-1}$, t_{age} : age of the star cluster, Z : metallicity (we assume $Z_{\odot} = 0.014$).

	Min	Max	Step size	Remark
$\log T$ (K)	3.5	5.5	0.1	Higher T : CIE
$\log n$ (cm^{-3})	-4	12	0.5	
$\log \Phi_{i,\text{cgs}}$	0	21	1	With cosmic rays
t_{age} (Myr)	1	5	1	Also $t_{\text{age}} = 10$ Myr
Z (Z_{\odot})	1/7	1	6/7	H II region abundances

provided in Appendix B. We have made the cooling curves themselves publicly available, and information on how to access them is also given in Appendix B.

We note that the basic idea behind this approach is not new. For example, a similar, but much larger grid of cooling curves has been published by Gnedin & Hollon (2012). However, in that work the stellar component of the considered spectral energy distributions was chosen to represent the interstellar radiation field of the Milky Way (MW), i.e. mainly old stars that evolved with a continuous star formation history over the course of 1 Gyr. This is very different to what is necessary for our purpose where we need the spectrum of a young star cluster in which all stars are coeval or are born in only a few distinct populations separated by no more than a few tens of Myr, such as Sandage-96, 30 Doradus, and the Orion Nebula Cluster (Vinkó et al. 2009; Sabbi et al. 2012; Beccari et al. 2017). Similarly, the tabulated cooling curves bundled with the GRACKLE chemistry code (Smith et al. 2017) or computed by Wiersma, Schaye & Smith (2009) or Emerick, Bryan & Mac Low (2019) account for both photoionization and collisional ionization, but consider radiation fields designed to represent the extragalactic background, rather than the spectrum of a young massive cluster, making them unsuitable for our purposes.

The parameter space covered by our models has been tailored to our regime of interest, namely shells driven by hot bubbles inside dense GMCs. There is thus no need to calculate the cooling function for hot gas illuminated by a cluster older than 10 Myr, as the H II region around such a cluster will no longer be expanding in the energy-driven limit. The temperature of the ISM which is directly illuminated by such a cluster will be constant at $\sim 10^4$ K (see Section 2.2.1). We also neglect shielding of radiation inside the bubble (but not inside the shell). This is well justified because the column density of the bubble is low, and the cooling curves provided are valid in the optically thin limit. For the stars, we use Pauldrach/Hillier atmospheres, i.e. WM-BASIC models (Pauldrach, Hoffmann & Lennon 2001) when the star cluster is younger than 3 Myr and CMFGEN models (Hillier & Miller 1998) thereafter. The elemental composition of the ISM has been chosen to represent that observed in H II regions (see table 7.2 in Ferland 2013). At $Z = 0.002$ we use the same ISM composition as at $Z = 0.014$ (solar) but scale all metal abundances down by a factor 1/7.

For the dynamical evolution of the system, we use the presented grid as a lookup table and linearly interpolate Λ_{net} between grid points. For $T > 10^{5.5}$ K, CIE is a reasonable assumption and in this temperature range we employ tabulated cooling curves by Gnat & Ferland (2012) for $Z = 0.014$ and Sutherland & Dopita (1993) for $Z = 0.002$. In the case of multiple generations of star clusters (see Section 2.3), we use the spectral shape of the youngest cluster but scale it by the total flux of ionizing photons. For rotating stars this is a reasonable approximation as the spectral shape of the ionizing

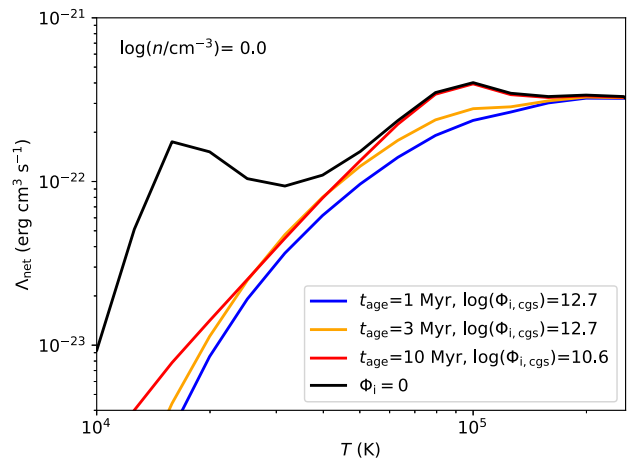


Figure 2. Net cooling curves for solar metallicity (with elemental composition appropriate for H II regions) and a particle density of 1 cm^{-3} . Cooling curves are shown by different colours for different ages t_{age} of the illuminating star cluster ($M_* = 10^6 M_{\odot}$). The ionizing photon flux ($\Phi_{i,\text{cgs}} = \Phi_i / (\text{cm}^{-2} \text{s}^{-1})$) has been calculated according to the time evolution of the cluster and at a distance of 10 pc.

part of the spectrum of an older cluster only significantly differs from that of a very young cluster when the emission rate of ionizing photons has dropped by more than one order of magnitude.⁴

An example of non-CIE cooling curves at a density of $n = 1 \text{ cm}^{-3}$ is shown in Fig. 2. At temperatures between 10^4 and 4×10^4 K, we see a large difference between the pure CIE cooling curve (black line) and the cooling curves for models with large ionizing fluxes, even for a relatively old stellar cluster. This difference is driven largely by the behaviour of the hydrogen, which dominates the CIE cooling rate at low temperatures. In the models with non-zero Φ_i , the hydrogen is far more ionized at low T than in the pure CIE run, and consequently the contribution made by Lyman α cooling to the total cooling rate is much smaller (cf. Efstathiou 1992), with the bulk of the cooling now coming from dust which has evaporated from the shell into the bubble, bremsstrahlung, and various emission lines of oxygen and carbon. A similar but less pronounced effect is visible close to 10^5 K, driven by changes in the He^+ abundance in the models with low t_{age} . Notably, in the model with $t_{\text{age}} = 10$ Myr, the cooling curve at this temperature is the same as in the CIE case, as a cluster of this age produces very few photons capable of ionizing He^+ to He^{2+} . It is also apparent that above a few times 10^5 K, the ionizing flux makes no difference to the cooling rate, since at these temperatures collisional ionization produces a more highly ionized state than can be produced by photoionization by stars. Further examples of cooling curves drawn from our set of models can be found in Appendix B and in the online data.

We do not treat in detail heating and cooling in the feedback-driven shell but instead assume that the temperatures of the ionized and neutral phase are 10^4 and 10^2 K, respectively. For the purpose of determining the approximate coupling between radiation and the ISM in the shell, which is necessary to determine the effect of radiation pressure, this is sufficient (for details see Rahner et al. 2017). For the modelling of emission lines, however, a detailed treatment of the chemistry inside the shell is indispensable. This can be carried out in a post-processing step, as we explore in detail elsewhere (Pellegrini et al. in preparation).

⁴We note that this does not hold true for non-rotating stars.

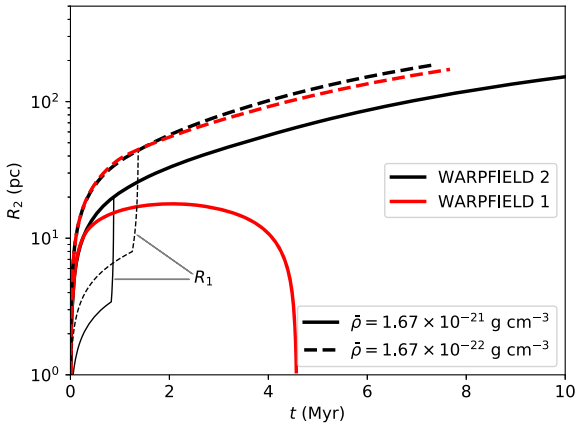


Figure 3. Comparison between the evolution of the shell radius R_2 for models with $M_{\text{cl},0} = 10^6 M_{\odot}$, $\varepsilon_{\text{SF}} = 0.05$, and two different mean densities, simulated with WARPFIELD1 (Rahner et al. 2017) and WARPFIELD2 (this paper). Thin lines show the evolution of the inner shock radius R_1 (only for WARPFIELD2 because WARPFIELD1 does not track R_1). Only the evolution of the first 10 Myr is shown even though the shell in a cloud with $\bar{\rho} = 1.67 \times 10^{-21} \text{ g cm}^{-3}$ survives until 30 Myr reaching a radius of 400 pc. The clouds initially have a constant density profile ($\alpha = 0$).

4 RESULTS

4.1 Comparison to WARPFIELD1

With respect to the previously published version of WARPFIELD (Rahner et al. 2017), hereafter referred to as WARPFIELD1, several important improvements have been made, as discussed in the previous sections. In short, cooling and energy leakage of the hot bubble are now treated in a less simplified manner: In WARPFIELD1 cooling was treated as removing all energy at once when $t = t_{\text{cool}}$ and fragmentation of the shell was only considered when $R_2 = R_{\text{cl}}$. Even though we now allow the shell to fragment earlier due to RT or gravitational instabilities, radiative cooling is less efficient now in decreasing the thermal pressure of the bubble. While a large percentage of the energy is still radiated away, the retained energy is still sufficient to drive the expansion significantly more than pure momentum-driving would. Also, while the high pressure of the wind bubble is retained, the density of the shell remains high (cf. Rahner et al. 2017) and more ionizing radiation is absorbed by the shell, increasing the effect of radiation pressure as a source of feedback. The net result of these improvements is that in general stellar feedback is somewhat more efficient in pushing the gas outward and destroying the cloud.

Two examples where this can be seen are presented in Fig. 3. In cases where ε_{SF} is close to the minimum SFE ε_{min} – which we here define as the lowest SFE that is needed to destroy the cloud via stellar feedback after a *single* star formation event – the ‘new’, somewhat stronger feedback can make the difference between continued expansion of the feedback-driven shell and a re-collapse of the ISM on to the star cluster. In cases where ε_{SF} is well above ε_{min} , the effect is a somewhat faster expansion and destruction of the cloud but overall the difference between the two versions of WARPFIELD is small (see dashed lines in Fig. 3 where the shells dissolve at a similar size and age). Typically, the minimum star formation efficiencies we obtain with WARPFIELD2 are a few per cent lower than those presented in Rahner et al. (2017), as will be shown in Section 4.3.

Fig. 3 also shows the evolution of the inner shock radius R_1 for the runs with WARPFIELD2. The previous version, WARPFIELD1, does not explicitly track the evolution of the inner shock. We note that R_1 increases with time as the thermal pressure of the bubble drops. The inner shock is only fully pushed into the shell (in which case $R_1 = R_2$) when the shell has fragmented and the hot material of the shock layer has leaked out through holes. In cases where shell fragmentation occurs late, energy-loss via strong cooling also causes R_1 to rapidly increase. However, the intervening shock layer only fully disappears after the shell has fragmented.

4.2 Variations in cloud density profile

The other major difference compared to WARPFIELD1 is our treatment of the density distribution of the cloud. In WARPFIELD1, this was assumed to be uniform, necessitated by our use of an analytic expression (Bisnovatyi-Kogan & Silich 1995) for the early, energy-driven phase, while in WARPFIELD2 we can treat any spherically symmetric density profile. In the following analysis, we consider not only homogeneous GMCs but also GMCs where the density ρ_{cl} follows a power-law profile with a homogeneous inner core:

$$\rho_{\text{cl}}(R) = \begin{cases} \rho_0 & \text{if } R \leq R_0 \\ \rho_0 \left(\frac{R}{R_0}\right)^{\alpha} & \text{if } R_0 < R \leq R_{\text{cl}} \\ \rho_{\text{amb}} & \text{if } R > R_{\text{cl}}. \end{cases} \quad (25)$$

We limit ourselves to the range $-2 \leq \alpha \leq 0$, where the case $\alpha = 0$ corresponds to homogeneous clouds, while the steep density profile $\alpha = -2$ corresponds to so-called singular isothermal spheres. Such systems are interesting, because they are commonly encountered in the study of isothermal, self-gravitating systems (Larson 1969; Penston 1969; Shu 1977; Whitworth & Summers 1985). Clumps and cores forming at the stagnation points of large-scale convergent flows in the turbulent galactic ISM (see e.g. McKee & Ostriker 2007; Klessen & Glover 2016, and references therein) typically have density profiles that mimic Bonnor–Ebert spheres (Ebert 1955; Bonnor 1956) with a flat inner core and a smooth transition to an approximate R^{-2} radial density profile at larger radii (Ballesteros-Paredes, Klessen & Vázquez-Semadeni 2003; Klessen et al. 2005), and hence for our purposes may be well approximated by an $\alpha = -2$ profile. This is certainly the preferred density structure for low-mass prestellar cores that will eventually form individual stars (e.g. Bacmann et al. 2000; Alves, Lada & Lada 2001; Könyves et al. 2010) and also seems applicable to high-mass systems (Motte, Bontemps & Louvet 2018). Once the central cluster has formed, the density profile is best fit by a power law with slope $\alpha = -1.5$ (e.g. Oginō, Tomisaka & Nakamura 1999) in the infalling envelope. Observations of molecular cloud clumps with embedded star clusters indicate exponents in the range $-2 \leq \alpha \leq -1$ (e.g. Beuther et al. 2002). For even higher masses, numerical simulations of star-forming giant clumps at redshift $z \approx 2$ also report values of $\alpha \approx -2$ (Ceverino et al. 2012). Because of these large variations, and also to account for the fact that the presence of turbulence can lead to significant deviations from simple analytic models and that the average density profile of the GMC as a whole may differ from that of the dense cores and clumps within it, we investigate a range of possible slopes and study the impact of this parameter on the dynamical evolution of the system and on the resulting minimum SFE, ε_{min} . In the suite of models presented here, we will concentrate on power-law exponents $\alpha = 0, -1, -1.5, -2$ and consider a range of average cloud densities $\bar{\rho}$.

We set the core density to $\rho_0 = 1.67 \times 10^{-19} \text{ g cm}^{-3}$, except in the case of $\alpha = 0$, where $\rho_0 = \bar{\rho}$. The value for the core radius R_0

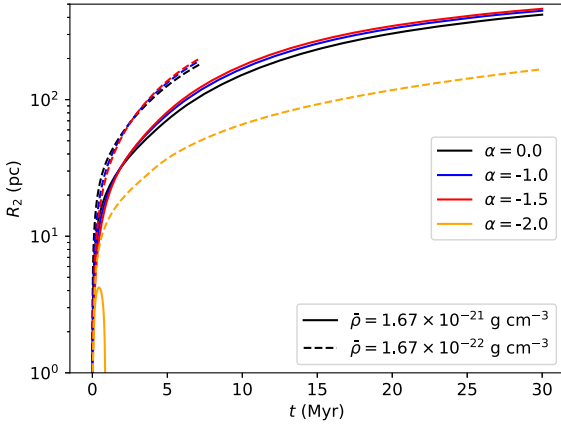


Figure 4. Evolution of the shell radius for different density slopes (colours) and initial average densities (line style). The models have $M_{\text{cl},0} = 10^6 M_{\odot}$, $\varepsilon_{\text{SF}} = 0.05$.

follows from the condition that

$$M_{\text{cl}} = 4\pi \int_0^{R_{\text{cl}}} R^2 \rho_{\text{cl}}(R) dR. \quad (26)$$

while the cloud radius R_{cl} is set by the cloud mass and the average density. The density of the ambient ISM ρ_{amb} (i.e. the ISM beyond the cloud radius) is set to $1.67 \times 10^{-25} \text{ g cm}^{-3}$ but changing this value by an order of magnitude has little impact on the eventual fate of the GMC (Rahner et al. 2017). Each model is thus uniquely specified by $M_{\text{cl},0}$, ε_{SF} , $\bar{\rho}$, α , and Z (although here we only consider $Z = Z_{\odot}$).

In Fig. 4, we present the evolution of clouds with $\bar{\rho} = 1.67 \times 10^{-21} \text{ g cm}^{-3}$ and $\bar{\rho} = 1.67 \times 10^{-22} \text{ g cm}^{-3}$, and different density slopes. Whereas the behaviour of clouds with $-1.5 \leq \alpha \leq 0$ is very similar, clouds with even steeper density profiles are considerably harder to destroy with stellar feedback. This is partly due to the more negative gravitational binding energy of dense clouds which is defined as

$$E_{\text{bind}} \equiv -G \int_{M_{\text{cl},0}} \frac{M(r)}{r} dm. \quad (27)$$

For the density profiles investigated here ($\alpha \geq -2$), this becomes

$$E_{\text{bind}} = - \left[U_0 + \frac{4\pi\rho_0 G}{R_0^\alpha} (u_1 + u_2) \right], \quad (28)$$

with

$$U_0 = 2\pi\rho_0 G M_* R_0^2 + \frac{16\pi^2}{15} \rho_0^2 G R_0^5, \quad (29)$$

$$u_1 = \left(M_0 - \frac{4\pi\rho_0}{3+\alpha} R_0^3 \right) \times \begin{cases} \frac{R_{\text{cl}}^{2+\alpha} - R_0^{2+\alpha}}{2+\alpha}, & \text{if } \alpha \neq -2 \\ \ln \left(\frac{R_{\text{cl}}}{R_0} \right), & \text{if } \alpha = -2, \end{cases} \quad (30)$$

$$u_2 = \frac{4\pi\rho_0}{R_0^\alpha (3+\alpha)} \frac{R_{\text{cl}}^{5+2\alpha} - R_0^{5+2\alpha}}{5+2\alpha}. \quad (31)$$

Here, M_0 is the sum of the masses of the core and the star cluster. Besides this obvious effect of making the material harder to unbind, the amount of cooling is also affected. As the bubble expands more slowly in a dense cloud, the density of the material accumulating inside the bubble is higher, leading to stronger radiative cooling and

thus a further decrease in the efficiency of energy-driven mechanical feedback.

4.3 Minimum star formation efficiencies

Most GMCs in the MW and other nearby galaxies have average surface densities in the range $10 \leq \bar{\Sigma} \leq 1000 M_{\odot} \text{ pc}^{-2}$ (Heyer et al. 2009; Hughes et al. 2010; Miura et al. 2012; Hughes et al. 2013; Colombo et al. 2014; Miville-Deschênes et al. 2017). If we assume that GMCs are gravitationally bound and that they continue forming stars until completely disrupted by stellar feedback, then we can use WARPFIELD to find the minimum star formation efficiencies of the GMCs as a function of their mass and surface density, i.e. the smallest possible fraction of their mass that they must convert into stars in order for them to be completely disrupted. In this section, we present results for clouds with surface densities in the observed range and cloud masses in the range $10^5 \leq M_{\text{cl},0} \leq 10^7 M_{\odot}$.

We sample this regime by varying $M_{\text{cl},0}$ and $\bar{\rho}$ with steps of $\Delta(\log M_{\text{cl},0}) = \Delta(\log \bar{\rho}) = 0.2$. The average surface density is related to average mass densities via

$$\frac{4\pi}{3} R_{\text{cl}}^3 \bar{\rho} = M_{\text{cl}} = \pi R_{\text{cl}}^2 \bar{\Sigma}. \quad (32)$$

We also consider several different density slopes, $\alpha = 0, -1, -1.5$, and -2 . For each set of input parameters we determine ε_{min} to a precision of 1 per cent, rounded up.

The derived minimum star formation efficiencies for different density slopes are presented in Fig. 5. As shown, for fixed α it is good first approximation to treat ε_{min} as independent of M_{cl} , when assuming $\bar{\Sigma}$ does not, or only very weakly, depend on the cloud mass as implied by the third Larson relation (Larson 1981). Instead, the minimum SFE is mainly determined by $\bar{\Sigma}$, as already argued by Fall et al. (2010). We note that the values for ε_{min} calculated here are lower than those derived in Kim et al. (2016), who ignore mechanical feedback, and Fall et al. (2010), who regard only comparatively small contributions by winds, SNe and indirect radiation pressure to the total feedback budget as reasonable. The presented minimum star formation efficiencies are also lower than the values calculated in Rahner et al. (2017) using WARPFIELD1 owing to the change in our treatment of cooling of the wind bubble and a sampling of the IMF up to $120 M_{\odot}$.⁵ We also note, that if – in contradiction to the third Larson relation – more massive clouds also have a significantly higher mean surface density (e.g. Miura et al. 2012; Colombo et al. 2014, see also Fig. 5), we expect the SFE in massive GMCs to be higher than in low-mass GMCs (see also Rahner et al. 2017).

Even though in our model, star formation occurs in a short burst⁶ and is not spread out over a long time period, we can approximate a SFE per free-fall time (see Krumholz & McKee 2005) by using the lifetime t_{life} of the cloud as the relevant time-scale, i.e.

$$\varepsilon_{\text{ff}} \approx \varepsilon_{\text{SF}} \frac{t_{\text{ff}}}{t_{\text{life}}}, \quad (33)$$

where t_{ff} is calculated from the average cloud density. If we assume that clouds form stars with a total SFE of $\varepsilon_{\text{SF}} = \varepsilon_{\text{min}}$, most of our models have $\varepsilon_{\text{ff}} \sim 0.3$ per cent in good agreement with observations on GMC scales (Leroy et al. 2017).

⁵In Rahner et al. (2017), $100 M_{\odot}$ was used as the upper mass cut-off of the ISM, i.e. feedback from the most massive stars was missing.

⁶In the case of re-collapse, we instead have several distinct bursts, but we do not discuss this case here.

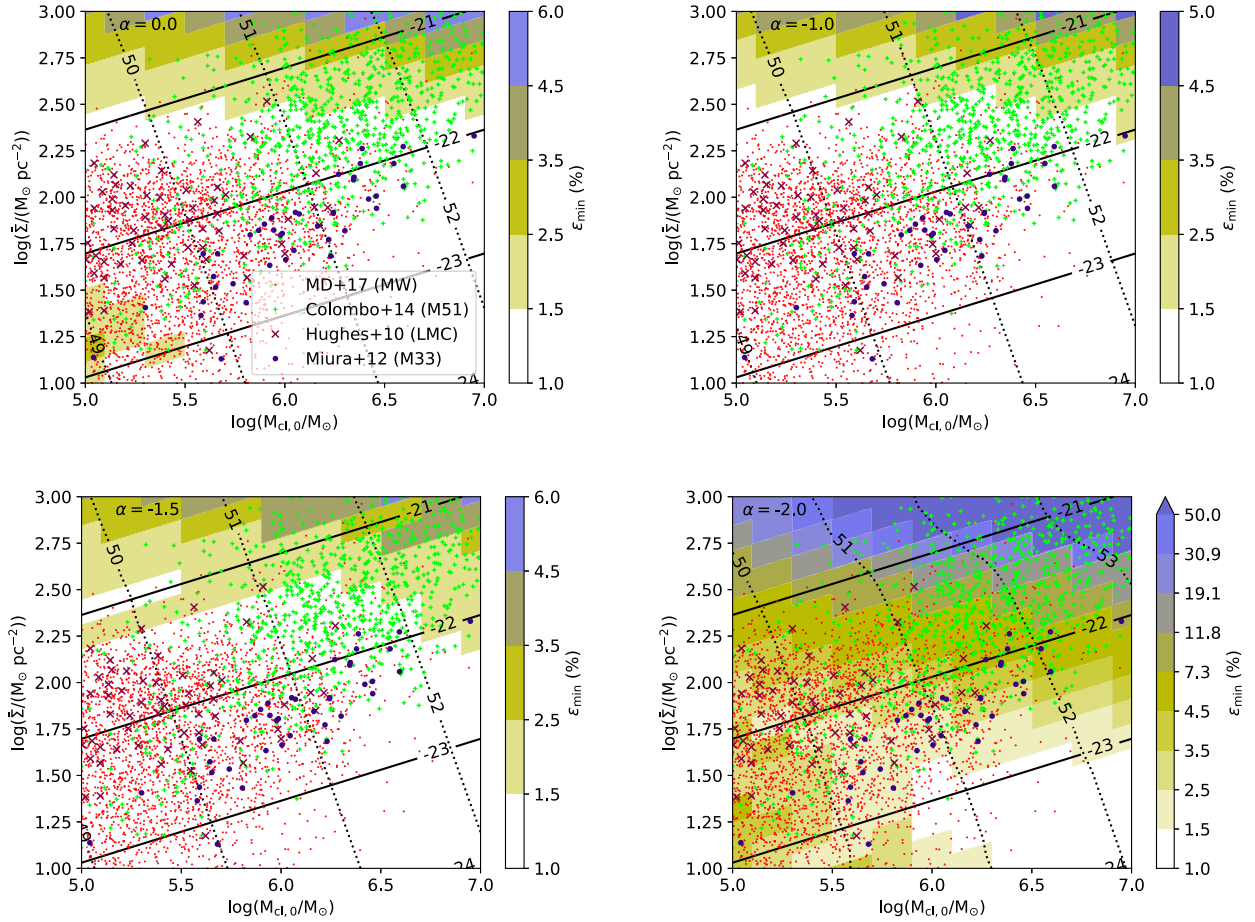


Figure 5. Minimum star formation efficiencies ε_{\min} for different initial density slopes. Markers show observed GMCs in the MW (Miville-Deschênes, Murray & Lee 2017), M51 (Colombo et al. 2014), the LMC (Hughes et al. 2010), and M33 (Miura et al. 2012). Black solid lines show $\log \bar{\rho}$ in g cm^{-3} , black dotted lines show $\log(-E_{\text{bind}})$ in erg. The sawtooth pattern is caused by our sampling of the parameter space (we use regular grids in $\log M_{\text{cl},0}$ and $\log \bar{\rho}$ instead of $\log M_{\text{cl},0}$ and $\log \bar{\Sigma}$).

It is notable that with few exceptions clouds with $\bar{\Sigma} \leq 100 M_{\odot} \text{pc}^{-2}$ and $\alpha \geq -1.5$ can be destroyed if $\varepsilon_{\text{SF}} \geq \varepsilon_{\min} \approx 1$ per cent. Such a low value for the minimum SFE is a strong indicator that stellar feedback alone is sufficient to explain the low observed star formation efficiencies of GMCs – which is not to say that in reality other physical processes like turbulence of the ISM (Elmegreen & Scalo 2004; Mac Low & Klessen 2004) and to a lesser degree magnetic fields (Shu, Adams & Susana 1987) do not also play a role in bringing ε_{SF} down.

We note, however, that if clouds form stars preferentially in one short burst with $\varepsilon_{\text{SF}} \approx \varepsilon_{\min}$, this presents a challenge to the survivability of these star clusters because star clusters with $\varepsilon_{\text{SF}} \gtrsim 10$ per cent tend to dissolve after the natal gas has been removed (Baumgardt & Kroupa 2007; Shukirgaliyev et al. 2017). We speculate that studies of star clusters with N -body simulations that include a centrally peaked star formation profile as in the model by Parmentier & Pflanzner (2013) together with slow gas removal with velocities of approximately 10 km s^{-1} as predicted by our WARPFIELD2 simulations will result in a higher survival rate even for low star formation efficiencies.

4.3.1 Giant clumps

Giant clumps at redshift $z \sim 1-3$ with gas masses of $10^7-10^9 M_{\odot}$ have typical surface densities of $\bar{\Sigma} \sim 100 M_{\odot} \text{pc}^{-2}$ and are consis-

tent with isothermal spheres, i.e. $\alpha = -2$ (Ceverino et al. 2012). In this paper we probe the lower mass end of such clumps. Our results indicate that they are more resilient against destruction by stellar feedback than clouds with shallower density profiles. As noted above, this is due to the larger binding energy of the giant clump and in particular of the inner region when $\alpha = -2$ (see equation 28). As more of the gas mass is accumulated in the inner regions, an expanding shell in a cloud with such a steep density profile decelerates faster, making it more susceptible to energy loss via leakage of hot gas after gravitational fragmentation and via strong cooling.

Our results indicate that giant clumps at the low-mass end ($M_{\text{cl},0} = 10^7 M_{\odot}$) can be destroyed by a single starburst with $\varepsilon_{\text{SF}} \geq 4$ per cent for $\bar{\Sigma} = 100 M_{\odot} \text{pc}^{-2}$ ($\varepsilon_{\min} = 1-12$ per cent for $30 \leq \bar{\Sigma} \leq 300 M_{\odot} \text{pc}^{-2}$). Were the star formation spread out over the lifetime of the clump ($\sim 30 \text{ Myr}$), this would correspond to $\varepsilon_{\text{ff}} = 0.5$ per cent (0.3–0.7 per cent for $30 \leq \bar{\Sigma} \leq 300 M_{\odot} \text{pc}^{-2}$). This result is in line with simulations by Oklopčić et al. (2017) but puts analytic models by Krumholz & Dekel (2010) into question who argue that star formation efficiencies per free-fall time of a few per cent are insufficient to disrupt a giant molecular clump (they focus on clumps with $M_{\text{cl},0} \geq 3 \times 10^7 M_{\odot}$ though). Our result does not yet take into account that the metallicity in galaxies at $z \sim 2$ is approximately a factor 2 lower than in present-day galaxies (Yuan, Kewley & Richard 2012), which will affect the amount of radiative

cooling, the strength of metal-line-driven winds of massive stars, and the coupling of radiation to the ISM. We plan to revisit giant clumps with WARPFIELD in the future.

5 CONCLUSION

In this paper we have presented improvements to the 1D stellar feedback code WARPFIELD (Rahner et al. 2017). WARPFIELD is a fast, publicly available code which models the formation of a shell around a massive cluster and how this shell is affected by stellar winds, radiation, and SNe, as well as gravity. The improvements which are part of a new code release, WARPFIELD2, include, but are not limited to, a better treatment of the early, energy-driven expansion phase of shells around massive clusters, their fragmentation, and the cooling of hot wind bubbles.

In order to model the cooling in the wind bubble correctly we have produced a large grid of cooling curves with CLOUDY (Ferland et al. 2017) that account for the ionizing radiation produced by the young massive cluster creating the wind bubble in addition to collisional ionization. The grid, which encompasses a wide range of temperatures, densities, photon fluxes of ionizing radiation, stellar ages, and two different metallicities (see Table 1 and Appendix B) is publicly available.

We have employed WARPFIELD2 to model the destruction of GMCs with various density profiles. Our main results are summarized as follows.

(i) With respect to the previous release, WARPFIELD1, feedback of a young massive cluster is more efficient in destroying the parental molecular cloud.

(ii) Clouds with a core of constant density followed by a power law of $\rho \propto R^\alpha$ are investigated. We find that clouds with $-1.5 \leq \alpha \leq 0$ react very similarly to feedback if the average density of the cloud is kept constant.

(iii) The minimum SFE ϵ_{\min} needed to destroy a cloud after a single starburst is between 1 and 6 per cent for GMCs with $-1.5 \leq \alpha \leq 0$ and with mean surface densities of pc^{-2} . The value of ϵ_{\min} is mainly set by $\bar{\Sigma}$. Varying the cloud mass is a second-order effect.

(iv) Typical star formation efficiencies per free-fall time are ~ 0.3 per cent, in good agreement with observations on GMC scales by Leroy et al. (2017).

(v) For $\alpha = -2$ (as suggested for giant clumps at $z \sim 2$), ϵ_{\min} can be much higher (from 1 per cent for $\bar{\Sigma} \sim 10 M_\odot \text{pc}^{-2}$ to $\gtrsim 50$ per cent for $\bar{\Sigma} \sim 1000 M_\odot \text{pc}^{-2}$). At a fiducial surface density of $100 M_\odot \text{pc}^{-2}$ we predict $\epsilon_{\min} \sim 5$ per cent.

(vi) Stellar feedback alone is sufficient in explaining the low observed star formation efficiencies in star-forming regions.

ACKNOWLEDGEMENTS

We thank the anonymous referee for constructive input that helped to improve this paper and Fabian Scheuermann for his help to tabulate CIE cooling curves. We acknowledge funding from the Deutsche Forschungsgemeinschaft in the Collaborative Research Centre (SFB 881) ‘The Milky Way System’ (subprojects B1, B2, and B8), the Priority Program SPP 1573 ‘Physics of the Interstellar Medium’ (grant numbers KL 1358/18.1, KL 1358/19.2, and GL 668/2-1), and the European Research Council in the ERC Advanced Grant STARLIGHT (project no. 339177). This research made use of SCIPY (Jones et al. 2001) and MATPLOTLIB (Hunter 2007).

REFERENCES

- Alves J. F., Lada C. J., Lada E. A., 2001, *Nature*, 409, 159
 Bacmann A., André P., Puget J.-L., Abergel A., Bontemps S., Ward-Thompson D., 2000, *A&A*, 361, 555
 Ballesteros-Paredes J., Klessen R. S., Vázquez-Semadeni E., 2003, *ApJ*, 592, 188
 Baumgardt H., Kroupa P., 2007, *MNRAS*, 380, 1589
 Beccari G. et al., 2017, *A&A*, 604, A22
 Beuther H., Schilke P., Menten K. M., Motte F., Sridharan T. K., Wyrowski F., 2002, *ApJ*, 566, 945
 Bisnovatyi-Kogan G. S., Silich S. A., 1995, *Rev. Mod. Phys.*, 67, 661
 Bonnor W. B., 1956, *MNRAS*, 116, 351
 Castor J., McCray R., Weaver R., 1975, *ApJ*, 200, L107
 Ceverino D., Dekel A., Mandelker N., Bournaud F., Burkert A., Genzel R., Primack J., 2012, *MNRAS*, 420, 3490
 Colombo D. et al., 2014, *ApJ*, 784, 3
 Cowie L. L., McKee C. F., 1977, *ApJ*, 211, 135
 Dale J. E., Wunsch R., Whitworth A., Palouš J., 2009, *MNRAS*, 398, 1537
 Ebert R., 1955, *Z. Astrophys.*, 37, 217
 Efstathiou G., 1992, *MNRAS*, 256, 43P
 Ekström S., Georgy C., Meynet G., Massey P., Levesque E. M., Hirschi R., Eggenberger P., Maeder A., 2012, *A&A*, 542, A29
 Elmegreen B. G., Lada C. J., 1977, *ApJ*, 214, 725
 Elmegreen B. G., Scalo J., 2004, *ARA&A*, 42, 211
 Emerick A., Bryan G. L., Mac Low M.-M., 2019, *MNRAS*, 482, 1304
 Fall S. M., Krumholz M. R., Matzner C. D., 2010, *ApJ*, 710, L142
 Ferland G. J., 2013, Hazy. www.nublado.org
 Ferland G. J. et al., 2017, *Rev. Mex. Astron. Astrofis.*, 53, 385
 Georgy C., Ekström S., Meynet G., Massey P., Levesque E. M., Hirschi R., Eggenberger P., Maeder A., 2012, *A&A*, 542, A29
 Gnat O., Ferland G. J., 2012, *ApJS*, 199, 20
 Gnedin N. Y., Hollon N., 2012, *ApJS*, 202, 13
 Gupta S., Nath B. B., Sharma P., Shchekinov Y., 2016, *MNRAS*, 462, 4532
 Harper-Clark E., Murray N., 2009, *ApJ*, 693, 1696
 Hennebelle P., Falgarone E., 2012, *A&AR*, 20, 55
 Heyer M., Krawczyk C., Duval J., Jackson J. M., 2009, *ApJ*, 699, 1092
 Hillier D. J., Miller D. L., 1998, *ApJ*, 496, 407
 Hindmarsh A. C., 1983, *IMACS Trans. Sci. Comput.*, 1, 55
 Hughes A. et al., 2010, *MNRAS*, 406, 2065
 Hughes A. et al., 2013, *ApJ*, 779, 46
 Hunter J. D., 2007, *Comput. Sci. Eng.*, 9, 90
 Jones E. et al., 2001, SciPy: Open source scientific tools for Python. Available at: <http://www.scipy.org>
 Kawamura A. et al., 2009, *ApJS*, 184, 1
 Kim J.-G., Kim W.-T., Ostriker E. C., 2016, *ApJ*, 819, 137
 Klessen R. S., Glover S. C. O., 2016, *Star Formation in Galaxy Evolution: Connecting Numerical Models to Reality*, Saas-Fee Advanced Course, Vol. 43. Springer-Verlag, Berlin, p. 85
 Klessen R. S., Ballesteros-Paredes J., Vázquez-Semadeni E., Durán-Rojas C., 2005, *ApJ*, 620, 786
 Könyves V. et al., 2010, *A&A*, 518, L106
 Kreckel K. et al., 2018, *ApJ*, 863, L21
 Kroupa P., 2001, *MNRAS*, 322, 231
 Krumholz M. R., Dekel A., 2010, *MNRAS*, 406, 112
 Krumholz M. R., McKee C. F., 2005, *ApJ*, 630, 250
 Krumholz M. R., Tan J. C., 2007, *ApJ*, 654, 304
 Krumholz M. R. et al., 2014, *Protostars and Planets VI*. Univ. Arizona Press, Tucson, p. 243
 Larson R. B., 1969, *MNRAS*, 145, 271
 Larson R. B., 1981, *MNRAS*, 194, 809
 Leroy A. K. et al., 2017, *ApJ*, 846, 71
 Mac Low M. M., Klessen R. S., 2004, *Rev. Mod. Phys.*, 76, 125
 Mac Low M.-M., McCray R., 1988, *ApJ*, 324, 776
 Martínez-González S., Silich S., Tenorio-Tagle G., 2014, *ApJ*, 785, 164
 McCray R., Kafatos M., 1987, *ApJ*, 317, 190

- McKee C. F., Ostriker E. C., 2007, *ARA&A*, 45, 565
- Michaut C., Cavet C., Bouquet S. E., Roy F., Nguyen H. C., 2012, *ApJ*, 759, 78
- Miura R. E. et al., 2012, *ApJ*, 761, 37
- Miville-Deschênes M.-A., Murray N., Lee E. J., 2017, *ApJ*, 834, 57
- Molinari S. et al., 2014, *Protostars and Planets VI*. Univ. Arizona Press, Tucson, p. 125
- Motte F., Bontemps S., Louvet F., 2018, *ARA&A*, 56, 41
- Murray N., 2011, *ApJ*, 729, 133
- Murray N., Quataert E., Thompson T. A., 2010, *ApJ*, 709, 191
- Ogino S., Tomisaka K., Nakamura F., 1999, *PASJ*, 51, 637
- Oklopčić A., Hopkins P. F., Feldmann R., Kereš D., Faucher-Giguère C.-A., Murray N., 2017, *MNRAS*, 465, 952
- Ostriker J. P., Cowie L. L., 1981, *ApJ*, 243, 127
- Parmentier G., Pfalzner S., 2013, *A&A*, 549, 132
- Pauldrach A. W. A., Hoffmann T. L., Lennon M., 2001, *A&A*, 375, 161
- Penston M. V., 1969, *MNRAS*, 145, 457
- Petzold L., 1983, *SIAM J. Sci. Stat. Comput.*, 4, 136
- Rahner D., Pellegrini E. W., Glover S. C. O., Klessen R. S., 2017, *MNRAS*, 470, 4453
- Rahner D., Pellegrini E. W., Glover S. C. O., Klessen R. S., 2018, *MNRAS*, 473, L11
- Recchi S., Wünsch R., Palouš J., Dinnbier F., 2017, *Ap&SS*, 362, 183
- Rugel M. et al., 2018, *A&A*, preprint (arXiv:1812.0075)
- Ryu D., Vishniac E. T., 1987, *ApJ*, 313, 820
- Sabbi E. et al., 2012, *Astron. J. Lett.*, 37, 6
- Shu F. H., 1977, *ApJ*, 214, 488
- Shu F. H., Adams F. C., Susana L., 1987, *ARA&A*, 25, 23
- Shukirgaliyev B., Parmentier G., Bercezik P., Just A., 2017, *A&A*, 605, 119
- Silich S., Tenorio-Tagle G., 2013, *ApJ*, 765, 43
- Silich S., Tenorio-Tagle G., 2017, *MNRAS*, 465, 1375
- Smith B. D. et al., 2017, *MNRAS*, 466, 2217
- Spitzer L., 1956, *Physics of Fully Ionized Gases*. Interscience Publishers, New York
- Sutherland R., Dopita M., 1993, *ApJS*, 88, 253
- Szécsi D., Wünsch R., 2018, preprint (arXiv:1809.01395)
- Tenorio-Tagle G., Palouš J., Silich S., Medina-Tanco G. A., Muñoz-Tuñón C., 2003, *A&A*, 411, 397
- Townsley L. K., Feigelson E. D., Montmerle T., Broos, Patrick S., Chu Y.-H., Garmire G. P., 2003, *ApJ*, 593, 874
- Vinkó J. et al., 2009, *ApJ*, 695, 619
- Vishniac E. T., 1983, *ApJ*, 274, 152
- Vutisalchavakul N., Evans N. J., II, Heyer M., 2016, *ApJ*, 831, 73
- Wang P., Li Z.-Y., Abel T., Nakamura F., 2010, *ApJ*, 709, 27
- Weaver R., McCray R., Castor J., Shapiro P., Moore R., 1977, *ApJ*, 218, 377
- Whitworth A., Summers D., 1985, *MNRAS*, 214, 1
- Wiersma R. P. C., Schaye J., Smith B. D., 2009, *MNRAS*, 393, 99
- Wünsch R., Palouš J., Tenorio-Tagle G., Ehlerová S., 2017, *ApJ*, 835, 60
- Yuan T.-T., Kewley L. J., Richard J., 2012, *ApJ*, 763, 9

SUPPORTING INFORMATION

Supplementary data are available at [MNRAS](#) online.

Table B1. The online data encompasses net cooling curves for the parameter space presented in Table 1. A shortened example of the data is presented in Table B1..

Please note: Oxford University Press is not responsible for the content or functionality of any supporting materials supplied by the authors. Any queries (other than missing material) should be directed to the corresponding author for the article.

APPENDIX A: BUBBLE STRUCTURE

When thermal conduction and radiative cooling are included in the self-similarity solution of Weaver et al. (1977), the velocity structure and the temperature structure of the bubble are given by the set of differential equations,

$$v' = \frac{\beta + \delta}{t} + \left(v - \frac{\tilde{\alpha}r}{t} \right) \frac{T'}{T} - \frac{2v}{r}, \quad (\text{A1})$$

$$T'' = \frac{P_b}{CT^{5/2}} \left[\frac{\beta + 2.5\delta}{t} + \frac{P_b}{4k^2} \frac{\Lambda_{\text{net}}}{T^2} + 2.5 \left(v - \frac{\tilde{\alpha}r}{t} \right) \frac{T'}{T} \right] - \frac{2.5T'^2}{T} - \frac{2T'}{r}, \quad (\text{A2})$$

where v is the gas velocity and where primes indicate differentiation with respect to the radius r . Here,

$$\tilde{\alpha} \equiv \frac{\partial \ln R_2}{\partial \ln t}, \quad (\text{A3})$$

$$\beta \equiv -\frac{\partial \ln P_b}{\partial \ln t}, \quad (\text{A4})$$

$$\delta \equiv \left(\frac{\partial \ln T}{\partial \ln t} \right)_{\xi}, \quad (\text{A5})$$

with $\xi = r/R_2$, and k is the Boltzmann constant. We use a constant thermal conduction coefficient of $C = 6 \times 10^{-7} \text{ erg s}^{-1} \text{ cm}^{-1} \text{ K}^{-7/2}$. It is related to the thermal conductivity κ via

$$\kappa = C \cdot T_e^{5/2}, \quad (\text{A6})$$

where T_e is the electron temperature. In reality, C is not a constant but

$$C = 4.6 \times 10^{13} (10^8 \text{ K})^{-5/2} \left(\frac{\ln \Lambda}{40} \right)^{-1} \text{ s}^{-1} \text{ cm}^{-1} \text{ K}^{-7/2}, \quad (\text{A7})$$

where the Coulomb logarithm is (Cowie & McKee 1977)

$$\ln \Lambda = 29.7 + \ln \left(\sqrt{\frac{1 \text{ cm}^{-3}}{n}} \frac{T_e}{10^6 \text{ K}} \right) \quad \text{for } T > 4.2 \times 10^5 \text{ K}. \quad (\text{A8})$$

For reasonable values of n and T_e , C as derived from equation (A7) does not differ by more than 30 per cent from the constant value cited above (Spitzer 1956).

The boundary conditions (BCs) for solving the structure equations (A1) and (A2) are

$$\lim_{r \rightarrow R_2} T = 0, \quad (\text{A9})$$

$$\lim_{r \rightarrow R_2} v = \dot{R}_2, \quad (\text{A10})$$

$$\lim_{r \rightarrow R_1} v = 0. \quad (\text{A11})$$

Equations (A1) and (A2) are solved from R_2 to R_1 via a shooting method, that is, a guess is made for the missing BC at R_2 . If the solution of the ODE system also fulfils the BC at R_1 , the choice of the right-hand side BC was correct. Otherwise, another guess is made and the correct right-hand side BC is determined via a root finding algorithm. More details are provided in Weaver et al. (1977).

In order to determine β , it is necessary to know the value of \dot{P}_b (see equation A4), but the energy equation (equation 5) only gives an expression for \dot{E}_b . To close the system of equations a relation between \dot{P}_b and \dot{E}_b must be derived. This relation follows from equations (6) and (7):

$$\dot{E}_b = \frac{2\pi\dot{P}_bd^2 + 3E_b\dot{R}_2R_2^2\left(1 - \frac{c}{E_b+c}\right) - a\frac{R_1^3E_b^2}{(E_b+c)}}{d\left(1 - \frac{c}{E_b+c}\right)}, \quad (\text{A12})$$

with

$$a \equiv \frac{3\dot{F}_{\text{ram}}}{2F_{\text{ram}}}, \quad (\text{A13})$$

$$c \equiv \frac{3}{4}F_{\text{ram}}R_1, \quad (\text{A14})$$

$$d \equiv R_2^3 - R_1^3. \quad (\text{A15})$$

In summary, \dot{E}_b sets the temperature profile $T(r)$ of the bubble via β and the temperature profile in turn sets \dot{E}_b via equations (12) and (5). In order to solve the implicit ODE system governing the dynamics of the bubble, equations (4), (5), and (15), for the first time-step we start with the self-similarity values for $\tilde{\alpha}$, β , and δ (where cooling is not included), i.e. $\tilde{\alpha} = 3/5$, $\beta = 4/5$, $\delta = -6/35$ (Weaver et al. 1977), and afterwards calculate the derivatives via a root finding algorithm.

APPENDIX B: COOLING CURVES

For this paper, 144 408 CLOUDY models have been run to derive cooling and heating values for a wide parameter range (see Table 1). As an example, we show in Table B1 the heating and cooling rates per unit volume for a selection of different densities, temperatures, and ionizing photon fluxes for the case of a 1 Myr-old star cluster with solar metallicity. The net cooling rate utilized in WARPFIELD2 is simply the cooling rate minus the heating rate and hence is not tabulated. For an arbitrary combination of t_{age} , n , T , and Φ_i , cooling and heating rates can be derived from the tabulated values using quadrilinear interpolation. For $t_{\text{age}} < 1$ Myr, we consider the same spectral shape of the star cluster as for $t_{\text{age}} = 1$ Myr. This constitutes only a minor error as the change of the spectrum at early times is small.

In Figs B1 and B2, we present example cooling curves (showing the net cooling rate, Λ_{net}) for the ISM at various densities and at distances of 10 and 30 pc from an ageing star cluster ($t_{\text{age}} = 1, 3, 10$ Myr) with $M_* = 10^6 M_\odot$. For an older star cluster, the cooling curve approaches the CIE curve. Cosmic rays from the Galactic background are included, providing an extra source of heating and ionization, although they are a minor effect in the presence of a young massive cluster emitting a large number of ionizing photons. With growing age and decreasing mass of the cluster and with increasing distance from it, cosmic rays rise in importance.

For temperatures above $10^{5.5}$ K, we use CIE cooling curves from Gnat & Ferland (2012) and Sutherland & Dopita (1993). The full data (including CIE curves at $T > 10^{5.5}$ K) are available for download under <https://bitbucket.org/drahner/warpfield>.

Table B1. Shortened cooling table for a star cluster with $t_{\text{age}} = 1$ Myr and $Z = 0.014$ (solar). ID: identification number of CLOUDY model, n : ion number density, T : temperature, Φ_i : number flux of ionizing photons, n_e : electron number density, $nm_e\Gamma$: change rate of internal energy density due to heating, $nm_e\Lambda$: change rate of internal energy density due to cooling (see equation 13). The three rightmost columns contain derived quantities. For the shape of the spectrum, we consider a fully sampled Kroupa IMF. For a full table, refer to the online data.

ID	n (cm^{-3})	T (K)	Φ_i ($\text{cm}^{-2} \text{s}^{-1}$)	n_e (cm^{-3})	$nm_e\Gamma$ ($\text{erg cm}^{-3} \text{s}^{-1}$)	$nm_e\Lambda$ ($\text{erg cm}^{-3} \text{s}^{-1}$)
1	1.0×10^{-4}	3.162×10^3	1.0×10^0	4.4×10^{-5}	1.467×10^{-30}	3.737×10^{-33}
2	3.162×10^{-4}	3.162×10^3	1.0×10^0	1.01×10^{-4}	4.236×10^{-30}	2.628×10^{-32}
...
33	1.0×10^{12}	3.162×10^3	1.0×10^0	1.5×10^5	1.978×10^{-15}	5.039×10^{-8}
34	1.0×10^{-4}	3.162×10^3	1.0×10^1	5.29×10^{-5}	1.566×10^{-30}	4.766×10^{-33}
35	3.162×10^{-4}	3.162×10^3	1.0×10^1	1.19×10^{-4}	4.458×10^{-30}	3.242×10^{-32}
...
12034	1.0×10^{12}	3.162×10^5	1.0×10^{21}	1.19×10^{12}	2.15×10^{-2}	1.697×10^2

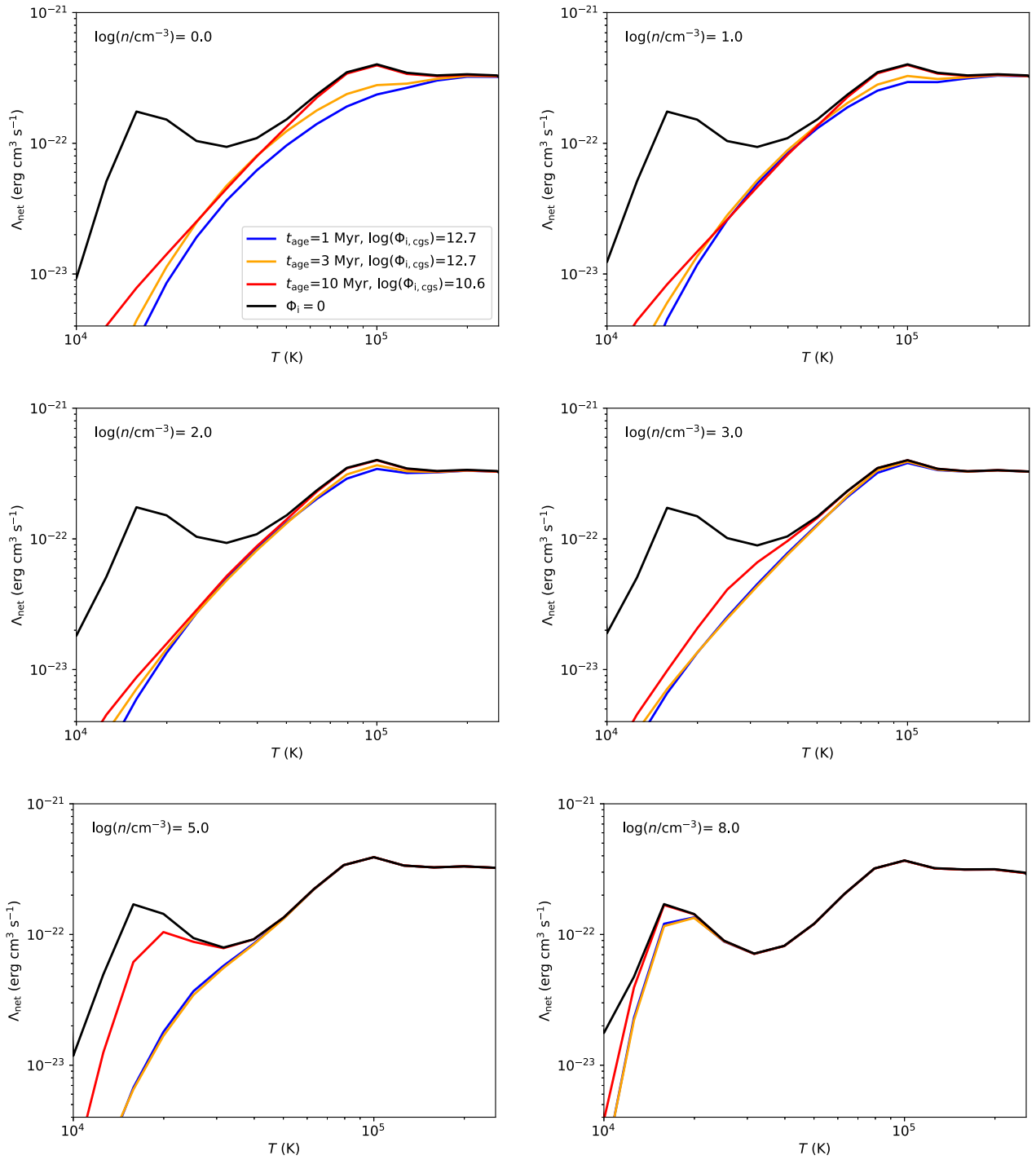


Figure B1. Net cooling curves for solar metallicity (with elemental composition appropriate for H II regions) and various particle densities. Cooling curves are shown by different colours for different ages t_{age} of the illuminating star cluster ($M_* = 10^6 M_{\odot}$). The ionizing photon flux ($\Phi_{i,\text{cgs}} = \Phi_i/(\text{cm}^{-2} \text{s}^{-1})$) has been calculated according to the time evolution of the cluster and at a distance of 10 pc.

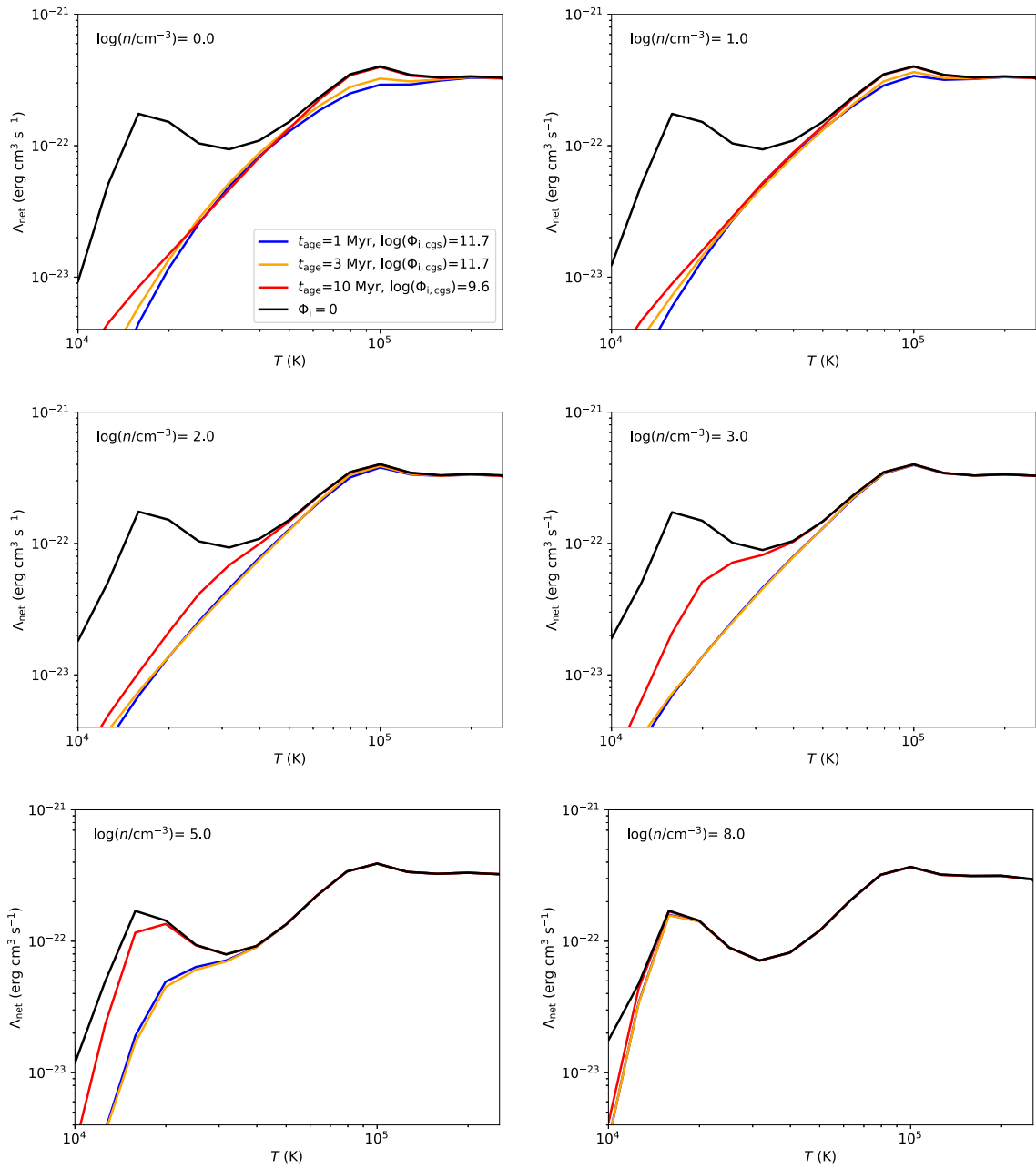


Figure B2. Same as Fig. B1 but here the distance between the star cluster and the illuminated ISM is 30 pc.

This paper has been typeset from a \LaTeX file prepared by the author.

Chapter 3

Conclusion and Outlook

3.1 Conclusion

In the previous chapter I have presented a novel, semi-analytic, one-dimensional model to simulate stellar feedback in massive¹ star-forming regions. This model simultaneously and self-consistently calculates the structure and the dynamics of shells which are driven by feedback (stellar winds, supernovae, and radiation pressure). The method, implemented in the publicly available computer code `WARPFIELD`, is computationally inexpensive: Version 1 of the code, presented in Section 2.1, takes ~ 1 second on a single CPU to simulate 1 Myr in the evolution of a star-forming region, while version 2, presented in Section 2.3, is somewhat more expensive but still needs only ~ 100 seconds per Myr of cloud evolution (state-of-the-art three-dimensional hydrodynamical codes, e.g. `FLASH` (Fryxell et al. 2000), need $\sim 10^5 - 10^6$ CPU hours when stellar feedback is included).² `WARPFIELD` allows the user to investigate the effect of stellar feedback in a large parameter space of GMC and star cluster properties. In addition, it is straightforward to couple the code to more sophisticated radiative transfer codes in order to produce synthetic observations of star-forming regions (see Section 3.2). In summary, the method presented in the previous chapter fulfils the criteria outlined in Section 1.3 for an efficient new scheme to simulate the effect of feedback in star-forming regions.

Let us now return to the question formulated in Section 1.3: How does stellar feedback regulate star formation in giant molecular clouds? In the individual publications presented in Chapter 2 we have already drawn several distinct conclusions related to this question, limited to the scope of the respective paper. In the following, I will put particular emphasis on how these results contribute to a coherent picture of feedback-regulated star formation, where scientific progress has been achieved, and where further studies are still necessary.

The results presented in this thesis fall in two categories. First, we have shown that stellar feedback can destroy giant molecular clouds and thereby impede star formation. More specifically, we have investigated *by what means* in detail star formation suppresses further star formation, i.e. how the

¹gas masses $\gtrsim 10^5 M_\odot$ and star cluster masses $\gtrsim 10^4 M_\odot$

²This is of course highly resolution-dependent and dependent on which particular feedback processes are implemented. The numbers quoted here are only meant to give a general idea about the computational cost.

Conclusion and Outlook

various feedback processes interact and how the strength of each process compares to the strength of the others as a function of time. Our modelling efforts in this regard include (i) the usage of tracks of stellar evolution for both the radiative and the mechanical output of massive stars, (ii) a model for the coupling of radiation and matter (see Section 2.1), and (iii) a model for the cooling of shock- and radiation-heated gas and for leakage of hot gas from the wind bubble due to shell fragmentation (see Section 2.3).

Second, we have investigated *to what extent* star formation is suppressed by stellar feedback. This includes the calculation of minimum star formation efficiencies necessary for cloud destruction for a large parameter space of cloud and cluster properties (Sections 2.1 and 2.3) and – as illustrated by the example of the massive star-forming region 30 Doradus in Section 2.2 – what consequences one can expect when stellar feedback from a massive cluster is initially insufficient to completely shut off star formation.

The Stellar Feedback Budget

In the literature there is some debate on which feedback processes are important. In part, the disagreement arises because the authors discuss different systems. For example, as already mentioned in Section 1.3 thermal feedback from photoionization (HII regions) can disrupt molecular clouds with masses of and below $10^4 M_{\odot}$ but is unimportant in more massive GMCs. Protostellar outflows, which were briefly discussed in Section 1.1.3, are probably only important for destroying natal clouds with even lower masses (Krumholz et al. 2018). For massive GMCs this leaves radiation pressure, stellar winds, and supernovae, which are the focus of this thesis.

For individual stars, both the bolometric luminosity L and the mechanical wind luminosity L_w are highly mass-dependent. At the high-mass end of the IMF, L_w increases faster with stellar mass than L does (see Eqs. 1.13 and 1.40). Whether stellar winds are important or not when compared to radiation thus hinges, among other things, on the presence of very massive stars (see also Haid et al. 2018). This thesis solely focuses on massive star clusters, i.e. those where the IMF is fully sampled. It would be questionable (and probably even wrong) to apply the results presented here to low-mass clusters.

Even for massive clusters, limiting oneself to comparing a cluster’s bolometric luminosity to the total mechanical wind luminosity is misleading. Before the death of the most massive stars, the bolometric luminosity of a massive cluster is ~ 200 times higher than the mechanical wind luminosity (see Figures 1.7 and 1.9). However, photons do not scatter sufficiently often to transfer a large fraction of the bolometric luminosity to the ISM (Reissl et al. 2018). In the single-scattering case, the momentum per unit time transferred to the ISM by radiation from a young ($t \leq 4$ Myr) $10^5 M_{\odot}$ -cluster is $L/c \sim 10^{31}$ dyne while the ram-pressure force of stellar winds is $2L_w/\langle v_{\infty} \rangle \sim 10^{31}$ dyne as well. Hence, winds (in the momentum limit) and radiation pressure (in the single-scattering case) are of roughly equal importance.³ A more detailed analysis is only possible with a sophisticated model

³The momentum limit is a lower limit for the efficiency of winds. The single-scattering case is neither a lower nor an upper limit for the efficiency of radiation pressure (since photons can be absorbed more than once or not all).

that takes the interaction of mechanical and radiative feedback into account. This is where `WARPFIELD` can contribute.

One key result of this dissertation is that individual feedback processes must not be considered in isolation. Mechanical feedback, i.e. stellar winds and SNe, compresses the ISM to high densities. The coupling of ionizing radiation is strongly influenced by the density of the gas (and not just the column density), so that the effect of radiation pressure is enhanced when other feedback processes are present. Conversely, radiative feedback leads to a faster expansion of the shell and thus quick adiabatic cooling of the shocked wind material. This, in turn, means that radiative cooling becomes important earlier as the temperature of the shocked material quickly approaches the peak of the cooling curve at $\sim 10^5$ K. To complicate matters, radiative cooling is partly counteracted by radiative heating from the star cluster. In addition, the stability of the shell against fragmentation, which is crucial for the confinement of shock-heated wind material, is influenced by both mechanical and radiative feedback. As a result, mechanical feedback tends to increase the effectiveness of radiation, whereas radiative feedback tends to decrease the effectiveness of stellar winds. In summary, mechanical and radiative feedback are intrinsically interconnected and – at least for massive star clusters – it would be a fallacy to ignore either of them.

Using `WARPFIELD` we have shown that stellar winds tend to dominate during the early expansion phase, $t \lesssim 0.1$ Myr, and at $t \sim 3$ Myr when the most massive stars enter the Wolf-Rayet phase with high mass-loss rates.⁴ Supernova feedback tends to dominate over other feedback terms at late times ($t \gtrsim 5$ Myr) except in very massive GMCs ($M_{\text{cl},0} \gtrsim 10^7 M_{\odot}$) where radiation remains strongly coupled to the ISM and where radiation pressure is thus at least of equal importance. The metallicity of stars and of the ISM also affects the evolution of the GMC in a highly non-linear manner. Radiation in low-metallicity clouds is less coupled to the ISM because dust abundance scales with metallicity. With regard to stellar winds, on the one hand mass loss rates are lower at low metallicity (Eq 1.14), but on the other hand radiative cooling is also less efficient (Eq. 1.34).

Altogether, the relative importance of the various feedback mechanisms is both strongly time- and environment-dependent. Simply using a constant scale factor to express the importance of other feedback terms compared to radiation pressure (as in Krumholz and Matzner 2009) does not do justice to the complexity of the problem.⁵ Furthermore, and contrary to what is claimed in Krumholz et al. (2018), winds can be the dominant source of feedback, at least for a limited time span of $\lesssim 1$ Myr. There is a strong observational bias, however, to detect systems which are not dominated by stellar winds because these are clusters and bubbles which are not deeply embedded any more.

⁴These results have been obtained with an early version of `WARPFIELD` where radiative cooling of the bubble and shell fragmentation are treated in a simplistic manner (cf. Section 2.1). Qualitatively, the results hold up when a more sophisticated treatment of these processes is included. A more quantitative discussion will be the subject of a forthcoming paper.

⁵On the other hand, since the general long-term evolution of cloud is not sensitive to the origin of feedback (radiative or mechanical) such a simplification seems justified when computing minimum star formation efficiencies (see below).

Regulation of Star Formation by Stellar Feedback

Independent of which feedback process dominates, at a given point in time and with a given number of newly-formed massive stars the energy- and momentum injection from all feedback processes together may not yet be sufficient to destroy the natal GMC and thus to fully shut off star formation. In the absence of other processes which may destroy the star-forming region, such as galactic shear, star formation will proceed until the combined stellar feedback is able to dissolve the GMC. In an idealized model, we have investigated whether the bimodal age distribution in the massive cluster NGC 2070, which resides in the massive star-forming region 30 Doradus, could be the effect of incomplete cloud disruption. At early times, feedback impedes star formation, but as the power of feedback fades, gravitational collapse induces renewed star formation. Assuming the formation of the inner, young cluster R136 has been caused by the recollapse of cloud material, we have found a parameter range of cloud and cluster properties which broadly agrees with observations.

However, this picture of recollapse-induced renewed star formation neglects potentially important factors. Inhomogeneities in the gas distribution and triggering of star formation by stellar feedback may lead to star formation occurring at different locations (if sufficiently close, these new stars could still merge with the main cluster). In addition, so far this study and a similar study of W49A by Rugel et al. (2019) have merely shown general consistency between observations and the picture of recollapse-induced renewed star formation. Further evidence for or against this hypothesis can be obtained from future three-dimensional hydrodynamic simulations or the generation of more detailed synthetic observations (see below). If the results hold up, they point to a previously unidentified mode of star formation. Following the nomenclature of Dale et al. (2007) who introduced the term “weak triggering” for feedback-accelerated star formation, one could refer to this as “weak negative feedback” because feedback here merely delays star formation (in contrast to “strong negative feedback” where star formation is suppressed).

This leads us to the last topic discussed in Chapter 2 of this thesis: At what point is stellar feedback sufficient to halt star formation? This is conveniently expressed in terms of the minimum star formation efficiency ϵ_{\min} , which is the star formation efficiency above which feedback destroys the cloud. This is not necessarily equal to the SFE ϵ_{SF} which the cloud will actually achieve. Stellar feedback originating from one star formation site does not immediately affect star formation in other dense regions within the same cloud; hence cases where $\epsilon_{\text{SF}} > \epsilon_{\min}$ are possible. Conversely, one could imagine that $\epsilon_{\text{SF}} < \epsilon_{\min}$ if other processes than stellar feedback are important for disrupting the cloud. However, in those GMCs where feedback is the dominant mechanism in setting the star formation efficiency, one would expect observed SFEs and theoretically predicted minimum SFEs to be similar.

As presented in Section 2.3 we derive minimum SFEs in the range 1 – 6 % except in cases where the gas density profile is strongly peaked. In such cases, ϵ_{\min} can exceed 50 % for clouds with high average surface densities. Such strongly bound clouds aside, the derived values for ϵ_{\min} agree well with observed SFEs in GMCs of the order 1 – 10 % (Lada et al. 2010; Murray 2011). As a first order approximation, the SFE scales with the average gas surface density of the cloud, in agreement with

Fall et al. (2010); Grudić et al. (2018). Our predictions for the star formation efficiency per free-fall time ϵ_{ff} as derived from ϵ_{min} also agrees well with observations which typically find $\epsilon_{\text{ff}} \sim 1\%$ (Evans et al. 2014; Lee et al. 2016). This indicates that stellar feedback alone can explain the observed inefficiency of star formation but it does not prove yet that other processes such as turbulence, driven e.g. by accretion flows from the large-scale gas reservoir, do not also play a role.

We cannot, however, explain why some observations point to a decline in SFE with increasing cloud mass (e.g. Ochsendorf et al. 2017). Indeed, given that average gas surface densities of clouds show no correlation or even a slightly positive correlation with cloud mass (Colombo et al. 2014; Hughes et al. 2010; Miura et al. 2012; Miville-Deschênes et al. 2017) we would rather expect the opposite. In order to investigate whether this discrepancy may be due to observational bias, detailed synthetic observations of our simulated star-forming regions would certainly be helpful.

3.2 Outlook

Synthetic Observations

How individual stars form can only be directly observed in the very nearest star-forming systems. In more distant environments, observations of “star formation” are actually observations of young massive stars. These are detected either directly (e.g. in the far ultraviolet continuum) or more commonly indirectly, in the form of reprocessed radiation from dust or gas at certain wavelengths. The emission line spectrum of HII regions and photodissociation regions is a widely used diagnostic of gas properties such as density, temperature, pressure, or metallicity (Kewley et al. 2001).

However, in order to interpret this nebular emission, it is vital to understand both the physical processes that regulate how radiation is reprocessed in the ISM and those that set the geometrical structure of the ISM in the first place (e.g. stellar feedback). Information about these processes is deeply buried in the observations of real astronomical objects. While some pieces of this information can be reconstructed, others cannot. Therefore, theoretical modelling together with synthetic observations is imperative to disentangle the complicated clockwork of nebular emission. With the advent of large spectroscopic surveys of resolved and isolated HII regions, such as the SITELE survey of NGC 628 (Rousseau-Nepton et al. 2018), the PHANGS-MUSE large program of nearby galaxies, and SIGNALS (Rousseau-Nepton et al., *subm.*), which will provide the largest database of extragalactic HII regions to date, the need is growing for comprehensive modelling of emission lines from star-forming regions with vastly varying properties.

In forthcoming papers (Pellegrini et al., *in prep.*, Reissl et al., *subm.*) we couple WARPFIELD to the plasma simulation code CLOUDY (Ferland et al. 2017) and the radiative transfer code POLARIS (Reissl et al. 2016) to obtain synthetic observations of several tens of thousands of modelled star-forming regions in approximately 60 emission lines, including major HII region diagnostics such as $H\alpha$, $H\beta$, $OIII$, NII , and SII . We call this scheme the WARPFIELD EMISSION PREDICTOR (WARPFIELD-EMP). Whereas previous studies, e.g. Kewley et al. (2001), have quantified the effects that derived parameters – such

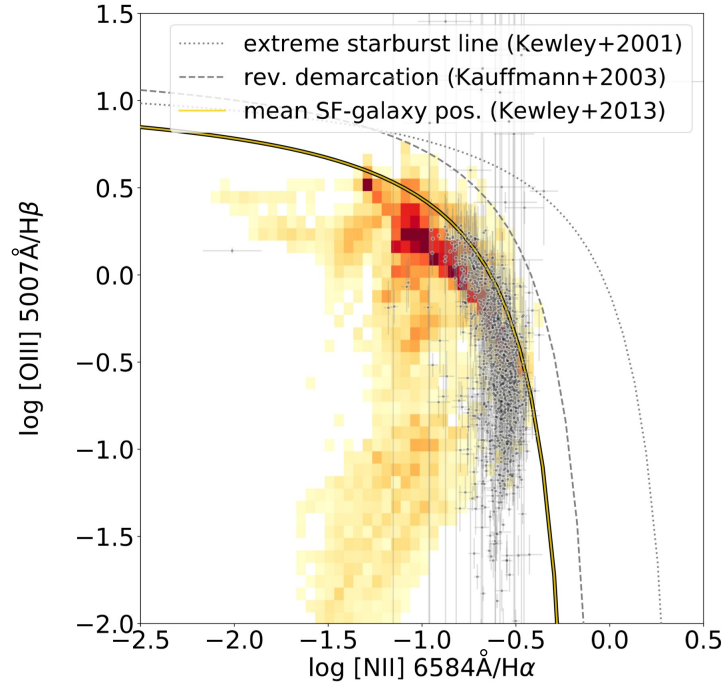


Fig. 3.1 Comparison of the distribution of WARPFIELD-EMP models of star-forming regions (represented by the two-dimensional histogram with dark red showing a high number of models) for a range of cloud properties but fixed metallicity ($Z = Z_{\odot}$) and observed HII regions in NGC 628 (represented by small circles with error bars; Rousseau-Nepton et al. 2018) in a BPT-diagram. The dashed and dotted demarcation lines by Kauffmann et al. (2003); Kewley et al. (2001) mark the threshold between star-forming regions (towards the bottom left) and regions dominated by active galactic nuclei (towards the top right). The average position of star-forming galaxies is marked by the solid line (Kewley et al. 2013). The WARPFIELD-EMP models are still preliminary. Figure taken from Pellegrini et al., in prep.

as the ionization parameter of the cloud – have on these emission lines, this model is the first to be able to show the impact of varying basic properties of the star-forming regions on their emission lines: the density (profile), the mass, and the metallicity of the parent molecular cloud as well as its SFE.

WARPFIELD-EMP works as follows: First, the effect of stellar feedback from a young massive cluster on its parent molecular cloud is simulated (via WARPFIELD). If feedback is insufficient to expel the residual gas, more stars are allowed to form. In a post-processing step the emission of the ISM illuminated by the stars is modelled by using the pressure set by the feedback processes as a boundary condition (via CLOUDY). As a last step, the emission is ray-traced through the ISM, thus allowing us to correct for dust extinction and reprocessing, and projected to the observational plane (via POLARIS).⁶ This yields an efficient approach to produce both unresolved and spatially resolved synthetic observations of nebular emission.

⁶POLARIS also accounts for a limited telescope resolution.

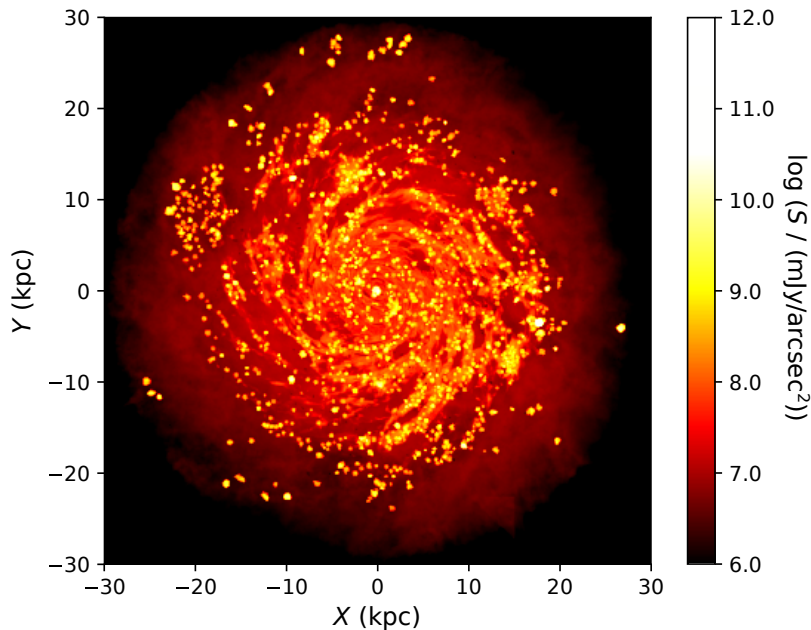


Fig. 3.2 Synthetic $H\alpha$ observation of a Milky Way type galaxy showing the surface brightness S . The large-scale gas distribution is taken from a magneto-hydrodynamical simulation from the Auriga project (Grand et al. 2017). In post-processing, dense gas regions are populated with WARPFIELD-EMP models of star-forming regions, the diffuse ionized gas is modelled with CLOUDY, and the radiation is ray-traced to the observer with POLARIS. Here, the observer views the galaxy face-on. Figure taken from Pellegrini et al., in prep.

The position of an object in a diagnostic diagram, such as the commonly used version of the “Baldwin, Phillips & Terlevich” (BPT) diagram where $[NII]/H\alpha$ and $[OIII]/H\beta$ are plotted against each other, is often used to distinguish the ionization mechanism of nebular gas (Baldwin et al. 1981; Kewley et al. 2001; Veilleux and Osterbrock 1987). In the region of the BPT-diagram where massive stars are driving the nebular emission this scheme allows us to predict properties of the cloud and of the star cluster which are not directly accessible by observations.

A comparison of a large grid of WARPFIELD-EMP models with HII regions observed in the galaxy NGC 628 is shown in Figure 3.1. We can infer which of these regions are undergoing a strong starburst, what evolutionary phase a given HII region is in and what the age distribution of embedded stars is. We can even predict the emission properties of objects whose emission is not yet observable by current observational surveys. Interestingly, while usually a large part of the scatter in a BPT-diagram is attributed to differences in metallicity (e.g. Kewley et al. 2001), the grid used to create the synthetic HII regions shown in Figure 3.1 uses a fixed metallicity (solar). Hence, the scatter in Figure 3.1 is due to variations in other GMC properties which are typically not considered in the literature. Note however, that the presented synthetic observations are still preliminary.

Conclusion and Outlook

In order to correctly model the emission properties of whole galaxies, it is necessary to build a synthetic population of simulated star-forming regions that takes into account the observed distribution of cloud and cluster masses, cloud densities, and metallicities in nearby galaxies. Such a synthetic population of WARPFIELD-EMP models can then be used to populate either a mock galaxy from semi-analytic models or a galaxy that has been simulated with a three-dimensional magneto-hydrodynamical code but where the simulation lacks the necessary ingredients to model the reprocessing of stellar radiation during runtime of the simulation. In post-processing, emission from the WARPFIELD-EMP models is then ray-traced to the observer (who could be located inside or outside the galaxy) using POLARIS. Figure 3.2 shows an example of a synthetic observation resulting from this method.

Cluster Dissolution

As discussed in Section 1.2.4, the removal of gas from a young star cluster by stellar feedback often leaves the stars in a supervirial state. The cluster’s dynamical response to gas expulsion (referred to as dynamical relaxation) can lead to the ejection of individual stars from the cluster or even the dissolution of the cluster as a whole. Whether the cluster dissolves or not is sensitive to the speed with which the residual gas is removed. Often the removal of gas is assumed to occur exponentially with the characteristic timescale being a free parameter (Baumgardt and Kroupa 2007; Geyer and Burkert 2001). Using WARPFIELD, one can not only make predictions about the gas removal rate but also about the geometric structure of the feedback-driven ISM which sets the gravitational potential.

A promising next step will be to couple the time-dependent gravitational potential as obtained from simulations with WARPFIELD to an N -body code in order to compute the dynamical response of the star cluster. Preliminary results of simulations using such a coupled scheme, where the same centrally peaked gas density profile as in Parmentier and Pfalzner (2013) and Shukirgaliyev et al. (2017) has been used, show that the ISM is pushed away somewhat faster than the cluster expands. A more detailed analysis of a large parameter space, focussing on the survivability of clusters, is still pending.

A Final Word

In summary, the presented semi-analytic model, which is implemented in the publicly available computer code WARPFIELD, is a powerful tool to understand the physics of star-forming regions. The method is computationally inexpensive, thus enabling large parameter studies, it combines the effect of various stellar feedback processes and is thus sufficiently realistic, and it couples easily to spectral synthesis and radiative transfer codes making synthetic observations possible. In this regard, WARPFIELD opens up a huge variety of possible future lines of research.

Acknowledgements

First and foremost I want to thank my supervisors Simon Glover and Ralf Klessen. I truly appreciate their guidance, the numerous fruitful discussions, and the trust they gave me, which allowed me to develop my own ideas. I am deeply indebted to them for their continuous support, in particular during my parental leave and the time afterwards. I am also extremely grateful to Eric Pellegrini for countless hours of discussions during which I learned a lot about astrophysics and for his valuable input on many topics, not limited to the ones presented in this thesis.

In addition, I would like to extend my gratitude to Geneviève Parmentier for immediately agreeing to being my second referee and to Henrik Beuther for supporting me, my projects, and my plans on various occasions. In 2016, Ralph Pudritz gave me the opportunity to spend six weeks in his group at McMaster University. During this time I learned a lot from him and his student Corey Howard and I am indebted to both of them.

My fellow group members Robin Tress, Mattia Sormani, Maximilian Disch, Claes-Erik Rydberg, Mattis Magg, Maria Jimenez-Donaire, Anna Schauer, Katharina Wollenberg, Ondrej Jaura, Sam Geen, Sacha Hony, Stefan Reißl, and Bhaskar Agarwal made the time at ITA – during and after work hours – always enjoyable. Because of them the past three and a half years were a great pleasure.

Without the support from my family, I would not be where I am now. I want to thank Susanne, Günter, and Leni for their help which extends beyond this dissertation. Finally, Salomé and Johannes are the reason why every evening I return from work with a smile on my face. Thank you!

Appendix A

Abbreviations, Nomenclature, and Glossary

Abbreviations

A&A Astronomy and Astrophysics

A&ARv The Astronomy and Astrophysics Review

A&AS Astronomy and Astrophysics Supplement Series

AJ The Astronomical Journal

ApJ The Astrophysical Journal

ApJS The Astrophysical Journal Supplement Series

Ap&SS Astrophysics and Space Science

ARA&A Annual Review of Astronomy and Astrophysics

CLOUDY (*spectral synthesis code applicable to the interstellar medium*)

CMF Core Mass Function

CPU Central Processing Unit

FLASH (*adaptive mesh refinement (magneto-)hydrodynamics code*)

GMC Giant Molecular Cloud

I-front Ionization Front

IMF Initial Mass Function

Abbreviations, Nomenclature, and Glossary

ISM Interstellar Medium

ITA Institute for Theoretical Astrophysics

LMC Large Magellanic Cloud (*a satellite galaxy of the Milky Way*)

MNRAS Monthly Notices of the Royal Astronomical Society

MUSE Multi Unit Spectroscopic Explorer

NGC New General Catalogue (of nebulae and clusters of stars)

ODE Ordinary Differential Equation

PASJ Publications of the Astronomical Society of Japan

PASP Publications of the Astronomical Society of the Pacific

PHANGS Physics at High Angular resolution in Nearby Galaxies

POLARIS POLARized Radiation Simulator (*3D Monte-Carlo continuum radiative transfer code*)

R136 (or RMC 136) Radcliffe Observatory Magellanic Clouds catalogue object 136

SFE Star Formation Efficiency

SIGNALS the Star formation, Ionized Gas, and Nebular Abundances Legacy Survey (*survey of nearby star-forming galaxies*)

SITELLE Spectromètre Imageur à Transformée de Fourier pour l'Etude en Long et en Large de raies d'Emission (*optical imaging Fourier transform spectrometer*)

SN Supernova

SNe Supernovae (*plural of Supernova*)

SNR Supernova Remnant

SvA Soviet Astronomy

WARPFIELD Winds and Radiation Pressure – Feedback Induced Expansion, coLlapse, and Dissolution (*stellar feedback dynamics code*)

WARPFIELD-EMP WARPFIELD EMission Predictor

ZAMS Zero-Age Main-Sequence

Nomenclature

c_s Sound speed

E Energy

E_b Energy of the wind/supernova bubble

ϵ_{ff} Star formation efficiency per free-fall time

ϵ_{SF} Star formation efficiency

F Force

L **or** L_{bol} Bolometric luminosity

L_w Mechanical luminosity of stellar winds

M Mass

$M_{\text{cl},0}$ Cloud mass before star formation

$M_{\text{cl},1}$ Cloud mass after star formation

M_* Stellar mass (of an individual star or of a star cluster)

\dot{M} Mass loss rate (due to winds or supernovae)

n Number density

P Pressure

R **or** r Radius

R_2 **or** R_{sh} (Inner) radius of the feedback-driven shell

ρ Mass density

t Time

T Temperature

t_{ff} **or** τ_{ff} Free-fall time

v Velocity

v_∞ Terminal velocity of ejecta

Z Metallicity

Glossary

Asymptotic giant branch star A large, cool, post-main sequence star which has completed helium core burning

Brown dwarf Stellar object whose mass is too low for hydrogen burning ($M_* \lesssim 0.08 M_\odot$)

B star A hot ($T_{\text{eff}} \gtrsim 10^4$ K), blue-white star with strong HeI and H γ (Balmer) absorption lines

Dust (interstellar \sim) Grains composed of carbon, silicates, iron, and organic compounds, typically less than 1 μm in size

Effective radius Projected radius within which half of an object's light is emitted

Extinction (interstellar \sim) Obscuration by intervening dust and gas which scatter and absorb radiation

Luminous blue variable star A very luminous, very massive, post-main sequence star ($L > 10^6 L_\odot$, $M_* > 85 M_\odot$) with a highly variable brightness

Main sequence Region in the color-magnitude diagram where 90 % of stars lie; while a star is on the main sequence it fuses hydrogen to helium in its core

Metallicity Mass fraction of elements heavier than helium

M dwarf A cool ($T_{\text{eff}} \lesssim 3700$ K), red star whose spectrum is dominated by molecular absorption bands, in particular titanium oxide and vanadium oxide

OB association A group of stars dominated by O and B stars which is only loosely bound

O star A very hot ($T_{\text{eff}} \gtrsim 2.5 \times 10^4$ K), blue-white star with very few lines

Ram pressure The pressure caused by bulk motion of a fluid (in contrast to thermal pressure which is caused by random motions)

Velocity dispersion Velocity measure of random motions; specifically, the standard deviation of the velocity distribution centred on the mean velocity

Wolf-Rayet star A massive post-main-sequence star with a very high effective temperature ($2.5 \times 10^4 \lesssim T_{\text{eff}} \lesssim 1 \times 10^5$ K) and with a high wind mass loss rate; not as variable as a luminous blue variable star

Zero-age main sequence Region in the color-magnitude diagram where stars enter the main sequence and begin equilibrium hydrogen burning

Only astrophysical terms which are not explained in the main body of this thesis are presented in the glossary. The definitions follow Binney and Tremaine (2008); Carroll and Ostlie (2007); Green and Jones (2015); Seeds and Backman (2013).

References

- Ali, A., Harries, T. J., and Douglas, T. A. (2018). Modelling massive-star feedback with Monte Carlo radiation hydrodynamics: photoionization and radiation pressure in a turbulent cloud. *MNRAS*, 477:5422–5436.
- Alsabti, A. W. and Murdin, P. (2017). Supernovae and Supernova Remnants: The Big Picture in Low Resolution. In Alsabti, A. W. and Murdin, P., editors, *Handb. Supernovae*, pages 3–28. Springer, Cham, Switzerland.
- Alves, J., Lombardi, M., and Lada, C. J. (2007). The mass function of dense molecular cores and the origin of the IMF. *A&A*, 462:L17–L21.
- André, P., Men, A., Bontemps, S., Könyves, V., Motte, F., Schneider, N., Didelon, P., Minier, V., Henning, T., Royer, P., Merín, B., Vavrek, R., Attard, M., Arzoumanian, D., Wilson, C. D., Ade, P., and Aussel, H. (2010). From filamentary clouds to prestellar cores to the stellar IMF : Initial highlights from the Herschel Gould Belt Survey. *A&A*, 518:L102.
- Arcavi, I. (2017). Hydrogen-Rich Core-Collapse Supernovae. In Alsabti, A. W. and Murdin, P., editors, *Handb. Supernovae*, pages 239–276. Springer, Cham, Switzerland.
- Aschwanden, M. J., Poland, A. I., and Rabin, D. M. (2001). The New Solar Corona. *ARA&A*, 39:175–210.
- Avedisova, V. S. (1972). Formation of Nebulae by Wolf-Rayet Stars. *SvA*, 15(5):708–713.
- Baldwin, J. A., Phillips, M. M., and Terlevich, R. (1981). Classification parameters for the emission-line spectra of extragalactic objects. *PASP*, 93:5–19.
- Bally, J. (2011). Observations of Winds, Jets, and Turbulence Generation in GMCs. In Alves, J., Elmegreen, B. G., Girart, J. M., and Trimble, V., editors, *Computational Star Formation*, volume 270 of *IAU Symposium*, pages 247–254.
- Bally, J. (2016). Protostellar Outflows. *ARA&A*, 54:491–528.
- Banerjee, S., Kroupa, P., and Oh, S. (2012a). Runaway massive stars from R136: VFTS 682 is very likely a "slow runaway". *ApJ*, 746:15.
- Banerjee, S., Kroupa, P., and Oh, S. (2012b). The emergence of super-canonical stars in R136-type starburst clusters. *MNRAS*, 426:1416–1426.
- Bastian, N., Covey, K. R., and Meyer, M. R. (2010). A Universal Stellar Initial Mass Function? A Critical Look at Variations. *ARA&A*, 48:339–389.
- Baumgardt, H. and Kroupa, P. (2007). A comprehensive set of simulations studying the influence of gas expulsion on star cluster evolution. *MNRAS*, 380(4):1589–1598.
- Bertoldi, F. and McKee, C. F. (1992). Pressure-confined clumps in magnetized molecular clouds. *ApJ*, 395:140–157.

References

- Bethe, H. A. and Wilson, J. R. (1985). Revival of a stalled supernova shock by neutrino heating. *ApJ*, 295:14–23.
- Binney, J. and Tremaine, S. (2008). *Galactic Dynamics*. Princeton University Press, Princeton, USA, second edition.
- Bisnovatyi-Kogan, G. S. and Silich, S. A. (1995). Shock-wave propagation in the nonuniform interstellar medium. *Rev. Mod. Phys.*, 67(3):661–712.
- Blandford, R. and Bühler, R. (2017). Supernova of 1054 and its Remnant, the Crab Nebula. In Alsabti, A. W. and Murdin, P., editors, *Handb. Supernovae*, pages 83–95. Springer, Cham, Switzerland.
- Blitz, L. (1993). Giant Molecular Clouds. In Levy, E. H. and Lunine, J. I., editors, *Protostars Planets III*, pages 125–161. University of Arizona Press, Tucson, USA.
- Boily, C. M. and Kroupa, P. (2003). The impact of mass loss on star cluster formation - II. Numerical N-body integration and further applications. *MNRAS*, 338(3):673–686.
- Bolatto, A. D., Wolfire, M., and Leroy, A. K. (2013). The CO-to-H₂ Conversion Factor. *ARA&A*, 51:207–268.
- Bonnell, I. A., Bate, M. R., Clarke, C. J., and Pringle, J. E. (2001a). Competitive accretion in embedded stellar clusters. *MNRAS*, 323:785–794.
- Bonnell, I. A., Clarke, C. J., Bate, M. R., and Pringle, J. E. (2001b). Accretion in stellar clusters and the initial mass function. *MNRAS*, 324:573–579.
- Bonnell, I. A., Larson, R. B., and Zinnecker, H. (2007). The Origin of the Initial Mass Function. In Reipurth, B., Jewitt, D., and Keil, K., editors, *Protostars Planets V*, pages 149–164. University of Arizona Press, Tucson, USA.
- Boss, A. P., Keiser, S. A., Ipatov, S. I., Myhill, E. A., and Vanhala, H. A. T. (2010). Triggering collapse of the presolar dense cloud core and injecting short-lived radioisotopes with a shock wave. I. Varied shock speeds. *ApJ*, 708:1268–1280.
- Carroll, B. W. and Ostlie, D. A. (2007). *An Introduction to Modern Astrophysics*. Pearson Addison Wesley, San Francisco, USA, second edition.
- Castor, J., McCray, R., and Weaver, R. (1975a). Interstellar bubbles. *ApJ*, 200:L107.
- Castor, J. I., Abbott, D. C., and Klein, R. I. (1975b). Radiation-driven winds in Of stars. *ApJ*, 195:157–174.
- Chabrier, G. (2003). Galactic Stellar and Substellar Initial Mass Function. *PASP*, 115:763–795.
- Chandar, R., Fall, S. M., Whitmore, B. C., and Mulia, A. J. (2017). The Fraction of Stars That Form in Clusters in Different Galaxies. *ApJ*, 849(2):128.
- Chandrasekhar, S. (1931). The Highly Collapsed Configurations of a Stellar Mass. *MNRAS*, 91:456.
- Cheng, Y., Tan, J. C., Liu, M., Kong, S., Lim, W., Andersen, M., and Da Rio, N. (2018). The Core Mass Function in the Massive Protocluster G286.21+0.17 Revealed by ALMA. *ApJ*, 853(2):160.
- Chevalier, R. A. (1974). The Evolution of Supernova Remnants. I. Spherically Symmetric Models. *ApJ*, 188:501–516.

- Cignoni, M., Sabbi, E., Marel, R. P. V. D., Tosi, M., Zaritsky, D., Anderson, J., Lennon, D. J., Aloisi, A., Marchi, G. D., Gouliermis, D. A., Grebel, E. K., Smith, L. J., and Zeidler, P. (2015). Hubble Tarantula Treasury Project. II. The star-formation history of the starburst region NGC 2070 in 30 Doradus. *ApJ*, 811(2):76.
- Clark, P. C., Klessen, R. S., and Bonnell, I. A. (2007). Clump lifetimes and the initial mass function. *MNRAS*, 379:57–62.
- Colgate, S. A. (1973). The Velocity and Composition of Supernova Ejecta. *NASA Special Publication*, 332:68.
- Colombo, D., Hughes, A., Schinnerer, E., Meidt, S. E., Leroy, A. K., Pety, J., Dobbs, C. L., García-Burillo, S., Dumas, G., Thompson, T. A., Schuster, K. F., and Kramer, C. (2014). The PdBI Arcsecond Whirlpool Survey (PAWS): Environmental Dependence of Giant Molecular Cloud Properties in M51. *ApJ*, 784:3.
- Combes, F. (1991). Distribution of CO in the Milky Way. *ARA&A*, 29:195–237.
- Courant, R., Friedrichs, K., and Lewy, H. (1928). Über die partiellen Differenzgleichungen der mathematischen Physik. *Math. Ann.*, 100(1):32–74.
- Crowther, P. A., Schnurr, O., Hirschi, R., Yusof, N., Parker, R. J., Goodwin, S. P., and Kassim, H. A. (2010). The R136 star cluster hosts several stars whose individual masses greatly exceed the accepted 150 M_{\odot} stellar mass limit. *MNRAS*, 408(2):731–751.
- Crutcher, R. M. (2012). Magnetic Fields in Molecular Clouds. *ARA&A*, 50:29–63.
- Dale, J. E. and Bonnell, I. (2011). Ionizing feedback from massive stars in massive clusters: fake bubbles and untriggered star formation. *MNRAS*, 414:321–328.
- Dale, J. E., Clark, P. C., and Bonnell, I. A. (2007). Ionization-induced star formation - II. External irradiation of a turbulent molecular cloud. *MNRAS*, 377(2):535–544.
- Dale, J. E., Ercolano, B., and Bonnell, I. A. (2012a). Ionization-induced star formation - IV. Triggering in bound clusters. *MNRAS*, 427(4):2852–2865.
- Dale, J. E., Ercolano, B., and Bonnell, I. A. (2012b). Ionizing feedback from massive stars in massive clusters - II. Disruption of bound clusters by photoionization. *MNRAS*, 424(1):377–392.
- Dale, J. E., Haworth, T. J., and Bressert, E. (2015). The dangers of being trigger-happy. *MNRAS*, 450(2):1199–1211.
- Dale, J. E., Ngoumou, J., Ercolano, B., and Bonnell, I. A. (2014). Before the first supernova: Combined effects of H II regions and winds on molecular clouds. *MNRAS*, 442(1):694–712.
- Deb, S., Kothes, R., and Rosolowsky, E. (2018). A Case Study of Triggered Star Formation in Cygnus X. *MNRAS*, 481:1862–1872.
- Draine, B. T. and Bertoldi, F. (1996). Structure of Stationary Dissociation Fronts. *ApJ*, 468:269–289.
- Duronea, N. U., Cappa, C. E., Bronfman, L., Borissova, J., Gromadzki, M., and Kuhn, M. A. (2017). Triggered massive star formation associated with the bubble HII region Sh2-39 (N5). *A&A*, 606:A8.
- Duyvendak, J. J. L. (1942). Further Data bearing on the identification of the Crab Nebula with the Supernova of 1054 A.D. Part I. The Ancient Oriental Chronicles. *PASP*, 54:91.
- Dwarkadas, V. V., Dauphas, N., Meyer, B., Boyajian, P., and Bojazi, M. (2017). Triggered Star Formation inside the Shell of a Wolf-Rayet Bubble as the Origin of the Solar System. *ApJ*, 851:147.

References

- Eddington, A. S. (1926). *The Internal Constitution of the Stars*. Cambridge University Press, Cambridge, UK.
- Ekström, S., Georgy, C., Meynet, G., Massey, P., Levesque, E. M., Hirschi, R., Eggenberger, P., and Maeder, A. (2012). Grids of stellar models with rotation. *A&A*, 542:A29.
- Elmegreen, B. and Chiang, W. (1982). Runaway Expansion of Giant Shells Driven by Radiation Pressure from Field Stars. *ApJ*, 253:666–678.
- Elmegreen, B. G. and Burkert, A. (2010). Accretion-driven turbulence and the transition to global instability in young galaxy disks. *ApJ*, 712:294–302.
- Elmegreen, B. G. and Lada, C. J. (1977). Sequential formation of subgroups in OB associations. *ApJ*, 214:725–741.
- Elmegreen, B. G. and Scalo, J. (2004). Interstellar Turbulence I: Observations and Processes. *ARA&A*, 42:211–73.
- Evans, N. J., Heiderman, A., and Vutisalchavakul, N. (2014). Star formation relations in nearby molecular clouds. *ApJ*, 782:114–126.
- Fall, S. M., Krumholz, M. R., and Matzner, C. D. (2010). Stellar Feedback in Molecular Clouds and Its Influence on the Mass Function of Young Star Clusters. *ApJ*, 710(2):L142–L146.
- Fellhauer, M. and Kroupa, P. (2005). Star Cluster Survival in Star Cluster Complexes under Extreme Residual Gas Expulsion. *ApJ*, 630(2):879–886.
- Ferland, G. J., Chatzikos, M., Guzmán, F., Lykins, M. L., Van Hoof, P. A. M., Williams, R. J. R., Abel, N. P., Badnell, N. R., Keenan, F. P., Porter, R. L., and Stancil, P. C. (2017). The 2017 Release of CLOUDY. *Rev. Mex. Astron. Astrofis.*, 53:385–438.
- Figer, D. F. (2005). An upper limit to the masses of stars. *Nature*, 434:192–194.
- Foglizzo, T. (2017). Explosion Physics of Core-Collapse Supernovae. In Alsabti, A. W. and Murdin, P., editors, *Handb. Supernovae*, pages 1053–1073. Springer, Cham, Switzerland.
- Frank, A., Ray, T., Cabrit, S., Hartigan, P., Arce, H., Bacciotti, F., Bally, J., Benisty, M., and Eisloffel, J. (2014). Jets and Outflows From Star to Cloud: Observations Confront Theory. In Beuther, H., Klessen, R. S., Dullemond, C. P., and Henning, T., editors, *Protostars Planets VI*, pages 451–474. University of Arizona Press, Tucson, USA.
- Fryxell, B., Olson, K., Ricker, P., Timmes, F. X., Zingale, M., Lamb, D. Q., MacNeice, P., Rosner, R., Truran, J. W., and Tufo, H. (2000). FLASH: An Adaptive Mesh Hydrodynamics Code for Modeling Astrophysical Thermonuclear Flashes. *ApJS*, 131:273–334.
- Fukui, Y. and Kawamura, A. (2010). Molecular Clouds in Nearby Galaxies. *ARA&A*, 48:547–580.
- Fukui, Y., Mizuno, N., Yamaguchi, R., Mizuno, A., Onishi, T., Ogawa, H., Yonekura, Y., Kawamura, A., Tachihara, K., Xiao, K., Yamaguchi, N., Hara, A., Hayakawa, T., Kato, S., Abe, R., Saito, H., Mano, S., Matsunaga, K., Mine, Y., Moriguchi, Y., Aoyama, H., Asayama, S., Yoshikawa, N., and Rubio, M. (1999). First Results of a CO survey of the Large Magellanic Cloud with NANTEN; Giant Molecular Clouds as Formation Sites of Populous Clusters. *PASJ*, 51:745–749.
- Gal-Yam, A. (2017). Observational and Physical Classification of Supernovae. In Alsabti, A. W. and Murdin, P., editors, *Handb. Supernovae*, pages 195–237. Springer, Cham, Switzerland.

- Gatto, A., Walch, S., Mac Low, M. M., Naab, T., Girichidis, P., Glover, S. C. O., Wunsch, R., Klessen, R. S., Clark, P. C., Baczynski, C., Peters, T., Ostriker, J. P., Ibáñez-Mejía, J. C., and Haid, S. (2015). Modelling the supernova-driven ISM in different environments. *MNRAS*, 449(1):1057–1075.
- Gatto, A., Walch, S., Naab, T., Girichidis, P., Glover, S. C. O., Klessen, R. S., Clark, P. C., Peters, T., Derigs, D., Baczynski, C., and Puls, J. (2017). The SILCC project – III. Regulation of star formation and outflows by stellar winds and supernovae. *MNRAS*, 466:1903–1924.
- Gayley, K. G. (1995). An improved line-strength parameterization in hot-star winds. *ApJ*, 454:410–419.
- Geen, S., Hennebelle, P., Tremblin, P., and Rosdahl, J. (2016). Feedback in Clouds II: UV photoionization and the first supernova in a massive cloud. *MNRAS*, 463:3129–3142.
- Geen, S., Rosdahl, J., Blaizot, J., Devriendt, J., and Slyz, A. (2015). A detailed study of feedback from a massive star. *MNRAS*, 448(4):3248–3264.
- Geen, S., Soler, J. D., and Hennebelle, P. (2017). Interpreting the star formation efficiency of nearby molecular clouds with ionizing radiation. *MNRAS*, 471:4844–4855.
- Georgy, C., Meynet, G., Ekström, S., Wade, G. A., Petit, V., Keszthelyi, Z., and Hirschi, R. (2017). Possible pair-instability supernovae at solar metallicity from magnetic stellar progenitors. *A&A*, 599:L5.
- Geyer, M. P. and Burkert, A. (2001). The effect of gas loss on the formation of bound stellar clusters. *MNRAS*, 323(4):988–994.
- Girichidis, P., Federrath, C., Banerjee, R., and Klessen, R. S. (2012). Importance of the initial conditions for star formation - II. Fragmentation-induced starvation and accretion shielding. *MNRAS*, 420(1):613–626.
- Glover, S. C. O. and Brand, P. W. J. L. (2001). On the photodissociation of H₂ by the first stars. *MNRAS*, 321:385–397.
- Glover, S. C. O. and Mac Low, M.-M. (2011). On the relationship between molecular hydrogen and carbon monoxide abundances in molecular clouds. *MNRAS*, 412:337–350.
- Gnat, O. and Ferland, G. J. (2012). Ion-By-Ion Cooling Efficiencies. *ApJS*, 199(1):20.
- Goldbaum, N. J., Krumholz, M. R., Matzner, C. D., and Mckee, C. F. (2011). The global evolution of giant molecular clouds. II. The role of accretion. *ApJ*, 738:101.
- Goodwin, S. (2013). Star Formation. In Oswald, T. D. and Barstow, M. A., editors, *Planets, Stars Stellar Syst. Vol. 4 Stellar Struct. Evol.*, pages 243–277. Springer, Dordrecht, Netherlands.
- Goodwin, S. P. (2009). The effect of the dynamical state of clusters on gas expulsion and infant mortality. *Ap&SS*, 324(2):259–263.
- Gouliermis, D. A., Stephens, I. W., Looney, L. W., Gruendl, R. A., Chu, Y.-H., Weisz, D. R., Seale, J. P., Chen, C.-H. R., Wong, T., Hughes, A., Pineda, J. L., Ott, J., and Muller, E. (2018). Isolated massive star formation Myth or reality? *Mem. S.A.It*, 89:57.
- Grand, R. J. J., Gómez, F. A., Marinacci, F., Pakmor, R., Springel, V., Campbell, D. J. R., Frenk, C. S., Jenkins, A., and White, S. D. M. (2017). The Auriga Project: the properties and formation mechanisms of disc galaxies across cosmic time. *MNRAS*, 467:179–207.
- Green, D. A. (2014). A catalogue of 294 Galactic supernova remnants. *Bulletin of the Astronomical Society of India*, 42:47–58.

References

- Green, D. A. (2017). Historical Supernovae in the Galaxy from AD 1006. In Alsabti, A. W. and Murdin, P., editors, *Handb. Supernovae*, pages 37–48. Cham, Switzerland.
- Green, S. F. and Jones, M. H. (2015). *An Introduction to the Sun and Stars*. Cambridge University Press, Cambridge, UK, second edition.
- Grudić, M. Y., Hopkins, P. F., Faucher-Giguère, C.-A., Quataert, E., Murray, N., and Kereš, D. (2018). When feedback fails: the scaling and saturation of star formation efficiency. *MNRAS*, 475:3511–3528.
- Haid, S., Walch, S., Seifried, D., Dinnbier, F., and Naab, T. (2018). The relative impact of photoionizing radiation and stellar winds on different environments. *MNRAS*, 478:4799–4815.
- Haid, S., Walch, S., Seifried, D., Dinnbier, F., and Naab, T. (2019). SILCC-Zoom: The early impact of ionizing radiation on forming molecular clouds. *MNRAS*, 482:4062–4083.
- Haworth, T. J., Glover, S. C. O., Koepferl, C. M., Bisbas, T. G., and Dale, J. E. (2018). Synthetic observations of star formation and the interstellar medium. *New Astron. Rev.*, 82:1–58.
- Heger, A., Fryer, C. L., Woosley, S. E., Langer, N., and Hartmann, D. H. (2003). How massive single stars end their life. *ApJ*, 591:288–300.
- Heitsch, F., Mac Low, M.-M., and Klessen, R. S. (2001). Gravitational collapse in turbulent molecular clouds. II. Magnetohydrodynamical turbulence. *ApJ*, 547:280–291.
- Hennebelle, P. and Chabrier, G. (2008). Analytical theory for the initial mass function: CO clumps and prestellar cores. *ApJ*, 684:395–410.
- Hennebelle, P. and Falgarone, E. (2012). Turbulent molecular clouds. *A&ARv*, 20:55.
- Heyer, M. H. and Brunt, C. M. (2012). Trans-Alfvénic motions in the Taurus molecular cloud. *MNRAS*, 420:1562–1569.
- Hillier, D. J. and Miller, D. L. (1998). The treatment of non-LTE line blanketing in spherically expanding outflows. *ApJ*, 496:407–427.
- Hills, J. G. (1980). The effect of mass loss on the dynamical evolution of a stellar system - Analytic approximations. *ApJ*, 235(2):986.
- Howard, C., Pudritz, R., and Harris, W. (2016). Simulating radiative feedback and star cluster formation in GMCs: I. Dependence on gravitational boundedness. *MNRAS*, 461:2953–2974.
- Howard, C. S., Pudritz, R. E., and Harris, W. E. (2017). Simulating radiative feedback and star cluster formation in GMCs – II. Mass dependence of cloud destruction and cluster properties. *MNRAS*, 470:3346–3358.
- Hughes, A., Wong, T., Ott, J., Muller, E., Pineda, J. L., Mizuno, Y., Bernard, J.-P., Paradis, D., Maddison, S., and Fukui, Y. (2010). Physical properties of giant molecular clouds in the Large Magellanic Cloud. *MNRAS*, 406:2065–2086.
- Janka, H.-T. (2017). Neutrino-Driven Explosions. In Alsabti, A. W. and Murdin, P., editors, *Handb. Supernovae*, pages 1095–1150. Springer, Cham, Switzerland.
- Jeans, J. H. (1902). The Stability of a Spherical Nebula. *Philos. Trans. R. Soc. London Ser. A*, 199(4089):1–53.
- Kahn, F. D. (1974). Cocoons around Early-type Stars. *A&A*, 37:149–162.

- Kauffmann, G., Heckman, T. M., Tremonti, C., Brinchmann, J., Charlot, S., White, S. D. M., Ridgway, S. E., Brinkmann, J., Fukugita, M., Hall, P. B., Ivezi, Z., Richards, G. T., and Schneider, D. P. (2003). The host galaxies of active galactic nuclei. *MNRAS*, 346:1055–1077.
- Kawamura, A., Mizuno, Y., Minamidani, T., Filipovi, M. D., Staveley-Smith, L., Kim, S., Mizuno, N., Onishi, T., Mizuno, A., and Fukui, Y. (2009). The second survey of the molecular clouds in the large magellanic cloud by NANTEN. II. Star formation. *ApJS*, 184:1–17.
- Kennicutt, R. C. J. (1998). The Global Schmidt Law in Star-forming Galaxies. *ApJ*, 498:541–552.
- Kewley, L. J., Dopita, M. A., Leitherer, C., Davé, R., Yuan, T., Allen, M., Groves, B., and Sutherland, R. (2013). Theoretical evolution of optical strong lines across cosmic time. *ApJ*, 774:100.
- Kewley, L. J., Dopita, M. A., Sutherland, R. S., Heisler, C. A., and Trevena, J. (2001). Theoretical modeling of starburst galaxies. *ApJ*, 556:121–140.
- Kim, J.-G., Kim, W.-T., and Ostriker, E. C. (2016). Disruption of Molecular Clouds by Expansion of Dusty HII Regions. *ApJ*, 819(2):137.
- Kim, J.-G., Kim, W.-T., and Ostriker, E. C. (2018). Modeling UV Radiation Feedback from Massive Stars. II. Dispersal of Star-forming Giant Molecular Clouds by Photoionization and Radiation Pressure. *ApJ*, 859:68.
- Klessen, R. S. and Burkert, A. (2001). The formation of stellar clusters: Gaussian cloud conditions. II. *ApJ*, 549:386–401.
- Klessen, R. S. and Glover, S. C. O. (2016). Physical Processes in the Interstellar Medium. In Revaz, Y., Jablonka, P., Teyssier, R., and Mayer, L., editors, *Star Form. Galaxy Evol. Connect. Numer. Model. to Real. Saas-Fee Adv. Course 43. Swiss Soc. Astrophys. Astron.*, pages 85–250. Springer, Heidelberg, Germany.
- Klessen, R. S., Heitsch, F., and Mac Low, M.-M. (2000). Gravitational collapse in turbulent molecular clouds. I. Gasdynamical turbulence. *ApJ*, 535:887–906.
- Klessen, R. S. and Hennebelle, P. (2010). Accretion-driven turbulence as universal process: galaxies, molecular clouds, and protostellar disks. *A&A*, 520:17.
- Koen, C. (2006). On the upper limit on stellar masses in the Large Magellanic Cloud cluster R136. *MNRAS*, 365:590–594.
- Koester, D. (2002). White dwarfs: Recent developments. *A&ARv*, 11(1):33–66.
- Koo, B.-C. and McKee, C. (1992a). Dynamics of Wind Bubbles and Superbubbles. I. Slow Winds and Fast Winds. *ApJ*, 388:93–102.
- Koo, B.-C. and McKee, C. (1992b). Dynamics of Wind Bubbles and Superbubbles. II. Analytic Theory. *ApJ*, 388:103–126.
- Kroupa, P. (2001). On the variation of the initial mass function. *MNRAS*, 322:231–246.
- Kroupa, P. (2002). The Initial Mass Function of Stars: Evidence for Uniformity in Variable Systems. *Science*, 295:82–91.
- Kruijssen, D. J. M. and Longmore, S. N. (2014). An uncertainty principle for star formation - I. Why galactic star formation relations break down below a certain spatial scale. *MNRAS*, 439(4):3239–3252.

References

- Kruijssen, J. M. D., Schrubba, A., Hygate, A. P. S., Hu, C.-Y., Haydon, D. T., and Longmore, S. N. (2018). An uncertainty principle for star formation – II. A new method for characterizing the cloud-scale physics of star formation and feedback across cosmic history. *MNRAS*, 479(2):1866–1952.
- Krumholz, M., McKee, C., and Tumlinson, J. (2008). The Atomic-to-Molecular Transition in Galaxies. I. An Analytic Approximation for Photodissociation Fronts in Finite Clouds. *ApJ*, 689:865–882.
- Krumholz, M. R. (2018). Resolution requirements and resolution problems in simulations of radiative feedback in dusty gas. *MNRAS*, 480:3468–3482.
- Krumholz, M. R., Bate, M. R., Arce, H. G., Dale, J. E., Gutermuth, R., Klein, R. I., Li, Z., Nakamura, F., and Zhang, Q. (2014). Star Cluster Formation and Feedback. In Beuther, H., Klessen, R. S., Dullemond, C. P., and Henning, T., editors, *Protostars Planets VI*, pages 243–266. University of Arizona Press, Tucson, USA.
- Krumholz, M. R. and Matzner, C. D. (2009). The Dynamics of Radiation-Pressure-Dominated HII Regions. *ApJ*, 703(2):1352–1362.
- Krumholz, M. R., Matzner, C. D., and McKee, C. F. (2006). The global evolution of giant molecular clouds. I. Model formulation and quasi-equilibrium behavior. *ApJ*, 653:361–382.
- Krumholz, M. R. and McKee, C. F. (2005). A General Theory of Turbulence-Regulated Star Formation, From Spirals to ULIRGs. *ApJ*, 630(2003):250–268.
- Krumholz, M. R., McKee, C. F., and Bland-Hawthorn, J. (2018). Star Clusters Across Cosmic Time. *ARA&A*, preprint(arXiv:1812.01615v2).
- Krumholz, M. R. and Tan, J. C. (2007). Slow Star Formation in Dense Gas: Evidence and Implications. *ApJ*, 654:304–315.
- Kuiper, R. and Hosokawa, T. (2018). First hydrodynamics simulations of radiation forces and photoionization feedback in massive star formation. *A&A*, 616:101.
- Kuiper, R., Klahr, H., Beuther, H., and Henning, T. (2010). Circumventing the Radiation Pressure Barrier in the Formation of Massive Stars Via Disk Accretion. *ApJ*, 722(2):1556–1576.
- Lada, C. J. and Lada, E. a. (2003). Embedded Clusters in Molecular Clouds. *ARA&A*, 41:57–115.
- Lada, C. J., Lombardi, M., and Alves, J. F. (2010). on the Star Formation Rates in Molecular Clouds. *ApJ*, 724(1):687–693.
- Lada, C. J., Margulis, M., and Dearborn, D. (1984). The formation and early dynamical evolution of bound stellar systems. *285*, 285:141–152.
- Lamb, J. B., Oey, M. S., Werk, J. K., and Ingleby, L. D. (2010). The sparsest clusters with O stars. *ApJ*, 725:1886–1902.
- Lamberts, A., Fromang, S., and Dubus, G. (2011). High-resolution numerical simulations of unstable colliding stellar winds. *MNRAS*, 418:2618–2629.
- Lamers, H. and Cassinelli, J. (1999). *Introduction to Stellar Winds*. Cambridge University Press, Cambridge, UK.
- Larson, R. B. (1969). Numerical Calculations of the Dynamics of a Collapsing Proto-Star. *MNRAS*, 145:271–295.
- Larson, R. B. (1973). Processes in collapsing interstellar clouds. *ARA&A*, 11:219–238.

- Larson, R. B. (1981). Turbulence and star formation in molecular clouds. *MNRAS*, 194:809–826.
- Larson, R. B. and Starfield, S. (1971). On the Formation of Massive Stars and the Upper Limit of Stellar Masses. *A&A*, 13:190–197.
- Lee, E. J., Miville-Deschênes, M.-A., and Murray, N. W. (2016). Observational evidence of dynamic star formation rate in milky way giant molecular clouds. *ApJ*, 833:229.
- Lee, P. L. and Goodwin, S. P. (2016). Surviving gas expulsion with substructure. *MNRAS*, 460:2997–3001.
- Leitherer, C., Ekström, S., Meynet, G., Schaerer, D., Agienko, K. B., and Levesque, E. M. (2014). The Effects of Stellar Rotation. II. A Comprehensive Set of Starburst99 Models. *ApJS*, 212(1):14.
- Licquia, T. C. and Newman, J. A. (2015). Improved estimates of the Milky Way’s stellar mass and star formation rate from hierarchical Bayesian meta-analysis. *ApJ*, 806:96.
- Limongi, M. (2017). Supernovae from massive stars. In Alsabti, A. W. and Murdin, P., editors, *Handb. Supernovae*, pages 513–565. Springer, Cham, Switzerland.
- Liu, M., Tan, J. C., Cheng, Y., and Kong, S. (2018). The Core Mass Function across Galactic Environments. II. Infrared Dark Cloud Clumps. *ApJ*, 862(2):105.
- Lockwood, G. J., Helbig, H. F., and Everhart, E. (1964). Measurements of Thermal Dissociation of Hydrogen, Using Fast Protons. *J. Chem. Phys.*, 41:3820.
- Mac Low, M.-M. (1999). The energy dissipation rate of supersonic, magnetohydrodynamic turbulence in molecular clouds. *ApJ*, 524:169–178.
- Mac Low, M. M. and Klessen, R. S. (2004). Control of star formation by supersonic turbulence. *Rev. Mod. Phys.*, 76(1):125–194.
- Mac Low, M.-M. and McCray, R. (1988). Superbubbles in disk galaxies. *ApJ*, 324:776–785.
- Martínez-González, S., Silich, S., and Tenorio-Tagle, G. (2014). On the Impact of Radiation Pressure on the Dynamics and Inner Structure of Dusty Wind-Driven Shells. *ApJ*, 785(2):164.
- Massey, P. (2003). Massive Stars in the Local Group: Implications for Stellar Evolution and Star Formation. *ARA&A*, 41:15–56.
- Matzner, C. D. (2002). On the Role of Massive Stars in the Support and Destruction of Giant Molecular Clouds. *ApJ*, 566(1):302–314.
- Matzner, C. D. (2007). Protostellar outflow-driven turbulence. *ApJ*, 659:1394–1403.
- Matzner, C. D. and Jumper, P. H. (2015). Star cluster formation with stellar feedback and large-scale inflow. *ApJ*, 815(1):68.
- Matzner, C. D. and Mckee, C. F. (1999). The Expulsion of Stellar Envelopes in Core-Collapse Supernovae. *ApJ*, 510:379–403.
- McKee, C. F. and Ostriker, E. C. (2007). Theory of Star Formation. *ARA&A*, 45:565–687.
- McKee, C. F. and Ostriker, J. P. (1977). A theory of the interstellar medium - Three components regulated by supernova explosions in an inhomogeneous substrate. *ApJ*, 218:148.
- Minkowski, R. (1941). Spectra of Supernovae. *PASP*, 53:224.

References

- Miura, R. E., Kohno, K., Tosaki, T., Espada, D., Hwang, N., Kuno, N., Okumura, S. K., Hirota, A., Muraoka, K., Onodera, S., Minamidani, T., Komugi, S., Nakanishi, K., Sawada, T., Kaneko, H., and Kawabe, R. (2012). Giant molecular cloud evolutions in the nearby spiral galaxy M33. *ApJ*, 761:37.
- Miville-Deschênes, M.-A., Murray, N., and Lee, E. J. (2017). Physical properties of molecular clouds for the entire Milky Way disk. *ApJ*, 834:57.
- Motte, F., André, P., and Neri, R. (1998). The initial conditions of star formation in the ρ Ophiuchi main cloud: wide-field millimeter continuum mapping. *A&A*, 336:150–172.
- Murray, N. (2011). Star formation efficiencies and lifetimes of giant molecular clouds in the Milky Way. *ApJ*, 729:133.
- Nutter, D. and Ward-Thompson, D. (2007). A SCUBA survey of Orion - the low-mass end of the core mass function. *MNRAS*, 374:1413–1420.
- Ochsendorf, B. B., Meixner, M., Roman-Duval, J., Rahman, M., and Evans, N. J. (2017). What Sets the Massive Star Formation Rates and Efficiencies of Giant Molecular Clouds? *ApJ*, 841:109.
- O’Dell, C. R., York, D. G., and Henize, K. G. (1967). Structure of the Barnard Loop Nebula as determined from Gemini 11 photographs. *ApJ*, 150:835.
- Offner, S. S. R., Clark, P. C., Hennebelle, P., Bastian, N., Bate, M. R., Hopkins, P. F., Moraux, E., and Whitworth, A. P. (2014). The Origin and Universality of the Stellar Initial Mass Function. In Beuther, H., Klessen, R. S., Dullemond, C. P., and Henning, T., editors, *Protostars Planets VI*, pages 53–75. University of Arizona Press, Tucson, USA.
- Offner, S. S. R. and Liu, Y. (2018). Turbulent action at a distance due to stellar feedback in magnetized clouds. *Nature Astronomy*, 2:896–900.
- Osterbrock, D. and Ferland, G. (2006). *Astrophysics of gaseous nebulae and active galactic nuclei*. University Science Books, Sausalito, USA, second edition.
- Owocki, S. (2013). Stellar Winds. In Oswalt, T. D. and Barstow, M. A., editors, *Planets, Stars Stellar Syst. Vol. 4 Stellar Struct. Evol.*, pages 735–788. Springer, Dordrecht, Netherlands.
- Oxford Dictionary (2019). <https://en.oxforddictionaries.com/definition/feedback>. Accessed: 2019-03-06.
- Padoan, P. and Nordlund, Å. (2002). The stellar initial mass function from turbulent fragmentation. *ApJ*, 576:870–879.
- Parmentier, G. and Gilmore, G. (2007). The origin of the Gaussian initial mass function of old globular cluster systems. *MNRAS*, 377:352–372.
- Parmentier, G. and Pfalzner, S. (2013). Local-density-driven clustered star formation. *A&A*, 549:132.
- Pauldrach, A. W. A., Hoffmann, T. L., and Lennon, M. (2001). Radiation-driven winds of hot luminous stars XIII. A description of NLTE line blocking and blanketing towards realistic models for expanding atmospheres. *A&A*, 375:161–195.
- Peters, T., Klessen, R. S., Low, M.-M. M., and Banerjee, R. (2010). Limiting Accretion Onto Massive Stars By Fragmentation-Induced Starvation. *ApJ*, 725(1):134–145.
- Puls, J., Springmann, U., and Lennon, M. (2000). Radiation driven winds of hot luminous stars XIV. Line statistics and radiative driving. *A&AS*, 141:23–64.
- Puls, J., Vink, J. S., and Najarro, F. (2008). Mass loss from hot massive stars. *A&ARv*, 16:209–325.

- Rathborne, J. M., Jackson, J. M., and Simon, R. (2006). Infrared dark clouds: precursors to star clusters. *ApJ*, 641:389–405.
- Reissl, S., Klessen, R. S., Low, M.-M. M., and Pellegrini, E. W. (2018). Astronomy Spectral shifting strongly constrains molecular cloud disruption by radiation pressure on dust. *A&A*, 611:70.
- Reissl, S., Wolf, S., and Brauer, R. (2016). Astrophysics Radiative transfer with POLARIS I. Analysis of magnetic fields through synthetic dust continuum polarization measurements. *A&A*, 593:87.
- Reynolds, S. P. (2017). Dynamical Evolution and Radiative Processes of Supernova Remnants. In Alsabti, A. W. and Murdin, P., editors, *Handb. Supernovae*, pages 1981–2004. Springer, Cham, Switzerland.
- Rho, J., Hewitt, J. W., Bieging, J., Reach, W. T., Andersen, M., and Güsten, R. (2017). Discovery of Broad Molecular Lines and of Shocked Molecular Hydrogen from the Supernova Remnant G357.7+0.3: HHSMT, APEX, Spitzer, and SOFIA Observations. *ApJ*, 834:12.
- Rogers, H. and Pittard, J. M. (2013). Feedback from winds and supernovae in massive stellar clusters - I. Hydrodynamics. *MNRAS*, 431:1337–1351.
- Roman-Duval, J., Heyer, M., Brunt, C. M., Clark, P., Klessen, R., and Shetty, R. (2016). Distribution and mass of diffuse and dense CO gas in the Milky Way. *ApJ*, 818:144.
- Rousseau-Nepton, L., Robert, C., Martin, R. P., Drissen, L., and Martin, T. (2018). NGC628 with SITELLE: I. Imaging spectroscopy of 4285 H II region candidates. *MNRAS*, 477:4152–4186.
- Rugel, M. R., Rahner, D., Beuther, H., Pellegrini, E. W., Wang, Y., Soler, J. D., Ott, J., Brunthaler, A., Anderson, L. D., Mottram, J. C., Henning, T., Goldsmith, P. F., Heyer, M., Klessen, R. S., Bihr, S., Menten, K. M., Smith, R. J., Urquhart, J. S., Ragan, S. E., Glover, S. C. O., Bigiel, F., and Roy, N. (2019). Feedback in W49A diagnosed with radio recombination lines and models. *A&A*, 622:A48.
- Sabbi, E., Lennon, D. J., Gieles, M., Mink, S. E. D., Walborn, N. R., Anderson, J., Bellini, A., Panagia, N., Van Der Marel, R., and Maíz-Apellániz, J. (2012). A double cluster at the core of 30 Doradus. *ApJ Letters*, 37:6–11.
- Salaris, M. and Cassisi, S. (2005). *Evolution of Stars and Stellar Populations*. John Wiley & Sons, Chichester, UK.
- Salpeter, E. E. (1955). The luminosity function and stellar evolution. *ApJ*, 121:161.
- Schmidt, M. (1959). The rate of star formation. *ApJ*, 129(2):243.
- Schruba, A., Leroy, A. K., Walter, F., Sandstrom, K., and Rosolowsky, E. (2010). The scale dependence of the molecular gas depletion time in M33. *ApJ*, 722:1699–1706.
- Sedov, L. I. (1961). *Similarity and Dimensional Methods in Mechanics*. Academic Press, New York, USA, second edition.
- Seeds, M. A. and Backman, D. E. (2013). *Foundations of Astronomy*. Brooks/Cole, Canada, twelfth edition.
- Shetty, R., Glover, S. C., Dullemond, C. P., and Klessen, R. S. (2011). Modelling CO emission - I. CO as a column density tracer and the X factor in molecular clouds. *MNRAS*, 412:1686–1700.
- Shu, F. H. (1992). *The Physics of Astrophysics. Vol. II: Gas Dynamics*. University Science Books, Sausalito, USA.

References

- Shu, F. H., Adams, F. C., and Lizano, S. (1987). Star formation in molecular clouds - Observation and theory. *ARA&A*, 25:23–81.
- Shukirgaliyev, B., Parmentier, G., Berczik, P., and Just, A. (2017). Impact of a star formation efficiency profile on the evolution of open clusters. *A&A*, 605:119.
- Shukirgaliyev, B., Parmentier, G., Just, A., and Berczik, P. (2018). The long-term evolution of star clusters formed with a centrally-peaked star-formation-efficiency profile. *ApJ*, 863:171.
- Silich, S. and Tenorio-Tagle, G. (2013). How Significant Is Radiation Pressure in the Dynamics of the Gas Around Young Stellar Clusters? *ApJ*, 765(1):43.
- Silich, S. and Tenorio-Tagle, G. (2017). Gas expulsion versus gas retention: what process dominates in young massive clusters? *MNRAS*, 465(2):1375–1383.
- Solomon, P. M., Rivolo, A. R., Barrett, J., and Yahil, A. (1987). Mass, Luminosity, and Line Width Relations of Galactic Molecular Clouds. *ApJ*, 319:730–741.
- Spitzer, L. (2004). *Physical processes in the interstellar medium*. WILEY-VCH, Weinheim, Germany. (Original work published 1978).
- Stahler, S. W. and Palla, F. (2004). *The Formation of Stars*. WILEY-VCH, Weinheim, Germany.
- Stephens, I. W., Gouliermis, D., Looney, L. W., Gruendl, R. A., Chu, Y.-H., Weisz, D. R., Seale, J. P., Chen, C.-H. R., Wong, T., Hughes, A., Pineda, J. L., Ott, J., and Muller, E. (2017). Stellar Clustering Around "Isolated" Massive YSOs in the LMC. *ApJ*, 834:94.
- Strömberg, B. (1939). The physical state of interstellar hydrogen. *ApJ*, 89(2):526.
- Sukhbold, T., Ertl, T., Woosley, S. E., Brown, J. M., and Janka, H.-T. (2016). Core-collapse supernovae from 9 to 120 solar masses based on neutrino-powered explosions. *ApJ*, 821:38.
- Townsley, L. K., Broos, P. S., Chu, Y.-H., Gruendl, R. a., Oey, M. S., and Pittard, J. M. (2011). The Integrated Diffuse X-Ray Emission of the Carina Nebula Compared to Other Massive Star-Forming Regions. *ApJS*, 194(1):16.
- Tutukov, A. V. (1978). Early Stages of Dynamical Evolution of Star Cluster Models. *A&A*, 70:57–61.
- Urquhart, J. S., König, C., Giannetti, A., Leurini, S., Moore, T. J., Eden, D. J., Pillai, T., Thompson, M. A., Braiding, C., Burton, M. G., Csengeri, T., Dempsey, J. T., Figura, C., Froebrich, D., Menten, K. M., Schuller, F., Smith, M. D., and Wyrowski, F. (2018). ATLASGAL - Properties of a complete sample of Galactic clumps. *MNRAS*, 473(1):1059–1102.
- Veilleux, S. and Osterbrock, D. E. (1987). Spectral Classification of Emission-Line Galaxies. *ApJS*, 63:295–310.
- Vink, J. S., De Koter, A., and Lamers, H. J. G. L. M. (2000). New theoretical mass-loss rates of O and B stars. *A&A*, 362:295–309.
- Vink, J. S., De Koter, A., and Lamers, H. J. G. L. M. (2001). Mass-loss predictions for O and B stars as a function of metallicity. *A&A*, 369:574–588.
- Walch, S. and Naab, T. (2015). The energy and momentum input of supernova explosions in structured and ionized molecular clouds. *MNRAS*, 451(3):2757–2771.
- Walch, S. K., Whitworth, A. P., Bisbas, T., Wunsch, R., and Hubber, D. (2012). Dispersal of molecular clouds by ionizing radiation. *MNRAS*, 427(1):625–636.

- Weaver, R., McCray, R., Castor, J., Shapiro, P., and Moore, R. (1977). Interstellar bubbles. II. Structure and evolution. *ApJ*, 218(2):377–395.
- Weidner, C. and Kroupa, P. (2006). The maximum stellar mass, star-cluster formation and composite stellar populations. *MNRAS*, 365:1333–1347.
- Weidner, C. and Vink, J. S. (2010). The masses, and the mass discrepancy of O-type stars. *A&A*, 524:98.
- Weingartner, J. C. and Draine, B. T. (2001). Dust Grain-Size Distributions and Extinction in the Milky Way, Large Magellanic Cloud, and Small Magellanic Cloud. *ApJ*, 548:296–309.
- Whitworth, A. (1979). The erosion and dispersal of massive molecular clouds by young stars. *MNRAS*, 186:59–67.
- Yorke, H. W. (1986). The dynamical evolution of HII regions - recent theoretical developments. *ARA&A*, 24:49–87.
- Yorke, H. W. and Sonnhalter, C. (2002). On the Formation of Massive Stars. *ApJ*, 569:846–862.
- Zinnecker, H. and Yorke, H. W. (2007). Toward Understanding Massive Star Formation. *ARA&A*, 45:481–563.
- Zuckerman, B. and Palmer, P. (1974). Radio Radiation from Interstellar Molecules. *ARA&A*, 12:279–313.